Ab 110

DOE/ET-0065/6

~~$8~~
~~9-11-79~~
203
10/1/79

Damage Analysis and Fundamental Studies

Quarterly Progress Report
April-June, 1979

July 1979

U.S. Department of Energy
Assistant Secretary for Energy Technology
Office of Fusion Energy

Available from:

National Technical Information Service (NTIS)
U.S. Department of Commerce
5285 Port Royal Road
Springfield, Virginia 22161

Price:	Printed copy:	$9.50
	Microfiche:	$3.00

DOE/ET-0065/6
UC-20,20c

Damage Analysis and Fundamental Studies

Quarterly Progress Report
April-June, 1979

July 1979

U.S. Department of Energy
Assistant Secretary for Energy Technology
Office of Fusion Energy
Washington, D.C. 20545

THIS PAGE

WAS INTENTIONALLY

LEFT BLANK

FOREWORD

This report is the sixth in a series of Quarterly Technical Progress Reports on *"Damage Analysis and Fundamental Studies"* (DAFS) which is one element of the Fusion Reactor Materials Program, conducted in support of the Magnetic Fusion Energy Program of the U. S. Department of Energy. Other elements of the Materials Program are:

- *Alloy Development for Irradiation Performance (ADIP)*
- *Plasma-Materials Interaction (PMI)*
- *Special Purpose Materials (SPM).*

The DAFS program element is a national effort composed of contributions from a number of National Laboratories and other government laboratories, universities, and industrial laboratories. It was organized by the Materials and Radiation Effects Branch, Office of Fusion Energy, DOE, and a Task Group on *Damage Analysis and Fundamental Studies* which operates under the auspices of that Branch. The purpose of this series of reports is to provide a working technical record of that effort for the use of the program participants, for the fusion energy program in general, and for the Department of Energy.

This report is organized along topical lines in parallel to a Program Plan of the same title (to be published) so that activities and accomplishments may be followed readily relative to that Program Plan. Thus, the work of a given laboratory may appear throughout the report. Chapters 1 and 2 report topics which are generic to all of the DAFS Program: DAFS Task Group Activities and Irradiation Test Facilities, respectively. Chapters 3, 4, and 5 report the work that is specific to each of the subtasks around which the program is structured: A. Environmental Characterization, B. Damage Production, and C. Damage Microstructure Evolution and Mechanical Behavior. The Table of Contents is annotated for the convenience of the reader.

This report has been compiled and edited under the guidance of the Chairman of the Task Group on *Damage Analysis and Fundamental Studies*, D. G. Doran, Hanford Engineering Development Laboratory, and his efforts, those of the supporting staff of HEDL and the many persons who made technical contributions are gratefully acknowledged. T. C. Reuther, Materials and Radiation Effects Branch, is the Department of Energy counterpart to the Task Group Chairman and has responsibility for the DAFS Program within DOE.

Klaus M. Zwilsky, Chief
Materials and Radiation
Effects Branch
Office of Fusion Energy

THIS PAGE

WAS INTENTIONALLY

LEFT BLANK

CONTENTS

A Subtask Group meeting on damage production calculations and models was held at Livermore on June 7-8.

Procurement has begun of DAFS specimen materials.

A deuteron beam diagnostics system has been installed in order to improve neutron utilization. Irradiation, dosimetry and handling services are routinely being provided for user laboratories.

Flux-spectral measurements in core position E7 of the Oak Ridge Research Reactor are summarized; the fraction of neutrons below 1 MeV is less than indicated by neutronic calculations. The analysis of ORR-MFE1 dosimetry is nearly completed.

CONTENTS (Cont'd)

CONTENTS (Cont'd)

Page

5A. High Energy Neutron Cross Sections for Transport and Damage Calculations (HEDL) 33

The evaluation of 20 to 60 MeV neutron cross sections for neutron transport and damage calculations is described.

5B. Deuteron and Neutron Induced Activation of FMIT Accelerator and Beam Transport Structural Materials (HEDL) 35

Calculations of deuteron and neutron induced activation of FMIT structural materials identify Fe and Co as the largest contributors for all irradiation and cooling times examined.

5C. Deuteron and Neutron Induced Activation of the Lithium Target (HEDL) 36

A preliminary measurement of deuteron-induced production of ^{7}*Be, one of the most troublesome radioactivants in the FMIT lithium target system, gave a higher yield than anticipated.*

6A. Cross Section Prediction (HEDL) 40

The few parameters in the model for angular distributions of outgoing particles can be expressed as functions of ℓ*, the order of the Legendre polynomial.*

CONTENTS (Cont'd)

Page

6B. Neutron Yield Experiments (HEDL) 40

Results of measurements of the yield and spectra of neutrons from 35 MeV deuterons on thick targets of both natural lithium and ^6Li *are described.*

6C. Microscopic Neutron Yield Model (HEDL) 43

The microscopic neutron yield model is being updated using HEDL-UCD experimental results, least-squares adjustment techniques and nuclear models.

7A. Use of the Magnetic Fusion Energy Computer Center (BNL) 45

Transfer of damage analysis calculations to the MFECC is progressing.

7B. Cross Sections for Atomic Displacements by Gamma Rays (BNL) 45

The displacement cross sections for both gamma rays and neutrons have been evaluated for Al_2O_3.

CONTENTS (Cont'd)

CONTENTS (Cont'd)

Page

5A. RTNS-II Irradiation Program (HEDL) 84

Two ambient temperature irradiations at RTNS-II have been completed to estimated fluences of 3 x 10^{17} n/cm^2 and 1 x 10^{18} n/cm^2. Specimens were TEM disks of pure metals, Fe-Ni-Cr, Fe-Ni-Cr-Mo, and representative alloy development program materials.

5B. RTNS-II Furnace Development (HEDL) 88

Construction of a high temperature, ultra high vacuum furnace for general use at RTNS-II has been completed.

5C. LPTR Furnace Development (HEDL) 88

A furnace to be used in the Livermore Pool-Type Reactor (LPTR) is being designed at LLL as a joint LLL-HEDL project.

CHAPTER 5. SUBTASK C: DAMAGE MICROSTRUCTURE EVOLUTION AND MECHANICAL BEHAVIOR

1. Oxide Dispersoid Stability in Irradiated Alloys (MIT) 94

The stability of incoherent oxide dispersoids may be significantly altered by MFR first wall irradiation conditions; evaluation must be on a case by case basis.

CONTENTS (Cont'd)

Page

2. Void Nucleation at Heterogeneities (MIT) 104

Dislocations and interfaces are potential void nucleation sites only when not point defect sinks; in the presence of inert gas, they are excellent catalysts.

3A. Effect of Time/Temperature History of Helium Doping and Atomic Displacement Damage on Microstructural Evolution in 20% Cold Worked 316 SS (MFE Heat) (W-R&D) 119

By varying the helium implantation and atomic displacement rates independently, it is found that the instantaneous helium implantation rate is an important factor in cavity formation.

3B. Microstructural Effects of Dual-Ion Bombardment in Aged 316 SS (W-R&D) 123

Bombardment of 316 SS, aged at 800°C to produce large grain boundary carbides prior to dual-ion irradiation, results in large cavities at the carbide/austenite interfaces for bombardment temperatures above 650°C.

3C. Damage Rate Dependence of the Rapid Cavity Growth Rate Regime in Solution Annealed 316 SS (W-R&D) 128

The rapid cavity growth regime observed in solution annealed 316 SS under dual-ion bombardment at 600°C is shown to occur only for atomic displacement rates below $\sim 1.5 \times 10^{-4}$ *dpa/s for helium injection rates of* 2×10^{-4} *appm/s to* 3×10^{-3} *appm/s.*

CONTENTS (Cont'd)

CONTENTS (Cont'd)

Page

7. Effect of Temperature and Microstructure on Crack Propagation in Unirradiated and Irradiated Austenitic Stainless Steel (University of Virginia) 193

The nature of crack propagation observed in in-situ HVEM tensile tests of 304 and 316 stainless steels can be correlated with the nature of the failure mode.

8. Effects of Near Surface Damage and Helium on the Performance of the First Wall (MIT) 209

The in-core cycling system functions as expected, with a cycle time of four minutes. Safety related out-of-core experiments show that specimen wall thickness could be increased.

9. Leak Rate Fatigue Experiment (PNL) 218

Thin unirradiated 304 SS tubes have been cycled at $500^{\circ}C$ *at maximum tangential stresses ranging from 224 MPa to 348 MPa. No indication of a leak was observed in* 10^4 *cycles at stresses below 286 MPa while at higher stresses the majority of failures were due to rupture.*

10. Radiation Induced Segregation and Irradiation Creep (ANL) 226

Irradiations of Ni and Ni - 4 at.% Si with 21 MeV deuterons at 2×10^{-6} *dpa* $\cdot$ s^{-1} *to* ~ 0.08 *dpa showed greater radiation induced creep in Ni; hardening was observed only in the alloy.*

THIS PAGE

WAS INTENTIONALLY

LEFT BLANK

FIGURES

Page

CHAPTER 3

1. Experiments at the Oak Ridge Research Reactor

5A. High Energy Neutron Cross Sections for Transport and Damage Calculations

5C. Deuteron and Neutron Induced Activation of the Lithium Target

6B. Neutron Yield Experiments

7B. Cross Sections for Atomic Displacements by Gamma Rays

FIGURES (Cont'd)

FIGURES (Cont'd)

FIGURES (Cont'd)

3C. Damage Rate Dependence of the Rapid Cavity Growth Rate Regime in Solution Annealed 316 SS

3D. Numerical Analysis of Cavity Size Distributions

5. The Radiation Disorder Model of Phase Stability

FIGURES (Cont'd)

6. Correlation of 16 MeV Protons with Fusion Neutrons

FIGURES (Cont'd)

7. Effect of Temperature and Microstructure on Crack Propagation in Unirradiated and Irradiated Austenitic Stainless Steel

8. Effects of Near Surface Damage and Helium on the Performance of the First Wall

FIGURES (Cont'd)

Page

9. Leak Rate Fatigue Experiment

10. Radiation Induced Segregation and Irradiation Creep

FIGURES (Cont'd)

TABLES

Page

CHAPTER 3

1. Experiments at the Oak Ridge Research Reactor

2. Helium Accumulation Fluence Dosimetry for the MFE Spectral Characterization and MFE-1 Irradiations at the Oak Ridge Research Reactor

7B. Cross Sections for Atomic Displacements by Gamma Rays

CHAPTER 4

1. Functions Describing Disordering Replacements and Secondary Displacements in Collision Cascades in Polyatomic Materials

TABLES (Cont'd)

TABLES (Cont'd)

CHAPTER 1

DAFS TASK GROUP ACTIVITIES

THIS PAGE

WAS INTENTIONALLY

LEFT BLANK

DAFS TASK GROUP ACTIVITIES

I. Subtask Group B - Damage Production (M. W. Guinan, Chairman)

A meeting was held at Livermore on June 7-8 to discuss the current status of displacement calculations and of atomistic displacement production models. Attendees included M. W. Guinan (Chairman), C. M. Logan and J. H. Kinney, LLL ; W. D. Wilson and L. G. Haggmark, SLL; L. R. Greenwood, ANL; D. M. Parkin, LASL; M. T. Robinson, ORNL; and D. G. Doran, H. L. Heinisch, and J. O. Schiffgens, HEDL.

The discussions of displacement calculations centered on extension of cross sections above 20 MeV, possible improvements in the treatment of certain reactions, and the advisability of all laboratories using a common code or set of displacement cross sections. Further intercode comparisons, and review of the recent extensions above 20 MeV by Greenwood, were called for.

Current cascade simulation work is in progress at ORNL, LLL, and HEDL. Both LLL and HEDL are trying to meld low energy many-body calculations, in bcc and fcc lattices, respectively, with Robinson's binary collision code MARLOWE. Of particular concern is an effective treatment of the locally excited lattice immediately following the defect forming stage of a cascade.

The minutes of this meeting should become available during the next quarter.

II. Subtask Group C - Damage Microstructure Evolution and Mechanical Behavior (G. R. Odette, Chairman)

R. W. Powell (HEDL) prepared a suggested list of materials for DAFS irradiations, circulated it for comments, and initiated procurement. He has also developed a preliminary test plan for DAFS reactor irradiations for review.

An ad hoc committee, consisting of R. W. Powell, Chairman, J. A. Spitznagel (W-R&D), J. A. Sprague (NRL), J. L. Brimhall (PNL), and F. V. Nolfi (ANL) reviewed the conditions of the MFE-1 experiment in the Oak Ridge Research Reactor (ORR). This experiment was terminated early because the desired temperatures were exceeded at many specimen locations.(1) Consensus was reached on the disposition of the specimens. Those deemed worthy of examination will be distributed by ORNL during the next quarter.

(1) Alloy Development for Irradiation Performance, Quarterly Progress Report, July - September 1978, DOE/ET-0058/3.

CHAPTER 2

IRRADIATION TEST FACILITIES

THIS PAGE

WAS INTENTIONALLY

LEFT BLANK

I. PROGRAM

Title: RTNS-II Operations
Principal Investigator: C. M. Logan/D. W. Heikkinen
Affiliation: Lawrence Livermore Laboratory

II. OBJECTIVE

The objective of this work is to operate the RTNS-II facility for the fusion materials program.

III. RELEVANT DAFS PROGRAM PLAN TASK/SUBTASK

Various

IV. SUMMARY

A deuteron beam diagnostics system has been installed in order to improve neutron utilization. Irradiation, dosimetry and handling services are routinely being provided for user laboratories.

V. ACCOMPLISHMENTS AND STATUS

In order to make the most effective use of neutrons produced at RTNS-II it is necessary to accurately control the spatial position of the neutron source. Except for small effects caused by nonuniform tritium distribution in the target, the location, size and shape of the neutron source are determined by the deuteron beam profile and position on the tritium target. Steering and focusing systems permit controlling beam position and profile but some method of observation is required. We have devised such a system.

When the deuteron beam strikes the titanium-tritide target, visible light is emitted. The ion source at RTNS-II is mounted vertically and the beam is extracted downward. The D^+ component is then bent 90° and injected into the acceleration column. The ion source and bend magnet are located in the high-voltage terminal. The beam transport system delivers the accelerated beam to the rotating target. We have reconfigured the vacuum system in the region of the bend chamber to permit installation of a television camera which looks down the beam line at the light emitted from the beam interaction with the rotating target. The television signal is then transmitted down from the high voltage terminal via a fiber optic system. By prealigning the camera with the beam transport system and the sample to be exposed to neutrons, a real-time image can be displayed revealing the location of the neutron source with respect to the sample being irradiated. The television signal can be processed to translate brightness variations into color bands. This diagnostic tool provides the operator with an easily interpreted graphic display which enables him to accurately control the neutron source.

During this quarter two runs have been completed on capsules assembled by HEDL. Each run was a room temperature exposure of many 3 mm disks for later examination by TEM and microhardness. Irradiation continues on a composite capsule containing samples of metals from PNL, TFTR diagnostic window glass from ANL, and superconductors from both LLL and BNL. A portion of the PNL samples have been completed. Dosimetry and material handling services are being routinely provided.

A users meeting was held at RTNS-II on June 7, 1979 to discuss future plans.

VI. REFERENCES

None

VII. FUTURE WORK

Irradiations will continue next quarter. A major effort will be devoted to installing and performing the LLL creep experiment.

VIII. PUBLICATIONS

Clinton M. Logan, "Rotating Target Neutron Source II," invited paper, American Physical Society, March 1979.

THIS PAGE
WAS INTENTIONALLY
LEFT BLANK

CHAPTER 3

SUBTASK A: ENVIRONMENTAL CHARACTERIZATION

THIS PAGE

WAS INTENTIONALLY

LEFT BLANK

I. PROGRAM

Title: Dosimetry and Damage Analysis
Principal Investigator: L. R. Greenwood
Affiliation: Argonne National Laboratory

II. OBJECTIVE

To establish the best practicable dosimetry for mixed-spectrum reactors and to provide dosimetry and damage analysis for MFE experimenters.

III. RELEVANT DAFS PROGRAM TASK/SUBTASK

SUBTASK II. A.1.1. Flux-spectral definition in a tailored fission reactor.

IV. SUMMARY

Analysis of the low power spectral measurement in the Oak Ridge Research Reactor (ORR) has been completed and the primary results have been disseminated. Analysis of the dosimetry wires from ORR-MFE1 is continuing.

V. ACCOMPLISHMENTS AND STATUS

A. Experiments at the Oak Ridge Research Reactor - - L. R. Greenwood and R. R. Heinrich (ANL)

Analysis has been completed for the low power spectral measurement in the Oak Ridge Research Reactor. Four 24" long aluminum capsules were irradiated in core position E7 during January at a power level of 1 MW (61.53 MWH). Spectral sets of 10 dosimetry wires were placed at eight locations giving a total of 28 separate activation measurements at each location. Four wires (Ni, Co-Al, Fe, and Ti) were also placed in each capsule to measure the flux gradients.

Figure 1 shows the measured flux-spectrum at the maximum flux position, about 3" below midplane. Figure 2 shows thermal and fast (E_n >1 MeV) flux gradients as a function of height above midplane.

Table I summarizes the measured flux-spectra at each of the eight locations and Table II compares our results with neutronics calculations by T. Gabriel (ORNL). Whereas our fast flux (>1 MeV) agrees very well with calculations, our measurements indicate substantially fewer neutrons below 1 MeV than predicted by calculation. Three possible explanations for the difference have been formulated, as follows. First, the calculations did not include a large graphite cylinder in a nearby core location which would indeed moderate the spectrum. Secondly, the measurement was at a reduced power level of 1 MW whereas calculations were at 30 MW. Finally, the neutronics calculations (7 group, 3D) may not represent the ORR configuration adequately. Hopefully, these effects can be sorted out by later comparisons to experiments in the same location at full power (ORR-MFE2) and at other locations (ORR-MFE 1). Helium accumulation fluence monitors were also included and are being analyzed at Rockwell International by H. Farrar IV and D. Kneff.

More complete results of the spectral analysis have been forwarded to E. Bloom (ORNL) and many DAFS and ADIP Task Group members. Copies are available on request.

Damage calculations are now being performed for the spectral irradiation. Results are listed in Table III for the region of highest flux.

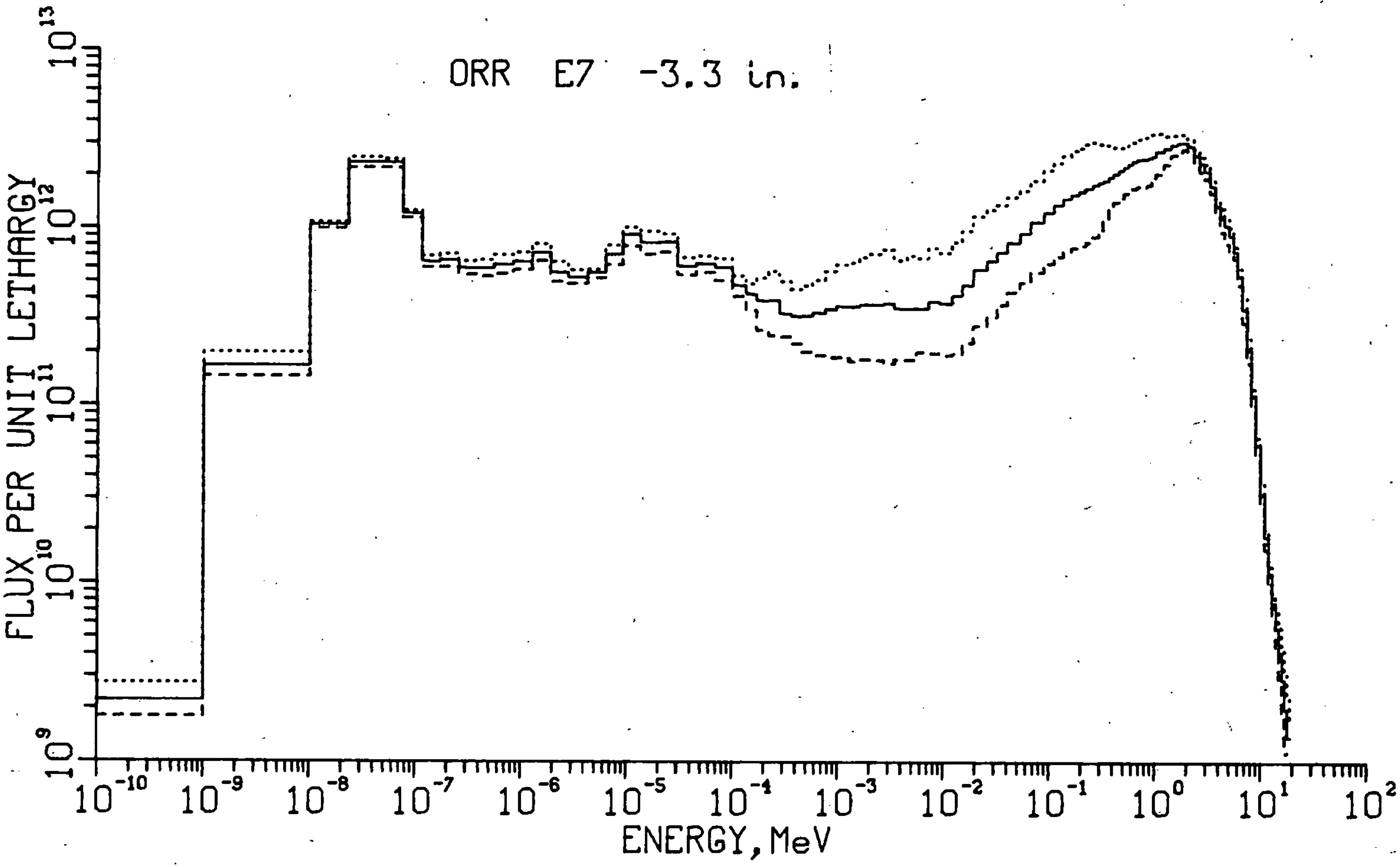

FIGURE 1. Capsule 1, -3.3 Inches Below Midplane.

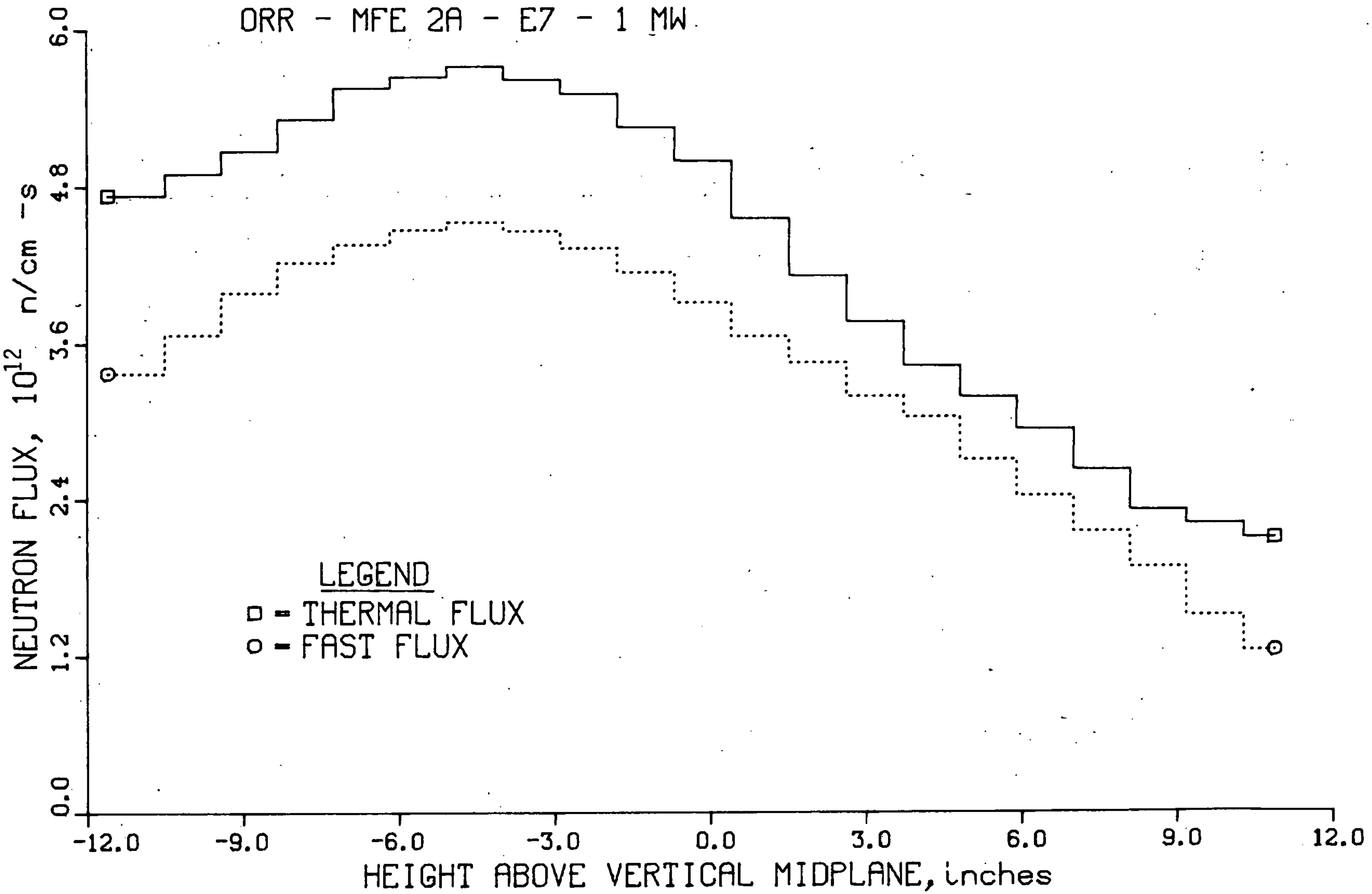

FIGURE 2. Fast and Thermal Flux Gradients for Capsule 4 West.

TABLE I. Group Flux Values, ORR - E7 - MFE2A
Power = 1 MW, $\phi \times 10^{12}$ n/cm^2-s

Height in. (Row)		Energy Limits, MeV[a]							Total
	Lower:	1.0^{-10}	5.5^{-7}	9.2^{-6}	1.275^{-3}	1.2^{-2}	0.19	0.920	
	Upper:	5.5^{-7}	9.2^{-6}	1.275^{-3}	1.2^{-2}	0.19	0.920	15	
	(Thermal)						(Fast	)	
	Capsule 1 - NW corner of E7								
-7.1 (26)		4.90	1.58	2.50	0.63	1.98	2.37	3.98	17.9 ± 2.6
-3.3 (22)		5.38	1.80	2.75	0.69	2.12	2.91	4.41	20.1 ± 2.8
+0.9 (18)		4.72	1.64	2.47	0.62	1.90	2.51	3.89	17.7 ± 2.5
+5.2 (13)		3.39	1.28	1.89	0.45	1.41	1.92	2.98	13.3 ± 1.9
+9.1 (9)		2.42	0.81	1.28	0.31	0.91	1.21	2.03	9.0 ± 1.3
	Capsule 2 - SE corner of E7								
-4.8 (20)		5.38	1.73	2.57	0.65	1.95	2.42	3.98	18.7 ± 2.6
+1.2 (16)		4.57	1.58	2.37	0.58	1.76	2.27	3.68	16.8 ± 2.4
+7.2 (12)		2.84	1.02	1.67	0.40	1.19	1.61	2.53	11.3 ± 1.6

[a] The notation 1.0^{-10} means 1.0×10^{-10}

TABLE II. ORR - LP - MFE2A - E7

Comparison of ANL Group Fluxes with
Neutronics Calculations
(Results Normalized to 30 MW)

Lower Energy, MeV	Group Flux (10^{13} n/cm^2-s)					
	ROW 22			ROW 9		
	ANL	Calc.*	Ratio ANL/Calc	ANL	Calc.*	Ratio ANL/Calc
1×10^{-10}	16.1	28.5	0.56 ± .03	7.3	10.9	0.67 ± .03
5.5×10^{-7}	5.4	6.9	0.78 ± .08	2.4	2.8	0.86 ± .09
9.2×10^{-6}	8.3	11.3	0.73 ± .11	3.8	4.7	0.81 ± .12
1.3×10^{-3}	2.1	5.7	0.37 ± .22	0.93	2.4	0.39 ± .23
1.2×10^{-2}	6.4	9.4	0.68 ± .41	2.7	3.9	0.69 ± .41
0.19	8.7	11.7	0.74 ± .19	3.6	4.9	0.73 ± .18
>0.92	13.2	14.7	0.90 ± .07	6.1	6.2	0.98 ± .07
TOTAL	60.3	88.0	0.69 ± .10	27.0	35.8	0.75 ± .11

*Seven Group, 3D calculations provided by T. Gabriel (1979)

TABLE III. Calculated Damage Rates for ORR

Core Position E7, 3.3" below midplane (max. flux)
Spectral averages include thermal neutrons

Element	$<\sigma d>$ (KeV-b)	$<\sigma he>$ (mb)	DPA[a] (per year)	He[a] (appm/year)
Al	35.8 ± 3.7	0.19 ± .01	9.39	3.36
Ti	32.3 ± 2.3	0.040 ± .004	5.72	0.71
V	33.5 ± 2.7	0.006 ± .001	5.93	0.11
Cr	30.8 ± 2.2	0.030 ± .002	5.45	0.53
Fe	26.8 ± 1.9	0.081 ± .006	4.74	1.43
Ni	28.8 ± 2.7	1.20 ± .07[b]	5.10	21.2[b]
Cu	28.1 ± 2.4	0.08 ± .01	4.97	1.42
Nb	27.7 ± 2.5	0.016 ± .001	4.90	0.28
316 SS	27.8 ± 2.0	0.055 ± .005	4.92	0.97

---

[a] Calculation assumes full power of 28 MW;
$\phi = 5.63 \times 10^{14}$ n/cm^2-s; $\phi\tau = 1.77 \times 10^{22}$ n/cm^2

[b] ^{58}Ni(n,γ) ^{59}Ni(n,α) process <u>not</u> included

VII. FUTURE WORK

The ANL dosimetry data will be integrated with helium fluence data for both irradiations now being analyzed by H. Farrar IV at Rockwell International. The analysis of activation data for ORR-MFE 1 should be completed during the next quarter.

I. PROGRAM

Title: Helium Generation in Fusion Reactor Materials
Principal Investigators: D. W. Kneff, H. Farrar IV
Affiliation: Rockwell International, Energy Systems Group

II. OBJECTIVE

The objective of this part of the fusion program at Rockwell International is to develop and apply helium accumulation fluence dosimetry to the measurement of neutron fluences and energy spectra in mixed-spectrum fission reactors utilized for fusion materials testing.

III. RELEVANT DAFS PROGRAM PLAN TASK/SUBTASK

TASK II.A.1	Fission Reactor Dosimetry
SUBTASK II.A.1.1	Flux-Spectral Definition in a Tailored Fission Reactor
SUBTASK II.A.1.2	Enhance Technique

IV. SUMMARY

Helium analyses have been performed on 14 helium accumulation dosimetry samples irradiated in the MFE spectral characterization irradiation, and on 17 samples irradiated in the MFE-1 experiment in the Oak Ridge Research Reactor (ORR). Preliminary analysis results are presented for selected samples of ^{10}B, Ni, Fe, and Cu.

V. ACCOMPLISHMENTS AND STATUS

Helium Accumulation Fluence Dosimetry for the MFE Spectral Characterization and MFE-1 Irradiations at the Oak Ridge Research Reactor -- D. W. Kneff, Harry Farrar IV, and M. M. Nakata (Rockwell International, Energy Systems Group)

Helium analyses have been initiated for the helium accumulation materials incorporated in the MFE spectral characterization and MFE-1 experiments in the Oak Ridge Research Reactor (ORR). These materials were included in the irradiations for neutron dosimetry, as described in detail in a previous quarterly report.(1) The materials used in both irradiations were combined with radiometric dosimetry materials provided by Argonne National Laboratory (ANL).

The helium accumulation materials included in the MFE spectral irradiation were located in dosimetry monitor tube Number 1, which was placed along the northwest cooling tubes in the west section of ORR core position E7. This core position is the same as that subsequently used for the irradiation experiment MFE-2. The spectral irradiation lasted 63.767 h in January 1979, with an average power level of 0.965 MW.

Those helium accumulation dosimetry materials included in the MFE-1 irradiation were located in dosimetry monitor tube Number 9. This monitor tube was irradiated in a position along the northeast cooling tubes in the north section of ORR core position C7. The irradiation lasted 134.74 days, with an average power level of 22.524 MW.

An initial 31 samples from these two irradiations were analyzed for helium by high-sensitivity gas mass spectrometry during the report period. These included 14 helium accumulation fluence monitor (HAFM) capsules and 17 bare wire segments. Preliminary results for the bare wire segments, plus two blank vanadium capsules, are presented in Tables 1 and 2 for the MFE spectral characterization and MFE-1 experiments, respectively. More accurate results will be reported when data reduction is complete.

The Ni-0.13% ^{10}B used in the spectral characterization irradiation (Table 1) is an alloy acquired from the Knolls Atomic Power Laboratory for use as a neutron dosimeter in light water reactor applications. It

TABLE 1

PRELIMINARY HELIUM GENERATION RESULTS FOR SELECTED HELIUM ACCUMULATION MATERIALS IRRADIATED IN THE ORR SPECTRAL CHARACTERIZATION EXPERIMENT

Sample Name	Material	Core Location (cm)*	Sample Mass (mg)	Etch Depth (mm)	Number of ^{4}He Atoms Released	^{4}He Concentration (appm)†
NI-2A	Ni	+3.3	2.961	0	6.9×10^{11}	0.023
NI-2E	Ni	+3.3	1.695	0.05	9.7×10^{10}	0.006
NI-2G	Ni	+3.3	1.908	0.23	1.0×10^{11}	0.005
NI10B-2C	Ni-0.13% ^{10}B	+3.3	1.902	0	4.6×10^{14}	3090**
NI10B-2D	Ni-0.13% ^{10}B	+3.3	2.054	0.03	4.8×10^{14}	2990**
NI10B-2F	Ni-0.13% ^{10}B	+3.3	2.281	0.16	5.5×10^{14}	3080**
V-R7	V	+4.0	38.33	0.006	6.3×10^{12}	0.014

*Vertical distance above core centerline
†Atomic parts per million (10^{-6} atom fraction)
**With respect to ^{10}B content

TABLE 2

PRELIMINARY HELIUM GENERATION RESULTS FOR SELECTED HELIUM ACCUMULATION MATERIALS INCLUDED IN THE ORR MFE-1 IRRADIATION

Sample Name	Material	Core Location (cm)*	Sample Mass (mg)	Etch Depth (mm)	Number of ^{4}He Atoms Released	^{4}He Concentration (appm)†
NI-4A	Ni	+21.7	2.123	0	2.2×10^{14}	10
NI-4E	Ni	+21.7	2.180	0.12	2.3×10^{14}	10
NI-4F	Ni	+21.7	1.585	0.12	1.7×10^{14}	10
FE-1A	Fe	+21.7	1.720	0	2.4×10^{12}	0.13
FE-1B	Fe	+21.7	1.974	0.14	2.0×10^{12}	0.094
FE-1C	Fe	+21.7	1.546	0.23	1.5×10^{12}	0.090
NI-5B	Ni	+ 1.9	2.304	0	1.1×10^{15}	47
NI-5G	Ni	+ 1.9	2.001	0.18	1.0×10^{15}	49
NI-5H	Ni	+ 1.9	1.550	0.18	7.7×10^{14}	48
CU-2C	Cu	+ 1.9	1.824	0.16	3.1×10^{12}	0.18
CU-2D	Cu	+ 1.9	2.259	0.16	3.9×10^{12}	0.18
V-5Z	V	+ 1.2	40.68	0.005	1.9×10^{15}	3.9

*Vertical distance above core centerline
†Atomic parts per million (10^{-6} atom fraction)

was chosen because the small ^{10}B concentration minimizes the effects of neutron self-shielding by the boron. The results in Table 1 provide evidence that the ^{10}B content in the alloy is homogeneous for the sample sizes analyzed, and demonstrate the use of an alloy dosimeter in low power MFE reactor experiments.

The high helium concentrations generated in the MFE-1-irradiated nickel (Table 2) demonstrate the considerable sensitivity of nickel as a neutron dosimeter for mixed-spectrum (comparable thermal and fast neutron flux) reactors. The spectrum-integrated cross section for helium production by the two-stage nickel reaction, $^{58}Ni(n,\gamma)^{59}Ni(n,\alpha)^{56}Fe$, has, in fact, recently been determined for various mixed-spectrum reactor environments from previous analyses of helium generation in nickel-bearing alloys. A joint Rockwell International-Oak Ridge National Laboratory paper on this subject is now being prepared for publication in the Journal of Nuclear Materials. The present nickel results are also of direct application to helium production in all nickel-bearing alloys being irradiated in ORR for the fusion reactor materials program.

The possibility of helium concentration surface effects in the helium accumulation materials, which would be produced by the absorption of external helium, has been examined by etching different samples to varying surface depths. The results in Tables 1 and 2, however, show no evidence of large surface helium concentrations. The small increases in helium concentration observed for unetched samples NI-2A (relative to NI-2E and 2G, Table 1) and FE-1A (relative to FE-1B and 1C, Table 2) are attributed to helium recoil from adjacent materials (Ni-0.13% ^{10}B and Ni, respectively), which have much higher helium generation cross sections.

Interpretation of the helium results from the HAFM capsules has been made more difficult by relatively high helium concentrations measured in the vanadium used for HAFM encapsulation. Helium concentrations near ORR core centerline have been found to be ~14 atomic parts per billion (14×10^{-9} atom fraction) for the MFE spectral irradiation, and ~4 atomic parts per million (4×10^{-6} atom fraction) for MFE-1. These relatively high helium levels in the vanadium are not due to helium in the original material,(2) and cannot be attributed to neutron reactions with the vanadium itself.(3) Absorption of helium into the vanadium from external sources has been ruled out by the measurements discussed above of helium in samples with varying surface etch depths. At present, the most likely source of the helium appears to be neutron reactions with boron or lithium impurities, both of which have sufficiently high (n,α) cross sections. A boron concentration of ~ 4 weight ppm would produce the measured amount of helium for both irradiation experiments. In the case of MFE-1, the helium concentration due to boron would have reached its maximum possible value (~4 appm), due to the total burnup of ^{10}B. At this time, it appears that platinum may be a more practical HAFM encapsulating material for future irradiations, because of its much lower expected boron impurity level, and because of the favorable experience in using this material in EBR-II neutron environments. The possible effects of small boron and lithium impurities in all of the helium accumulation materials for light water reactor dosimetry applications are of concern, and plans call for measuring these effects in the future. At this time, no impurity corrections have been made for the results presented in Tables 1 and 2.

VI. REFERENCES

1. D. W. Kneff and H. Farrar IV, "Helium Accumulation Fluence Dosimetry for Irradiations MFE-1 and MFE-2 at the Oak Ridge Research Reactor," in Damage Analysis and Fundamental Studies, Quarterly Progress Report January-March 1978, DOE/ET-0065/1, U.S. Department of Energy, p. 21 (August 1978).

2. H. Farrar IV, Fast Reactor Fluence Dosimetry, Technical Progress Report for Period December 1976 - May 1977, AI-ERDA-13198, Atomics International, Canoga Park, CA, p. 20, August 1977.

3. See, for example, E. P. Lippincott, W. N. McElroy, and H. Farrar IV, "Helium Production in Reactor Materials," in Nuclear Cross Sections and Technology, Vol. I, R. A. Schrack and C. D. Bowman, eds., pp. 375-377, National Bureau of Standards Special Publication 425, U.S. Department of Commerce (1975).

VII. FUTURE WORK

Helium analyses of the helium dosimetry materials included in the ORR irradiations will continue. Near-term emphasis will be placed on analyzing the nickel samples from all irradiation locations, and on further investigation into the source of the helium levels measured in vanadium. Modified sample preparation procedures will be set up for future helium analyses of the encapsulated materials, to minimize or eliminate the contribution of helium from the vanadium.

I. PROGRAM

Title: Dosimetry and Damage Analysis
Principal Investigator: L. R. Greenwood
Affiliation: Argonne National Laboratory

II. OBJECTIVE

To establish the best practicable dosimetry at high energy neutron sources.

III. RELEVANT DAFS PROGRAM TASK/SUBTASK

TASK II. A.2. Flux-spectral definition at high energy neutron sources.

IV. SUMMARY

Neutron and proton flux and spectral measurements have been made at the Argonne ZGS facility to mock-up the Intense Pulsed Neutron Source (IPNS) now under construction. Separate measurements were made for Ta and U targets at E_p = 500 MeV and preliminary results are presented.

V. STATUS AND ACCOMPLISHMENTS

A. Dosimetry at the IPNS Spallation Source - - L. R. Greenwood (ANL)

Neutron and proton dosimetry has been provided for two irradiations at a mock-up of the IPNS spallation neutron source at the ZGS at Argonne. A 500 MeV proton beam was stopped in either a Ta or a U target. Neutron dosimeters were placed in two tubes parallel and perpendicular to the beam axis. Proton dosimeters were also included in these tubes. The incident proton beam also passed through a thin aluminum foil placed upstream from the target. This foil was then used to determine the absolute proton beam intensity as well as the spatial distribution of the beam.

Our dosimetry results will be crucial to the understanding of the IPNS spallation source for (1) validation of neutronics calculations, (2) evaluation of the Ta and U targets, (3) absolute neutron and proton fluxes, (4) proton beam characteristics, and (5) materials damage calculations. Preliminary results show that the total neutron flux per incident proton is 0.040 for Ta and 0.058 for the U target at the location designated for materials effects irradiations. The protons at this location have an average energy between 100-200 MeV with a flux about 1% of the neutron flux and appear to be produced by scattering of the primary protons incident on the target. The neutron spectrum is similar to that found in a fast fission reactor except for a weak tail extending to very high energies.

VII. FUTURE WORK

The analysis of the data should be completed during the next quarter. Neutron spectra will be provided at the primary materials irradiation site and flux gradients will be determined over the entire volume. Displacement damage calculations will also be performed using our recently developed high energy cross section files.

I. PROGRAM

Title: Dosimetry and Damage Analysis
Principal Investigator: L. R. Greenwood
Affiliation: Argonne National Laboratory

II. OBJECTIVE

To improve neutron spectra measurement techniques and to determine errors in the flux-spectrum as well as calculated damage parameters.

III. RELEVANT DAFS PROGRAM TASK/SUBTASK

Task II.A.3. Sensitivity Studies

IV. SUMMARY

The computer code STAYSL written by F. G. Perey (ORNL) is now operational at Argonne. Tests are being conducted to compare the variance-covariance least squares technique with the Monte Carlo technique of SANDANL currently used to unfold neutron spectra and associated errors.

V. ACCOMPLISHMENTS AND STATUS

A. Revision and Application of the STAYSL Computer Code - L. R. Greenwood (ANL)

Neutron spectra are currently unfolded from integral neutron activation measurements using the SANDII computer code. This code uses an iterative technique to find the flux-spectrum which agrees most closely with the integral measurements. The code SANDANL then performs an error analysis using a Monte Carlo technique to assess the influence of errors in neutron cross sections, integral activity rates, and the input spectrum.

We have recently obtained a new code called STAYSL[1] written by F. G. Perey (ORNL). This code uses a least squares technique to solve the full variance-covariance matrices. This technique is in principle superior to our present programs since it allows the introduction of known covariance effects and finds the best fit to all the input data by a x^2 test. The code thus requires only a single matrix operation to arrive at a solution rather than the repeated iterations required by SANDII.

Unfortunately, the STAYSL code was not written in a generalized format to allow for routine dosimetry problems since the input at present is quite cumbersome. We have therefore interfaced the STAYSL code with our existing SANDII code to generalize the input to STAYSL and to take advantage of the cross section development work that we have previously done.

This revised version of the STAYSL code is now operational and undergoing testing. In simple cases, where all covariance effects are ignored, the output appears to agree quite well with our existing codes. Efforts are now underway to experiment with covariance effects. The most important source of these covariances appears to be the input flux since the activation and cross section covariances are negligible by comparison. Cross section covariance error files will be published eventually in ENDF/B-V. Unfortunately, little guidance is available for devising proper input flux covariance matrices since the input spectra are generally obtained from neutronics calculations without any specification of errors. The output appears to be quite sensitive to the form of flux covariance selected.

VI. REFERENCES

1. F. G. Perey, Least-Squares Dosimetry

Unfolding: The Program STAYSL,
ORNL/TM-6062, 1977.

VII. FUTURE WORK

We plan to continue testing of the code to develop suitable covariance matrices for routine applications. Cross Section covariances will be included as they become available in ENDF/B-V.

I. PROGRAM

Title: Nuclear Data for FMIT (WH025/EDK)
Principal Investigator: R. E. Schenter
Affiliation: Hanford Engineering Development Laboratory (HEDL)

II. OBJECTIVE

The objective of this work is to supply immediate nuclear data needs for the design and operation of the Fusion Materials Irradiation Test (FMIT) facility.

III. RELEVANT DAFS PROGRAM PLAN TASK/SUBTASK

All tasks that are relevant to FMIT use, with emphasis upon:
SUBTASK II.A.2.3 Flux-spectra definition in FMIT
SUBTASK II.B.1.2 Acquisition of Nuclear Data

IV. SUMMARY

The evaluation of high energy neutron cross sections for neutron transport and damage calculations is described.

Calculations of deuteron and neutron induced activation of FMIT structural materials have been performed in order to determine the best designs from the standpoint of maintenance.

A preliminary measurement of deuteron-induced production of ^{7}Be, one of the most troublesome radioactivants in the FMIT lithium target system, gave a higher yield than anticipated.

V. ACCOMPLISHMENTS AND STATUS

A. High Energy Neutron Cross Sections for Transport and Damage Calculations -- R. E. Schenter and D. L. Johnson (HEDL)

Neutron transport calculations require extensive nuclear data for neutrons as a function of energy including differential elastic scattering cross sections, differential neutron emission spectra, and non-elastic cross sections for all important materials. Damage calculations also require such data.

For FMIT, these data are required for neutron energies up to about 50 MeV. For transport calculations in the FMIT test cell (calculational dosimetry) and for damage calculations in similar spectra, data will be required to about 35 MeV for important structural materials such as iron, nickel, and chromium. For transport calculations of FMIT shielding through thick concrete, the dose is dominated by neutrons near the highest energies in the spectrum (up to ∿50 MeV). Important elements for shielding are oxygen, iron, silicon, and calcium.

Evaluations of the total, elastic, non-elastic and removal cross sections have been completed for the major constituents of high density and ordinary concrete whose data was poorly known (O, Fe, Ca, and Si). Carbon was also evaluated. The energy range was 20 to 60 MeV which is above the ENDF/B energy range.

These evaluations were performed using recent UC Davis measurements (described in the last DAFS report (Ref. 1)) and other data available from the CSISRS library. Evaluations were accomplished using generalized least squares methods and codes (Ref. 2).

An example of the results is given in Figure 1 which shows the evaluation and data for the non-elastic cross section of neutrons on iron. The "a priori" curve is from the library of the Monte Carlo code used for FMIT shielding calculations. The older data was obtained from

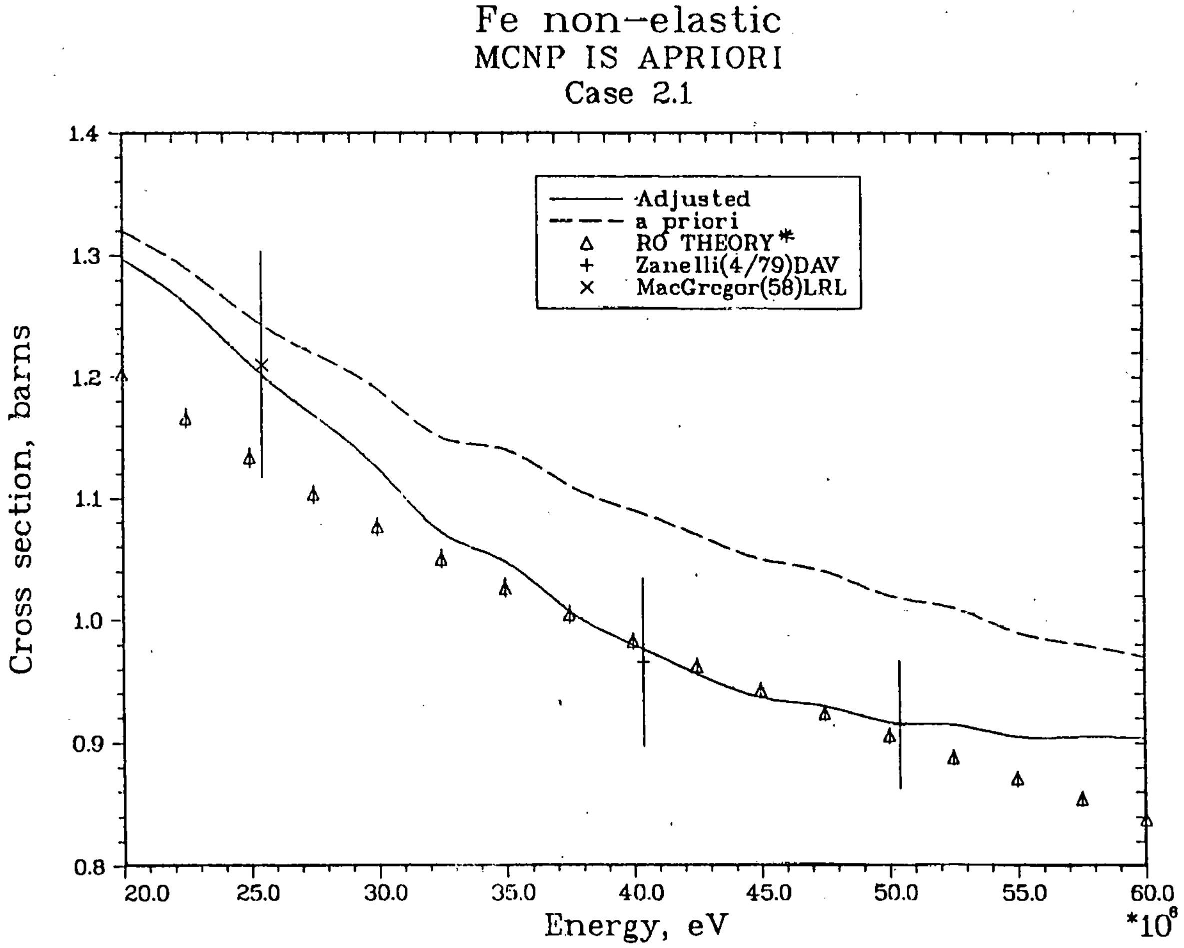

FIGURE 1. Updated Evaluation of Non-Elastic Cross Section for Neutrons on Iron Plus Experimental Data.

previous evaluations (Ref. 3 and 4) based predominantly on theory. The "adjusted" curve represents our latest evaluation which takes into account the experimental data as well as the previous evaluation. Note that for the important higher energies, the new evaluation is about 10% lower than the previous evaluation. The symbols labeled RO theory represent the parameterization

$$\sigma_{non} = \pi(r_o A^{1/3} + \bar{\lambda})^2$$

where A is the atomic mass number of the target, r_o is a radius parameter, and $\bar{\lambda}$ is the DeBroglie wave length of the incident neutron.

This parameterization has been shown to work very well for the non-elastic cross section of protons having similar energies. A slight energy dependence of r_o is required for good fits, however. For the case of neutrons on iron, the parameterization used was

$$r_o = 1.4288 - .003835 \, E_n \text{ fermis}$$

where E_n is the neutron energy in MeV. The energy dependence was estimated from proton data on similar targets (Ref. 5) whereas the constant term was fit to the two new UC Davis measurements (Ref. 1) shown in Figure 1. The parameterization gives an idea of the energy dependence that might be expected.

In the case of silicon, where no neutron non-elastic data was available, the parameterization which fit proton data (Ref. 5) was used as experimental neutron data.

B. Deuteron and Neutron Induced Activation of FMIT Accelerator and Beam Transport Structural Materials -- F. M. Mann and K. E. Mead (HEDL)

The unshielded gamma dose from deuteron bombardment of C, O, Aℓ, Mn, Fe, Co, Ni, Cu, and Au has been calculated for six bombardment times

(1 week, 1, 3, 6 and 12 months, and 20 years) and eight cooling times (1, 8, and 16 hours, 1, 2, and 3 days, 1 week, and 1 month).

The results for 6 month bombardment are shown in Figure 2. For all bombardment and cooling times studied, the dose is largest from Fe and Co.

Multigroup cross sections (weighted by the 0° and 90° Li(d,n) spectra) have been prepared from ENDF/B for many neutron-induced reactions.

C. Deuteron and Neutron Induced Activation of the Lithium Target -- D. L. Johnson (HEDL)

Longer lived radioactivants in the lithium target system can be a problem during operation and maintenance. The reactions ^{7}Li(d,2n), and ^{6}Li(d,n) produce significant quantities of ^{7}Be. This radioactivant is expected to be one of the most troublesome because of the quantity produced, its 53 day half-life, the fact that it emits gamma rays of about .48 MeV in energy, and also because it plates out on the inside walls of the piping.

Results of a preliminary measurement of the ^{7}Be production in a thick target (2 cm) of natural lithium bombarded with 35 MeV deuterons are as follows. The production rate was $6.8(10^{16})$ atoms/sec-amp and the number of curies at saturation can be expected to be $1.8(10^6)$ curies/amp. The uncertainties are estimated to be about 50%. These values appear to be about three times larger than previous evaluations, and repeat measurements will be required to resolve the discrepancy.

VI. REFERENCES

1. DAFS Quarterly Report (January - March 1979), DOE/ET-0065/5, May 1979.

2. F. Schmittroth, "Generalized Least-Squares for Data Analysis," HEDL-TME 77-51 (1978).

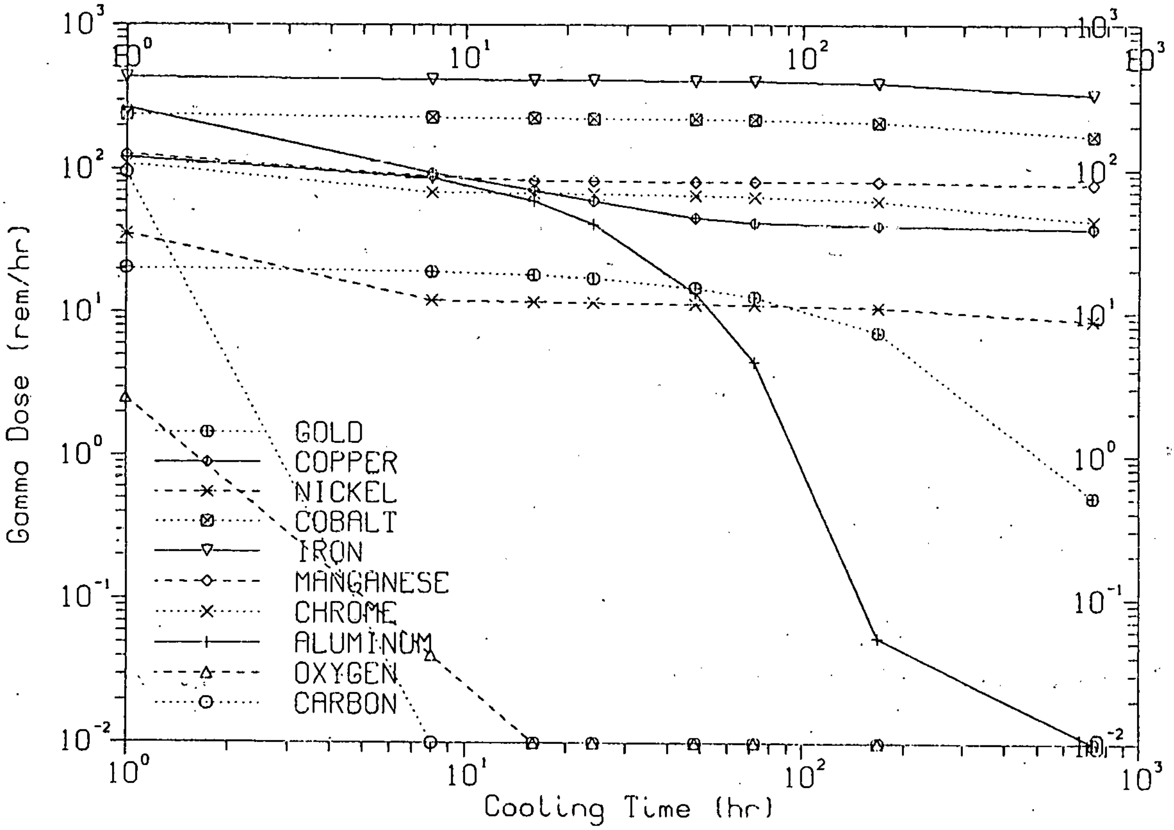

FIGURE 2. Unshielded Gamma Dose from Deuteron Bombardment, Bombardment Time = 6 Months

3. W. B. Wilson, "Nuclear-Data Development and Shield Design for Neutrons Below 60 MeV," LA-7159-T (February 1978).

4. R. G. Alsmiller and J. Barish, "Neutron-Photon Multigroup Cross Sections for Neutron Energies $\leq$ 60 MeV," ORNL/TM-6486, (August 1978).

5. W. F. McGill, et al., "Measurements of the Proton Total Reaction Cross Sections for Light Nuclei between 20 and 48 MeV," Physical Review C, Vol. 10 (1974) 2237.

VII. FUTURE WORK

Evaluation of high energy cross sections for neutron transport and damage calculations will be updated at some time in the future by using optical model analysis and more careful treatment of underlying uncertainties.

Evaluation of deuteron and neutron induced activation cross sections will be continued. Measurements are being considered to fill in the gaps and to check calculations.

VIII. PUBLICATIONS

A paper on the nuclear data needs of FMIT will be presented at the International Conference on Nuclear Cross Sections for Technology, Knoxville, Tennessee (October 1979).

I. PROGRAM

Title: Nuclear Data for Damage Studies and FMIT (WH025/EDK)
Principal Investigator: R. E. Schenter
Affiliation: Hanford Engineering Development Laboratory (HEDL)

II. OBJECTIVE

The objective of this work is to supply nuclear data needed for damage studies and in the design and operation of the Fusion Material Irradiation Testing (FMIT) facility.

III. RELEVANT DAFS PROGRAM PLAN TASK/SUBTASK

SUBTASK	II.A.2.3	Flux Spectra Definition in FMIT
TASK	II.A.4	Gas Generation Rates
SUBTASK	II.A.5.1	Helium Accumulation Monitor Development
SUBTASK	II.B.1.2	Acquisition of Nuclear Data

IV. SUMMARY

Results of measurements of the yield and spectra of neutrons from 35 MeV deuterons on thick targets of both natural lithium and ^{6}Li are described.

The microscopic neutron yield model is being updated using HEDL-UCD experimental results, least-squares adjustment techniques and nuclear models.

V. ACCOMPLISHMENTS AND STATUS

A. Cross Section Prediction -- F. M. Mann (HEDL) and C. Kalbach (Triangle Universities Nuclear Laboratory)

The model for angular distributions of outgoing particles has been extended to include more experimental results. It seems possible to express the few parameters as a linear function of $\ell*(\ell+1)$ where ℓ is the order of the Legendre polynomial.

B. Neutron Yield Experiments -- D. L. Johnson and F. M. Mann (HEDL), J. W. Watson, J. Ullmann, and W. G. Wyckoff (University of California at Davis)

Time-of-flight measurements of the neutron yields and spectra from 35 MeV deuterons on thick (2 cm) lithium for the FMIT facility were described in the last two DAFS quarterly reports.

The analysis of previous measurements has continued by determining the neutron spectral results for energy bins that are 1 MeV wide. The results are shown in Figures 1 and 2.

Additional measurements of the very low energy portion (<2 MeV) of the spectra were completed in May 1979. Spectra were obtained at 4°, 8°, 12°, 20°, 30°, 45°, and 70° which correspond to angles in previous measurements. These measurements differ from December 1978 measurements, which were described in the last DAFS quarterly, in the following way. These new measurements were made with a cyclotron beam deflection system that was built specially for this experiment. This system allowed longer times between cyclotron beam bursts on target and as a result, improved background subtraction.

Measurements were also made in May 1979 of the yield and spectra from 35 MeV deuterons on thick lithium that was enriched to $\sim$99% ^{6}Li.

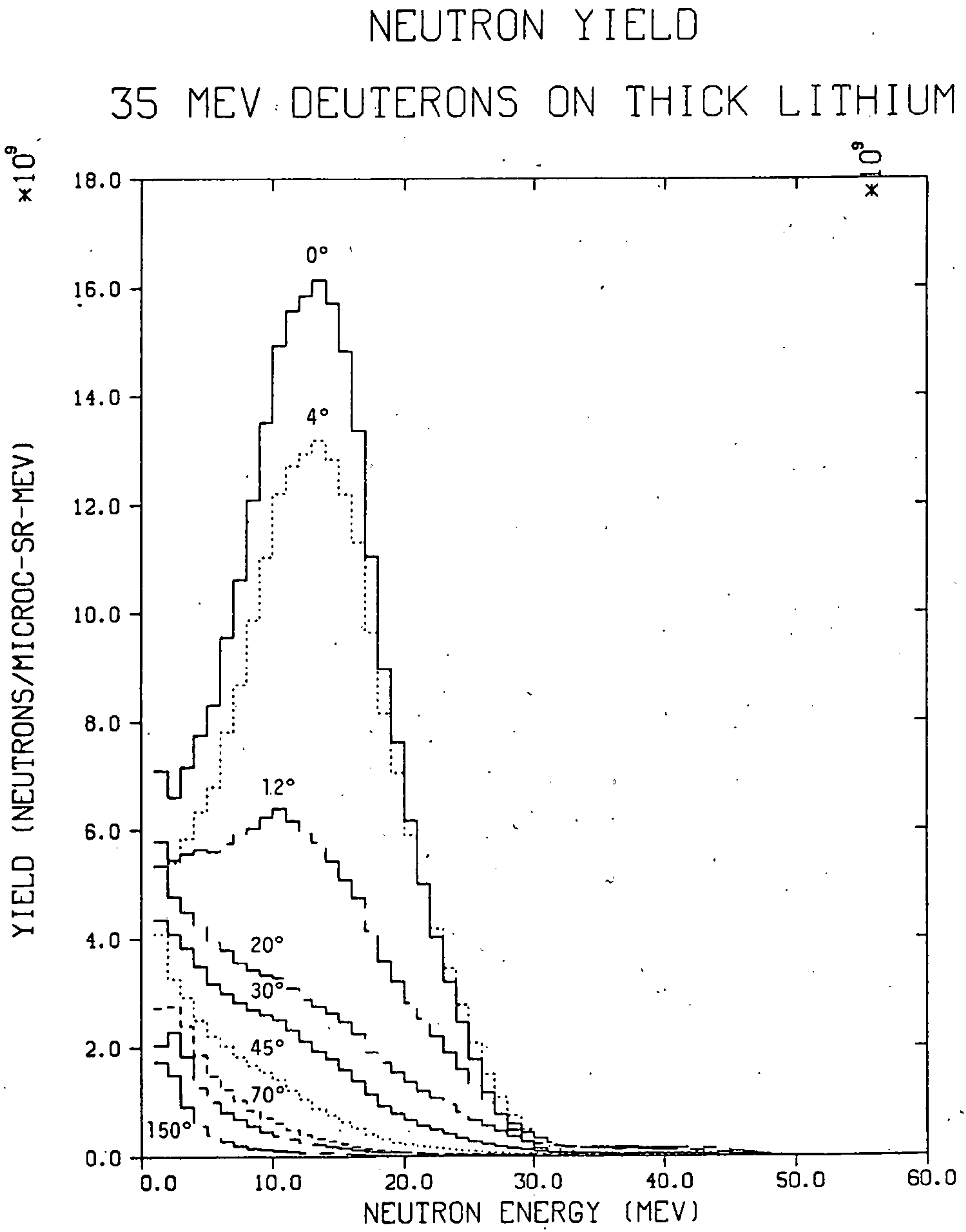

FIGURE 1. Linear Plot of d-Li Spectra.

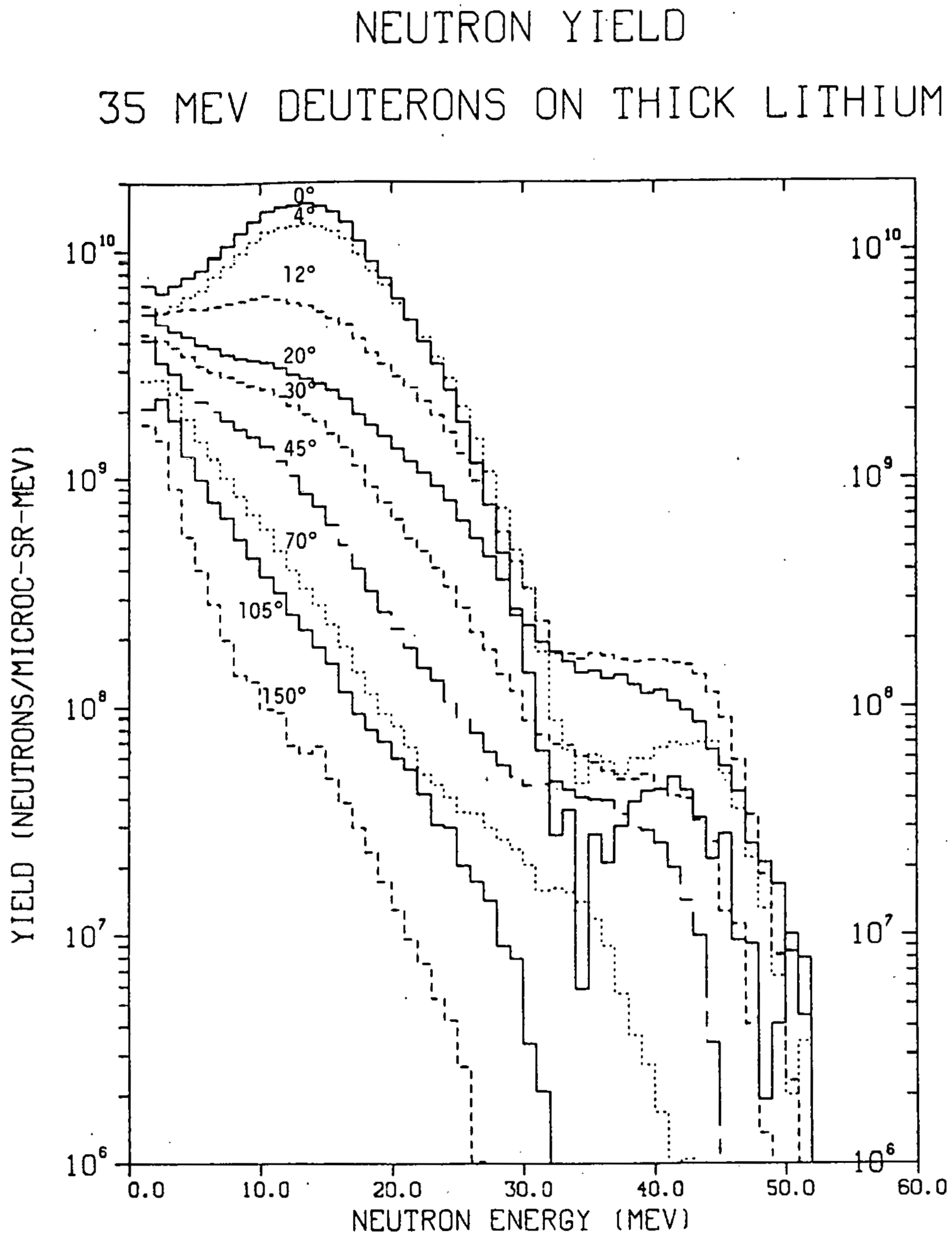

FIGURE 2. Logarithmic Plot of d-Li Spectra.

The setup was identical to that of the natural lithium measurements and data were taken at 30° and 45°. Preliminary indications are that the yield from ^{6}Li is about 30% less than from natural lithium if one makes the reasonable assumption that the neutron angular distributions are similar. Hence ^{6}Li does not appear to be a practical target material if maximum neutron yield is desired.

C. Microscopic Neutron Yield Model -- F. M. Mann and F. Schmittroth (HEDL)

Using the latest experimental results from the University of California at Davis (see above) and the least squares adjustment to d+Li neutron yields for $14 \leq E_d \leq 40$(1), the microscopic neutron yield model is being adjusted. Although the results are not complete, good agreement is found between the Davis data and the model.

VI. REFERENCES

1. DAFS Quarterly Report (January - March, 1979), DOE/ET-0065/5, May 1979.

VII. FUTURE WORK

The analysis of neutron yield measurements will be continued.

The adjustment of the microscopic yield model will be continued.

Papers on the experimental results of the Li(d,n) experiment and the microscopic neutron yield model will be presented at the International Conference on Nuclear Cross Sections for Technology, Knoxville, TN (October 1979).

VIII. PUBLICATIONS

None.

I. PROGRAM

Title: Damage Analysis and Dosimetry Radiation Damage Analysis
Principal Investigator: A. N. Goland
Affiliation: Brookhaven National Laboratory

II. OBJECTIVE

Radiation damage analysis studies associated with the use of electrical insulators in fusion reactors.

III. RELEVANT DAFS PROGRAMS PLAN TASK/SUBTASK

SUBTASK II.A.2.4 Flux Spectral Definition in FMIT

SUBTASK II.B.1 Calculation of Displacement Cross Sections

IV. SUMMARY

Transfer of damage energy calculations to the computer at the Magnetic Fusion Energy Computer Center continues. Milestones include having the source version of the MORSE-L computer code made available for general use so required changes can be made in the program, conversion of the Alsmiller-Barish cross section file to the format required by the MORSE-L code, and making several lengthy runs with MORSE-L as a first step in obtaining good statistics for a coupled neutron-gamma transport problem having FMIT geometry.

Cross sections for atomic displacements by gamma rays through Compton and photoelectric interactions with atomic electrons and through pair production in the fields of the nucleus and atomic electrons have been evaluated. The results are compared with those of previous authors, and, in order to cover the full gamma ray energy range of the Alsmiller-Barish cross sections, the evaluations have been extended to 15 MeV.

Finally, the displacement cross section for gamma rays in Al_2O_3 was evaluated by incorporating the total displacement functions of Parkin and Coulter to relate recoil energy to displacements in multicomponent materials.

V. ACCOMPLISHMENTS AND STATUS

A. Use of the Magnetic Fusion Energy Computer Center: A. N. Goland, H. C. Berry, G. F. Dell and O. W. Lazareth (BNL)

Transfer of damage analysis calculations to the computer at the Magnetic Fusion Energy Computer Center MFECC continues. The source version of the MORSE-L neutron transport code has been made available for general use, and incorporation of a subroutine for generating neutrons characteristic of a Li(d,n) source is in progress.

In addition, a cross section library for use with the MORSE-L program has been generated from the cross sections of Alsmiller and Barish.[1] The RSIC version of MORSE as well as the damage program DON have been sent to the MFECC, and attempts are being made to run them at the MFECC.

Several lengthy coupled neutron-gamma transport calculations for problems having FMIT geometry have been made using the 30 neutron-15 gamma group cross section library at MFECC with MORSE-L. Initial results show larger fluxes of gamma rays than were obtained at BNL using the RSIC version of MORSE and the Alsmiller-Barish cross sections. Both versions of MORSE will be run at the MFECC to determine if they give equivalent results.

B. Cross Sections for Atomic Displacements by Gamma Rays: A. N. Goland, H. C. Berry, G. F. Dell and O. W. Lazareth (BNL)

In anticipation of results from coupled neutron-gamma transport calculations using the Alsmiller-Barish cross sections, cross sections for atomic displacements by gamma rays have been calculated for gamma ray energies up to 15 MeV. The method of evaluation as well as the notation is that used by Oen and Holmes.[2] A brief description of the calculation follows.

The displacement cross section $\sigma_d(E_\gamma,T_d)$ for a gamma ray of energy E_γ displacing an atom having a displacement energy T_d is given as:

$$\sigma_d(E_\gamma,T_d) = \sum_i \int \frac{d\sigma^i(E_\gamma,E_o)}{dE_o}\, dE_o \bar{n}(E_o) \tag{1}$$

where

$\frac{d\sigma^i(E_\gamma,E_o)}{dE_o}$	is the atomic cross section for the transfer of kinetic energy E_o to an electron by a gamma ray having energy E_γ. The sum over the index "i" includes the Compton, photoelectric, and pair production interactions.
$\bar{n}(E_o)$	is the average number of displaced atoms produced over the range of an electron having original energy E_o.

The cross sections $d\sigma^i(E_\gamma,E_o)/dE_o$ were obtained from Bethe and Ashkin.[3] For the pair production cross section, effects of screening and contributions from the field of the electrons were included in the cross section. No further discussion of these cross sections will be made.

The expression for $\bar{n}(E_o)$ given by Oen and Holmes is:

$$\bar{n}(E_o) = \frac{N_a \int_o^{E_o} \sigma_d^e(E,T_d)\,dE}{(-dE/dx)} \tag{2}$$

with

N_a being the number of atoms/cm^3,

$-dE/dx$ being the energy loss by relativistic electrons,[3] and

$\sigma_d^e(E,T_d)$ being the cross section for displacing an atom by an electron.

Finally, $\sigma_d^e(E_\gamma,T_d)$ is expressed as:

$$\sigma_d^e(E_\gamma,T_d) = \int_{T_d}^{T_m} g(T)\,\frac{d\sigma^e}{dT}\,dT. \tag{3}$$

where

$d\sigma^e/dT$,the Mott cross section, is the cross section for giving an atom an energy T. It can be expressed in closed form to within 1% for $Z \lesssim 40$,[4] and it is integrable. This property simplifies the calculation.

T_m is the maximum energy transfer between an electron of kinetic energy E and an atom of mass M,[5] and

$g(T)$ is a function that relates recoil energy to displacements.

Several cases of interest are listed below.

1) $g(T) \equiv 1$ Equation 1 gives the primary displacement cross section. This is the case treated by Oen and Holmes.[2]

2) $$g(T) = \begin{matrix} 0 & T < T_d \\ 1 & T_d < T < 2T_d \\ \frac{T}{2T_d} & 2T_d < T \end{matrix}$$ Equation 1 gives the total displacement cross section.

3) $g(T) = a(T) + b(T)T$ g(T) is a linear interpolation of a particular function. Of particular interest are the numerical evaluations of the total displacement functions generated by Parkin and Coulter[6] to relate recoil energy to displacements in multicomponent materials.

Discussion of Results

Case 1 - primary displacement cross sections. A comparison of displacement cross sections for copper with the results of Oen and Holmes is shown in Fig. 1 for two displacement energies. The two sets of results show excellent agreement. The total displacement cross sections for copper from the Compton, photoelectric, and pair production processes as well as the sum of these cross sections for gamma ray energies up to 15 MeV are shown in Fig. 2.

Case 2 - total displacements cross sections. Total displacement cross sections were evaluated for Ge using a displacement energy of 30 eV. These cross sections are compared in Fig. 3 with the results of Cahn.[7] The present results are consistently higher than Cahn's results by a factor of nearly two. Cahn used an expression for (-dE/dx) that is different from the one used by Oen and Holmes. This may explain our good agreement with the results of Oen and Holmes and our poorer agreement with the results of Cahn.

Case 3 - total displacement cross sections in Al_2O_3. The total displacement functions n_{ij} generated for Al_2O_3 by Parkin and Coulter have been used to relate recoil energy to displacements. The displacement energies of 18 and 72 eV measured by Pells and Phillips[8] for Al_2O_3 were used when generating the displacement functions n_{ij}.

Four calculations are required to determine the number of Al and O atoms displaced when the primary displaced atom is either Al or O. The total number of displaced atoms of each type is obtained from a sum, weighted according to the atomic fraction of each atom, of the displacements produced by each type of primary displaced atom.

The displacement cross sections for Al and O in Al_2O_3 are shown in Fig. 4. These cross sections have been used with a gamma ray spectrum obtained from a previous[9] coupled neutron-gamma transport calculation to

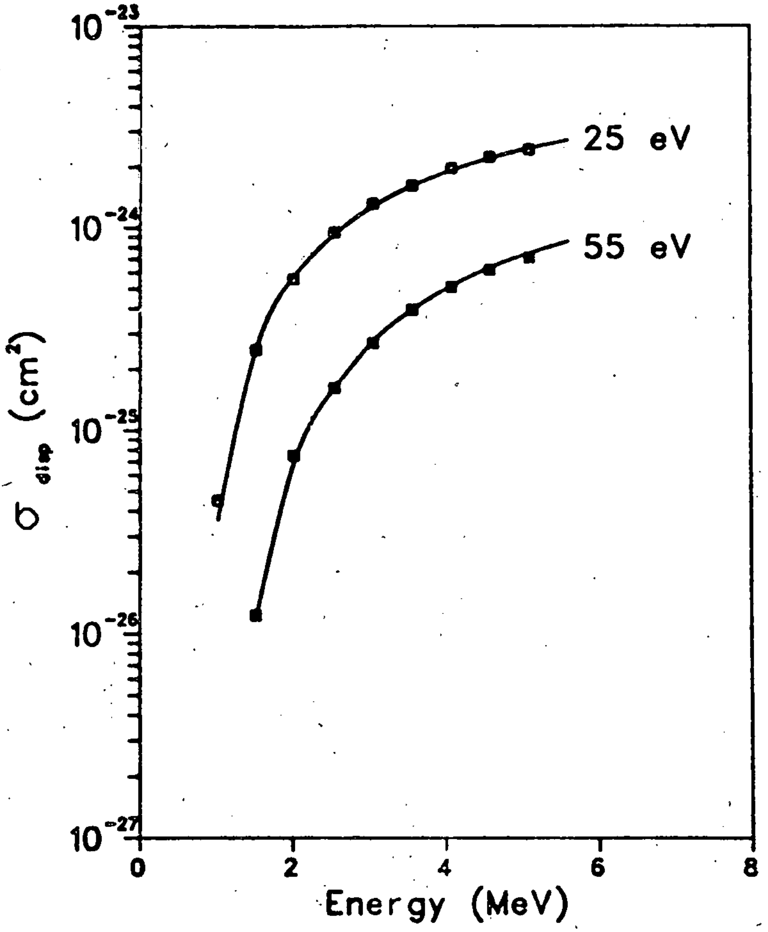

Fig. 1. Atomic cross section for producing primary displacements in copper through the Compton process for displacement energies of $T_d = 25$ eV and $T_d = 55$ eV. Points denote values of Oen and Holmes; lines denote present work.

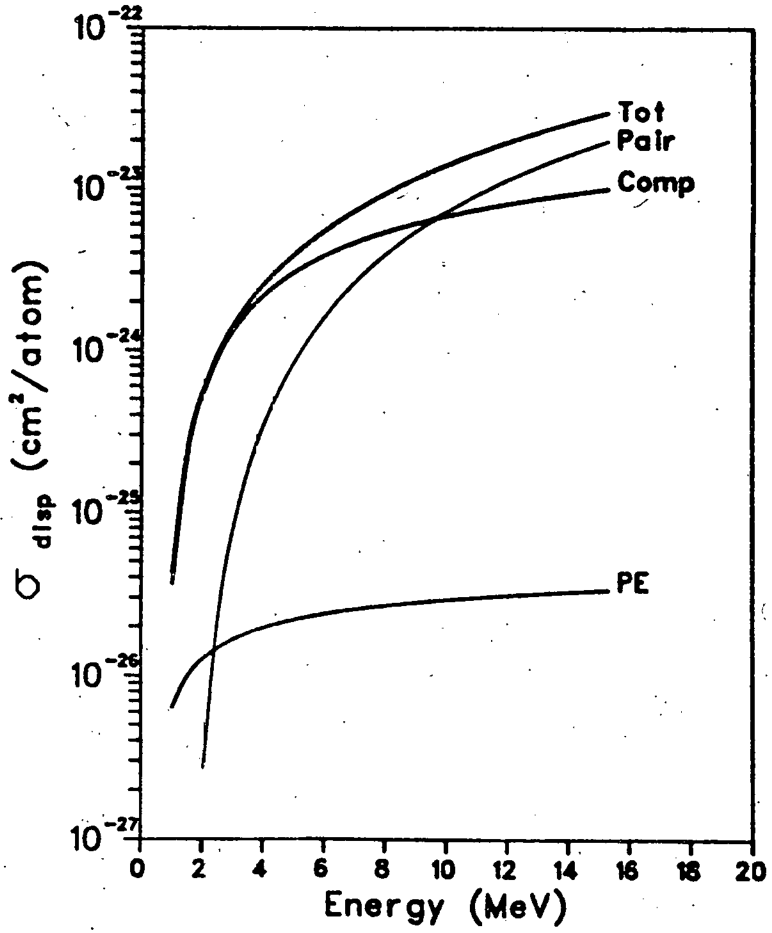

Fig. 2. Atomic cross section for total displacements in copper through the photoelectric, Compton, and pair production processes. $T_d = 25$ eV. Tot denotes the sum of the photoelectric (PE), Compton (Comp), and pair production (Pair) cross sections.

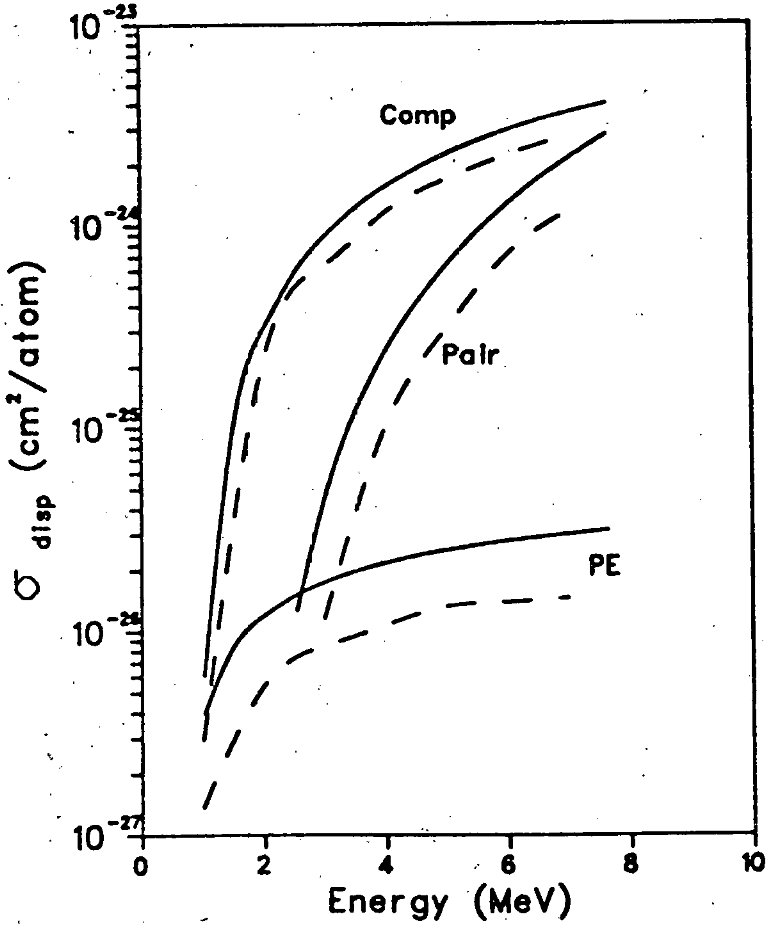

Fig. 3. Atomic cross section for total (primary plus secondary) displacements in Ge for photoelectric, Compton, and pair production processes. $T_d = 30$ eV. Dashed curves denote values of Cahn; solid curves denote present work.

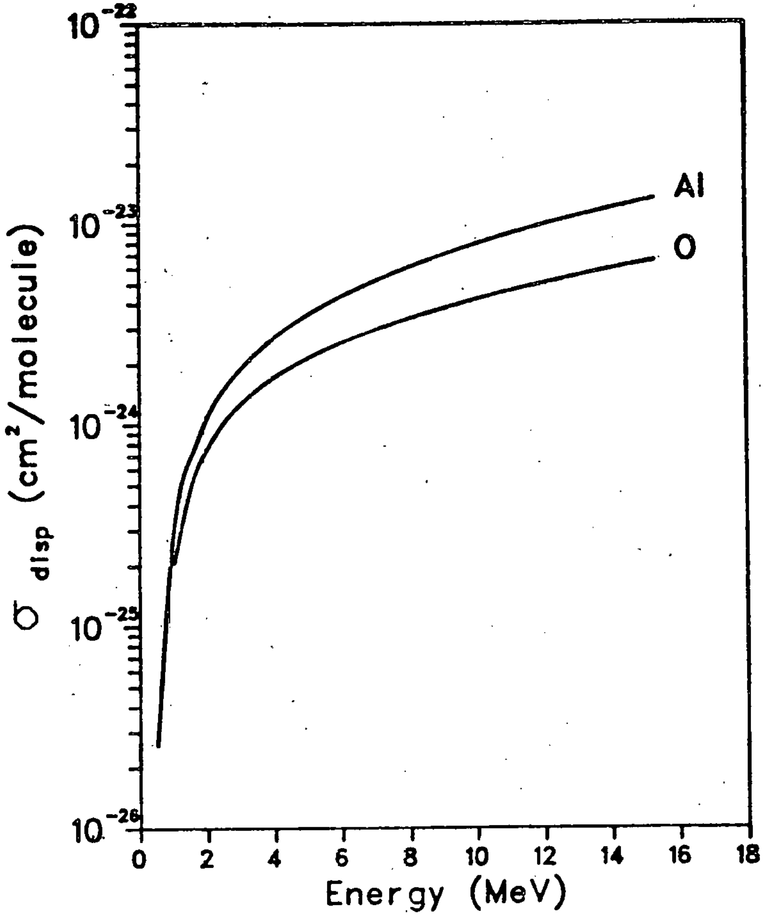

Fig. 4. Total displacement cross section/ molecule in Al_2O_3 from gamma rays, $T_d = 18$ eV for aluminum and $T_d = 72$ eV for oxygen.

obtain the number of displacements produced in Al_2O_3 by gamma rays. These displacements are compared in Table 1 with displacements produced by the neutron spectrum of Fig. 5. The displacements produced by neutrons were determined by using the total displacement functions of Parkin and Coulter in the damage program DON. Hence the method for relating primary recoil energy to total displacements is the same for both neutrons and gamma rays. For the two spectra of Fig. 5 the number of displacements produced by gamma rays is small compared to the number of displacements produced by neutrons. This is to be expected, since neutrons are much more efficient than electrons in transferring large recoil energies to atoms.

VI. REFERENCES

1. R. G. Alsmiller, Jr. and J. Barish, ORNL/TM 6486 (August 1978).
2. O. S. Oen and D. K. Holmes, J. Appl. Phys. 30, 1289 (1959).
3. H. A. Bethe and J. Ashkin, Experimental Nuclear Physics Vol. I, E. Segre, Ed., John Wiley, New York, 1953.
4. R. M. Curr, Proc. Phys. Soc. (London) A68, 156 (1955).
5. G. J. Dienes and G. H. Vineyard, Radiation Effects in Solids, Interscience Publishers, Inc., New York, 1957, p. 13.
6. D. M. Parkin and C. A. Coulter, Damage Analysis and Fundamental Studies Quarterly Technical Progress Report, July - September 1978, p. 73, DOE/ET-0065/3.
7. J. H. Cahn, J. Appl. Phys. 30, 1310 (1959).
8. G. P. Pells and D. C. Phillips, J. Nuc. Mat. 80, 207 (1979).
9. A. N. Goland, H. C. Berry, G. F. Dell and O. W. Lazareth, Damage Analysis and Fundamental Studies Quarterly Technical Progress Report, October - December 1978, p. 27, DOE/ET-0065/4.
10. B. S. Yarlagadda and J. E. Robinson, J. Nuc. Mat. 63, 466 (1976).

VII. FUTURE WORK

Future work will include: 1) continued use of the computer at the

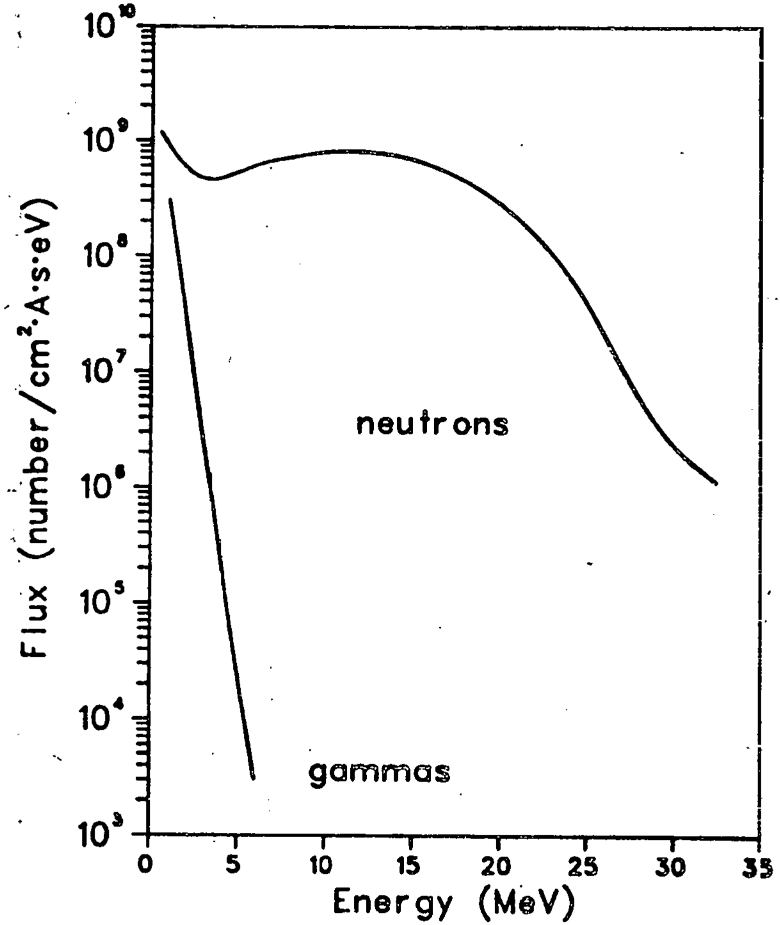

Fig. 5. Neutron and gamma ray spectra at a depth of 5 mm in an iron block located adjacent to a lithium target. MORSE simulation using 30 MeV deuterons.

MFECC to obtain more definitive neutron and gamma ray spectra, and 2) consideration of ionization assisted mechanisms[10] in gamma ray and electron induced displacement processes.

Table 1

Spectrum averaged displacement cross sections for Al_2O_3 from fluxes of neutrons and gamma rays in a block of iron located adjacent to a lithium target. Deuteron energy = 30 MeV.

	Neutrons	Gammas
Flux (number/cm^2·A·s)	$2.38 \cdot 10^{16}$	$1.34 \cdot 10^{14}$
$\bar{E}$ (MeV)	10.7	0.79
σ_d(Al) (barns/molecule)	5330	0.21
σ_d(O) (barns/molecule)	2055	0.13

THIS PAGE

WAS INTENTIONALLY

LEFT BLANK

CHAPTER 4

SUBTASK B: DAMAGE PRODUCTION

THIS PAGE

WAS INTENTIONALLY

LEFT BLANK

I. PROGRAM

Title: Radiation Damage Analysis and Computer Simulation
Principal Investigator: Don M. Parkin
Affiliation: Los Alamos Scientific Laboratory of the
University of California

II. OBJECTIVE

The objective of this work is to develop displacement functions for polyatomic materials.

III. RELEVANT DAFS PROGRAM PLAN TASK/SUBTASK

SUBTASK	II.B.2.3	Cascade Production Methodology
	II.B.4.1	Interface with other designs and other tasks
	II.B.4.2	Develop theory of spectral and rate effects

IV. SUMMARY

The computer code DISPL3 was developed to calculate functions that describe the production of disordering replacements and which atom types are responsible for producing secondary displacements in collision cascades in polyatomic materials. Results for Nb_3Sn show that the atom type which produces the majority of secondary displacements is a strong function of the initial PKA type and energy. In contrast, the fraction of disordering replacements produced in a collision cascade is nearly independent of PKA energy except at energies quite near threshold.

V. ACCOMPLISHMENTS AND STATUS

A. Functions Describing Disordering Replacements and Secondary Displacements in Collision Cascades in Polyatomic Materials -- D. M. Parkin (LASL) and C. A. Coulter (The University of Alabama)

1. Introduction

In previous investigations we have studied the properties of two kinds of functions characterizing properties of displacement cascades in polyatomic solids. The first of these, the total displacement function $n_{ij}(E)$,is defined as the average number of type-j atoms which are at any time displaced from their sites in a displacement cascade initiated by a PKA of type i and energy E; and the second, the net displacement function $g_{ij}(E)$, is the average number of type-j atoms displaced and not recaptured in subsequent replacement collisions in a similarly-initiated cascade. While the information provided by the functions $n_{ij}(E)$ and $g_{ij}(E)$ has been enlightening, these functions cannot directly provide answers to some interesting and important questions concerning displacement cascades. For example, $n_{ij}(E)$ tells how many type-j atoms are displaced in a cascade initiated by a type-i atom; but it does not tell what fraction of these type-j displacements is produced by each atom type represented in the material. Similarly, the difference between $n_{ij}(E)$ and $g_{ij}(E)$ tells what fraction of displaced type-j atoms is retrapped in subsequent replacement collisions; but it does not in general provide information about the types of the sites in which the trapping occurs. To obtain this kind of information we have introduced and studied two new kinds of functions. The first of these, an as-yet-unnamed displacement function denoted by $p_{ijk}(E)$, is defined as the average number of type-k atoms which are displaced from their sites by type-j atoms in a displacement cascade initiated by a PKA of type i and energy E. The second function, tentatively named the capture function and denoted by $h_{ijk}(E)$, is defined as the average number of type-j atoms trapped by replacement collisions in type-k sites in a displacement cascade initiated by a type-i PKA of energy E.

Using the method and results of Lindhard et al.,[1-3] integrodifferential equations were developed to determine the functions $p_{ijk}(E)$ and $h_{ijk}(E)$. A computer code was generated to numerically integrate these equations for arbitrary polyatomic materials, and the code was used to evaluate the two types of functions for Nb_3Sn. The integrodifferential equations and the results obtained from them are discussed in the next section.

2. Theory and Numerical Results

We shall use the notation of previous reports[4]: $\frac{d\sigma_{ij}(E,T)}{dT}$ is the differential scattering cross section for a moving type-i atom of energy E to elastically transfer kinetic energy T to a type-j atom; $\rho_j(T)$ is the probability that the type-j atom will then be displaced and $E^b{}_j$ the binding energy it loses in the process; and $\lambda_{ij}(E - T)$ is the probability that the incident atom left with energy E - T will be trapped in the type-j site if the type-j atom is displaced. In addition, M_{ij} is the kinematic energy transfer efficiency for the collision, $s_i(E)$ is the specific electronic stopping power of the material for a type-i atom of energy E, and f_i is the atomic fraction of type-i atoms in the material. Using these definitions one may write

$$s_i(E)p'_{ijk}(E) = \sum_\ell f_\ell \int_0^{M_{i\ell}E} dT\, \frac{d\sigma_{i\ell}(E,T)}{dT} \Big\{ \rho_\ell(T) \left[\delta_{ij}\delta_{k\ell} + P_{\ell jk}(T - E^b{}_\ell)\right] + \left[1 - \rho_\ell(T)\lambda_{i\ell}(E - T)\right] P_{ijk}(E - T) - P_{ijk}(E) \Big\} , \qquad (1)$$

$$s_i(E)h'_{ijk}(E) = \sum_\ell f_\ell \int_0^{M_{i\ell}E} dT\, \frac{d\sigma_{i\ell}(E,T)}{dT} \Big\{ \rho_\ell(T) \left[\delta_{ij}\delta_{k\ell}\lambda_{i\ell}(E - T) + h_{\ell jk}(T - E^b{}_\ell)\right] + \left[1 - \rho_\ell(T)\lambda_{i\ell}(E - T)\right] h_{ijk}(E - T) - h_{ijk}(E) \Big\} . \qquad (2)$$

It is seen that the two equations differ in only one term: $\rho_\ell(T)\delta_{ij}\delta_{k\ell}$ in the first equation gives the probability that the struck atom is actually displaced, and that it is of the desired type k while the displacing atom is of the desired type j; while $\rho_\ell(T)\delta_{ij}\delta_{k\ell}\lambda_{i\ell}(E - T)$ in the second equation gives the probability that in addition to all the foregoing the incident atom is trapped in the vacated site. The remaining terms have a significance discussed in previous reports.

Using sharp displacement and capture thresholds with $E^d_j = E^{cap}_{ij} = 36$ eV, Eqs. (1) and (2) were numerically integrated for parameters chosen to represent the material Nb_3Sn. To show the behavior of the functions more clearly, values of the trapping functions and displacement functions at a few energy values are presented in Tables 1 - 4 in a form which facilitates comparisons. Table 1 shows Nb trapping at various PKA energies as a function of PKA type and, for given PKA type, as a function of trapping site type. It is seen from the table that Nb trapping is preferentially in Nb sites by a ratio approximately 3.12 to 1 almost independently of PKA energy and type except for the case of a very low energy Sn PKA, where the Nb-site preference is even greater because Nb trapping on an Sn site requires an energetically-disfavored double displacement event. Thus it is seen that a small departure from stoichiometry in the trapping occurs at all energies, and is even more enhanced in the case of a low-energy Sn PKA.

Table 2 shows a very similar behavior for Sn trapping, with the trapping occurring preferentially in Nb sites by a ratio near 2.85 to 1 for both PKA types at almost all energies, the exception in this case being parallel to that of Nb trapping in that Sn trapping in Nb sites becomes relatively less favored for a low-energy Nb PKA. Again, a small but consistent departure from stoichiometry exists.

Table 3 shows Nb displacement at selected energies as a function of PKA type and, for each PKA type, as a function of the type of the atom producing the displacement. Here the dependence of atom type producing the displacement on energy is seen to be very strong. E.g., for an Nb PKA the ratio of Nb displacements produced by Nb atoms to those produced by Sn atoms is 230:1 at 50 eV, 8.9:1 at 500 eV, 3.82:1 at 10^4 eV, 3.1:1 at 10^6 eV, and 3.08:1 at 10^7 eV. By contrast, for an Sn PKA the ratio of Nb displacements produced by Nb atoms to those produced by Sn atoms is 1:62 at 50 eV, 1:2.26 at 500 eV, 1.65:1 at 10^4 eV, 2.71:1 at 10^6 eV, and 2.73:1 at 10^7 eV. Thus the ratio is near (but not equal to) the stoichiometric ratio at large PKA energies, but totally different from this ratio--as would be expected--for energies from threshold into the keV range. Table 4 shows analogous behavior for Sn displacement, where for an Nb PKA the ratio of Sn displacements by Nb atoms to those by Sn atoms varies from 190:1 at 50 eV to 3.02:1 at 10^7 eV, while for an Sn PKA

TABLE 1

Nb trapping as a function of PKA type, trapping site type, and energy

	Nb TRAPPING			
	Nb PKA		Sn PKA	
Energy (eV)	Nb site	Sn site	Nb site	Sn site
50	$5.3\text{x}10^{-2}$	$1.7\text{x}10^{-2}$	$2.3\text{x}10^{-3}$	$2.5\text{x}10^{-4}$
100	0.278	0.0902	0.0316	0.0102
500	0.834	0.266	0.546	0.175
10^3	1.51	0.481	1.22	0.392
10^4	12.9	4.13	12.8	4.09
10^5	112.1	35.8	114.4	36.6
10^6	791.6	252.8	859.0	274.4
10^7	2743	876	3480	1112

TABLE 2

Sn trapping as a function of PKA type, trapping site type, and energy.

	Sn TRAPPING			
	Nb Pka		Sn PKA	
Energy (eV)	Nb site	Sn site	Nb site	Sn site
50	2.5×10^{-4}	9.7×10^{-5}	5.4×10^{-2}	1.9×10^{-2}
100	1.01×10^{-2}	3.54×10^{-3}	0.251	0.087
500	0.175	0.0611	0.453	0.160
10^3	0.391	0.137	0.671	0.237
10^4	4.07	1.43	4.39	1.55
10^5	36.0	12.6	37.1	13.0
10^6	255	89.4	277	97.1
10^7	883	310	1120	393

TABLE 3

Number of Nb displacements as a function of PKA type, the type of the displacing atom, and energy.

Nb DISPLACEMENT

	Nb PKA		Sn PKA	
Energy (eV)	Nb proj.	Sn proj.	Nb proj.	Sn proj.
50	$5.7\text{x}10^{-2}$	$2.5\text{x}10^{-4}$	$8.6\text{x}10^{-4}$	$5.3\text{x}10^{-2}$
100	0.402	0.0106	0.0333	0.375
500	3.39	0.381	1.16	2.62
10^{3}	6.91	1.06	3.23	4.79
10^{4}	62.3	16.3	49.4	30.0
10^{5}	527	163	500	207
10^{6}	3690	1190	3870	1430
10^{7}	12780	4147	15720	5757

TABLE 4

Number of Sn displacements as a function of PKA type, the type of the displacing atom, and energy.

	Sn DISPLACEMENT			
	Nb PKA		Sn PKA	
Energy (eV)	Nb proj.	Sn proj.	Nb proj.	Sn proj.
50	1.8×10^{-2}	9.6×10^{-5}	2.5×10^{-4}	1.9×10^{-2}
100	0.131	3.74×10^{-3}	0.0107	0.128
500	1.12	0.130	0.381	0.888
10^3	2.29	0.361	1.06	1.62
10^4	20.6	5.52	16.3	10.1
10^5	175	55.3	165	69.9
10^6	1220	404	1280	484
10^7	4239	1405	5208	1950

the same ratio varies from 1:76 at 50 eV to 2.67:1 at 10^7 eV. It is interesting to note that the greatest deviation from stoichiometry occurs for an Sn PKA for displacement of both atom types.

It is striking that the ratios of the $p_{ijk}(E)$ considered vary rather strongly with energy while those of the $h_{ijk}(E)$ vary rather little. It should be noted, however, that the index k is held constant in the ratios of the p_{ijk}, while the index j is held constant in the ratios of the h_{ijk}. In any case, the results indicate that for the set of system parameters considered the fraction of disordering replacements produced in a collision cascade is nearly independent of PKA energy except at energies quite near threshold.

3. Conclusion

It is believed that this is the first calculation ever reported of displacements as a function of projectile type and trapping as a function of site type in a polyatomic material. However, the results obtained for Nb_3Sn for this set of parameters give only a limited indication of the varieties of behavior possible for other cominbations of mass ratios and of displacement and capture thresholds. Consideration of many additional cases will be necessary before some general understanding of the properties of the functions $p_{ijk}(E)$ and $h_{ijk}(E)$ will be possible.

VI. REFERENCES

1. J. Lindhard, V. Nielsen, and M. Scharff, Kgl. Danske Videnskab. Selskab, Mat.-fys. Medd. 36, No. 10 (1968).
2. J. Lindhard, M. Scharff, and H. E. Schiøtt, Kgl. Danske Videnskab. Selskab, Mat.-fys. Medd. 33, No. 14 (1963).
3. J. Lindhard, V. Nielsen, M. Scharff, and P. V. Thomsen, Kgl. Danske Videnskab. Selskab, Mat.-fys. Medd. 33 No. 10 (1963).

4. Don M. Parkin, DAFS Quarterly Progress Reports, DOE/ET-0065/1-5.

VII. FUTURE WORK

Further analysis of the properties of the functions describing collision cascades in polyatomic materials will be made.

VIII. PUBLICATIONS

1. C. Alton Coulter and Don M. Parkin, "Damage Energy Functions in Polyatomic Materials," submitted to J. Nucl. Mater.
2. C. Alton Coulter and Don M. Parkin," Total and Net Displacement Functions: General Formulation and Results For the Monatomic Case," submitted to J. Nucl. Mater.

I. PROGRAM

Title: Irradiation Effects Analysis
Principal Investigator: D. G. Doran
Affiliation: Hanford Engineering Development Laboratory

II. OBJECTIVE

The objective of this work is to document the computer code used to determine the characteristics of replacement sequences in face-centered cubic metals.

III. RELEVANT DAFS PROGRAM PLAN TASK/SUBTASK

SUBTASK II.B.2.3 Cascade Production Methodology

IV. SUMMARY

A draft has been completed of the documentation of the computer code COMENT.

V. ACCOMPLISHMENTS AND STATUS

A. Documentation of COMENT - J. O. Schiffgens and N. J. Graves (HEDL)

COMENT, a so-called "dynamical" code, solves the classical equations of motion of a large number of atoms interacting according to a given force law, and performs the desired ancillary analysis of the resulting data. The purpose of developing COMENT to its present degree of flexibility was to have available an atomistic simulation code which could be used to analyze a wide variety of atom dynamics, defect configurations, physical processes, and property changing mechanisms. That is, it was written as a dual purpose code intended to describe static defect configurations as well as the detailed motion of atoms in a crystal lattice. In its current form, analysis is limited to fcc lattices. COMENT can be used to simulate the effect of temperature, impurities, and preexisting defects on radiation induced defect production mechanisms, defect properties, defect migration, and defect stability. It has been used most recently to study replacement sequences in an fcc lattice.(1)

A report has been prepared which documents Version IV of COMENT and, in the process, defines current code options. An effort was made to so structure COMENT as to allow for additional options with minimum changes in the existing version of the code. It should be noted that, although COMENT was specifically written in FORTRAN IV and COMPASS (CDC 6000/7000 series assembly language) to take full advantage of CDC 6000/7000 series computer characteristics, it can, with a little effort, be adapted to other computer systems. The report contains sufficiently detailed information about the code to permit the ready addition and/or alteration of subroutines to satisfy particular user needs and interests.

COMENT consists of a calling program and thirty-two user defined subroutines. Fourteen subroutines are associated with the selection of program options; only a few of these are used in any given analysis. Seven subroutines are used to establish a variety of arrays and conditions required for each analysis; most of them are used once in a given calculation. The remaining eleven subroutines are used many times in each calculation; eight of these are used many times per time step during the integration and, therefore, are written in COMPASS. The COMPASS subroutines are described in sufficient detail to permit easy conversion to some other machine language or to FORTRAN.

VI. REFERENCES

1. J. O. Schiffgens, D. M. Schwartz, et al., "Computer Simulation of Replacement Sequences in Copper," Radiation Effects 39, pp. 221-231 (1978).

VII. FUTURE WORK

No further work is currently planned on developing the code COMENT.

VIII. PUBLICATIONS

An abstract of the code will be submitted for publication. The full documentation of the code will be available upon request as HEDL-TME 78-55.

I. PROGRAM

Title: 14 MeV Neutron Irradiations (WZJ-14)
Principal Investigator: M. Guinan / W. Barmore
Affiliation: Lawrence Livermore Laboratory

II. OBJECTIVE

The objective of this work is the characterization of the primary damage state resulting from 14 MeV neutron irradiations and the determination of the influence of neutron spectral effects on defect production and distribution.

III. RELEVANT DAFS PROGRAM TASK / SUBTASK

SUBTASK II.B.2.3 Cascade Production Methodology
II.B.3.2 Studies of Metals

IV. SUMMARY

The analysis of experimental results on resistivity damage rates at 4.2K in molybdenum using a modified Kinchin-Pease model (involving damage energy and an effective directional-averaged threshold) reveals a pronounced effect of primary knock-on energy on defect production efficiency. The production efficiency is low (.2 to .3) just above minimum threshold, rises rapidly to about 1.1 to 1.2 at primary knock-on energies of a few hundred eV (2 to 5 times minimum threshold), and then decreases throughout the low kilovolt range to a constant value of .3 to .4 independent of energy up to the MeV range.

Although the initial rise is easily understood as a result of the anisotropy of defect production, the subsequent decrease is not. A fully dynamic computer simulation of defect production in tungsten reveals both the anticipated rise as well as a subsequent decrease in the low kilovolt range resulting from recombination processes occurring in the cascade.

V. ACCOMPLISHMENTS AND STATUS

A. A Comparison of Experimental Defect Production Efficiency in Mo with Computer Simulations in W - M. W. Guinan, R. N. Stuart, J. H. Kinney, and C. E. Violet (LLL)

1. Introduction

The number of Frenkel pairs (FP's) produced by a primary knock-on atom (PKA) in metals has been traditionally estimated on the basis of the Kinchin-Pease model[1] for which the number of FP's, <n>, produced by a PKA of energy T is

$$\langle n\rangle = 1 \quad \text{for} \quad 2T_0 > T > T_0 \tag{1}$$

and

$$\langle n\rangle = \frac{T}{2T_0} \quad \text{for} \quad T > T_0$$

where T_0 is the minimum threshold displacement energy. In recent years Eq. 1 has been modified to take account of electronic losses[2] (replacing T with the damage energy, T_{DAM}), the anisotropy of displacement thresholds (replacing T_0 with the directional averaged threshold[3], T_A) and allowing for an energy dependent efficiency factor, K, to give

$$\langle n\rangle = \frac{K\,T_{DAM}}{2\,T_A}\ , \tag{2}$$

Both the analytic theory of random cascades and binary collision calculations predict that K = 0.8 at energies well above threshold.

2. Experimental Results for Molybdenum

For experimental analysis Eq. 2 is conveniently rewritten in terms of atom fraction per unit fluence, so that <n> is replaced by the FP production rate and T_{DAM} by the damage energy cross-section, σ_{DAM}. For resistivity measurements the FP production rate is given by $(1/\rho_f)d\rho/d\phi$, where ρ_f is the resistivity per atom fraction of FP's. Solving for K, we have

$$K = \frac{2T_A}{\rho_f \sigma_{DAM}} \frac{d\rho}{d\phi} . \qquad (3)$$

As part of an interlaboratory program, values of $d\rho/d\phi$ have been measured at 4.2K for a dilute molybdenum alloy(Mo-.03a/oZr) irradiated with electrons[4], fission neutrons[5], moderated fission neutrons[6], and high energy neutrons[7]. These are listed in Table 1 with other values obtained for pure Mo in a thermal spectrum[8] and a moderated fission spectrum[9].

3. Damage Energy Cross-Sections

For the fast and high energy neutron spectra damage energy cross-sections were calculated from the 1978 ENDL file[10] using the code of Logan and Russell[11] as modified by Kinney. For the thermal spectrum the result of Coltman et al[8] was used. For electrons, a Mott scattering code[12] was written to generate recoil spectra which were corrected for electronic losses by means of Robinson's analytical formula[13] for Lindhard's numerical results[14].

These results are listed in Table 1 with values of the median recoil energy, $T_{\frac{1}{2}}$, for each irradiation (the integral damage energy for recoils from T_0 to $T_{\frac{1}{2}}$ is one-half the integral damage energy over the entire recoil spectrum.). For the thermal neutron irradiation the mean recoil energy given by Reference 8 was used.

4. Experimental Damage Production Efficiencies

From the experimental resistivity damage rates and the calculated damage energy cross-sections values of K were determined from Eq. 3 using Luccasson's[3] values for ρ_f and T_A. These are given in Table 1 and plotted as a function of $T_{\frac{1}{2}}/T_0$ in Figure 1.

TABLE 1

EXPERIMENTAL RESISTIVITY DAMAGE RATES AND DAMAGE ENERGY CALCULATIONS FOR Mo

Spectrum	Reference	$d\rho/d\phi$(10^{-25} Ω-cm^3)	σ_{DAM}(b-keV)	$T_{\frac{1}{2}}$(keV)	$T_{\frac{1}{2}}/T_0$	K†
Electrons	4					
.95 MeV		.007	.179	.037	1.09	.39
1.15		.042	.613	.041	1.19	.69
1.35		.090	1.11	.043	1.27	.81
1.55		.140	1.60	.048	1.41	.87
1.85		.211	2.30	.053	1.57	.92
2.15		.296	2.94	.059	1.74	1.01
2.45		.380	3.52	.065	1.91	1.08
2.75		.452	4.04	.071	2.08	1.12
3.05		.487	4.51	.077	2.26	1.08
Neutrons§						
thermal	8	.039	.335	.169	4.97	1.16
fission(CP-5)	9	1.86	59.4	20.1	591.	.31
fission(LPTR)	6	3.13	67.4	27.2	800.	.46
fission(BSR)	5	3.47	82.1	39.0	1150.	.42
d-Be (35 MeV)	7	6.51	179.5	148.	4350.	.36
fusion (RTNS)	7	10.03	246.1	184.	5410.	.41

†From Eq. 3 with $\rho_f = 13 \times 10^{-4}$ Ω-cm and $T_A = 65$ eV.

§Based on fluence with $E_n > .1$ MeV for all but thermal spectrum.

5. Computer Simulations in Tungsten

Fully dynamic computer simulations of defect production have been carried out for PKA energies from threshold to 2.5 keV in a crystal containing 3500 atoms. Electronic losses were not included in the model so that direct comparisons could be made with binary calculations. The efficiency is found from Eq. 2 with T inserted for T_{DAM}, i.e.

$$K = \frac{2T_A}{T} \langle n \rangle . \qquad (4)$$

Values for $\langle n \rangle$ are determined at times long enough to allow the cascade to cool to the point where defect motion is no longer possible. This is accomplished by the application of damping at the periodic boundaries of the crystal. The results for K for two different pair-potentials are tabulated in Table 2 and shown in Fig. 1 with the Mo experimental data.

TABLE 2

COMPUTER SIMULATION RESULTS FOR TUNGSTEN

	T(eV)	T/T_0	$\langle n \rangle$	K
Potential I	71.5	1.1	.073	.33
T_0= 65eV	78.0	1.2	.162	.67
T_A=162eV	84.5	1.3	.216	.83
	91.0	1.4	.291	1.04
	97.5	1.5	.364	1.21
	130.0	2.0	.430	1.16
	162.5	2.5	.549	1.10
	195.	3.0	.649	1.08
	260.	4.0	.854	1.07
	325.	5.0	1.00 ± .05	.96 ± .05
	600.	9.2	1.62 ± .25	.87 ± .14
	2500.	38.5	3.3 ± .4	.43 ± .05
Potential II	600.	14.6	2.0 ± .4	.68 ± .14
T_0= 41eV	2500.	61.0	5.8 ± .9	.47 ± .07
T_A=103eV				

Potential I had previously been used for studies of defect diffusion[15] and a determination of the FP recombination volume[16]. Potential II is identical below 2 eV in order to fix the equilibrium defect properties, but is considerably softer at higher energies, resulting in a lower threshold. T_A was determined by integrating over the anisotropic threshold surface[17] as were the values of $\langle n \rangle$ for recoils less than $4T_0$. Above $4T_0$, $\langle n \rangle$ is the average of 10-16 cascades with random initial directions.

The dramatic decrease in efficiency in the low keV range is the result of both recombination of normally stable FP's and a high defect mobility induced by the subthreshold agitation remaining in the lattice during cooling of the cascade.

6. Conclusion

The close correspondence between the calculations and the experimental resistivity results strongly support the conclusion[18] that the reduced resistivity damage rates observed at PKA energies above a few keV in both f.c.c. and b.c.c. metals are primarily the result of defect recombination rather than the result of clustering.

VI. REFERENCES

1. G. H. Kinchin and R. S. Pease, Rep. Prog. Phys. 18, 1 (1955).
2. M. T. Robinson, in *Fundamental Aspects of Radiation Damage in Metals*, CONF-751006-P1 (U. S. ERDA, Oak Ridge, Tenn., 1976), p. 1.
3. P. Lucasson, IBID, p. 42.
4. P. Jung and G. Lucki, Rad. Effects 26, 99 (1975).
5. R. R. Coltman, Jr., private communication.
6. M. W. Guinan and C. E. Violet, unpublished data.
7. M. W. Guinan and C. E. Violet, in *Symposium on Neutron Cross-Sections from 10 to 40 MeV*, BNL-NCS-50681 (U. S. ERDA, Brookhaven National Lab., 1977), p. 361.

8. R. R. Coltman, Jr., C. E. Kablunde, and J. K. Redman, IBID Ref. 2, p. 445.

9. M. A. Kirk and L. R. Greenwood, J. Nucl. Mat. 80, 159 (1979).

10. R. J. Howerton, R. J. Doyas, T. C. Michels, and S. T. Perkins, Livermore Evaluated Neutron Cross-Section Library, Lawrence Livermore Lab. Rept. UCRL-50400 (1976).

11. C. M. Logan and E. W. Russell, Radiation Damage at the RTNS Facility at Lawrence Livermore Laboratory, Lawrence Livermore Lab. Rept. UCRL-52093 (1976).

12. J. H. Kinney and M. W. Guinan, unpublished.

13. M. T. Robinson, in Radiation Induced Voids in Metals, (U. S. AEC Symposium Series, Vol. 26, 1972), p. 1397.

14. J. Lindhard, V. Nielsen, M. Scharff, and P. W. Thomsen, K. Dan. Vidensk. Selsk., Mat.-Fys. Medd. 33, 10 (1963).

15. M. W. Guinan, R. N. Stuart, and R. J. Borg, Phys. Rev. B15, 699 (1977).

16. R. N. Stuart, M. W. Guinan, and R. J. Borg, Rad. Eff. 30, 129 (1976).

17. M. W. Guinan and R. N. Stuart, see next DAFS Quarterly.

18. R. S. Averback, R. Benedek, and K. L. Merkle, Phys. Rev. B18, 4156 (1978).

VII. FUTURE WORK

Calculations will be extended to 5 and perhaps 10 keV to determine if the efficiency begins to level out. Recombination models will be explored with the binary code MARLOWE to reproduce the dynamic results and extend the calculations into the 100 keV range.

VIII. PUBLICATIONS

This information will be presented as part of an invited paper at the AIME Symposium on the Applications of Refractory Metals in Fusion Reactors at Milwaukee, Wisconsin, September 17-20, 1979.

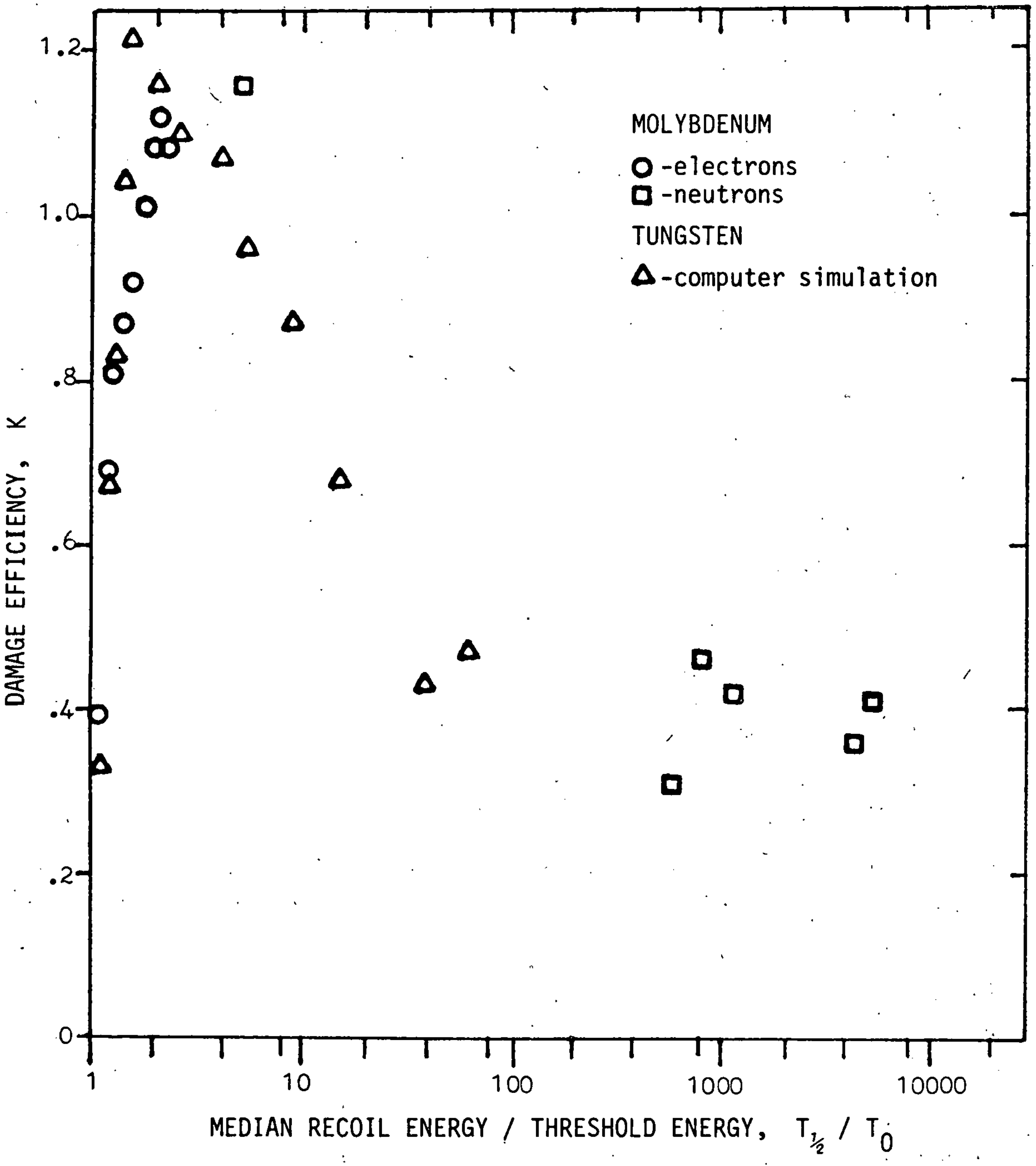

FIGURE 1. Damage production efficiency, K, as a function of normalized recoil energy, $T_{1/2} / T_0$. A comparison of experimentally derived efficiencies from both electron, ○, and neutron, □, irradiations of molybdenum with computer simulation results, △, for tungsten.

I. PROGRAM

Title: 14 MeV Neutron Irradiations (WZJ-14)
Principal Investigator: M. Guinan / W. Barmore
Affiliation: Lawrence Livermore Laboratory

II. OBJECTIVE

The objective of this work is the characterization of the primary damage state resulting from 14 MeV neutron irradiations through the development of computer models for the production and distribution of defects in high energy collision cascades.

III. RELEVANT DAFS PROGRAM TASK / SUBTASK

SUBTASK II.B.2.3 Cascade Production Methodology
II.B.3.2 Studies of Metals

IV. SUMMARY

A fully dynamic computer calculation has been made of the displacement threshold in tungsten as a function of the direction of the primary knock-on atom. Values for the displacement threshold were determined at 70 points in the stereographic triangle to provide a detailed map of the anisotropy.

The results are in good agreement with experiments on single crystals of the b.c.c. metals. The minimum threshold is found in the <100> direction, followed by values near <111> of 1.2 times the minimum and values near <110> of 2.3 times the minimum. The directional averaged threshold is found to be 2.5 times the minimum value. Experimentally, ratios of the threshold near <111> to that along <100> are about 1.2 for V, Cr, Fe, and Mo, while a ratio of 1.05 is reported for tungsten.

V. ACCOMPLISHMENTS AND STATUS

A. The Anisotropy of Defect Production in Tungsten - M. W. Guinan and R. N. Stuart (LLL)

1. Introduction

The number, $\langle n \rangle$, of Frenkel pairs (FP's) created by an energetic recoil of energy T in a metal is usually estimated from the modified Kinchin-Pease model,

$$\langle n \rangle = KT/2T_A , \tag{1}$$

where K is an energy dependent efficiency and T_A is the directional averaged threshold energy. In order to evaluate the results of fully dynamic computer simulations of defect production in tungsten[1] in terms of this model, a value for T_A is required.

2. Procedures

Calculations have been made using two different pair potentials for tungsten. Potential I is that of Johnson and Wilson[2] at near equilibrium separations and is matched at close separations to a repulsive potential derived by Wilson and Bisson[3] using density functional methods. Potential II is identical to I below 2 eV, but is matched to the potential used by Beeler and Besco[4] at close separations.

A detailed map of the threshold displacement surface has been made for potential I; a few selected calculations for potential II. Most of the results were obtained in a crystal with periodic boundary conditions containing 1500 atoms. We found, however, that for directions near <111> a much larger crystal (3500 atoms) was required to contain the longer replacement sequences. Use of the smaller crystal with periodic or rigid boundary conditions resulted in high values of the <111> threshold.

3. Results and Discusion

As expected, the minimum threshold is in the <100> direction in agreement with experiments[5] for b.c.c. metals and previous calculations for Fe[6]. The values obtained for the principal directions are given below in Table 1, and compared to experimental values for Mo[7] and W[8].

TABLE 1

DISPLACEMENT THRESHOLDS IN PRINCIPAL CRYSTALLOGRAPHIC DIRECTIONS

	Tungsten Computation		Experiment	
Direction†	I	II	Mo	W
<100>	65	41	35 ± 1	42 ± 1
<111>	78	50	45 ± 3	44 ± 1
<110>	150	--	>70	--
$\frac{T_d\langle 111\rangle}{T_d\langle 100\rangle}$	1.20	1.24	1.29 ± .11	1.05 ± .05

†The minimum values found near the directions indicated are given

The values for the ratios of the threshold near <111>, T_d<111>, to that in the <100> direction, T_d<100>, are also given in Table 1. The calculations fall between the experimental values for Mo and W, and are in reasonable agreement with those determined[5] for V, Cr, and Fe for which the ratios T_d<111>/T_d<100> are 1.16, 1.14, and 1.18 respectively.

A map of the threshold surface is given in Figure 1 where the ratio $T_d(\theta,\phi)/T_d$<100> is plotted over the stereographic triangle. Thresholds reach values equal to five times T_d<100> near the center of the triangle. The local minima near <110> and <111> can also be seen. The result of the present calculation for the ratio T_d<111>/T_d<100> of 1.2 is in better agreement with experiment than the value 2.0 from previous work[6].

VI. REFERENCES

1. M. W. Guinan, R. N. Stuart, C. E. Violet, and J. H. Kinney, see preceding contribution.

2. R. A. Johnson and W. D. Wilson, in Proceedings of the International Conference on Interatomic Potentials and Simulation of Lattice Defects (Eds. P. C. Gehlen, J. R. Beeler, Jr. and R. I. Jaffee), Plenum Press, N. Y., 1972, p. 301.

3. W. D. Wilson (private communication)

4. J. R. Beeler, Jr. and D. G. Besco, Phys. Rev. 134A, 530 (1964)

5. Peter Vajda, Rev. Mod. Phys. 49, 481 (1977).

6. C. Erginsoy, G. H. Vineyard, and A. Englert, Phys. Rev. 133, A595 (1964).

7. F. Maury, P. Vajda, M. Biget, A. Lucasson, and P. Lucasson, Rad. Effects 25, 175 (1975).

8. F. Maury, M. Biget, P. Vajda, A. Lucasson, and P. Lucasson, Rad. Effects 38, 53 (1978).

VII. FUTURE WORK

Calculations of displacement thresholds for Fe will be made to support studies of high energy cascades in a low Z b.c.c. metal analogous to those completed in tungsten.

VIII. PUBLICATIONS

None.

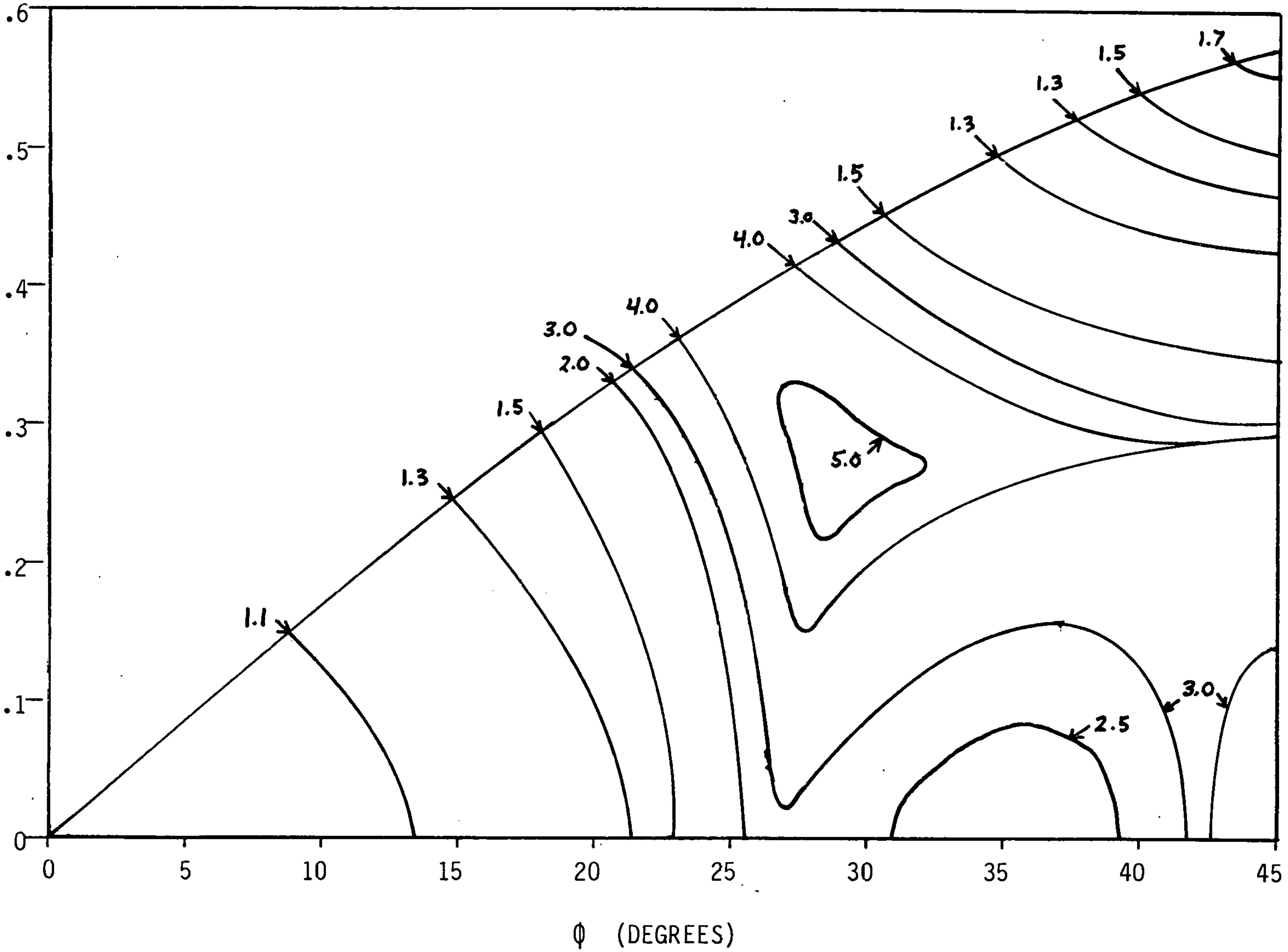

FIGURE 1. The anisotropy of the displacement threshold in tungsten is illustrated with labeled contours of the ratio $T_d(\theta,\phi)/T_d\langle 100\rangle$ in the standard stereographic triangle.

I. PROGRAM

Title: Irradiation Effects Analysis (WH011/EDA)
Principal Investigator: D. G. Doran
Affiliation: Hanford Engineering Development Laboratory

II. OBJECTIVE

The objective of this work is to determine the effects of high energy neutrons on damage production and evolution, and the relationships of these effects to effects produced by fission reactor neutrons. Specific objectives of current work are the planning and performance of an irradiation program at the Rotating Target Neutron Source (RTNS)-II and postirradiation testing.

III. RELEVANT DAFS PROGRAM PLAN TASK/SUBTASK

SUBTASK II.B.3.2	Experimental Characteristics of Primary Damage State; Studies of Metals
II.C.6.3	Effects of Damage Rate and Cascade Structure on Microstructure; Low-Energy/High-Energy Neutron Correlations
II.C.11.4	Effects of Cascades and Flux on Flow; High-Energy Neutron Irradiations
II.C.17.1	Microstructural Characterization; Monitor and Assess New Methodologies
II.C.18.1	Relating Low- and High- Exposure Microstructures; Nucleation Experiments

IV. SUMMARY

Two ambient temperature irradiations at RTNS-II have been completed to estimated fluences of 5×10^{17} and 1×10^{18} n/cm^2. Specimen materials include pure metals, an Fe-Ni-Cr ternary, an Fe-Ni-Cr-Mo quaternary, and

representative Path A and B alloys, all in the form of TEM disks. Some hardness increases have been noted, qualitatively consistent with the observation by TEM of small defect clusters and pinned dislocations. Micro tensile specimens will be irradiated during the next reporting period.

An ultra-high-vacuum furnace for general use at RTNS-II has been constructed and is undergoing final testing.

V. ACCOMPLISHMENTS AND STATUS

A. RTNS-II Irradiation Program - N. F. Panayotou, R. W. Powell, E. Opperman (HEDL)

1. Introduction

The RTNS-II located at the Lawrence Livermore Laboratory is being used to study the effects of high energy neutron (14 MeV) damage on material properties. An understanding of the primary damage state, subsequent microstructure evolution, and the resultant mechanical behavior is important in developing the capability of projecting fission reactor data to fusion reactor environments. HEDL plans to address each of these areas in its experimentation at RTNS-II. In addition, selective Be(d,n) irradiations will be performed at UC-Davis and fission reactor irradiations will be done at the Livermore Pool-Type Reactor (LPTR) to assess the spectral sensitivity of radiation-induced effects.

2. Specimen Preparation

Vanadium, procured from E. E. Bloom and T. K. Roche of ORNL, was fabricated into TEM disk specimens for the second HEDL irradiation at RTNS-II. Binary alloys are currently being fabricated. It is anticipated that they will be included in HEDL's third irradiation.

The recrystallization heat treatments developed by HEDL to produce minimum grain size in pure copper, nickel, titanium, niobium and vanadium have been transmitted to PNL and LLL researchers. It is desirable that the heat treatments used by all experimenters utilizing HEDL's metal stockpile be standardized where practicable.

Thermomechanical treatments for ADIP alloys are currently being developed and refined. To date, Path A and B alloys have been irradiated in both the recrystallized and 40% cold worked conditions. A cold work plus age treatment is being developed for the Path B alloys, in conjunction with the ADIP program.

Micro tensile specimens, shown in Figure 1, have been fabricated from stainless steel by chemical milling techniques. Room temperature tensile tests have been conducted using a device designed specifically for these micro specimens. These specimens can be irradiated at RTNS-II at both elevated and ambient temperatures using available hardware. The chemical milling technique is currently being extended to other metal systems. Micro tensile specimens, fabricated from the same material heat as our TEM disk specimens, will allow direct correlation of microhardness and strength results. This calibration will increase the precision of microhardness data as an indicator of changes in strength due to irradiation. The use of both specimen types is desirable. While a complete flow curve can be obtained from a tensile specimen, TEM disk specimens (about 10 mils thick) can be packed more tightly, taking better advantage of the limited high flux volume of RTNS-II. Furthermore, tensile specimens provide data at only a single fluence. Each TEM disk specimen can be tested for ambient temperature microhardness and reirradiated, thus providing several hardness (strength) values as a function of neutron fluence.

3. Status of Irradiations

During this reporting period two ambient temperature irradiations of TEM disk capsules were accomplished. HEDL experiment No. 1 was performed in April and is estimated to have received a peak dose of 5 x 10^{17} n/cm^2. HEDL experiment No. 2 was terminated on June 29 and is estimated to

MICRO TENSILE SPECIMEN

13mm OVERALL LENGTH
6mm GAGE SECTION

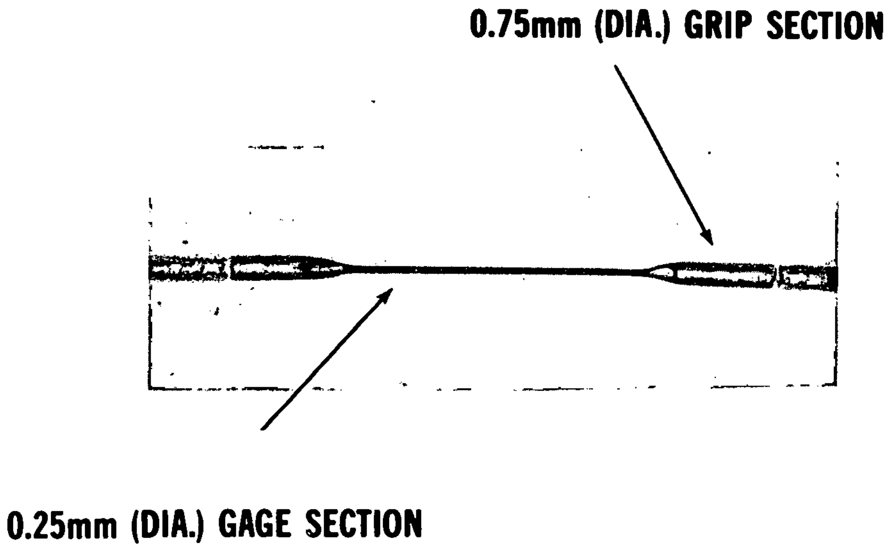

FIGURE 1. Micro tensile specimen fabricated from .75 mm (dia.) stainless steel wire by chemical milling techniques.

have received a peak dose of 1 x 10^{18} n/cm^2. These fluence estimates are based on a 1 cm^2 Gaussian spot and a source strength of 1 x 10^{13} n/cm^2. Capsule loading was designed to take advantage of the strong flux gradient; specimen fluences are expected to vary over a factor of 30 for each experiment. Both capsules contained TEM disk specimens of recrystallized pure metals (copper, niobium, titanium and nickel), an iron-nickel-chrome ternary and an iron-nickel-chrome-moly quaternary, as well as representative ADIP Path A and B alloys. The Path A and B alloys were irradiated in the 40% cold worked and the recrystallized condition. Experiment No. 1 focused on pure metals, the quaternary, and the ternary alloy, while experiment No. 2 focused on the Path A and B alloys. The latter experiment also included Ni-5% Si, and Ni-5% Al, supplied by M. W. Guinan of LLL, and recrystallized vanadium. Analysis of the dosimetry foils from both experiments is expected to be available during the next reporting period.

Two additional irradiations are currently scheduled for completion during the next reporting period. Both will be at ambient temperature and will have a maximum fluence of 1 x 10^{18} n/cm^2. HEDL experiment No. 3, scheduled to begin in late August, will emphasize the irradiation of TEM disk specimens of the binary alloys described in the preceeding quarterly. HEDL experiment No. 4, scheduled for late September, will involve the irradiation of micro tensile specimens. These specimens will be tested at room temperature after irradiation to provide flow data; the results will be correlated with microhardness, TEM, and other postirradiation test results where possible.

4. Specimen Analysis

Baseline microhardness data have been collected for all metals and alloys currently available. Preliminary microhardness test results from specimens irradiated in HEDL experiment No. 1 indicate that some of the pure metals show increases in microhardness with increasing neutron dose. The magnitude of the increase in hardness is in agreement with previous work over the same range of neutron fluence. These results are in qualitative agreement with initial TEM observations of small defect clusters and pinned dislocations.

B. RTNS-II Furnace Development - D. C. Kaulitz, S. C. Meyers (HEDL), C. M. Logan (LLL)

Construction of a high temperature furnace for general use at RTNS-II has been completed. This furnace will permit the irradiation of materials at temperatures up to a maximum of 800°C. The design base pressure of the furnace is 1×10^{-8} torr. The furnace heat zone is approximately 15 mm square and 40 mm long (in beam direction). Final testing of the furnace is in progress. Delivery of the furnace to the RTNS-II facility is expected during the next reporting period. A second furnace, designed to accommodate 50 mm tensile specimens perpendicular to the beam direction is currently being designed.

C. LPTR Furnace Development - N. F. Panayotou (HEDL), R. Van Konynenberg (LLL), M. W. Guinan (LLL)

A furnace to be used for irradiations in the Livermore Pool-Type Reactor (LPTR) at LLL is currently being designed at LLL as a joint LLL-HEDL project. The furnace will have a specimen volume comparable to the volume of HEDL's RTNS-II capsules. The irradiation of micro tensile and TEM disk specimens at RTNS-II can thus be duplicated in a fission reactor spectrum at a comparable displacement rate to permit the study of spectral effects.

VI. FUTURE WORK

Two irradiations are scheduled for the RTNS-II; one will emphasize TEM disks of binary alloys, and the other will be the first HEDL irradiation of micro tensile specimens.

TEM and microhardness examinations of RTNS-II irradiated specimens will continue.

The RTNS-II furnace will be delivered to the facility during the next quarter.

THIS PAGE

WAS INTENTIONALLY

LEFT BLANK

CHAPTER 5

SUBTASK C: DAMAGE MICROSTRUCTURE EVOLUTION AND MECHANICAL BEHAVIOR

THIS PAGE

WAS INTENTIONALLY

LEFT BLANK

I. PROGRAM

Title: Phase Stability Under Irradiation
Principal Investigator: K. C. Russell
Affiliation: Massachusetts Institute of Technology

II. OBJECTIVE

To understand and model the effects of irradiation on microstructural stability.

III. RELEVANT DAFS PROGRAM PLAN TASK/SUBTASK

SUBTASK II.C.1.2 Modeling and Analysis of Effects of Material Parameters on Microstructure

IV. SUMMARY

A. The stability of incoherent oxide dispersoids may be significantly altered by CTR first wall irradiation conditions.

B. Irradiation tends to stabilize oxide particles when the matrix dissolves oxygen interstitially and to destabilize when oxygen dissolves substitutionally.

C. The effect of irradiation is enough to reverse a several-fold solute supersaturation or undersaturation, over a range of irradiation conditions and temperatures.

D. Dispersoid stability must be evaluated on a case by case basis for each reactor system.

V. ACCOMPLISHMENTS AND STATUS

A. Oxide Dispersoid Stability in Irradiated Alloys -- M. S. Saiedfar (Massachusetts Institute of Technology, Cambridge, MA) and K. C. Russell (Massachusetts Institute of Technology, Cambridge, MA).

1. Introduction

Oxide dispersoid alloys include Cr_2O_3 or Al_2O_3 particles in a type 316 stainless steel (SS) matrix, Al_2O_3 particles in an aluminum matrix, and ThO_2 particles in a nickel matrix. The outstanding characteristic of such alloys is the retention of a reasonable level of strength to temperatures near the melting point, as shown in Figure 1.

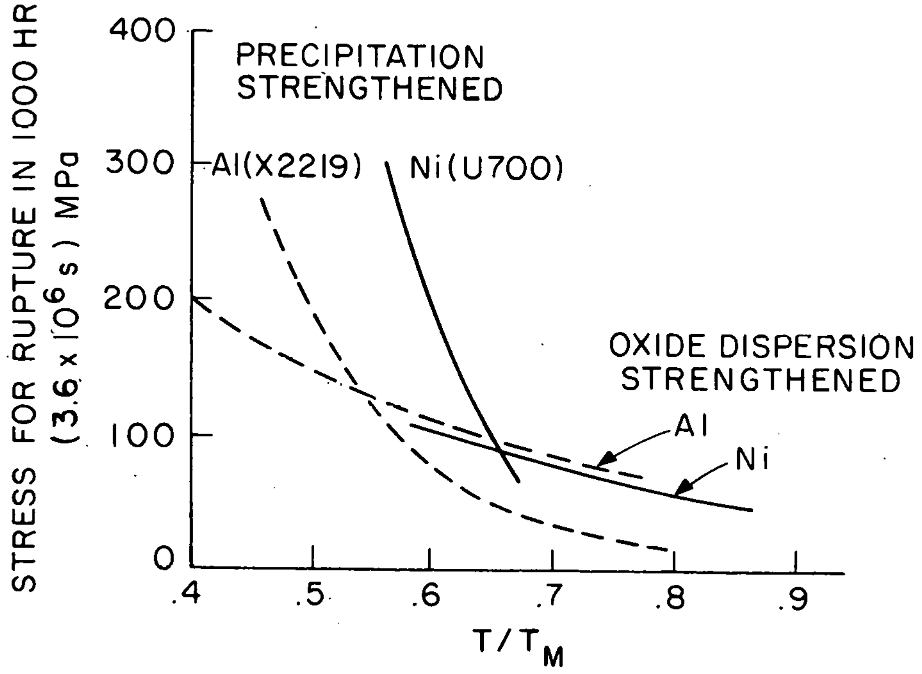

FIGURE 1. Comparison of strengths of dispersion-strengthened and precipitation-strengthened alloys. (After Ref. [1].)

The oxide particles are incoherent with the matrix, and are thus relatively inefficient as strengtheners, as compared to the usual partly or totally coherent particles. However, the oxides are thermodynamically very stable, hence are highly insoluble in the matrix. As such, even at temperatures near the melting point the oxides neither dissolve into the matrix nor coarsen (Ostwald ripen) to large sizes, the fate of most other precipitates at high temperatures. As such, the dispersoid strengthened alloys retain significant amounts of strength and maintain structural stability to temperatures near the melting point.

Oxide dispersoids are of interest in CTR first wall materials for three reasons. First, they are an attractive strengthening mechanism. Secondly, since these materials may contain only one or two metallic elements, one may avoid the formation of undesirable transmutation products which tend to form in more complex alloys after exposure to first wall neutron fluences. Thirdly, the high density of very small particles gives a high sink strength. The interfaces are thus potentially effective traps for transmutation-produced helium and for vacancies and self interstitials.

Before such materials may be seriously considered for first wall use, their stability under irradiation conditions must be assured. It is now well-known [2] that there are a number of mechanisms by which irradiation will alter the stability of alloy phases. This paper investigates two of these: enhanced diffusion and the chemical vacancy effect. The effects of solute segregation to or away from the particles is accounted for in an approximate way by varying the matrix solute supersaturation as a parameter. Extended calculations have been performed for Cr_2O_3 in 316 SS and Al_2O_3 in Al under both fusion neutron and heavy-ion displacement rates [3]. This short paper is based on results for stainless steel under first wall conditions.

2. Theory

The theory for the stability of incoherent particles under irradiation is described in detail elsewhere [4]. The particles are characterized by x, the number of atoms or molecules, and n, the number of excess vacancies they contain. If the precipitate has a larger atomic volume than the matrix (per substitutional atom), vacancies will be absorbed during growth, first to relieve strain energy, but by consuming supersaturated vacancies also contribute to the driving force, hence stability of the particles. In the reverse case of an undersized precipitate, growth usually requires vacancies to be emitted into a highly supersaturated matrix. This is difficult, so the excess vacancies tend to decrease precipitate stability.

Particle behavior is described by equations for the particle velocity in n and x directions. These are:

$$\dot{x} = \beta_x(1 - \exp[(1/kT)(\partial \Delta G^\circ/\partial x)]) \qquad (1)$$

$$\dot{n} = \beta_v(1-\beta_i/\beta_v - \exp[(1/kT)(\partial \Delta G^\circ/\partial n)]) \qquad (2)$$

In Eqs. (1,2) $\dot{x}$ and $\dot{n}$ are velocities (atoms or vacancies per second) in the n and x directions. β_x, β_v and β_i are the arrival rates of solute atoms, vacancies, and self interstitials at the particle, ΔG° is the free energy of forming the particle from the solute atoms and vacancies in the matrix, and kT is the Boltzmann factor.

Nodal lines are obtained by setting $\dot{x}$ and $\dot{n}$ individually to zero. Under certain conditions these nodal lines intersect in a critical point where the particle is immobilized -- like that critical nucleus in nucleation theory. Particles larger than this size are stable and will grow. In other cases, all particles are unstable and will ultimately decay. The critical particle size is given by

$$x^* = -32\pi\gamma^3\Omega^2/3(\Delta\phi)^3 \qquad (3)$$

where $\Delta\phi$ is an irradiation-modified potential given by

$$\Delta\phi = -kT \ln S_x \left[S_v(1-\beta_i/\beta_v)\right]^{\delta} - (kT/4B)\left[\ln S_v(1-\beta_i/\beta_v)\right]^2 \qquad (4)$$

where S_x and S_v are solute and vacancy supersaturations, and B is a positive constant. For a dispersoid of M_2O_3 where M denotes the metal,

$$\delta = \frac{\Omega-5\Omega_m}{5\Omega_m} \quad \text{and} \quad \delta = \frac{\Omega-2\Omega_m}{2\Omega_m}$$

for substitutional and interstitial oxygen atoms, respectively. Here, Ω_m and Ω are volumes per substitutional atom in matrix and precipitate, respectively. When $\Delta\phi < 0$ the nodal lines intersect as shown in Figure 2.

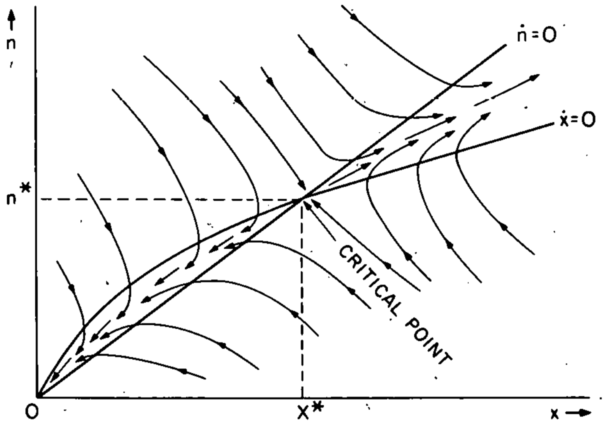

FIGURE 2. Phase space for dispersoid behavior, showing nodal lines, critical point, and directions of particle movement. (After Ref. [3].)

3. Calculations

Calculations were based on Eq. (3) for x^* and on Eqs. (1,2) for $\dot{x}$ and $\dot{n}$. Point defect concentrations were calculated by the method of Brailsford and Bullough [5], using measured dislocation densities [6]. The needed material parameters were obtained from handbooks or the literature. The results are not particularly affected by minor changes in the values of the material parameters.

4. Results and Discussion

It is not known whether oxygen dissolves interstitially or substitutionally in stainless steel. Accordingly, both possibilities were considered.

The location of the dissolved oxygen proved to be crucial, as calculations showed that the sign of the misfit, δ, in large part, dictated dispersoid stability. In the case of substitutional oxygen in the matrix, addition of either a Cr or O atom to the particle adds an atomic volume of space. Since the volume of Cr_2O_3 is less than that of five matrix atoms, $\delta < 0$. Figure 3 presents x^* - number of atoms in the critical size particle as a function of temperature for various solute supersaturations. Irradiation is seen to destabilize the particles. At low temperature, the vacancy supersaturation is high and x^* is large. At temperatures near .6 T_m, $S_v \rightarrow 1$ and x^* is unaffected by irradiation.

In the case of interstitial oxygen, only addition of a chromium atom to the particle adds on a lattice site. Since the volume of Cr_2O_3 is considerably larger than two matrix lattice sites, $\delta > 0$. As seen in Figure 4, irradiation stabilizes the particles. The effect is greatest at low temperatures, where S_v is very high ($> 10^{10}$). In addition, particles are stable in a matrix just saturated ($S_x = 1$) or even undersaturation ($S_x = .5$). In the latter case, a critical size exists only up to

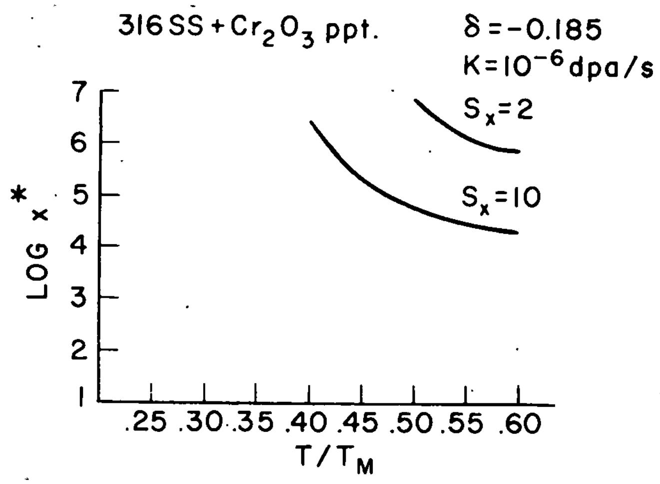

FIGURE 3. Critical particle size for Cr_2O_3 in 316 SS with δ < 0.

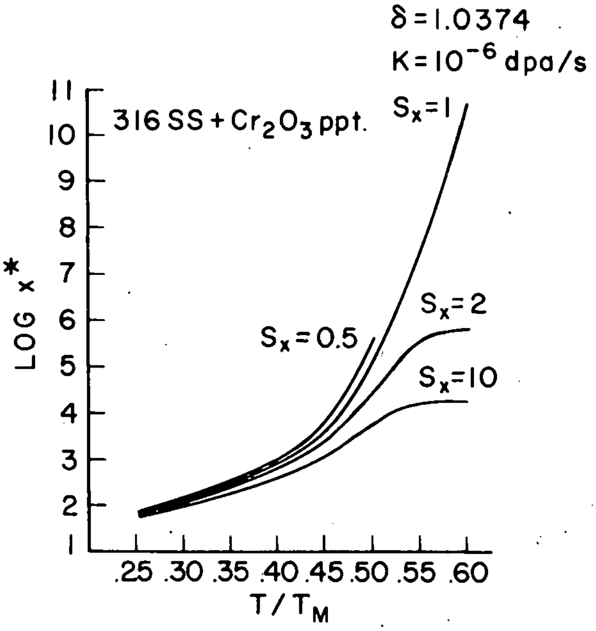

FIGURE 4. Critical particle size for Cr_2O_3 in 316 SS, with δ > 0.

a certain temperature, after which S_v is too small to keep $\Delta\phi < 0$.

Stated another way, under irradiation a particle with $\delta < 0$ may dissolve even in a supersaturated matrix, or a matrix locally supersaturated by solute segregation toward the particle. Conversely, a particle with $\delta > 0$ may grow in an undersaturated matrix or in a matrix made locally undersaturated by solute segregation away from the particle. The importance of these effects will depend on the amount and solubility of the dispersoid phase. In the case of a substantial volume fraction of a highly insoluble phase, very little growth or dissolution would be needed to adjust S_x to a value giving $\Delta\phi = 0$. In the reverse case of a small amount of a more soluble phase, significant growth or dissolution may have to occur before the matrix composition is adjusted to a value giving a stable situation.

Growth trajectories were calculated for particles under steady and pulsed irradiation. Figure 5 depicts the behavior of an oversized precipitate during a year of steady irradiation. Even in an undersaturated matrix the particle doubles its size in a year. At higher solute supersaturations, up to ten-fold growth is predicted.

The case for an undersized precipitate under pulsed irradiation is shown in Figure 6. In this case, $\Delta\phi > 0$ during irradiation and $\Delta\phi < 0$ during the thermal period.

The particle first of all gains some vacancies (n becomes less negative), then proceeds to decay. However, the size of the particle decreases by only about 10% over the course of a year. In both cases very little growth or dissolution occurred during the thermal cycle due to the low solubilities and low atomic mobilities.

Considerably different behavior could easily be observed under other material and/or irradiation conditions. It is quite possible

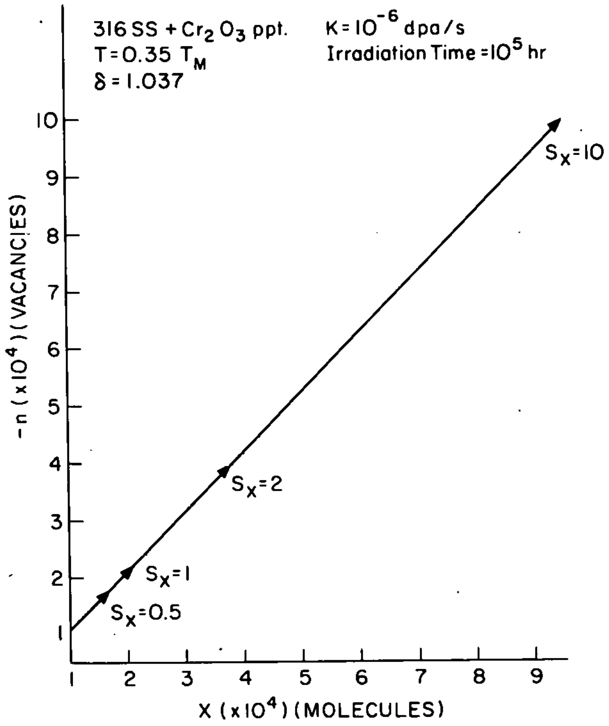

FIGURE 5. Particle behavior under steady irradiation ($\delta > 0$).

that the thermal processes could cancel out or even overwhelm processes occurring during irradiation. Based on the present Cr_2O_3 work, a highly insoluble dispersoid such as Al_2O_3 would probably be stable regardless of the sign of δ.

VI. REFERENCES

1. G. M. Ault and H. M. Burte, in: Oxide Dispersion Strengthening, Metallurgical Society Conferences, Vol. 47, eds. G. S. Ansell, T. D. Cooper, F. V. Lenel (Gordon and Breach, New York, 1968) 4.

2. J. A. Hudson, in: Precipitation Processes in Solids, ed. K. C. Russell and H. I. Aaronson (AIME, New York, in press).

3. M. S. Saiedfar, S.M. Thesis, M.I.T. (May 1978).

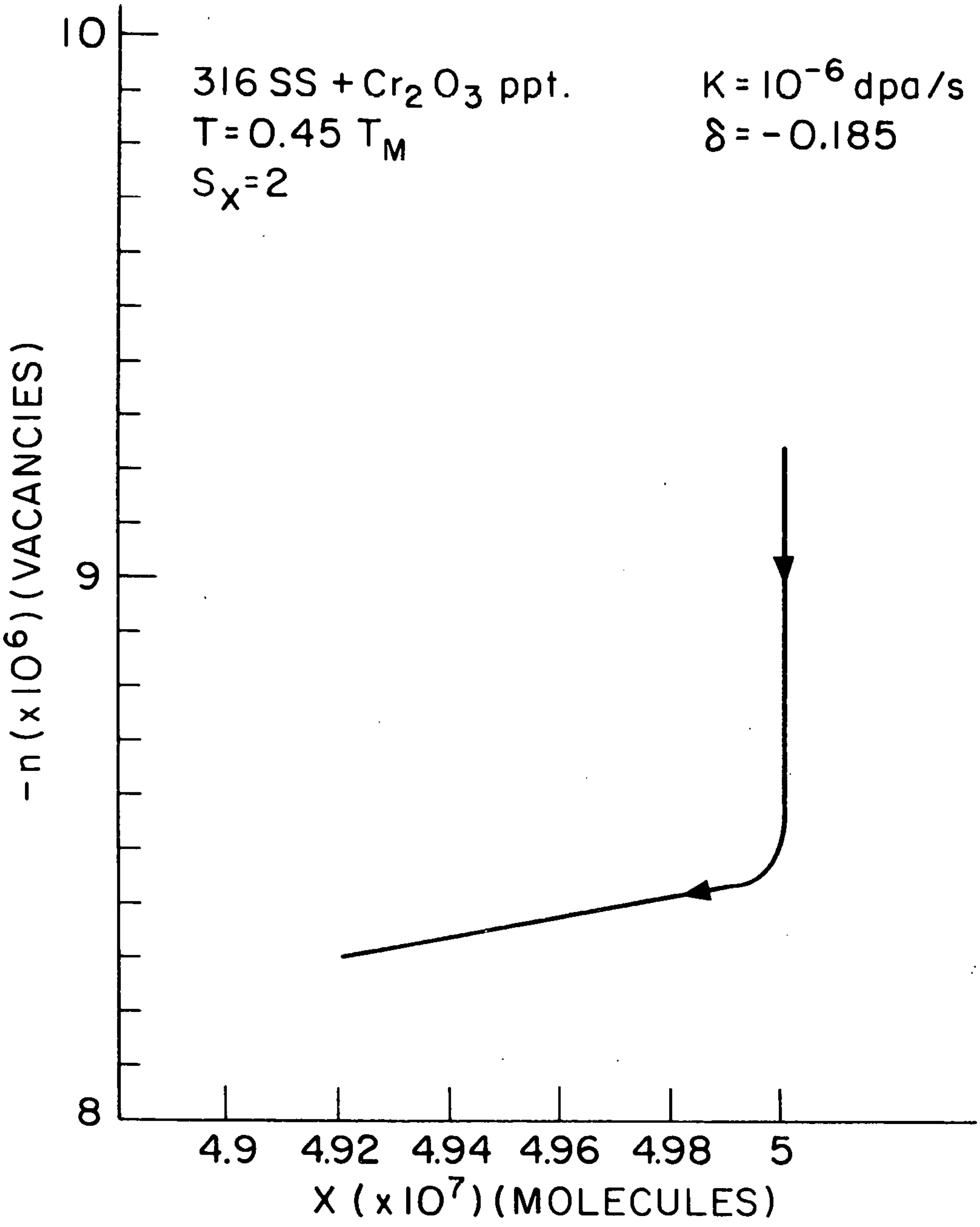

FIGURE 6. Particle behavior under pulsed irradiation ($\delta < 0$).

4. S. I. Maydet and K. C. Russell, J. Nucl. Mater. 64 (1977) 101.

5. A. D. Brailsford and R. Bullough, J. Nucl. Mater. 44 (1972) 121.

6. H. R. Brager and J. L. Straalsund, Met. Trans. 2 (1971) 1893.

VII. Future Work

The next step is modelling the stability of carbide and boride phases phases in irradiated stainless steel.

VIII. PUBLICATIONS

A paper entitled, "Oxide Dispersoid Stability in Irradiated Alloys", has been accepted by J. Nuclear Materials for publication as part of "First Topical Meeting on Fusion Reactor Materials", Miami Beach, January 29-31, 1979.

I. PROGRAM

Title: Void Swelling in Irradiated Metals
Principal Investigator: K. C. Russell
Affiliation: Massachusetts Institute of Technology

II. OBJECTIVE

The objective of this work is to analytically and numerically model homogeneous and heterogeneous void nucleation in irradiated metals.

III. RELEVANT DAFS PROGRAM PLAN TASK/SUBTASK

SUBTASK II.C.2.4 Modeling of Effects of Helium on Microstructure

IV. SUMMARY

The energetics and kinetics of void nucleation at dislocations and interfaces are analyzed. These are potential void nucleation sites only when they are not point defect sinks. Both kinds of site are found to be excellent catalysts in the presence of inert gas.

V. ACCOMPLISHMENTS AND STATUS

A. Void Nucleation at Heterogeneities -- S. A. Seyyedi (Massachusetts Institute of Technology, Cambridge, MA), M. Hadji-Mirzai (Massachusetts Institute of Technology, Cambridge, MA) and K. C. Russell (Massachusetts Institute of Technology, Cambridge, MA).

1. Introduction

The existence of irradiation-induced void swelling in breeder reactors cladding and ducts was discovered over a decade ago (1).

The need for understanding and a means to eliminate or control this swelling and the associated loss of dimensional stability has led to many experimental and theoretical studies.

The early theoretical analyses considered the problem piecemeal, and in some cases were in error. A recent theory (2) presented a unified analysis of homogeneous void nucleation in the presence and absence of inert gas. However, voids have been observed to nucleate heterogeneously near or on dislocations and internal interfaces. Very little has been done to develop a theory for such nucleation. The one analysis to date is by Bates (3) who considered void nucleation at the interface between the matrix and an incoherent particle. However, since such interfaces are excellent point defect sinks, there will be no vacancy supersaturation and void nucleation is impossible. Most dislocations are also point defect sinks, and void nucleation is likewise impossible. However, certain coherent and semi-coherent interfaces and certain partial dislocations are not point defect sinks, hence, are potential void nucleation sites.

We will develop the theory[a] for heterogeneous void nucleation at such dislocations and interfaces. In each case we first consider the void energetics, then the point defect arrival rates, and finally develop expressions for nodal lines and nucleation rates.

2. Theory

The analysis is based on a recent unified theory of homogeneous void nucleation in helium-containing metals (2). Voids are characterized in a two-dimensional phase space (see Figure 1) where the void is assigned coordinates specifying its vacancy content (n) and the number of gas atoms it contains (x). The void may move in the positive n-direction by capturing additional vacancies and move in the opposite direction either by thermal emission of vacancies or capture of self inter-

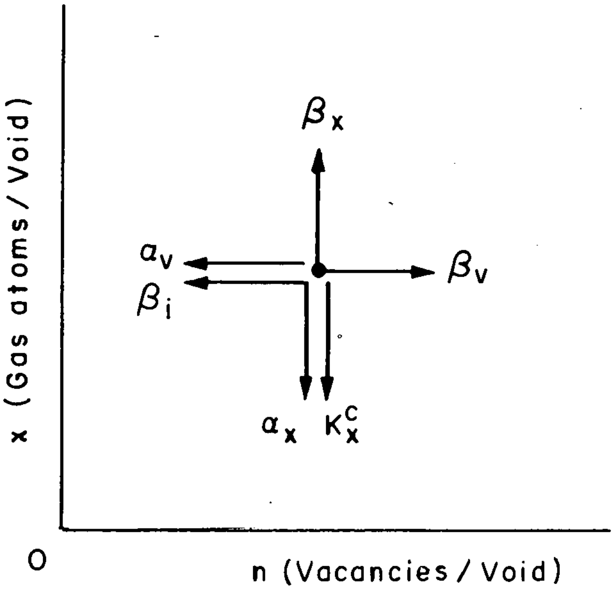

FIGURE 1. Point defect capture processes which alter the size or gas content of a void. (After Ref. 2.)

stitials. Movement in the positive x-direction is accomplished via gas atoms capture and in the opposite direction by radiation resolutions, wherein trapped gas atoms are injected back into the matrix. The corresponding component velocities in n,x phase space are given by:

$$\dot{n} = \beta^\circ_v n^{1/3}[1 - \beta^\circ_i/\beta^\circ_v - \exp(\frac{1}{kT}\frac{\partial \Delta G^\circ(n,x)}{\partial n})] \qquad (1)$$

$$\dot{x} = \beta^\circ_x n^{1/3}[1 - xK^c_x/\beta^\circ_x n^{1/3}] \qquad (2)$$

where β°_v and β°_x are the arrival rates of vacancies, interstitials, and gas atoms respectively, at a hypothetical void of one vacancy (the factor of $n^{1/3}$ accounts for the dependence of the capture rate upon void size). K^x_c is the rate (per gas atom) of radiation resolution, $\Delta G^\circ(n,x)$ is the free energy to form an (n,x)-mer from the vacancies and gas in a metal, and kT is the Boltzmann factor.

Such first-order differential equations as Eqs. (1,2) in which time does not appear explicitly (termed autonomous) and which may be linearized in the region of interest lend themselves to analysis through a branch of mathematics developed by Poincaré (4,5). This analysis emphasizes the loci of points where n or x are zero (nodal lines) and points of intersection, where $\dot{n} = \dot{x} = 0$ (critical points). The application of this formalism to radiation effects problems is described in detail elsewhere (6).

Taking the appropriate partial derivative of $\Delta G^\circ(n,x)$, inserting it into Eq. (1), and setting the individual velocities to zero yields the equations of the two nodal lines of interest:

for $\dot{n} = 0$

$$x = 2An^{1/3}/3 - n\ell n S_e \tag{3}$$

for $\dot{x} = 0$

$$x = \beta^\circ_x n^{1/3}/K^c_x \tag{4}$$

where $A = (36\pi\omega^2)^{1/3}\gamma/kT$, $S_e = S_v(1 - \beta^\circ_i/\beta^\circ_v)$, Ω = atomic volume, γ = surface energy, and S_v = vacancy supersaturation.

Simultaneous solution of Eqs. (3,4) shows intersections of the nodal lines (critical points) to occur at n values given (in the case of homogeneous nucleation) by:

$$n^{1/3} = \frac{A}{3\ell n S_e} \quad \frac{A}{3\Omega n S_e}(1 - \psi)^{1/2} \tag{5}$$

where $\psi = \dfrac{9\beta^\circ_x \ell n S_e}{A^2K^c_x}$ (6)

The value of ψ categorizes void nucleation. If $\psi < 1$, the nodal lines intersect at two points (in addition to the origin); if $\psi = 1$

the nodal lines are tangent; in the case where $\psi < 1$, the lines intersect only at the origin. Configurations for $\psi > 1$ and $\psi < 1$ are depicted schematically in Figure 2. When $\psi > 1$ no activation barrier to nucleation exists and any (n,x)-mer is free to develop spontaneously from individual point defects. A simple, closed form equation for the rate of void nucleation may then be written.

The power of the nodal line formalism may be appreciated by considering the alternative, namely, solution of some 1,000 simultaneous equations in 1,000 unknowns -- the concentrations of the voids of various sizes and gas contents. Such systems of equations may be solved numerically, but such a solution is time-consuming, subject to serious error, and obscures the physics of the process.

Nucleations on Dislocations

We follow in general the energetic model of Cahn (7) for nucleation of incoherent precipitates on dislocations. Whereas Cahn used the calculus of variations to determine the minimum energy nucleus form, we assume a cylinder of minimum surface-to-volume ratio for mathematical tractability. The free energy of forming such a void is then:

$$\Delta G^\circ(n,x) = -\frac{\mu b^2}{6\pi(1-\nu)}\left(\frac{\Omega}{2\pi}\right)^{1/3} n^{1/3} \left[\log \frac{\Omega}{2\pi} n\right] + \frac{8\pi\gamma\Omega^{2/3}}{3(2\pi)^{2/3}} n^{2/3} - nkT\ell n S_v - xkT + skT\ell n \frac{x}{x_e} \tag{7}$$

where μ = elastic shear modulus, b = Burgers vector, ν = Poisson ratio, and x_e = void gas content which would be in equilibrium with the matrix. This first term in Eq. (7) arises from release of dislocation strain energy, the second term from creation of surface energy, the third from the vacancy supersaturation, and the last two from the internal gas pressure.

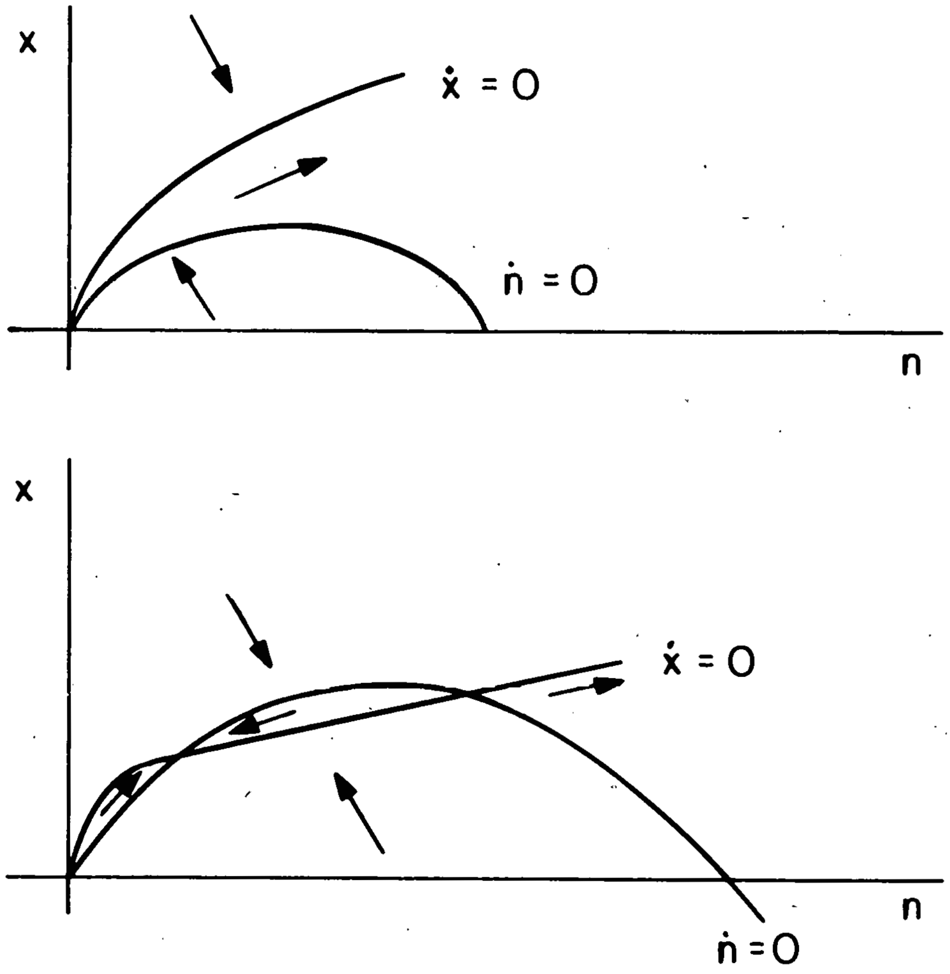

FIGURE 2. Schematic representation of nodal lines. At top, $\psi > 1$ and void nucleation is spontaneous. At bottom, $\psi < 1$ and activation is required. (After Ref. 2)

Only dislocations which are not vacancy sinks will be effective void nucleation sites, as otherwise $S_v = 1$. Therefore, β_v and β_i at dislocations are essentially the same as in the matrix. The dislocations are assumed to be helium traps, so there are two routes for helium arrival at the void -- through the matrix and along the dislocation.

Mobile interstitial gas atoms are provided by radiation resolution from dislocation traps. The arrival rate at a void in that matrix is then (2):

$$\beta^{\circ}_{xm} = \frac{C^{o}_{x} K^{T}_{x}}{a^{2} k^{2}_{x}} \qquad (8)$$

where C^{o}_{x} is the total gas concentration, K^{T}_{x} is the resolution rate from dislocations, k^{2}_{x} is the total sink strength for gas, and a is lattice spacing.

The helium arrival rate along dislocations is $\beta^{\circ}_{xd} = D^{d}_{x} p/a^{2}$ where p = probability a gas atom is next to the void, and D^{d}_{x} = helium diffusivity in the dislocation. Taking $p = (C^{o}_{x}/\Omega)/p_{d}a)$ where $p_{d} = k^{2}_{x}$ is the dislocation density, gives a helium arrival rate along the dislocation of:

$$\beta^{\circ}_{xd} = \frac{C^{o}_{x} D^{d}_{x}}{a^{4} p_{d}} \qquad (9)$$

Nucleation at Precipitates

The free energy of forming a spherical-lens shaped gas-containing void of radius r (see Figure 3) is given by

$$\Delta G^{\circ} = -\frac{4}{3}\pi r^{3} f(\theta) \cdot \frac{kT}{\Omega} \ell n S_{v} + 4\pi r^{2} \gamma_{mv} f(\theta) - xkT + xkT \ell n\, x/x_{e} \qquad (10)$$

where $f(\theta) = \dfrac{2 - 3\cos\theta + \cos^{3}\theta}{4}$.

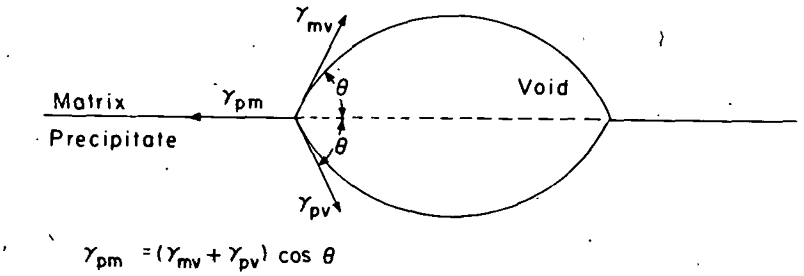

FIGURE 3. Lens shaped void formed at precipitate:matrix interface.

The precipitate is assumed to be coherent or semi-coherent with the matrix, so that the interface is not a sink for vacancies or interstitials. As such, $\beta°_v$ and $\beta°_i$ will be substantially the same as in the matrix. There are, however, again two paths by which helium may reach the heterogeneously nucleated void. One path is through the matrix, at a rate diminished by the depleted helium concentration near the precipitate. The other is by the "collector plate" mechanism (8), whereby the helium is trapped at the precipitate:matrix interface, and diffuses thereon to the void. The rate of arrival along the interface (per atom of perimeter) is

$$\beta°_{xp} = \frac{C^p_x D^p_x}{a^2} \tag{11}$$

where C^p_x = concentration of trapped helium at the precipitate, and D^p_x = diffusivity of helium in the matrix:precipitate interface.

To obtain C^p_x we assume that on a per-site basis the precipitate interface has the same helium concentration as the dislocations. This gives:

$$\beta°_{xp} = \frac{C^o_x D^p_x}{k^2_x a^4} \tag{12}$$

3. Results and Discussion

Nucleation at Dislocations

The ratio of helium arrival rates by the two paths is:

$$\frac{\overset{\circ}{\beta}_{xd}}{\beta^{\circ}_{xm}} = \frac{D^d_x}{a^2 K^T_x} \tag{13}$$

Helium mobilities in solids are generally not well known. To investigate the ratio of arrival rates, we assume that the pre-exponential factor for helium diffusion along dislocations is the same as for self diffusion. The activation energy is estimated to lie in the range between one-half and one-fourth that for helium diffusion in the matrix, namely 1.84 eV. The results are shown in Table 1 for 316 stainless steel under fusion reactor irradiation conditions. Diffusion along the dislocation is seen to be the dominant mechanism in all cases. This is mainly because of the high concentration of helium in the dislocation core. This is high enough to compensate for the low mobility in the dislocation relative to that of interstitial helium in the matrix.

TABLE 1

Relative Helium Arrival Rates

	$\beta^{\circ}_{xd}/\beta^{\circ}_{xm}$	
T/T_M	$Q^d = .92$ eV	$Q^d = .46$ eV
.30	7.61×10^{7}	3.13×10^{12}
.40	1.54×10^{10}	4.45×10^{13}
.50	3.74×10^{11}	2.20×10^{14}
.60	3.13×10^{12}	6.37×10^{14}

The ratio of helium and vacancy arrival rates is:

$$\frac{\beta^\circ_{xd}}{\beta^\circ_v} = \frac{C^o_x D^d_x}{a^2 K} \qquad (14)$$

Taking extreme conditions of $C^o_x = 1$ appm, $T = .6\ T_M$, and $Q_{SD} = .92$ eV, $\beta^\circ_{xd}/\beta^\circ_v > 10^5$. Under most conditions this ratio will be even greater, so that helium is expected to arrive at the void much more rapidly than vacancies.

The helium arrival rate at a void on a dislocation should be largely independent of void size, so that $\beta_x = \beta^\circ_{xd}$. Inserting the appropriate quantities is Eqs. (1,2) gives nodal lines of:

$$x = \frac{-\mu b^2}{6\ kT(1-\mu)} \left(\frac{\Omega}{2\pi}\right)^{1/3} \left[\frac{1}{3} \log \frac{\Omega}{2\pi}\ n + \frac{1}{2.303}\right] n^{1/3} + \frac{8\pi\gamma\Omega^{2/3}}{3kT(2\pi)^{2/3}} - n\ell S_e \qquad (15)$$

for $\dot{n} = 0$ and

$$x = \beta^\circ_{xd}/K^c_x \qquad \text{for } \dot{x} = 0. \qquad (16)$$

Nodal lines were calculated for type 316 stainless steel over the temperature range .35 to .6 T_m. In no case did the lines intersect, so that nucleation is spontaneous and rapid over the entire range. A typical result is shown in Figure 4, where the two nodal lines are seen to be very widely separated. The degree of separation is somewhat nonphysical, coming in part from using the ideal gas law to describe the helium in the void. Use of a more realistic gas law would reduce the separation by a large amount, but could hardly give intersection. As such, void nucleation on dislocations which are not vacancy sinks is expected to be spontaneous and rapid over a substantial range of temperatures, displacement rates, and helium contents. Conversely, both network dislocations and prismatic loops are excellent vacancy sinks, hence in the present context are not effective void nucleation sites. Partial dislocations, such as occur in interphase boundaries should be effective

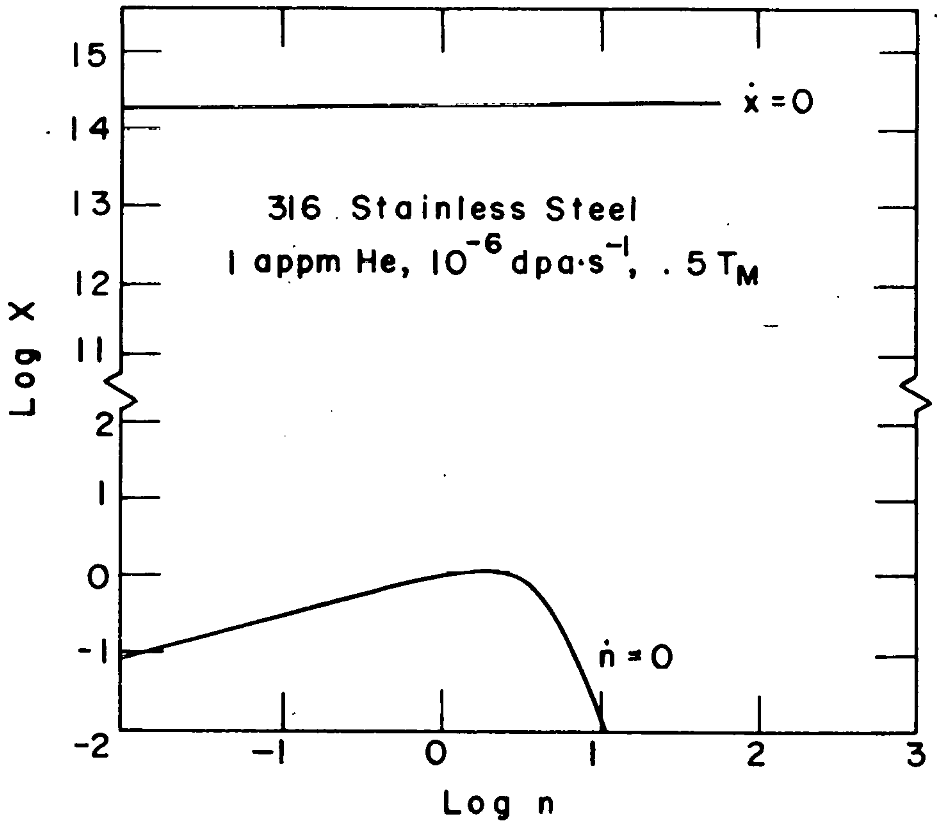

FIGURE 4. Nodal line configuration for nucleation on dislocations.

nucleation sites, as should be stair-rod dislocations.

Omission of the last two terms in Eq. (7) allows one to calculate the activation barrier to void nucleation in the absence of gas. This was done, and it was found that under fusion reactor displacement conditions void nucleation on nonvacancy-sink dislocations should be spontaneous at temperatures below about .55 T_m. Between .55 T_m and .6 T_m the activation barrier is reduced to about half that for homogeneous nucleation, but except just above .55 T_m is still too high to be overcome by thermal activation.

Nucleation at Interfaces

Defect arrival rate considerations are much the same as for nucleation on dislocations. The ratio of rates is:

$$\frac{\beta^\circ_{xp}}{\beta^\circ_{xm}} = \frac{D^p_x}{a^2 k^T_x} \tag{17}$$

which differs from Eq. (13) only in replacement of D^d_x by D^p_x. The two diffusivities are expected to be about the same. As long as the interface is both a helium trap and a short circuit diffusion path, $\beta^\circ_{xp} >> \beta^\circ_{xm}$, and most gas reaches the void by traveling along the interface.

Taking the appropriate partial derivative of Eq. (10), inserting it into Eq. (1), and setting the individual velocities to zero yields the equations of the two nodal lines of interest.

For $\dot{n} = 0$, $$x = \frac{2An^{2/3}}{3kT} f_1(\theta) - n \ell n S_e \tag{18}$$

and for $\dot{x} = 0$, $$x = \beta^\circ_{xp} / K^T_x \tag{19}$$

Due to the very large value of β°_{xp}, the $\dot{x}$ nodal line will usually lie far above the $\dot{n}$ nodal line. As such, void nucleation will be spontaneous under typical fusion first wall conditions. This situation is thus much the same as was found for nucleation at dislocations.

Many matrix:precipitate boundaries are of the semi-coherent type, wherein coherent patches are separated by a grid of misfit dislocations. In many cases these dislocations cannot climb (without leaving a high energy fault) but should be good helium traps. Such interfaces will thus have the full vacancy supersaturation and a high helium concentration, hence should be good void nucleation sites.

The situation is different in the absence of helium. In this case, the activation barrier for heterogeneous nucleation of the void shown in Figure 3 is related to that for homogeneous nucleation by

$$\Delta G^*_{het} = \Delta G^*_{hom} \left(\frac{V_{het}}{V_{sph}}\right)$$

where V_{het} is the volume of the heterogeneous void and V_{sph} is the volume of the sphere of the same curvature. The angle θ is governed by the balance of interfacial energies, as shown. Generally γ_{mv} and γ_{pv} are of the order 1000 mJ/m^2, while γ_{pm} is of the order 200-400 mJ/m^2, so the angle θ is thus close to 90°. The void will resemble an only slightly flattened sphere, and the activation energy for nucleation is reduced hardly at all.

Thus, in the absence of helium and in the capillarity approximation, precipitates are not expected to be very good void nucleation sites. In fact, many of the boundaries of interest are made up of dislocations, which were found to be good nucleation sites, even in the absence of helium. In this case, unless the void is larger than the inter-dislocation spacing, the dislocation formalism should be used.

VI. REFERENCES

1. C. Cawthorne and E.M. Fulton, "Voids in Irradiated Stainless Steel", Nature 216, (1966) 575-576.

2. K. C. Russell, "The Theory of Void Nucleation in Metals", Acta Met. 26 (1968), 1615-1630.

3. J. F. Bates, "Heterogeneous Void Nucleation in Metals", Scripta Met. 11 (1977), 265-270.

4. H. Poincaré, Les Methodes Nouvelles de la Mecanique Celeste , Vols I-III, Gauthiers-Villars, Paris (1892-1899).

5. R. L. Somorjai, in Physical Chemistry, Vol. XI-B, Academic Press, New York (1975) ed. H. Eyring, D. Henderson and W. Jost.

6. S. I. Maydet and K. C. Russell, "Phase Stability Under Irradiation: Point Defect Effects", J. Nuclear Mats. 64 (1977) 101-114.

7. J. W. Cahn, "Nucleation on Dislocations", Acta Met. 5 (1957), 169-174.

8. H. I. Aaronson, C. Laird, and R. R. Kinsman, "Mechanisms of Diffusional Growth of Precipitate Crystals", in Phase Transformations, publ. American Society for Metals, Metals Park, Ohio (1970), 313-396.

a. For details, see S. Seyyedi, S.M. Thesis, Massachusetts Institute of Technology, June 1978, and M. Hadji-Mirzai, S.M. Thesis, Massachusetts Institute of Technology, June 1978.

VII. FUTURE WORK

The next step will be to model simultaneous homogeneous and heterogeneous void nucleation in type 316 stainless steel under CTR first wall irradiation conditions.

VIII. PUBLICATIONS

"Void Nucleation at Heterogeneities" by S.A. Seyyedi, M. Hadji-Mirzai and K. C. Russell, to appear in the Proceedings of the International Conference on Irradiation Behaviour of Metallic Materials for Fast Reactor Core Components, June 4-8, 1979, in Ajaccio, Corsica, France.

I. PROGRAM

Title: Irradiation Response of Materials
Principal Investigators: S. Wood, J. A. Spitznagel and W. J. Choyke
Affiliation: Westinghouse Research and Development Center

II. OBJECTIVE

The objective of this work is to assess the phenomenology and mechanisms of microstructural evolution in materials exposed to simultaneous helium injection and creation of atomic displacement damage by a second ion beam.

III. RELEVANT DAFS PROGRAM TASK/SUBTASK

SUBTASK II.C.1, II.C.2, II.C.3, II.C.5, II.C.9, II.C.18

IV. SUMMARY

By varying the helium implantation and atomic displacement rates independently, it is seen that the instantaneous helium implantation rate is an important factor in cavity formation. Bombardment of 316 SS aged at 800°C to produce large grain boundary carbides prior to dual-ion irradiation results in large cavities at the carbide/austenite interfaces for bombardment temperatures above 650°C. The rapid cavity growth regime observed in solution annealed 316 SS under dual-ion bombardment at 600°C is shown to occur only for atomic displacement rates below $\sim 1.5 \times 10^{-4}$ dpa/s for helium injection rates of 2×10^{-4} appm/s to 3×10^{-3} appm/s. A computerized data file permitting conjunctive queries and parametric analysis of dual-ion irradiation data has been constructed.

V. ACCOMPLISHMENTS AND STATUS

A. Effect of Time/Temperature History of Helium Doping and Atomic Displacement Damage on Microstructural Evolution in 20% Cold Worked 316 SS (MFE Heat)

The ratio of the helium production rate to the atomic displacement rate is expected to be nearly constant for a small volume of the first wall or blanket structure of a fusion reactor during a D-T burn cycle. The calculated ratio will depend primarily on the chemical composition of the structural alloy. It is thus tempting to try and characterize microstructural evolution under conditions of simultaneous helium doping and creation of atomic displacement damage in terms of this ratio or the ratio of appm He:dpa.

One question that arises from the use of irradiation sources like the "mixed-spectrum" fission reactors is whether microstructural evolution can be adequately characterized by a time-average value of these ratios. It arises because, unlike the single-step (n,α) transmutation reactions expected from high energy neutrons in a fusion reactor, helium production in nickel-bearing alloys in a fission reactor occurs via a two step neutron capture process. Thus, the ratio of the helium production rate to the atomic displacement rate changes with time(1).

In dual-ion bombardment experiments, such as those reported here, the helium implantation and atomic displacement rates can be varied independently. This is a useful feature permitting one to study systematically the effects of changing the instantaneous and time-averaged rates of helium injection and atomic displacement. Such experiments should prove most useful in delineating nucleation dominated or growth dominated regimes of cavity, dislocation loop and precipitate formation. In an earlier report(2) we outlined several "beam history" experiments to be conducted at the High Energy Ion Bombardment Facility at the University of Pittsburgh. Three experiments with varying ion beam histories have now been conducted and the results of TEM examination at the first section depth (∿1.2 μm from the bombarded surface) are presented in Figures 1 and 2. The experiments are conveniently described by the "vector" diagrams discussed previously(2). In the experiment described schematically in Fig. 1, targets of 20% cold rolled 316 SS were bombarded with 28 MeV Si^{+6} ions only until a damage level of approximately 1.5 dpa was achieved at the first section depth. A Faraday cup, which intercepted the helium ion beam, was then removed and bombardment continued with both silicon and helium ions coimpinging on the targets. The instantaneous helium implantation rate for the period required to accumulate the last 1.5 dpa was ∿1.5×10^{-3} appm/s, giving an instantaneous appm He/dpa ratio of ∿13. The time-averaged helium injection rate (averaged over the total irradiation time) was ∿7.5×10^{-4} appm/s. While this value has little physical significance for the particular irradiation sequence shown in Figure 1, it will be useful for discussion purposes. For the conditions shown in Figure 2, the helium and silicon ion beams coimpinged on the targets during the first quarter of the irradiation. The helium beam was then intercepted by lowering a Faraday cup and exposure continued with only the high energy silicon ions bombarding the targets. At a first section damage level of ∿2.2 dpa the Faraday cup was removed and the irradiation finished with both silicon and helium ions bombarding the targets. The instantaneous helium implantation rate for the first and final quarters of the irradiation was ∿1.5×10^{-3} appm/s and the value averaged over the entire irradiation period was 7.5×10^{-4} appm/s. A third experiment involving continuous helium implantation over the first half of the irradiation period at a rate of ∿1.5×10^{-3} appm/s to a concentration of 20 appm (first section) and then no additional helium injection as the damage level was increased from 1.5 to 3 dpa was also run. TEM results, however, are not yet available.

As reported earlier(3), continuous bombardment of 20% cold rolled 316 SS at 600°C with coimpinging helium and silicon ions at an appm He/dpa ratio of ∿11 and an instantaneous helium injection rate of

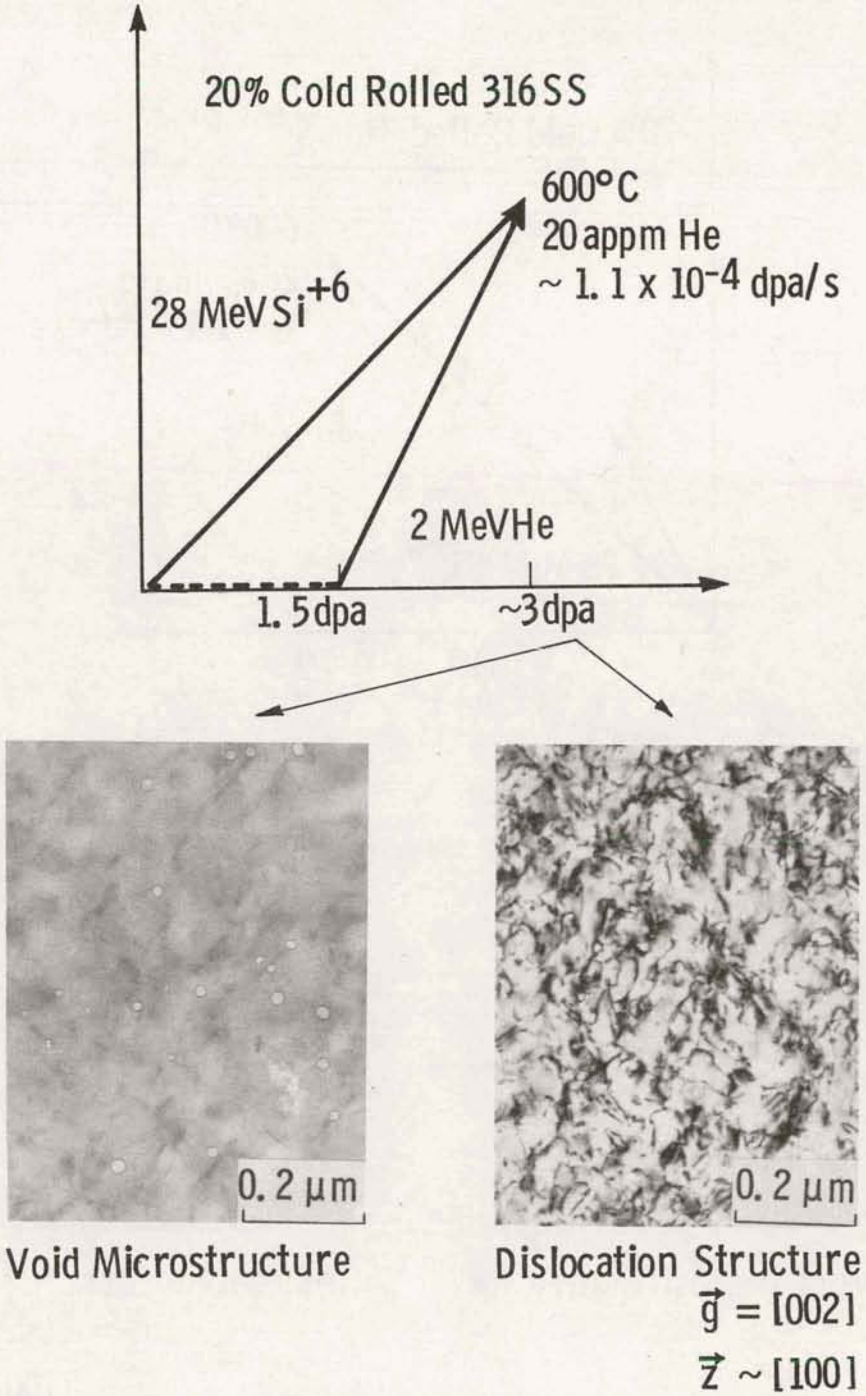

Fig. 1 - Microstructures produced in 316 SS after bombardment with He and Si^{+6} (note that the He beam was utilized only during the second half of the experiment).

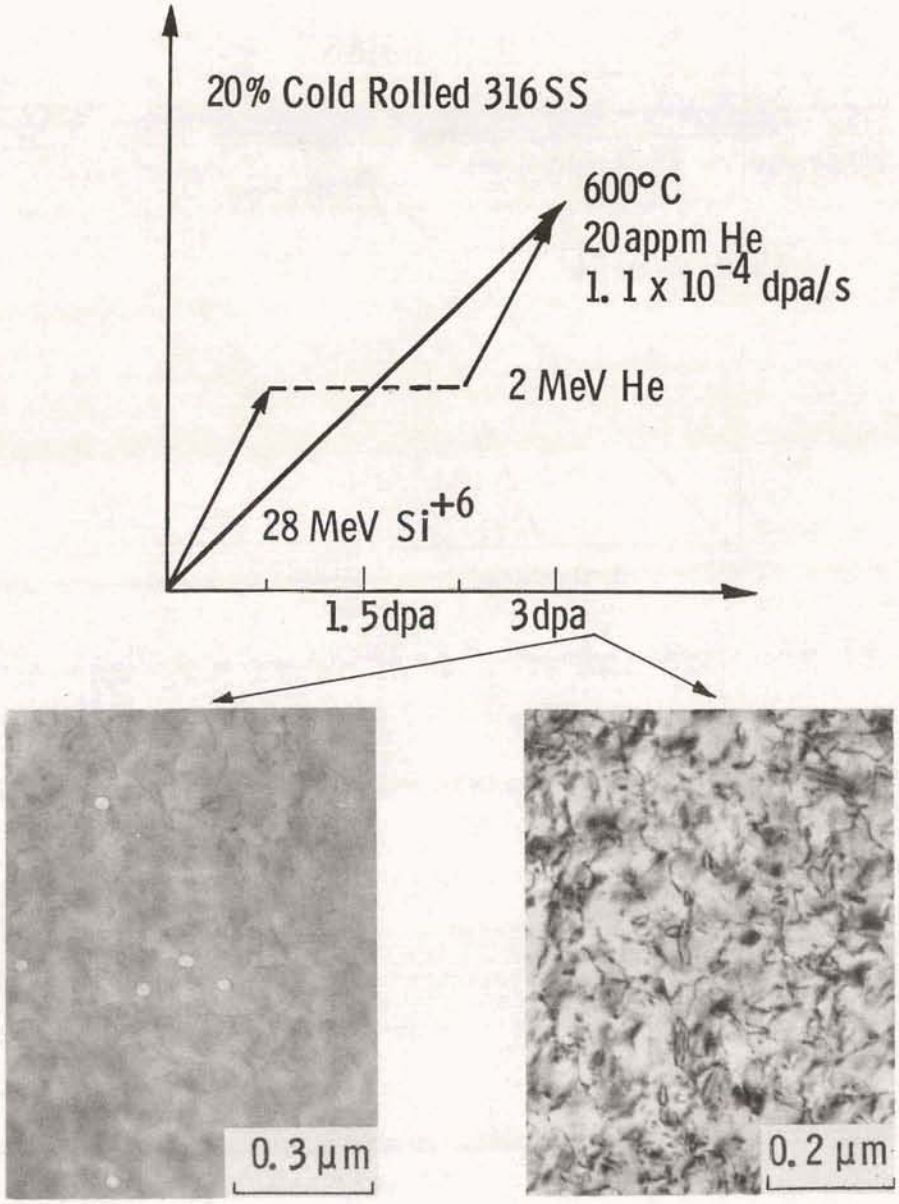

Void Microstructure

Dislocation Structure
$\vec{g} = [002]$
$\vec{z} \sim [100]$

Fig. 2 - Structural changes induced in cold rolled 316 SS after bombarding according to the above beam schedule.

$\sim 7.5 \times 10^{-4}$ appm/s produced no visible cavities. This is clearly not the case for the bombardment conditions shown in Figures 1 and 2 even though the time-averaged helium injection rate, the total amount of helium implanted and the average appm helium:dpa ratios are similar for the three runs. This observation suggests that, for the conditions of these experiments, the instantaneous helium implantation rate is an important factor in cavity formation. The "average" appm He/dpa ratio, total amount of helium implanted, or time-averaged helium injection rate are not likely to be very useful parameters for characterizing microstructural evolution when the time-history of atomic displacement damage and helium production are different.

For the experiments depicted in Figures 1 and 2 the instantaneous helium injection rates are the same (either zero or 1.5×10^{-3} appm/s). Changing the sequence of beam on-beam off time, however, has altered the nucleation and/or growth of the cavities as expected. An assessment of beam-history effects on cavity nucleation and growth kinetics will be made in the next quarter when computer processing of the data is complete. Visual observation suggests that the microstructures shown in Figures 1 and 2 are not dramatically different. If borne out by the numerical analysis of the data, this information will prove useful in assessing the need for translating irradiation capsules in mixed-spectrum fission reactor (ORR-MFE) experiments.

B. Microstructural Effects of Dual-Ion Bombardment in Aged 316 SS

Maziasz(4) has demonstrated the importance of various carbide and intermetallic phases on the nucleation and growth of helium bubbles in 316 SS. Prolonged exposure of fusion reactor first wall and blanket materials to temperatures in excess of 500°C are likely to result in precipitation of Cr-rich carbides or Fe-Mo intermetallic phases if austenitic stainless steels are used for these applications(4). It is generally not possible to study phenomena that depend on time-at-temperature (such as carbide precipitation) in charged particle experiments where exposure times are limited to a few hours or at most a few days. However, it should be possible to study the mechanisms by which these second phase particles alter bubble and dislocation loop nucleation and cavity growth if pre-aged specimens are used. In support of this contention HFIR experiments have shown that TiC particles dramatically change bubble sizes and spatial distributions independent of whether the steels were pre-treated to produce the TiC precipitates or whether the phase forms under irradiation(5).

To determine the effects of aging and intergranular face-centered cubic Cr-rich carbide ($M_{23}C_6$) particles on microstructural evolution under dual-ion bombardment, 316 SS from the MFE heat was given a 50% cold reduction, recrystallized by annealing at 1050°C for 0.5 h and subsequently aged at 800°C for 10 hours at Argonne National Laboratory. Specimens obtained from ANL were subsequently bombarded at the High Energy Ion Bombardment Facility at the University of Pittsburgh. For all of the experiments helium was continuously implanted at rates from 3.2×10^{-3} to 5.7×10^{-3} appm/s at damage rates of 3.4×10^{-4} to 4.6×10^{-4} dpa/s. Bombardment temperatures were (nominally) 550, 600, 650 and 700°C. Numerical analysis of the data is in progress. A comparison of TEM observations for targets sectioned to damage levels of 9-12 dpa after bombardment at the various temperatures is shown in Figures 3-5. Bombardment at 700°C, Figure 3, results in a strongly bimodal cavity size distribution. Visible cavities are preferentially associated with the unidentified acicular precipitates also observed in solution annealed and 20% cold worked 316 SS targets. There is very little association of the cavities with the network of extended dislocations. At lower irradiation temperatures, Figure 4, a bimodal cavity size distribution is still observed but the centroids are shifted to smaller cavity diameters. Preferential association of cavities with acicular precipitates is still observed but fewer precipitates form with decreasing irradiation temperature. Faulted dislocation loops appear below 600°C and association of cavities with dislocations becomes more prevalent as the number of acicular precipitates decreases. Finally at 550°C, Figure 5a, no

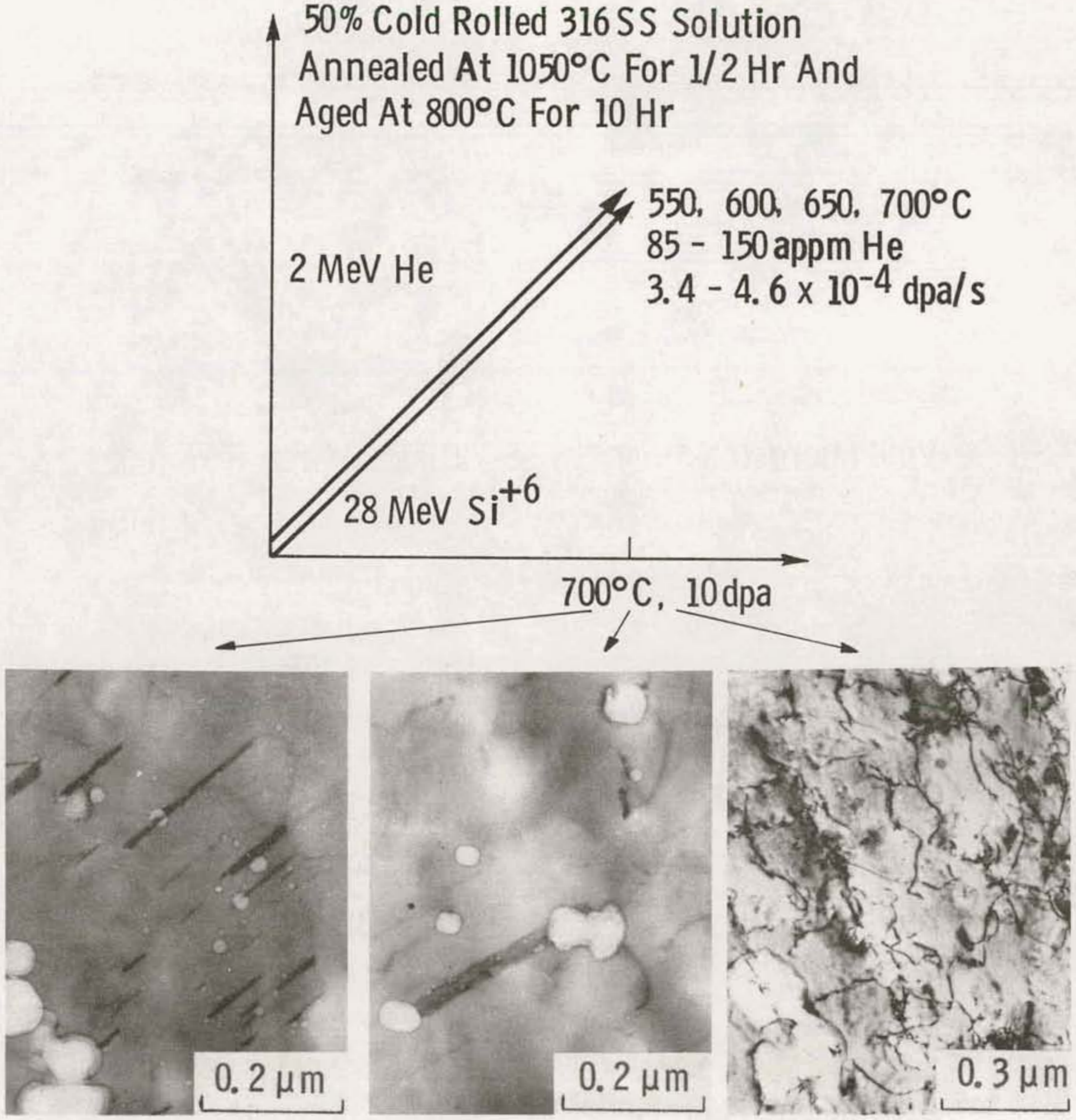

Void Microstructure

Void Nucleation On Acicular Precipitates

Dislocations $\vec{g} = [002]$, $\vec{z} \sim [110]$

Fig. 3 - Bombardment history for specimens aged to yield carbide precipitation prior to ion implantations, together with microstructures obtained at 700°C, 10 dpa.

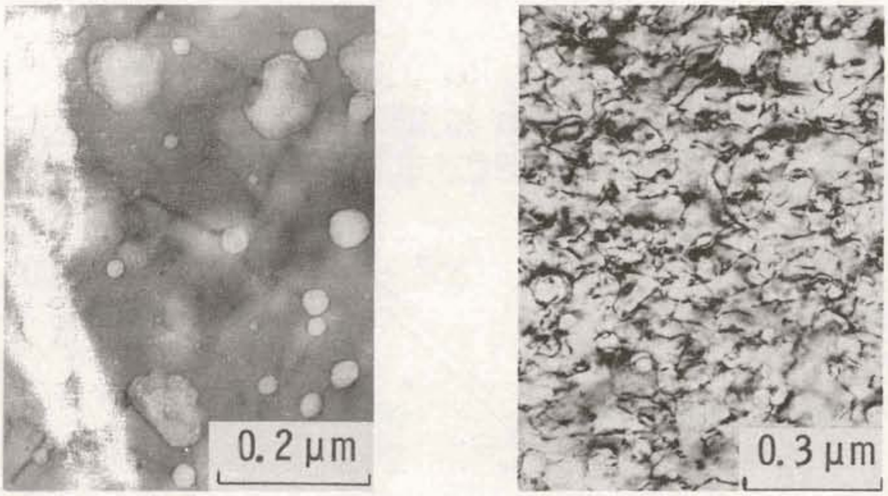

Void Microstructure

Dislocations, $\vec{g} = [002]$
$\vec{z} \sim [110]$

(a) 680°C, 10 dpa

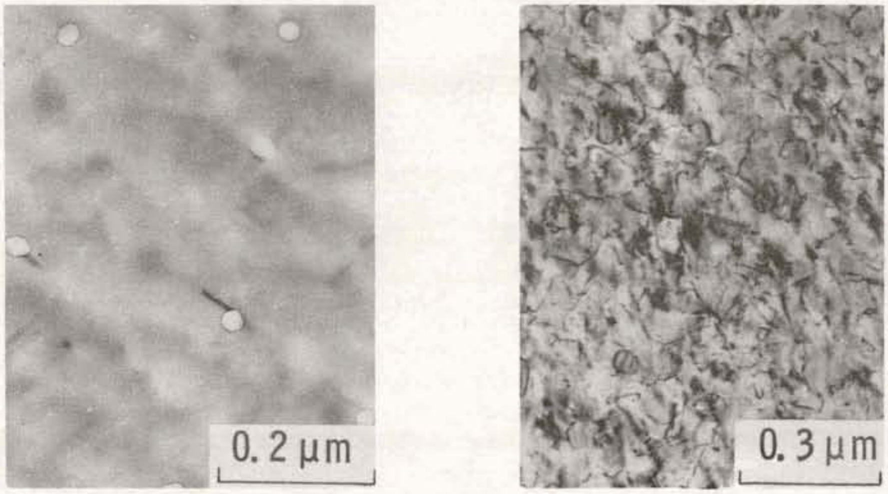

Void Microstructure

Dislocations, $\vec{g} = [002]$
$\vec{z} \sim [110]$

(b) 600°C, 12.3 dpa

Fig. 4 - Microstructures obtained for aged specimens of 316 SS irradiated according to the beam schedules in Fig. 3.

(a) Void Microstructure At 550°C, 9 dpa

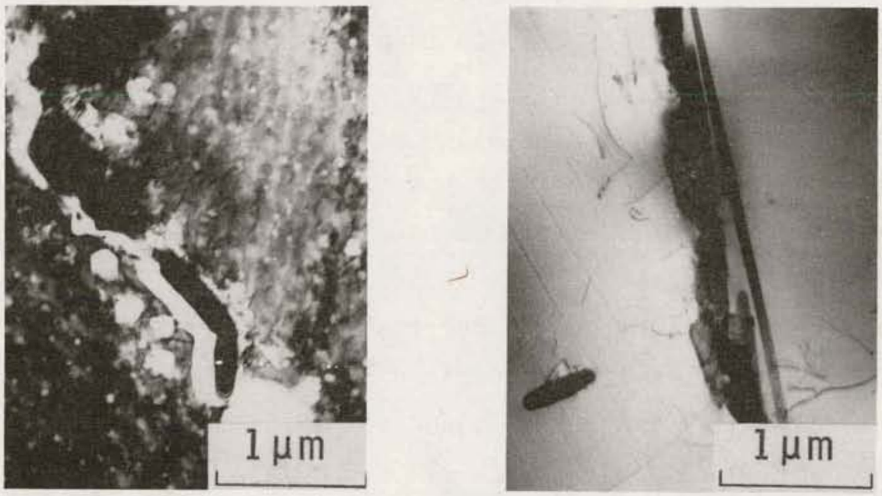

(b) Carbide Formation After 650°C Irradiation To 10 dpa

(c) Carbide Formation In Unirradiated, Aged 316 SS Specimen

Fig. 5 - (a) and (b) are microstructures obtained under the beam schedules given in Fig. 3; (c) shows carbide formation in unirradiated 316 SS.

acicular precipitates formed and a unimodal (nearly gaussian) cavity size distribution is observed. Visual observation suggests a double peak will exist in the swelling-temperature curve with cavity growth rates at 550°C and 680°C determining the swelling behavior. Clearly the unidentified acicular precipitates dominate cavity nucleation when they are present. The Cr-rich carbides were confined to the grain boundaries in the as-received material, Figure 5c, and no additional carbide precipitation was detected after dual-ion bombardment. At irradiation temperatures of 650°C and above, rapid growth of large intergranular cavities associated with the grain boundary carbide particles was observed, Figure 5b. Similar observations of rapid cavity growth at carbide/austenite interfaces in 316 SS irradiated in a mixed-spectrum fission reactor have previously been reported(4).

The dearth of intragranular carbide particles in the unirradiated specimens suggests that the 800°C aging treatment was above the "knee" of the time-temperature-precipitation curve(4). Attempts to determine the effects of intragranular carbides will require lower aging temperatures for the unirradiated samples. The 800°C aging treatment, however, represents one of the reference conditions for the MFE 316 SS heat and for an interlaboratory study (in progress) of the effects of different primary knock-on atom energy spectra on microstructural evolution at high helium levels. Detailed comparison of results from previous runs with solution annealed and 20% cold worked 316 SS targets must await further data reduction.

C. Damage Rate Dependence of the Rapid Cavity Growth Rate Regime in Solution Annealed 316 SS

Simultaneous implantation of helium and bombardment with the heavy ion beam at a damage rate of $\sim 1 \times 10^{-4}$ dpa/s may result in very rapid cavity growth at 600°C in solution annealed 316 SS as shown in an earlier report(2). In this reporting period experiments were conducted in an attempt to better define the range of temperatures for the anomalous growth. Targets bombarded at 575°C and 625°C showed no evidence for the rapid growth of cavities at low doses. Surprisingly, bombardment at 600°C did not produce rapid cavity growth either, Figures 6, 7. These results were puzzling because the phenomenon was very reproducible in previous experiments(2). Only two experimental conditions had changed since the earlier runs. The vacuum at the target was improved by approximately an order of magnitude by the addition of two turbomolecular pumps,and a slightly higher damage rate was necessary because new carbon stripping foils resulted in unexpectedly high Si^{+6} beam currents. Thus, average damage rates of 1.7×10^{-4} dpa/s to 2.7×10^{-4} dpa/s were used instead of the previous value of 0.9×10^{-4} dpa/s. To determine whether the conditions leading to the dendritic networks of cavities characteristic of the rapid growth regime were accentuated by lower damage rate, seven targets were simultaneously bombarded at 600°C at a calculated atomic displacement rate of 2.3×10^{-5} dpa/s. Under these conditions rapid cavity growth was again observed, Figure 8. Examination of data from runs with a variety of damage rates has now shown that rapid cavity growth is not observed at damage rates greater than $\sim 1.5 \times 10^{-4}$ dpa/s for helium injection rates of $\sim 2 \times 10^{-4}$ appm/s to $\sim 3 \times 10^{-3}$ appm/s. For damage rates where linking of large cavities occurs quickly the phenomenon can apparently be suppressed by raising the helium implantation rate to values on the order of 1×10^{-2} appm/s as reported previously(2). Thus, it appears that the occurrence of large cavities aligned in [110] directions,which link up at low doses to produce extensive networks,is the result of a delicate "balance" between atomic displacement rate, helium injection rate and irradiation temperature. Unfortunately, lower damage rates and helium injection rates characteristic of projected fusion reactor first wall conditions favor this anomalous cavity growth in solution annealed 316 SS from the MFE heat. Table 1 summarizes the observations to date. The effect of altering the vacuum ambient (oxygen partial pressure) on microstructural evolution in solution annealed 316 SS under dual ion bombardment will be investigated in the next reporting period.

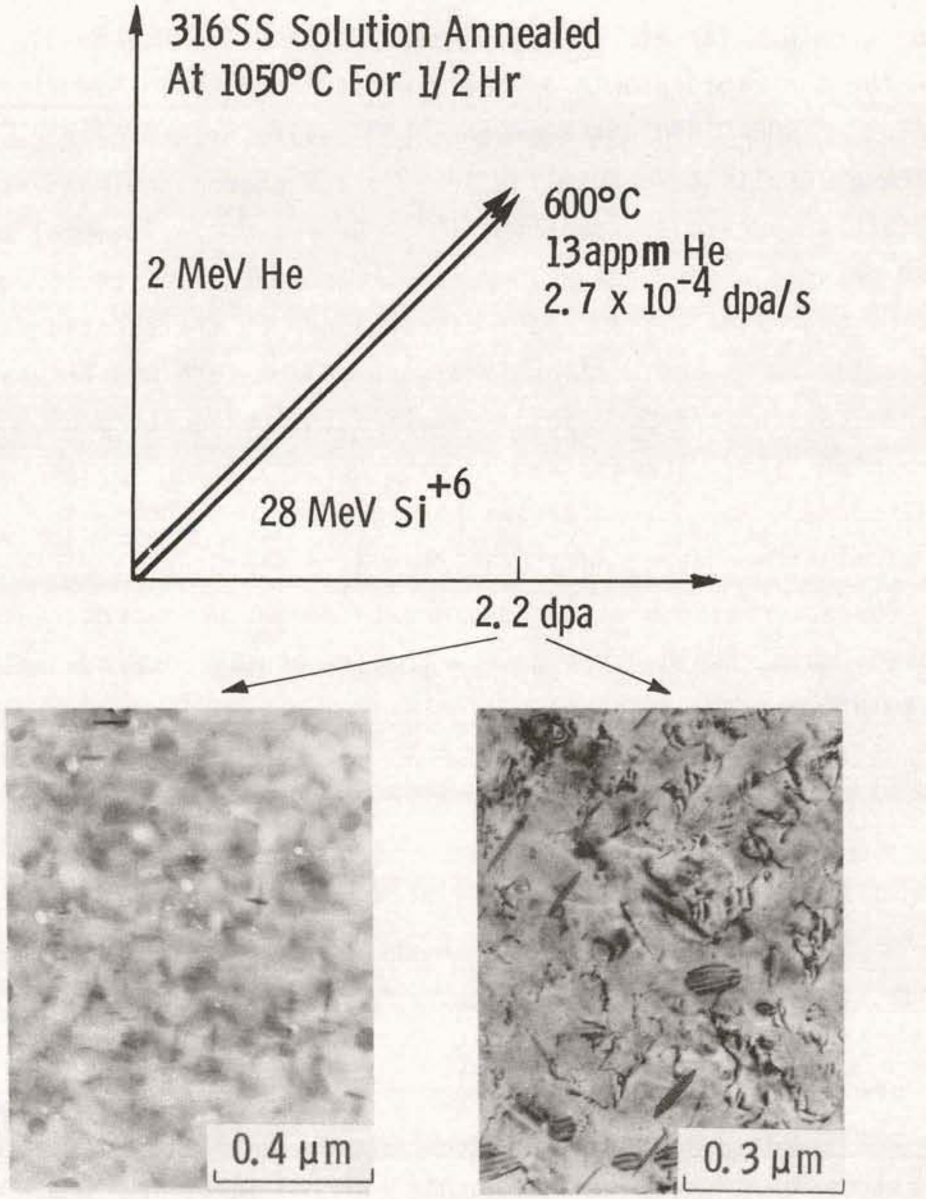

Void Microstructure

Dislocations (Faulted Loops) $\vec{g} = [002]$ $\vec{z} \sim [110]$

Fig. 6 - Effect of simultaneous bombardment on the void and dislocation structures in solution annealed 316 SS at 600°C.

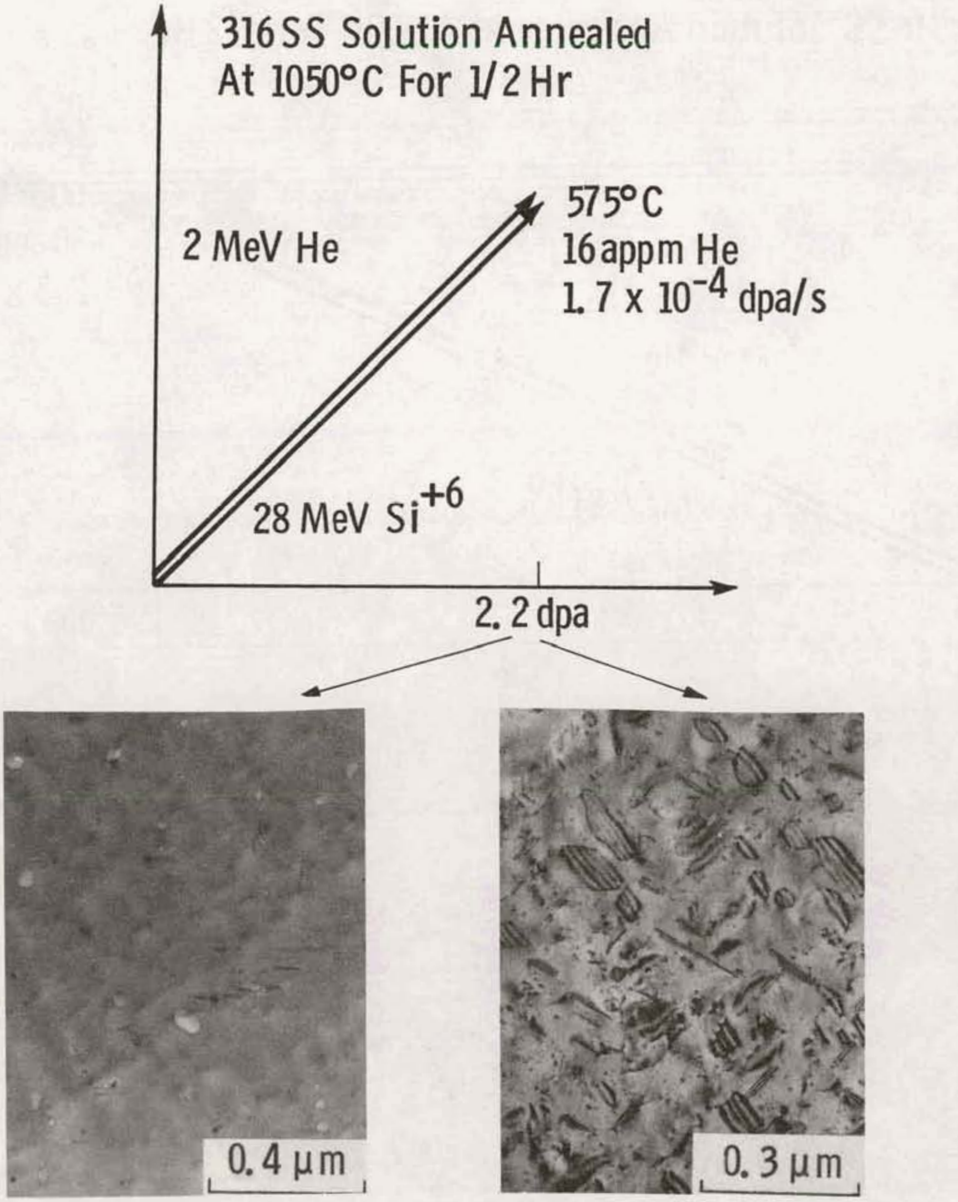

Void Microstructure

Dislocations (Faulted Loops)

$\vec{g} = [002]$

$\vec{z} \sim [110]$

Fig. 7 - Void and dislocation structures developed in solution annealed 316 SS after simultaneous bombardment at 575°C.

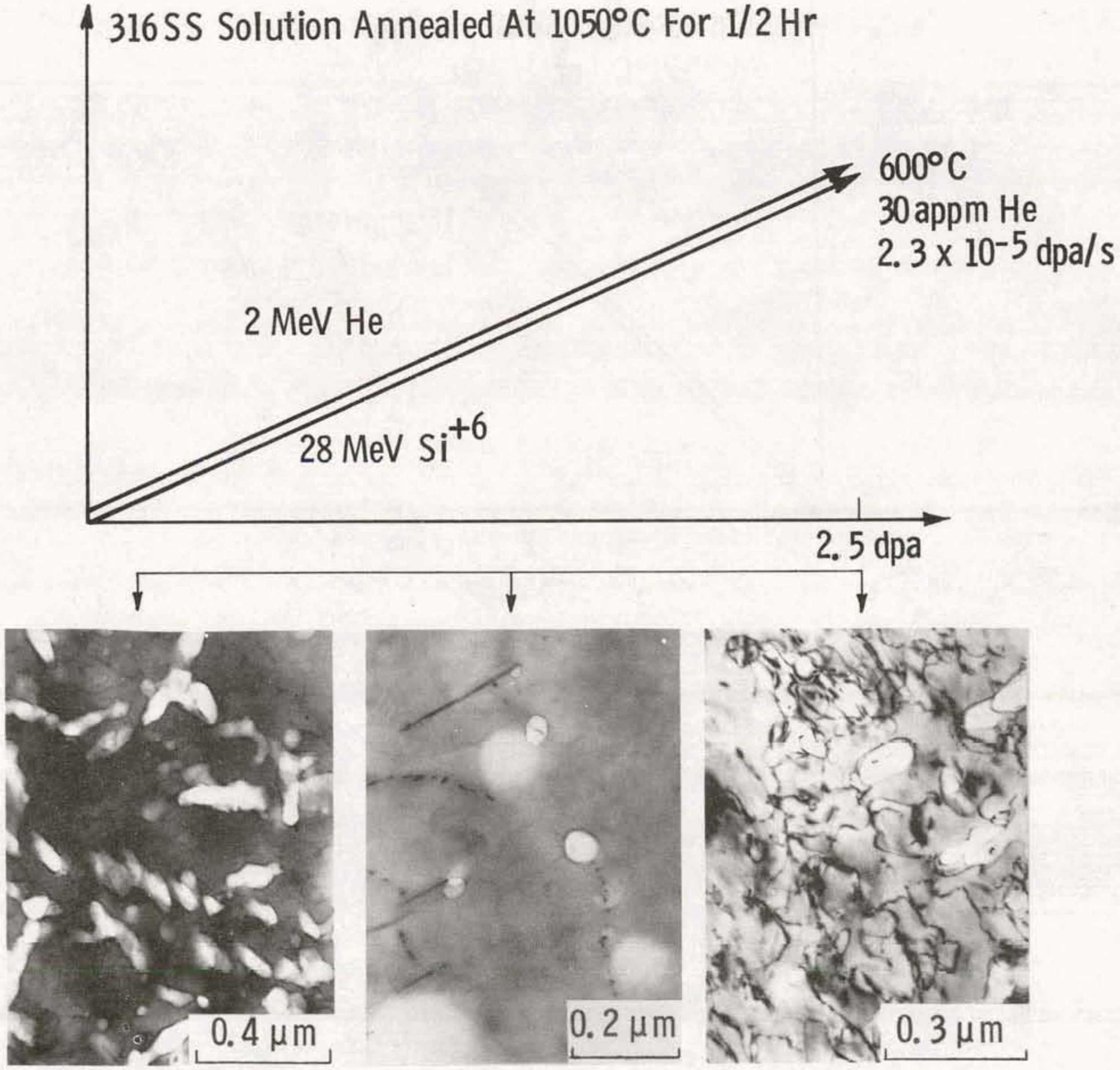

Void Microstructure

Precipitation On Dislocations

Dislocations, $\vec{g} = [002]$, $\vec{z} \sim [013]$

Fig. 8 - Microstructures produced in solution annealed 316 SS after a low damage rate, simultaneous bombardment experiment.

TABLE 1. SUMMARY OF EXPERIMENTAL OBSERVATIONS OF RAPID CAVITY GROWTH IN SOLUTION ANNEALED 316 SS RESULTING FROM ION BOMBARDMENT AT 600°C

Damage Level (dpa)	Damage Rate (dpa/s)	Helium Concentration (appm)	Relative Oxygen Partial Pressure[a]	Rapid Cavity Growth Observed	Mode of Helium Implantation
2	0.8×10^{-4}	88	High	Yes	Simultaneous
2.4	0.9×10^{-4}	18	High	Yes	Simultaneous
2.4	0.9×10^{-4}	18	High	Yes	Hot Preimplantation
5	1.0×10^{-4}	80	High	Yes	Simultaneous
5	1.9×10^{-4}	300	High	No	Simultaneous
2.2	2.7×10^{-4}	13	Low	No	Simultaneous
2.2[b]	1.7×10^{-4}	16	Low	No	Simultaneous
2.5	2.3×10^{-5}	30	Low	Yes	Simultaneous
2.7	1.0×10^{-4}	200	High	Yes	Simultaneous
3.8	1.5×10^{-4}	28	High	Yes	Hot Preimplantation

---

[a] Estimated values of $\sim 5 \times 10^{-6}$ N/m^2 and 1×10^{-6} N/m^2 for "high" and "low", respectively.

[b] Irradiation temperature was 575°C.

D. Numerical Analysis of Cavity Size Distributions

Experimental evidence obtained during the past year has shown that characterization of cavity, dislocation loop or precipitate size distributions in terms of average values alone can be seriously misleading. In order to understand the combined nucleation and growth aspects of point defect-solute clustering under the highly non-equilibrium conditions imposed by dual-ion (and fusion reactor) irradiation at elevated temperature, it is necessary to consider higher order moments of cluster size distributions. Variations in these moments caused by changes in bombardment temperature, dose (dpa level), pre-bombardment microstructure, appm He/dpa ratio and ratio of the helium injection rate to atomic displacement rate must then be unfolded to yield nucleation and growth rates. Theoretical predictions of nucleation and growth kinetics have concentrated on the effects of these parameters on average values of the defect-solute cluster size. Most computer models such as Russell's cavity nucleation theory based on the nodal line/critical point formalism of Poincaré(6) and the BEK(7) fully dynamic rate model of cluster growth, however, can treat multiple size classes.

To facilitate interaction of experiment and theory, we have constructed computerized data files under separate funding which permit conjunctive queries to delineate parametric sensitivity of cavity, dislocation loop and precipitate size distributions. The computer code uses an inverted file system and random access disk storage. Thus, the code quickly scans the data from all dual-ion runs; selects the data from the files which satisfies the imposed criteria (e.g., a specified combination of irradiation temperature, damage rate, appm He/dpa level, etc.); calculates the desired statistics (moments of size distributions, maximum equilibrium bubble size, etc.); and plots (calcomp) the statistics versus a specified irradiation parameter.

As a simple example of the use of the computerized file system, we asked for combined plots of cavity size distributions measured for 316 SS (MFE heat) for 20% cold-worked and solution annealed (1050°C) targets bombarded simultaneously with 2 MeV helium and 28 MeV Si^{+6} at 650°C. Additional criteria were imposed for ranges of damage rate (0.9×10^{-4} dpa/s to 1.2×10^{-4} dpa/s), dpa level (2-3 dpa), helium injection rate (6×10^{-4} appm/s to 7×10^{-4} appm/s) and implanted helium concentration (16-18 appm). Thirty-three data sets satisfied the criteria. "Vector" diagrams describing the experiments and representative micrographs are included in an earlier report(2). In addition to plotting the combined data for each different pre-irradiation condition, a computation of the maximum possible equilibrium bubble diameter (D_C) for each case was requested. To determine D_C, the code starts at the smallest observed cavity size and calculates the number of helium atoms in each size class using the Van der Waals equation and surface energies obtained from extrapolations of "zero creep" data as described elsewhere(8). When the helium concentration summed over the size classes equals the implanted helium concentration, the code designates the last size class filled with helium as D_C. Clearly D_C is an important parameter related (theoretically) to the transition between gas-driven bubble growth and bias-driven void growth(9). Figures 9 and 10 are the combined cavity size plots for solution annealed and cold-worked conditions, respectively. The average cavity sizes in both cases are nearly identical (∿40 nm) but the swelling in the solution annealed targets averaged 0.33% while for the 20% cold worked condition the swelling was ∿10%. The difference is due to an order of magnitude higher cavity density in the cold-worked targets ($\sim 3 \times 10^{14}$ cavities/cm^3) relative to the solution annealed specimens. Similar observations have been made for HFIR-irradiated 316 SS samples. Unlike the effects of cold work at low helium levels (e.g., EBR-II irradiation) where swelling is suppressed at low doses, cold work enhances swelling at high helium levels presumably by increasing the number of cavity nucleation sites. This supposition is supported by an analysis of the cavity size distributions. There is a high concentration of small cavities in the cold worked samples. The maximum equilibrium

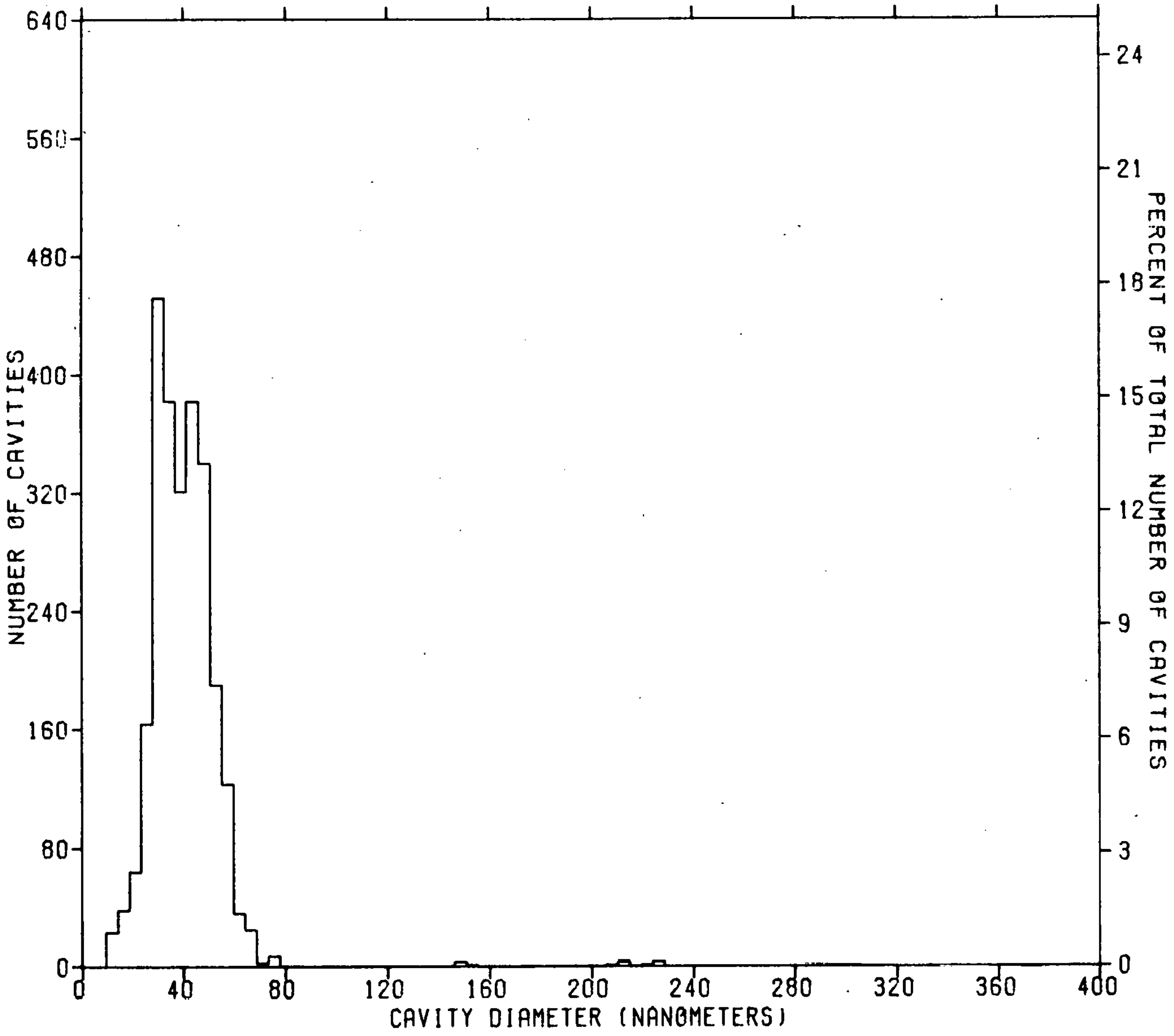

Fig. 9 - Combined cavity size distribution for solution annealed 316 SS after dual-ion bombardment at 650°C (twelve data sets satisfying parameter ranges described in text; combined plot obtained using computerized data file).

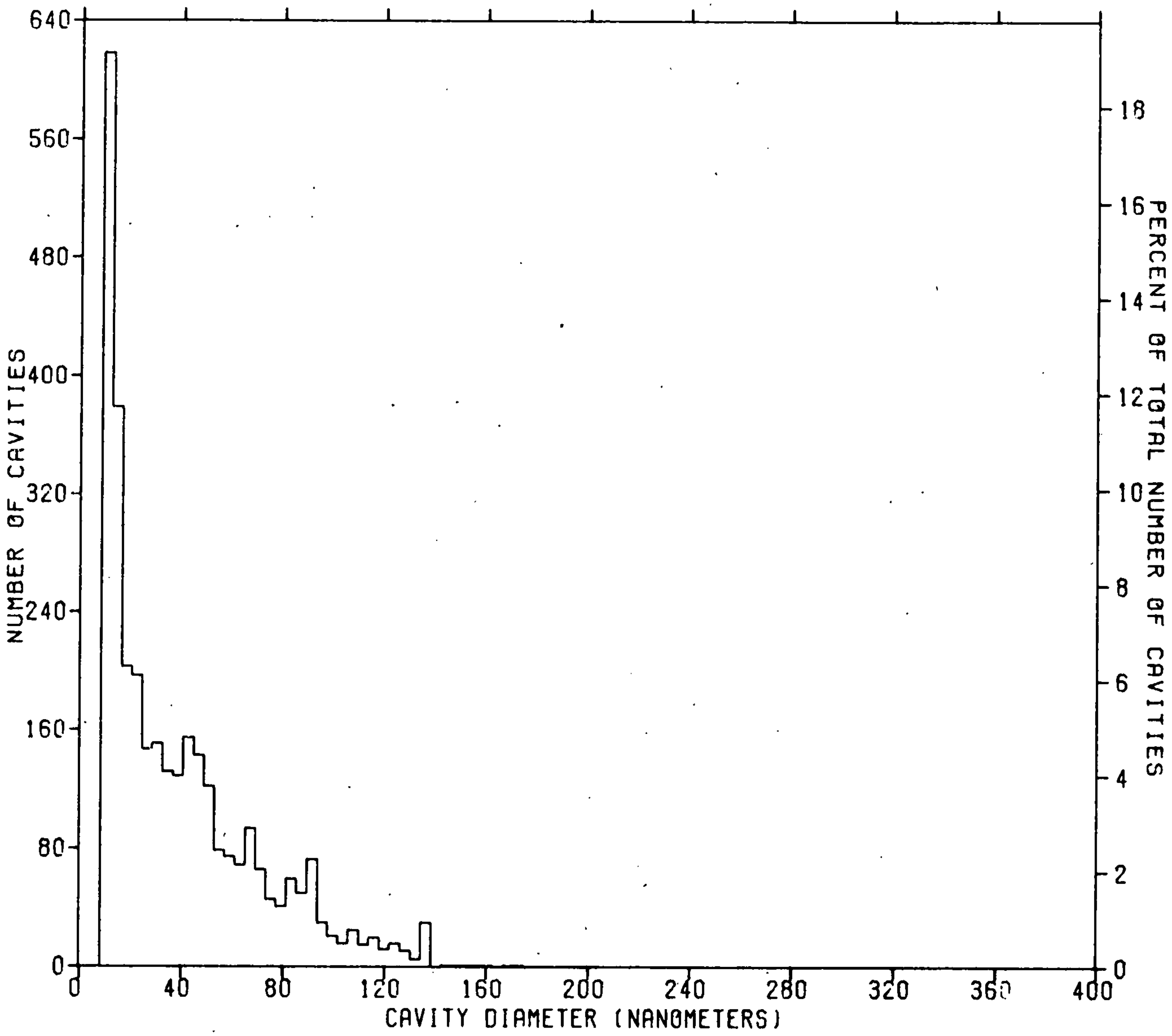

Fig. 10 - Combined cavity size distribution for 20% cold-rolled 316 SS after dual-ion bombardment at 650°C (twenty-one data sets satisfying parameter ranges described in text; combined plot obtained using computerized data file).

bubble sizes (D_C) for the distributions shown in Figures 9 and 10 are 20.5 nm and 7.2 nm, respectively. While there is considerable uncertainty in the accuracy of these values because of the assumptions required to calculate them, their relative magnitudes suggest that the conditions for rapid bias-driven growth are also enhanced by the higher dislocation density(9). A similar analysis for samples bombarded at 750°C shows enhanced bubble nucleation in cold-worked targets but no bias-driven cavity growth. A more complete discussion of the cavity size distributions and the influence of helium injection rate, atomic displacement rate, irradiation temperature, and pre-irradiation microstructure will be presented in a subsequent report.

VI. REFERENCES

1. J. J. Holmes and J. L. Straalsund, "Irradiation Sources for Fusion Materials Development," Proceedings of the First Topical Meeting on Fusion Reactor Materials, Bal Harbour, Florida, January (1979), To be published in J. Nucl. Mater.
2. S. Wood, J. A. Spitznagel and W. J. Choyke, DAFS Quarterly Report No. 5, January-March (1979).
3. J. A. Spitznagel and W. J. Choyke, DAFS Quarterly Report No. 3, July-September (1978).
4. P. J. Maziasz, "Precipitation Response of Austenitic Stainless Steel to Simulated Fusion Irradiation," submitted to J. Nucl. Mater.
5. E. E. Bloom and P. J. Maziasz, private communication (1979).
6. K. C. Russell, Acta Met. 26, p. 1615 (1978).
7. R. Bullough, B. L. Eyre and K. Krishan, Proc. Roy. Soc. Cond. A346 (1975).
8. J. R. Cost and K. Y. Chen, J. Nucl. Mater. 67, p. 265 (1977).
9. M. H. Wood, M. R. Hayns and R. Bullough, "The Dependence of Cavity Nucleation Density Upon Gas Implantation Rate and Its Importance in Dual Beam Irradiation Conditions," UKAEA Report AERE-R9099, May (1978).

VII. FUTURE WORK

TEM and computerized data file analyses of interrupted helium beam and temperature change experiments will be continued. Targets of 316 SS (MFE heat) in the solution annealed condition will be subjected to dual-ion bombardment at atomic displacement rates from $\sim 10^{-5}$ dpa/s to 5×10^{-4} dpa/s with oxygen partial pressures from $\sim 1 \times 10^{-6}$ N/m^2 to 5×10^{-6} N/m^2 in the target chamber to study the effects of the vacuum ambient on the rapid cavity growth regime. Dual-ion bombardment studies of a vanadium alloy (either V-20 Ti, Vanstar 7 or V-15 Cr-5 Ti) will be initiated to determine the effects of different H and CO partial pressures in the target chamber on microstructural evolution.

VIII. PUBLICATIONS

None

I. PROGRAM

Title: Synergistic Helium Production by Boron Doping of Splat Cooled Alloys

Principal Investigator: O. K. Harling

Affiliation: Nuclear Reactor Laboratory, Massachusetts Institute of Technology

II. OBJECTIVE

This work is directed toward the development of better simulation techniques for the synergistic production of helium and displacement damage in first wall structural materials.

III. RELEVANT DAFS PROGRAM PLAN TASK/SUBTASK

A number of tasks are relevant since adequate experimental simulation of fusion reactor irradiation effects is a major reason for the DAFS program. Some of the tasks/subtasks which are significantly affected are:

TASK II.A.4	Gas Generation Rates
II.C.2	Effects of Helium on Microstructure
II.C.8	Effects of Helium and Displacement on Fracture
II.C.13	Effects of Helium and Displacement on Crack Initiation and Propagation.

VI. SUMMARY

Splat quenched stainless steel ribbons containing 5000 appm B, and 5000 appm B and 5000 appm Zr were prepared using the melt spinning technique.

V. ACCOMPLISHMENTS AND STATUS

A. Boron Doping of Stainless Steel by Rapid Quenching - S. Best, G. Dansfield, H. Frost, J. Megusar, O. Harling, and K. Russell (M. I. T.)

1. Introduction

It is generally understood that existing irradiation facilities, i.e. accelerators and fission reactors, will have to be used for the initial irradiation testing of controlled thermonuclear reactor (CTR) structural materials. Damage rates and helium production rates should simulate the expected rates in CTR's. Only fission reactors offer the required large testing volumes with fast neutron fluxes which produce damage rates which equal or exceed those expected for near term CTR's. Helium production rates, with the exception of nickel alloys in mixed spectrum reactors, cannot be reproduced by direct nuclear reaction on the alloy constituents. The present studies are directed toward the development of techniques for the production of helium during fission reactor irradiations. Current efforts emphasize the doping of structural alloys with boron. To assure the uniform distribution of boron, the alloy is produced by rapid quenching from the melt. Cooling rates of 10^5 - 10^9°C/sec offer the possibility of uniform boron concentrations which are much higher than those which can be maintained without segregation during normal solidification rates. The usefulness of this approach to boron doping will also depend upon the maintenance of a uniform boron distribution during thermo-mechanical consolidation, and during the use of the consolidated material in the temperature, stress and radiation environment of the fission reactor. Furthermore, the effect of boron on the physical properties of the boron doped alloys, whether segregated to grain boundaries or uniformly distributed, must be understood.

2. Melt Spinning of Boron Doped Stainless Steel

As discussed in a previous DAFS Quarterly Report,(1) the mobility of boron (at a concentration of 5000 appm and at test temperatures of interest) dictates that any boron added to an alloy of interest must be tied up in small stable precipitates to prevent significant segregation. It has been proposed that a fine dispersion of stable ZrB_2 particles can be obtained by rapid quenching of a boron doped alloy from the melt followed by suitable heat treatment.

Melt spinning provides a convenient method by which many small lots (∿10 gms) of material having varied compositions may be rapidly quenched from the melt. For this reason melt spinning was used to prepare several splat cooled stainless steel samples alloyed with 5000 appm B, and 5000 appm B plus 5000 appm Zr. These splats will be used in an initial investigation of the behavior of boron and of the precipitation kinetics of zirconium boride particles.

The melt spinning apparatus used in this experiment consists of a copper wheel which rotates about a quartz crucible which holds the charge of material to be melt spun. The material is induction heated under an argon atmosphere and when it is entirely molten it is poured as a stream through a small slit in the bottom of the crucible onto the rapidly rotating copper disc. The resultant rapidly quenched material is a ribbon approximately 1 cm wide.

In this work, boron doped alloys were prepared from very low carbon stainless steel (heat # 8178) supplied by Allegheny Ludlum. The starting composition of this material is shown in Table 1.

TABLE 1. Composition of Stainless Steel

Content* (wt %)

Cr	Ni	Mo	Mn	Si	S	C	N	O
16.73	16.49	2.27	1.21	0.49	0.0035	0.0054	0.0016	0.0052

*Balance Fe

From this stainless steel, master alloys containing large amounts of B and Zr were prepared in a vacuum arc melting device under an argon atmosphere. Stainless steel samples doped with 5000 appm B, and 5000 appm B plus 5000 appm Zr were then made using small pieces of these master alloys. The boron/zirconium doped samples plus several samples containing no boron or zirconium were then melt spun. An initial investigation showed that the dendrite arm spacing of the melt spun ribbons ranges approximately from 2 to 5 μm. Further study of these specimens is planned for the near future.

A new vacuum melting furnace was completed and put into operation to produce boron loaded molten SS in pound lots for the roll quench apparatus. Adequate quantities of roll quenched SS + B are now being produced for mechanical property testing.

VI REFERENCES

1. S. Best, G. Dansfield, H. Frost, J. Megusar, O. Harling, and K. Russell, "Damage Analysis and Fundamental Studies Quarterly Progress Report", January-March 1979, DOE/ET-0065/5, pp. 69-85.

VII. FUTURE WORK

The boron doped melt spun material previously described in this report will be examined to determine the as-splatted boron distribution and to study the effect of various heat treatments on the precipitation and thermal stability of zirconium boride particles.

If good stability can be attained for the zirconium boride particles without irradiation, then an irradiation experiment will be planned and carried out. We would attempt to design this irradiation to investigate the radiation stability of the boride precipitates, the role of ^{7}Li [from the ^{10}B(n, α) reaction] and to examine the effect of the addition of a small volume fraction of precipitates on the irradiation performance of the material of interest.

I. PROGRAM

Title: Radiation Damage Studies for Fusion Reactors
Principal Investigators: P. Wilkes and G.L. Kulcinski
Affiliation: University of Wisconsin-Madison

II. OBJECTIVE

To develop a fundamental understanding of the formation of voids, loops and precipitates in heavy ion and electron irradiated materials.

III. RELEVANT DAFS PROGRAM TASK/SUBTASK

II.C.6. Effects of Damage Rate and Cascade Structure on Microstructure.

IV. SUMMARY

This report covers a recent section of our work probing the causes of phase instability in ordered second phase particles. We have developed a new theoretical approach to radiation disordering which we here show to explain current available data on irradiated order compounds. The predicted order is then used to compute the free energy of the phase under irradiation and hence the relative stability with adjacent phases. We show how this approach can give radiation modified phase diagrams.

V. ACCOMPLISHMENTS AND STATUS

The Radiation Disorder Model of Phase Stability -- K-Y. Liou (ANL) and P. Wilkes (University of Wisconsin)

A detailed theory is presented for radiation induced order-disorder phase transformations. Both radiation enhanced ordering and radiation induced disordering are described and the temperature and radiation rate dependent balance between them is obtained. The theory is applied to the case of Cu_3Au.

The free energy of partially or completely disordered phases is then calculated so that radiation modified phase diagrams can be determined. Such diagrams are presented for the Ti-Co, Nb-Rh and Ti-Ru systems. Several experimental observations of phase instabilities are explained on the basis of the theory.

1. Introduction

Experiments have shown that under irradiation precipitates may either grow or shrink, that equilibrium phases may dissolve and be replaced with non-equilibrium phases and that precipitation sequences may be altered. The situation is evidently very complex and several different mechanisms are operating to modify microstructural phase stability under irradiation.

The mechanisms that have been proposed and in some cases demonstrated, can be classified.

a) Radiation Enhanced Diffusion. The increase in point defect population caused by atomic displacements causes an increase in diffusion rates.(1) This often permits sluggish phase transformations to proceed to completion under irradiation when thermal reaction had apparently ceased.

b) Radiation Induced Segregation.(2) During irradiation large numbers of point defects are generated, diffuse to sinks and annihilate. Any coupling between solute atoms and this flux of defects will induce a flux of solute towards or away from the sinks. The segregation induced by the solute flux can cause the composition of local regions to cross the phase boundary so that precipitation can occur.(3) Elsewhere in the matrix a corresponding depletion of solute can cause precipitate dissolution.

c) Other Flux Coupling Phenomena. A coupling between defect fluxes and solute atoms may occur near precipitates to aid the defect annihilation. For example,(4) an incoherent precipitate may annihilate vacancies at its surface only if the resultant volume strain is relieved by transfer of solute into or out of the precipitate (depending on the relative solute - atom sizes in the matrix and precipitate). Alternatively Martin(5) has proposed that solute concentration fluctuations may attract defects and enhance recombination. The resultant depletion of defects induces a further defect flux into the region and this may drag more solute and enhance the intensity of the fluctuation to the point where precipitation can occur.

d) Cascade and Displacement Effects. The damage process may directly affect precipitates by removing solute atoms from a precipitate by energetic knock-on or by cascade dissolution at the surface of a precipitate.(6,7)

e) Defect Concentration Effects. In contrast to the effect of defect fluxes which is involved in a), b) and c), it has been proposed(8) that the steady-state defect concentration under irradiation may itself destabilize a phase and permit an alternative phase to precipitate instead. This paper represents a new approach to mechanism e). The steady-state defect concentrations under irradiation are generally too small to produce the ~ 10-100 kJ/mole in internal energy required to destabilize equilibrium phases.

However, in ordered alloys in addition to vacancy and interstitial defects caused by atom displacements, there are anti-structure atoms caused by atom replacements. Since the replacements often exceed the displacements by between one and two orders of magnitude the steady-state concentration of anti-structure atoms can be much larger than for other defects. If the ordered phase has a high ordering energy and a slow reordering rate, the energy involved in radiation-induced disordering can easily reach the levels required to modify phase stability.

In this paper we propose a detailed model for the disordering of phases by irradiation and the calculation of radiation modified phase diagrams.

2. Radiation Induced Disorder

There is abundant evidence that radiation induces disorder.(9-12) An irradiation process which creates atomic displacements will also create replacements. In an ordered alloy both events produce point defects; displacements producing frenkel pairs and replacements producing anti-structure atoms. Since these events are caused by the incident particles with energies much greater than the thermal energy per atom, the defect production itself is independent of temperature (except for any temperature induced defocussing of collision sequences).

Any disordered alloy will return to its equilibrium degree of order provided the appropriate diffusion process can operate. The radiation-produced vacancies and interstitials enhance diffusion (provided that they are mobile) so that radiation can also enhance the reversion to the equilibrium degree of order.

In an ordered alloy under irradiation we therefore have two opposing processes continuing, a disordering and a reordering, with some steady-state degree of order being established when the two rates balance. The purpose of this section is to describe a simple model for calculating this steady-state order. We consider only long range order of stoichiometric ordered phases.

The Bragg-Williams definition of the long range order parameter for a binary alloy with atoms arranged on two sub-lattices α and β is

$$S = \frac{f_{A\alpha} - X_A}{1 - X_A} \tag{1}$$

where $f_{A\alpha}$ is the probability of an A atom being at an α lattice site, and X_A is the atomic fraction of A atoms. S=1 when the alloy is completely ordered and S=0 when it is completely random. When the ordered alloy is irradiated, a rate equation can be written for the balance between the disordering and reordering rates

$$\frac{dS}{dt} = \left(\frac{dS}{dt}\right)_{Irr} + \left(\frac{dS}{dt}\right)_{Th'} \cdot \tag{2}$$

The second term on the right-hand side is the irradiation enhanced thermal reordering rate.

The solution of this steady-state equation gives the steady-state degree of order under irradiation. In order to find this we must first express the ordering and disordering rates in terms of the irradiation and material parameters and to this we now turn.

2.1. Irradiation Disordering

The unit of radiation damage, displacement per atom (dpa), which has been commonly used for void swelling studies, is not appropriate for radiation induced disorder. We need instead the total number of atoms replaced by other atoms during irradiation. A replacement event can be either a direct replacement or the production of an interstitial which recombines with a vacancy or migrates to a defect sink. If we assume that atoms are randomly replaced by other atoms, it can be easily shown by probability considerations that

$$\left(\frac{dS}{dt}\right)_{Irr} = - \left(\frac{\nu_r}{\nu_d}\right) kS \tag{3}$$

where k is the dpa rate, ν_r is the number of replacements and ν_d is the number of displacements.

There are different mechanisms by which an ordered alloy can be disordered by irradiation. In the case of disordering due to focussed replacement sequences (or dynamic crowdions), disordering depends on crystallographic directions and equation (3) should be multiplied by a geometric factor. Disordering can occur locally in displacement spikes by uncorrelated recombinations of frenkel pairs or by formation of defect clusters (vacancy loops formed by cascade collapse for example). The mixing of atoms in these regions is probably random and can, therefore, be approximated by equation (3). In general, we introduce a disordering efficiency ε and write

$$\left(\frac{dS}{dt}\right)_{Irr} = - \varepsilon kS \; . \tag{4}$$

The parameter ε is of the order of the ratio (ν_r/ν_d), which depends on the structure of displacement cascade or the types of irradiation. Under neutron or heavy-ion irradiation conditions, ε could vary from approximately 10 to 100.(33) While under electron irradiation, ε is approximately 1 ~ 3.

2.2. Irradiation Enhanced Thermal Reordering

Nowick and Weisberg(13) consider an order-disorder transition as a chemical reaction in which a pair of A-B atoms at the wrong lattice sites is interchanged to give an A-B pair at the right lattice sites.

$$(AB)_w \underset{K_2}{\overset{K_1}{\rightleftarrows}} (AB)_r \; . \tag{5a}$$

The rate constants for the reaction are given by

$$K_1 = \nu_1 \exp\,(-U/k_BT) \tag{5b}$$

$$K_2 = \nu_2 \exp\,[-(U+V)/k_BT] \tag{5c}$$

where U is the energy barrier for the reaction and the activation energy

V is the energy reduction when a wrong A-B pair transforms into a right A-B pair. V depends on the instantaneous configuration of atoms (or the degree of order), ν_1 and ν_2 are frequency factors.

Nowick, et al.(13) show that at low temperatures where S approaches unity the solution of the chemical rate equation reduces to

$$\frac{1-S}{1-S_e} = \coth\,(xt+y) \tag{6a}$$

where S_e is the equilibrium order parameter, y is a constant.

For our purpose we require the time derivative of S,

$$\left(\frac{dS}{dt}\right)_{th} = \frac{x(1-S)^2}{(1-S_e)} - (1 - S_e)x \tag{6b}$$

with the rate constant x in the absence of irradiation being(13)

$$x = (\nu_r \nu_w)^{1/2} \left[\frac{X_A}{X_B}\right]^{1/2} Z_\beta \exp\,[-(U+V_o/2)/k_B T] \tag{7}$$

where V_o is the activation energy when S=1. Z_β is the number of β sites which are nearest neighbors to an α site while ν_r and ν_w are the frequency factors for a right and wrong pair, respectively. If the activation entropy is neglected, these frequencies are close to the Debye frequency. Although equation (6a) is derived for S close to one, it has been shown to fit experimental data from Cu_3Au and Ni_3Mn quite well for the whole range of order.(13-17) This has been justified by Nowick et al.(13) in a detailed mathematical argument in which the theoretical prediction gave a satisfactory fit up to 30°C from the critical temperature. In systems where the order parameter is close to unity up to the transition temperature (e.g. Cu_3Au) or for ordered compounds as discussed later in this paper, the model is at its best.

The mass reaction model described above, however, does not relate the kinetics of order-disorder transition to the point defects. To modify the model for alloys under irradiation, one simply considers vacancies and interstitials as species of catalyst for the chemical reaction in equation (5a).

Consider first the vacancy mechanism; there are different paths for the order-disorder reaction of an A-B pair. Figure 1 shows the most probable path which consists of two successive jumps of the A and B atoms involving only one vacancy. By this reaction path, the Boltzmann factor with the energy barrier U can be written as

$$\exp\,(-U_v/k_BT) = C_v \exp\,(-E^m_{vo}/k_BT)\;(Z_\alpha + Z_\beta - 2) \qquad (8)$$

where C_v is the concentration of vacancies and E^m_{vo} is the vacancy migration energy for those vacancy jumps which cause the re-ordering (this need not be identical to E^m_v for the non-ordering jumps in the alloy).

Transition from a wrong A-B pair to a right A-B pair by this reaction path can begin with a vacancy either at one of the Z_α sites around a β type vacancy or at one of the Z_β sites around an α vacancy. The total number of such reaction paths for the A-B pair considered is therefore $(Z_\alpha + Z_\beta - 2)$. In both CsCl and $AuCu_3$ type superlattices, $Z_\alpha + Z_\beta - 2 = 14$.

The pre-exponential factor for a reaction path of non-successive jumps involving two vacancies is $(C_v)^2$. This and other less probable paths are, therefore, negligible compared to the most probable path of two successive jumps involving only one vacancy.

Order-disorder by an interstitialcy mechanism is less understood because of the more complicated interstitial migration process. Experimental evidence(18-20) and theoretical calculations(21,22) show that interstitials in pure metals (Al, Cu, Ni, Mo, Fe) are in the configuration of <100> dumbbells for fcc and <110> dumbbells for the bcc structure. These self-interstitials migrate by combined rotational and translational jumps as shown in Figure 2.(23) In such cases an A-B pair on the wrong sites can be transferred to right sites by three successive jumps involving one dumbbell. This dumbbell must contain the appropriate atom necessary to give a right atom in its final jump. An example in fcc is shown in Figure 3. Other reactions for the A-B pair involving more than one interstitial can be neglected compared to the most probable path involving only one interstitial.

However, migration of dumbbell interstitials may be different in alloys. When there is a large difference between the effective atomic volumes of the alloying elements the undersized atoms are preferentially accommodated at the dumbbells. As a result only the undersized atoms are diffusing by this mechanism and the order-disorder reaction is little affected. In general, each reaction path containing three successive jumps should be weighted by a geometric factor and a size dependent probability factor. While the kinetics of order-disorder transition by the interstitialcy mechanism is still under study, we can introduce an interstitialcy reordering efficiency, σ, and express the Boltzmann factor with the energy barrier U in equation (8) as:

$$\exp\,(-U_i/k_BT) = \sigma\, C_i\, \exp\,(-\, E^m_{io}/k_BT) \qquad (9)$$

where C_i is the concentration of the interstitials and E^m_{io} is an effective (ordering) migration energy of the dumbbell. The parameter σ contains geometric factors determined by the numbers of the reaction paths and the probability factors for reactions to take place by these paths.

By combining equations (8) and (9), equation (7) can be rewritten as:

$$x = \{\nu_v C_v \exp\,(-\, E^m_{vo}/k_BT)\,(Z_\alpha+Z_\beta-2) + \nu_i\, \sigma\, C_i\, \exp\,(-E^m_{io}/k_BT)\}\, \left[\frac{X_A}{X_B}\right]^{1/2} Z_\beta \exp\,(-V_o/2k_BT) \qquad (10)$$

where

$$2\nu_v = (\nu_r\ \nu_w)_v^{1/2}$$

$$3\nu_i = (\nu_r\ \nu_w)_i^{1/2}$$

$$V_o = \begin{Bmatrix} -14\Omega \text{ for bcc} \\ -6\Omega \text{ for fcc} \end{Bmatrix} \text{ using the quasi-chemical model for the}$$

$$\text{ordering energy } \Omega = V_{AB} - \frac{V_{AA}+V_{BB}}{2} .$$

The factors two and three in these frequencies reflect the fact that a single pair inversion requires two vacancy jumps or three interstitial jumps.

By inserting x from equation (10) into equation (6b) the radiation enhanced ordering rate can now be determined in terms of the material parameters.

The steady-state defect concentrations (C_{-V} and C_i) can be calculated, following Brailsford and Bullough,(24) by solving the steady-state rate equations:

$$\frac{\partial C_i}{\partial t} = k - D_i C_i k_i^2 - \alpha C_i V_v = 0$$

$$\frac{\partial C_v}{\partial t} = k' - D_v C_v k_v^2 - \alpha C_i C_v = 0$$

where α is a defect recombination parameter; k_i^2 and k_v^2 are the effective sink strengths for the interstitials and the vacancies respectively in the crystal under irradiation. Appropriate sink strengths can be used depending on the types of defect sinks present under different irradiation parameters. For simplicity we consider a stable radiation induced dislocation network to be the major sink and express the sink strengths as a function of the dislocation density ρ_d,

$$k_i^2 = Z_i \rho_d$$

$$k_v^2 = Z_v \rho_d \ .$$

The bias factors Z_i and Z_v given by Brailsford and Bullough are close to unity and differ by a few percent.

2.3. The Order-Disorder Transformation Under Irradiation

Having obtained both the ordering and disordering rates from the previous sections we can now determine the steady-state order by inserting them in the rate equation (2).

The general solution to this rate equation with an initial condition $S = S_o$ at $t = 0$ is

$$S(t) = 1 - p + \frac{p-q}{1 - \left(\frac{S_o+q-1}{S_o+p-1}\right) \exp(zt)} \qquad (11\text{-a})$$

where $z = \{\varepsilon^2 \ k^2 + 4 \ x \ [x + \varepsilon k/(1 - S_e)]\}^{1/2}$,

$p = (-\varepsilon k + z) \ (1 - S_e)/(2x)$,

$q = (-\varepsilon k - z) \ (1 - S_e)/(2x)$,

S_e is the equilibrium long range order parameter and x the reaction constant to be determined. We intend to comment on this time variation of order under irradiation in a later paper; here we concentrate on the steady state solution when equation (2) is set equal to zero and $t \to \infty$ in equation (11a). This gives

$$S = 1 - p = 1 + \frac{(\varepsilon k - z)(1 - S_e)}{2x} \qquad (11\text{-b})$$

with the dose in dpa, $\phi = kt$. Equation (11b), therefore, gives the steady-state order as a function of dose rate.

Expression (11b) contains the equilibrium order parameter in the absence of irradiation (S_e) which can be obtained from order-disorder transition theory (see refs. 25, 26 for reviews). Using the quasi-chemical model of Fowler-Guggenheim(27,28) and Takagi,(29) the free energy as a function of the long-range order parameter for the CsCl type superlattice is given by

$$F(S) = F(1) + \frac{k_B T}{2} \{(1+S)\ \ell n\ (1+S) + (1-S)\ \ell n\ (1-S) - 2\ \ell n\ 2$$

$$+ Z/2\ [(1+S)\ \ell n\ (\frac{\xi+S}{1+S}) + (1-S)\ \ell n\ (\frac{\xi-S}{1-S}) - 2\ \ell n\ (\frac{\xi+1}{2})]\} \qquad (12)$$

where $\xi = [1 + (1-S^2)\ (\exp(-2\Omega/k_B T)-1)]^{1/2}$ and Z is the coordination number. For the $AuCu_3$ type superlattice, however, this approach using nearest neighbor pairs fails to predict an order-disorder transition. The pair theory was modified by Yang and Li(30,31) who considered a group of four atoms at a tetrahedral quadruplet of sites as the basic unit and applied the quasi-chemical model to the $AuCu_3$ type superlattice. They successfully predicted a stable superlattice below a given critical temperature. An equivalent calculation by McGlashan(32) using Yang and Li's approach for an AB_3 superlattice is summarized below.

$$\frac{F(S)}{k_{BT}} = (1/4)\ (3S+1)\ \ell n\ (\frac{3S+1}{4}) + (3/2)\ (1-S)\ \ell n\ \frac{3(1-S)}{4} + (3/4)\ (S+3)$$

$$\ell n\ (3/4(S+3)) - 3\ \ell n\ 3 + \ell n\ (a/a^*) + 3\ \ell n\ (h/h^*) + 3\ S\ \ell n$$

$$(cf^*/c^*f) - \frac{X_A+3X_B}{k_B T}\ . \qquad (13)$$

The constants are

$$a^* = (3S+1)\ (1-S)^3/256$$
$$c^* = (3S+1)\ (1-S)\ (S+3)^2/256$$

$$f^* = 3(1-S)^3\ (S+3)/256$$

$$h^* = 3(1-s)\ (S+3)^3/256$$

The parameters a, c, h, f are determined by the equations

$$a = \frac{3S+1}{4} - 3b - 3c - d$$

$$h = 3/4\ (1-S) - 3g - 3f - e$$

$$\frac{a}{\zeta^3} = \frac{b\eta^3}{\zeta^2} = \frac{c\eta^4}{\zeta} = d\eta^3 \tag{14}$$

$$\frac{e\eta^3}{\zeta^3} = \frac{f\eta^4}{\zeta^2} = \frac{g\eta^3}{\zeta} = h$$

with ζ given by the solution of

$$\frac{3S+1}{1-S} = \frac{(1-3\zeta^2\eta^{-4}-2\zeta^3\eta^{-3})(1+3\zeta^{-1}\eta^{-3}+3\zeta^{-2}\eta^{-4}+\zeta^{-3}\eta^{-3})}{(1+2\zeta^{-1}\eta^{-3}+\zeta^{-2}\eta^{-4})(1+3\zeta\eta^{-3}+3\zeta^2\eta^{-4}+\zeta^3\eta^{-3})} \tag{15}$$

and where $\eta = \exp\ (\Omega/k_BT)$.

The thermal equilibrium long-range order parameter S_e can, therefore, be determined by minimizing F(S) with respect to S using one or the other of these models as appropriate.

2.4. Application to Cu_3Au

The present model of order-disorder transition under irradiation is here applied to the Au Cu_3 superlattice. The resulting long-range order parameter as a function of temperature for a series of dose rates is shown in Figure 4, and the variables for this calculation are shown in Table 1.

TABLE 1

VARIABLES FOR LONG-RANGE ORDER CALCULATION

ε	ρ_d	Z_v	Z_i	E_v^f	$E_{v_o}^m$	D_o	$(\nu_r\nu_w)^{1/2}$	σ
10	$1\times10^{11}\text{cm}^{-2}$	1.0	1.02	1.28 eV	1.4 eV	$0.78\frac{\text{cm}^2}{\text{sec}}$	10^{13}sec^{-1}	0

The interstitialcy reordering mechanism is neglected by setting $\sigma=0$ because of the large difference between the effective atomic volumes of copper and gold. The defect parameters for pure Cu are used in this calculation. The ordering energy Ω (used in calculating S_e) is fixed such that the critical temperature predicted coincides with the experimental value, $T_c = 663^oK$.

The values of vacancy formation energy and pre-exponent D_o are those for copper since no value is available for Cu_3Au. The value chosen for E_v^m is that found in the 420^{o}K annealing stage in Cu_3Au where most of the irradiation induced resistivity anneals out thermally.(50) The remaining quantities in Table 1 are chosen as reasonable estimates.

Figure 4 indicates that at low enough temperatures the order parameter will always approach zero for disordering radiation because the defects are frozen-in and unable to diffuse. There is therefore no ordering reaction. At high temperatures near the critical temperatures the ordering rate due to the thermal equilibrium defect concentration dominates and radiation makes little difference except for the highest damage rates. The steady-state curve then approaches the calculated equilibrium curve appropriate to the quasi-chemical model. At intermediate temperatures the radiation enhanced defects increase the ordering rate and balance the radiation disordering to give intermediate values for the order parameter.

It should be noted that at low values of S the assumption that the ordering energy is independent of S breaks down. However, this only affects the thermal back reaction (i.e., the thermal disordering rate) which is already very small at these temperatures. In any case the curves approach zero order rather rapidly and an enhancement in the disordering rate will merely decrease S a little more rapidly with decreasing temperature.

As shown in Fig. 4, a dose rate as low as 10^{-10} dpa/sec is able to disorder the $AuCu_3$ superlattice below ~ 430^{o}K. A dose rate of k > 1×10^{-2} dpa is necessary to completely disorder the ordered alloy at all temperatures. A partial phase diagram under irradiation, based on these results, is shown in Fig. 5. The low temperature limit of the ordered phase is taken from Fig. 4. The remaining boundaries of the ordered region are assumed to diverge smoothly from their equilibrium positions as shown.

Several investigators(33-38) have irradiated Cu_3Au; however, all these workers appear to have studied transient phenomena over limited dose ranges so that no measures of steady-state properties have been made. Most workers monitored resistivity and the connection between this and order is not simple.

In spite of these difficulties the basic features of the theory correspond with experiment. At room temperature and below, ordered alloys are progressively disordered(33) as Fig. 4 predicts. At higher temperatures highly ordered alloys disorder while disordered alloys order(33-35) indicating that the intermediate values of S predicted in Fig. 4 would eventually be attained. Since the available data does not reach steady-state, however, the quantitative predictions of Fig. 4 cannot yet be tested.

The best data available is that of Kirk and Blewitt(33) which suggests that at 423^{o}K and a dose rate ~ 10^{-11} dpa/sec of fast neutrons a value of $1 > S > 0.5$ would be attained although the sample did not reach steady-state. This result agrees very well with the curves of Fig. 4. It would be desirable to have dislocation densities available for future experiments of this type.

Given the well-known deficiencies of the quasi-chemical and chemical rate models for ordering, detailed fits to the data (especially close to the critical temperature) are not to be expected. However, viewed as a simple phenomenological approach giving physical meaning to parameters needed to fit the data, the current model is obviously attractive.

The transition from steady-state disorder to order over a narrow temperature range under irradiation has also been observed in Ni_3Fe, Mg_3Cd and Ni_3Si(51) for 1 MeV electron irradiation. Zr_3Al has shown similar effects.(9,52) The basic features of the model, therefore, would seem to have general application to ordered systems.

Finally, it should be noted that the irradiation induced increase in the degree of order is an example of radiation enhancement of a sluggish reaction. Figure 6 shows schematically how this can occur. Consider a phase which has not been aged for sufficient time to produce the equilibrium degree of order, the maximum order obtained is, therefore, less than unity (S_0). Under irradiation, however, in the temperature range just below T_C, radiation enhanced diffusion increases the thermal reordering rate causing the steady-state order parameter to lie above the original incompletely equilibrated level (Fig. 6). The arrows on the diagram indicate the direction in which the order parameter will change under irradiation.

3. Radiation Induced Phase Instability

The change in the order-disorder region of an alloy described in Section 2.4 is an example of an irradiation modified phase transition. When a strongly ordered intermetallic compound is in thermal equilibrium with other phases of the alloy, disordering of this ordered compound can change the whole alloy phase structure. As described in the thermal equilibrium theory of order-disorder transitions, atoms in the alloy are arranged to obtain the degree of order which minimizes the free energy. When the alloy is irradiated, it is displaced from thermal equilibrium to a steady-state of long-range order S where the free energy is higher than this equilibrium value. Under irradiation, therefore, a new free energy balance between adjacent phases may be established giving a lower free energy than can be attained with the partially (or entirely) radiation disordered compound.

Figure 7 shows the modification of compositions of alloy phases α and γ determined by the common tangents of free energy curves when irradiation induces an increase of free energy δF of the intermetallic compound β.

Since in the above sections the free energy of an ordered phase under irradiation has been obtained, this can be inserted into equilibrium calculations of phase diagrams containing such phases to obtain the irradiation modified phase fields. This assumes, of course, that the free energy of disordered phases is unaffected by irradiation and that they can achieve a new equilibrium when an ordered phase dissolves.

To illustrate this part of the calculation we take several systems for which calculated phase diagrams have been published and which contain strongly ordering phases. Diagrams for the systems Ti-Co, Nb-Rh and Ti-Ru have been calculated by Kaufman(39) using a set of thermodynamic data listed in ref. 39. The calculational procedure is based on sub-regular solution theory as developed by Kubachewski and co-workers,(40-43) and adopted in a set of computer programs using a wide range of thermodynamic data by Kaufman.(39,42,43) These computer programs were modified to use the free energy of the compounds calculated from section (2), for the steady-state degree of order under irradiation using data given in

TABLE 2

PARAMETERS USED IN CALCULATING STEADY-STATE DEGREE OF ORDER

	ε	$\rho_d(cm^{-2})$	Z_v	Z_i	$E_v^f(eV)$	E_{vo}^m (eV)	D_o $(\frac{cm^2}{sec})$	σ	$E_i^m(eV)$	D_{io} $(\frac{cm^2}{sec})$	$\Omega(eV)$	$(\nu_v\nu_i)^{1/2}$ (sec^{-1})
TiRu	10	10^{11}	1.0	1.02	1.6	2.0	1.0	0	-	-	0.18	10^{13}
$TiCo_3$	10	10^{11}	1.0	1.02	1.6	2.0	1.0	0.01	0.15	0.01	0.20	10^{13}
$NbRh_3$	10	10^{11}	1.0	1.02	1.0	2.0	1.0	0.01	0.15	0.01	0.16	10^{13}

(1) $\alpha/D_i = 10^{17}$ cm^{-2} used in all cases to compute defect concentrations (where α is the recombination parameter).(24)

(2) The E_v^f and D_o of pure Ti were used as an approximation in TiRu and $TiCo_3$ and estimated values were used in $NbRh_3$ calculation.

(3) The ordering energy Ω is obtained from thermodynamic data in Ref. 39 and is assumed to be temperature independent.

(4) $\sigma = 0$ in the TiRu compound because the large size different makes interstitialcy reordering unlikely. The σ values of 0.01 for $TiCo_3$ and $NbRh_3$ are estimates.

(5) The energies of motion of the disorder/order vacancy motion are assumed to be larger than their equivalents in the pure metals. For the purposes of calculation a factor of two has been taken (i.e. E_v^m = 1 eV in all cases).

table 2.

In the case of the Ti-Co and Nb-Rh systems the increase in free energy was insufficient to remove the compounds $TiCo_3$ and $NbRh_3$ from the phase diagram. Instead the phase boundary of the terminal solid solution was progressively shifted to higher solubilities, reflecting the change in common tangent contact point on the free energy curve for the terminal solutions. The limit of the effect of radiation occurs when the compound is fully disordered at lower temperatures. At intermediate temperatures the boundary lies between the thermal equilibrium value (fully ordered compound) and the higher solubility appropriate for a balance with the fully disordered compound. The separation of the phase boundary from the equilibrium position occurs at higher temperatures for higher irradiation rates as Figures 8 and 9 show. The irradiation rates chosen (10^{-7} and 10^{-3} dpa/sec) are appropriate to fast reactor neutrons and heavy ion irradiations, respectively. These results show that particles of the ordered phase in the α matrix will shrink under irradiation and may dissolve entirely if the alloy composition is close to the phase boundary.

The calculated equilibrium phase diagram (following Kaufman)(39) for the TiRu system is shown in Fig. 10a, and agrees closely with experiment. The diagram contains the strongly ordering compound TiRu, for which the free energy shift on disordering is particularly large, since the equi-atomic composition maximizes the number of wrong bonds when disordered. The order parameter calculated from our model is shown in Figure 11; the variation of vacancy concentration at steady-state is also shown. The parameters used in the calculations are found in table 2.

The large increase in free energy as the compound disorders under irradiation, lifts the compound's free energy curve above the common tangent for the adjacent phases. A new balance state then occurs based on the mixtures of these two phases (β and ε') giving a new two-phase region on the diagram (Figure 10b and c). At the equi-atomic composition the free energy of the β phase itself is lower than the disordered TiRu so that the β field extends over this range as the figure shows.

The temperature at which the TiRu phase disappears depends upon the irradiation rate. A critical degree of disorder is required to remove the phase above the β free energy and this depends upon the disordering rate which in turns depends upon the irradiation rate (Figs. 10b and c).

The diagram shows that the disordered compound will transform to β. If the compound exists as particles in an ε' matrix (the β+ε' region) the new β phase may form by in-situ transformation of the disordered TiRu or by nucleation and growth from the supersaturated ε' produced by TiRu dissolution.

The detailed mode of transformation of the destabilized compound will depend upon kinetic features which remain to be explored and are not included in the current model.

Once again the detailed numerical predictions (such as the temperature at which a phase boundary shifts or disappears) should not be regarded as accurate in detail since they depend on the parameters in table 2, several of which are estimated. However, the general pattern of the phase diagrams is expected to be observed.

4. Discussion

4.1. Examples of Radiation-Disorder Instabilities

Williams, Stiegler and Wiffen(46) irradiated W-Re alloys in EBR-II to the doses of 6.1 ~ 37 x 10^{21} neutrons/cm^2 (> 0.1 MeV). They reported formation of χ-phase (WRe_3) in a single-phase (bcc W-rich solid solution) region close to the (bcc+σ) phase boundary. σ is an ordered phase (near 50 at% Re) between the tungsten-rich bcc and the disordered χ-phase in the thermal equilibrium phase diagram. Kaufman et al.(47)

estimated the increase of the free energy of σ-phase necessary for the formation of χ phase to be ~ 5440 J/mole (1.3 kcal/mole). They used Maydet and Russel's theory(4) to compute the irradiation-induced effective free energy change which turned out to be well below the value necessary for the suppression of σ-phase. 5 ~ 10 kJ/mole, however, could be easily attained by disordering the ordered σ phase resulting in its dissolution and replacement by the disordered χ phase, as in the Ti-Ru case. Though the mechanism of the phase instability of W-Re system can now be understood, the quantitative computation of the irradiation modified phase diagram must await a complete crystallographic structure determination of the complicated σ-phase.

A similar disappearance of σ-phase has been observed in the Fe-Ni-Cr system. Brown and Cawthorne(48) were unable to detect σ-phase after irradiation at temperatures up to 700°C. In this range σ-phase is regularly observed and its presence is predicted from thermodynamic calculations. In its place a γ' precipitate formed. The absence of σ-phase has been confirmed by Bilsby.(49) Thermodynamic data are unavailable for both the σ and γ' phases at the present time. In addition, the details of the ordering arrangement in σ-phase are unclear. It is, therefore, not possible to calculate the ternary diagram at the present time. However, the fact that the strongly ordered, equi-atomic σ-phase disappears certainly suggests radiation disordering as a possible cause.

Our model so far has considered only the effect of chemical bonding in the ordered structures. The next step is the more difficult one of calculating the energy change under irradiation when the order is due to the size difference of atoms (e.g. Laves phases). Obviously, a similar phenomenology will apply but the calculation of the free energy of such phases when they are disordered by irradiation is very difficult. It seems likely that such effects will be very large, readily destabilizing such phases.

Finally, it should be noted that a large change in free energy on disordering does not guarantee a large phase diagram change. If the ordered phase is much more stable than surrounding phases even large shifts will not destabilize it entirely.

4.2. Implications for Alloy Design

The calculations presented demonstrate that radiation induced disordering is capable of radically altering phase diagrams under irradiation. Since radiation disordering as a phenomenon has already been demonstrated experimentally, it is clear that we have a sound explanation for phase instabilities under irradiation.

In our model we make no attempt to improve on current theories of order-disorder; our objective has been to provide a clear conceptual framework for further experiment. Experimental results for the reordering and disordering rates under irradiation, together with the necessary thermodynamic data, are all that are required to determine phase diagrams.

From the alloy design point of view we can conclude that phases having the following characteristics are likely candidates for radiation induced destabilization.

a) A very high ordering energy
b) A similar stability (free energy) to adjacent phases
c) Close to equi-atomic concentration.

Our model offers a guide to a particular type of phase stability which must be combined with solute segregation and other mechanisms to obtain an overall picture of alloy stability under irradiation. Such a comprehensive approach will require that all the various aspects described in the introduction be included. One can now begin to distinguish how this problem should be attacked within the framework of our current understanding.

Firstly, alloy design should be based on a knowledge of the true equilibrium state of the material and its approach to this equilibrium under irradiation. Secondly, solute-defect coupling should be evaluated based on measurements and theory currently available. Thirdly, second phases used to strengthen the material, or which may form under irradiation need to be evaluated. This latter step will include the model of this paper, but kinetic effects associated with nucleation of new phases stabilized by irradiation will need to be added so that radiation phase diagrams can be used to predict which phases will actually occur in practice.

Clearly, this requires a major research effort, a substantial part of which will involve measurements of basic thermodynamic properties in systems of interest.

4.3. Limitations of the Model

Probably the most important assumption made in the calculations described here is that when a given compound disorders and becomes unstable with respect to a mixture of two adjacent phases, a new equilibrium will be attained. Since this involves the nucleation and growth of a new phase in the structure, whether or not equilibrium is attained depends on the kinetic factors. Both nucleation and growth depend on diffusion and this will be enhanced by irradiation, because of the larger defect population. However, at very low temperatures defects will remain frozen and the new phase will be unable to form. Under these conditions the radiation phase diagram will not be obeyed and the two-phase region will be found in practice to consist of a supersaturated solution produced by the dissolution of ordered particles. The relevant free energy which the disordered compound must then exceed is that of the supersaturated matrix rather than the free energy of the two phase mixture.

Even if diffusion is permitted new phases may not nucleate. However, at this point a unified approach would consider radiation affected nucleation which has been discussed for incoherent precipitates by Maydet and Russel(4) and for coherent precipitates by Martin.(5) In both these approaches nucleation may be either promoted or inhibited. Further discussion on the kinetics of the steady-state conditions is retained for a later paper.

Our model is also limited by the fact that we have selected a simple phenomenological approach to order-disorder so as to provide a framework for using experimental values of ordering and disordering rates under irradiation. The calculational details, therefore, rest on the assumptions of quasi-chemical or sub-regular solution theory and the long range order approximation. However, in an area of high technological interest, it is better to use simple models with phenomenological adjustment to produce detailed agreement with experiment rather than to attempt very complex ab-initio calculations with less general models.

5. Conclusions

1. Starting from current knowledge on the disordering of structures under irradiation we have been able to show that the free energy changes produced are sufficient to cause many ordered phases to become unstable.

2. Phase diagrams under irradiation can be calculated if ordering or disordering rates are known (together with necessary thermodynamic data for the equilibrium diagram).

3. In general at low temperature, phases which have undergone an order-disorder transition on cooling can be forced to revert to the disordered form by irradiation. The temperature for this has been calculated for Cu_3Au as a function of dose rate.

4. Several cases of radiation phase instabilities may be explicable by this mechanism.

VI. REFERENCES

1. Y. Adda, M. Beyeler, G. Brebec, Thin Solid Films 25 (1975), p. 107.
2. P.R. Okamoto and H. Weidersich, Jnl. Nucl. Materials 53 (1976), p. 336.
3. D.I. Potter and D.G. Ryding, Jnl. Nucl. Materials 71 (1977), p. 14.
4. S.I. Maydet and K.C. Russell, J. Nucl. Materials 64 (1977), p. 101.
5. G. Martin, Workshop on Solute Seg. and Phase Stability, Gatlinburg (1978), to be published in Jnl. Nucl. Matls.
6. R.S. Nelson, J.A. Hudson and D.J. Mazel, Jnl. Nucl. Materials 44 (1972), p. 318.
7. P. Wilkes, Workshop on Solute Seg. and Phase Stability, Gatlinburg (1978), to be published in Jnl. Nucl. Matls.
8. P. Wilkes, K.Y. Liou, R.G. Lott, Rad. Effects 29 (1976), p. 249.
9. L.M. Howe, M.H. Rainville, J. Nucl. Matls. 68 (1977), p. 215.
10. M.L. Jenkins, M. Wilkens, Phil. Mag. 34 (1976), p. 1155.
11. T.L. Francavilla, R.A. Meussner, S.T. Sekula, Sol. State Comm. 23 (1977), p. 207.
12. A.R. Sweedler, D.E. Cox, Phys. Rev. B 12 (1975), p. 147.
13. A.S. Nowick, L.R. Weisberg, Acta. Met. 6 (1958), p. 260.
14. V.S. Polenok, Fiz. Metal. Metalloved, 36 (1973), p. 188.
15. J. Rothstein, Phys. Rev. 94, 1429 (1954), p. 1429.
16. F.P. Burns, S.L. Quimby, Phys. Rev. 97 (1955), p. 1567.
17. M. Kirk, J.B. Cohen, Met. Trans. 7A (1976), p. 307.

18. P. Ehrhart, Proceedings of the Int'l. Conf. on the *Properties of Atomic Defects in Metals*, Argonne, Ill., U.S.A., 1976 (1978), p. 200.

19. W. Schilling, Proceedings of the Int'l. Conf. on the *Properties of Atomic Defects in Metals*, Argonne, Ill., U.S.A. (1978), p. 465.

20. H.G. Haubold, *Fundamental Aspects of Radiation Damage in Metals*, ERDA Report Conf. 751006 NT15, Springfield, Virginia (1976), p. 268.

21. R.A. Johnson, *J. Phys. F: Metal-Phys*. *3* (1973), p. 295.

22. P.H. Dederichs, *Fundamental Aspects of Radiation Damage in Metals*, ERDA Report Conf. 751006 NT15, Springfield, Virginia (1976), p. 187.

23. F.W. Young, Jr., Proc. of the Int'l. Conf. on the *Properties of Atomic Defects in Metals*, Argonne, Illinois, U.S.A., 1976 (1978), p. 310.

24. Brailsford and Bullough, *Jnl. Nucl. Materials* *44* (1972), p. 121.

25. T. Muto, Y. Takagi, *Solid State Phys*., F. Seitz and D. Turnbull, ed., Vol. 1 (1955), p. 193.

26. L. Guttman, *Solid State Phys*., Vol. 3 (1956), p. 145.

27. R.H. Fowler, E.A. Guggenheim, *Proc. Roy. Soc*., *A174* (1940), p. 189.

28. E.A. Guggenheim, *Mixtures*, Oxford University Press (1952).

29. Y. Takagi, *Proc. Phys.-Math. Soc. Japan*, *23* (1941), p. 44.

30. C.N. Yang, *J. Chem. Phys*. *13* (1945), p. 66.

31. C.N. Yang, Y.Y. Li, *Chinese J. Phys*. *7* (1947), p. 59.

32. M.L. McGlashan, Thesis, Reading University (1951), described in ref. 28.

33. M.A. Kirk and T.A. Blewitt, *Met. Trans*. *9A* (1978), p. 1729.

34. T.H. Blewitt and R.R. Coltman, *Acta. Met*. *2* (1954), p. 549.

35. H.L. Glick, F.C. Brooks, W.F. Witzig, W.E. Johnson, *Phys. Rev*. *87* (1952), p. 1074.

36. S. Siegel, Phys. Rev. 75 (1949), p. 1823.

37. J.A. Brinkman, C.E. Dixon, C.J. Meechan, Acta. Met. 2 (1954), p. 38.

38. R.A. Dugdale, Phil. Mag. (1956), p. 537.

39. L. Kaufman and H. Bernstein, "Computer Calculation of Phase Diagrams", Academic Press, N.Y. (1970).

40. O. Kubachewski, Phase Stability in Metals and Alloys (eds. Rudman, Stringer and Jaffee), N.Y. (1967), p. 63.

41. O. Kubachewski, W. Slough, Prog. Mat. Sci. 14 (1969), p. 1.

42. O. Kubachewski, J.A. Catterall, Thermochemical Data of Alloys, Pergamon Press, N.Y. (1956).

43. F.H. Hayes, F. Muller, O. Kubachewski, J. Inst. Met. 98 (1970), p. 20.

44. L. Kaufman, Prog. Mat. Sci. 14 (1969), p. 45.

45. L. Kaufman and H. Bernstein, "Phase Diagrams" (A. Alper, ed.), Academic Press, N.Y. 1 (1970), p. 45.

46. R.K. Williams, J.O. Stiegler, F.W. Wiffen, ORNL-TM-4500 (1974).

47. L. Kaufman, J.S. Watkin, J.H. Gittus, A.P. Miodownkik, Calphad 1 (1977), p. 280.

48. C. Brown and C. Cawthorne, Jnl. Nucl. Matls., 66 (1977), p. 201.

49. Bilsby, private communication quoted in ref. 47.

50. J. Gilbert and H. Herman, Rad. Effects, 20 (1973), p. 37.

51. E.P. Butler and P.R. Swann, Proc. Fifth Int. Conf. on High Voltage Electron Microscopy, Kyoto (1977), p. 555.

52. G.C. Carpenter and C.M. Schulson, J. Nucl. Matls., 23 (1978), p. 180.

VII. FUTURE WORK

This paper completes theoretical work in this area on this contract.

Current work in precipitate stability and void formation will be reported in subsequent issues.

VIII. PUBLICATIONS

The above report has been submitted as a paper to Jnl. Nucl. Materials.

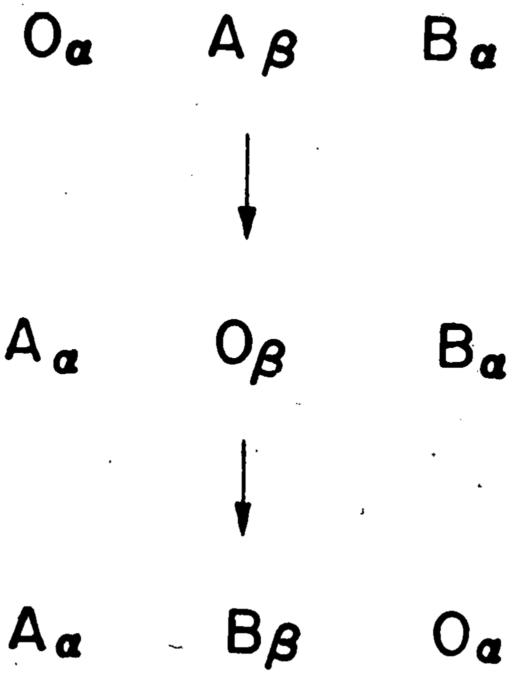

FIGURE 1. The motion of a vacancy (o) jumping from left to right in a lattice made up of two sub-lattices (α and β sites) can order a disordered lattice. The top line (before the jump) is disordered with B atoms on α sites and A atoms on β sites. After two jumps (bottom line) the atoms are ordered on the sites (A on α and B on β).

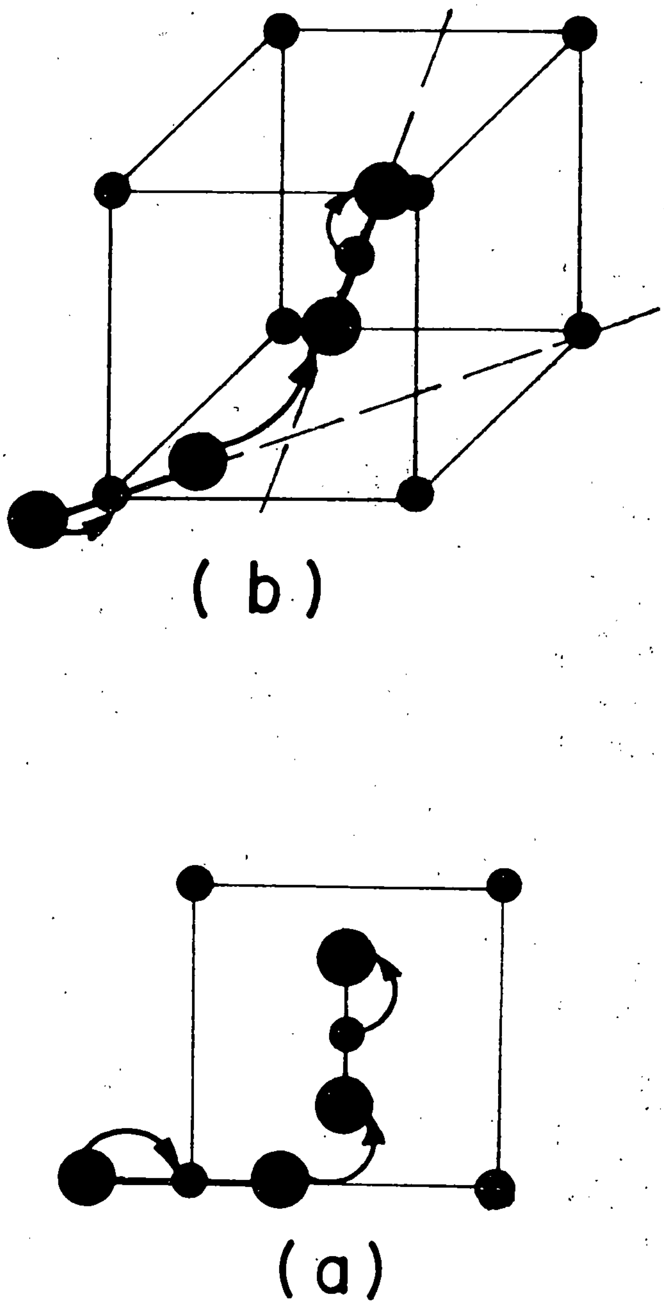

FIGURE 2. Interstitialcy motion in fcc(a) and bcc(b).

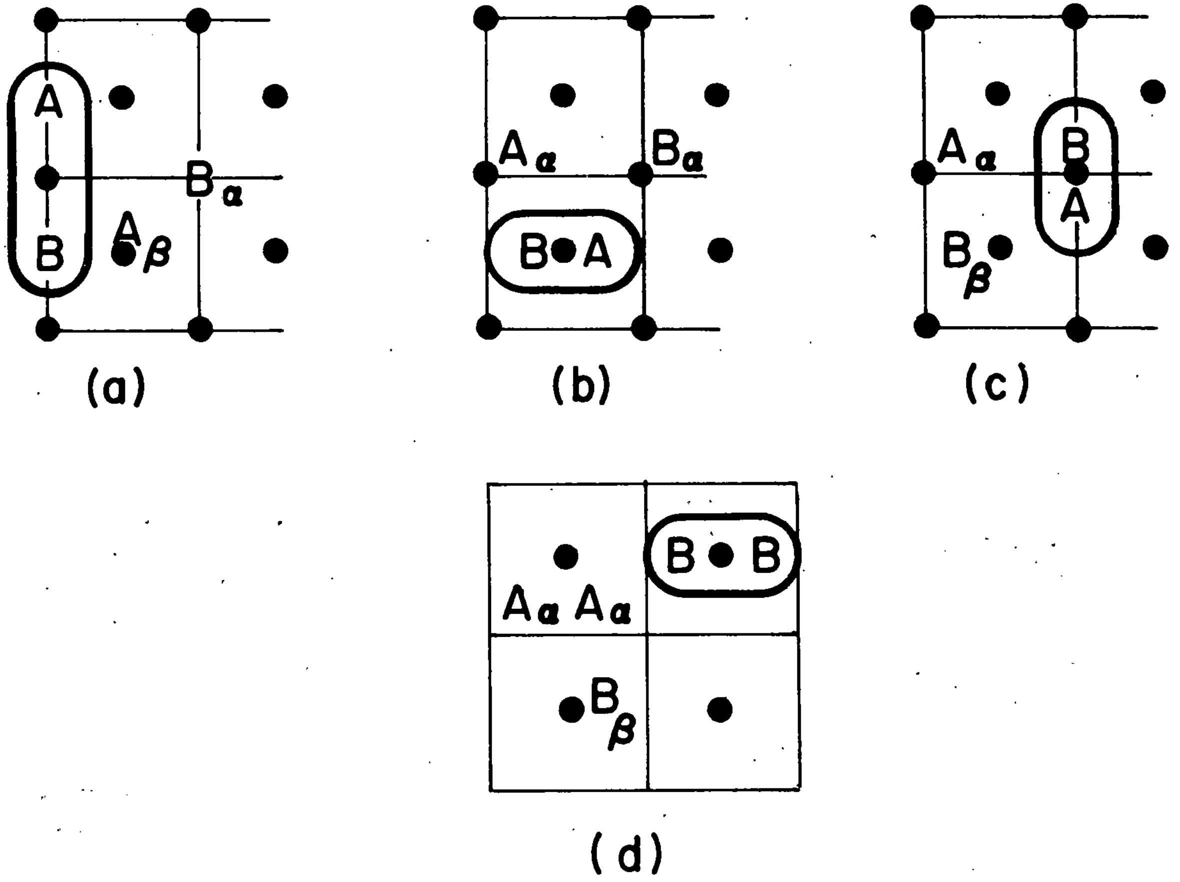

FIGURE 3. Interstitial motion in the Cu$_3$Au type lattice. The interstitial dumbbell is ringed. Note that its motion causes an ordering with A atoms on the α sites (linked by lines) and B atoms on the β (face centered) sites.

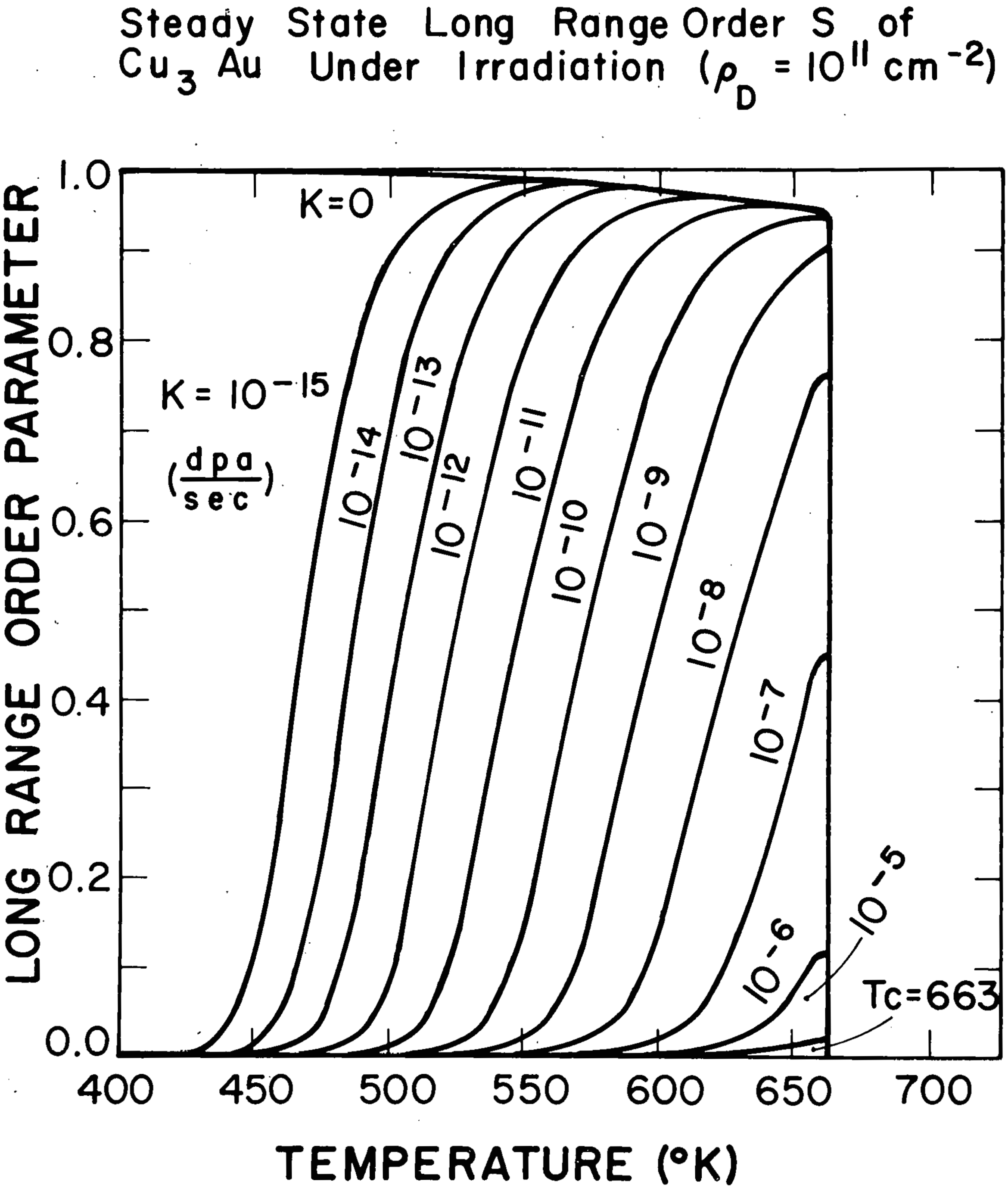

Steady State Long Range Order S of Cu_3Au Under Irradiation ($\rho_D = 10^{11}\ cm^{-2}$)

FIGURE 4. The steady state long range order parameters Cu_3Au under irradiation for various irradiation rates k (in dpa/sec) as indicated.

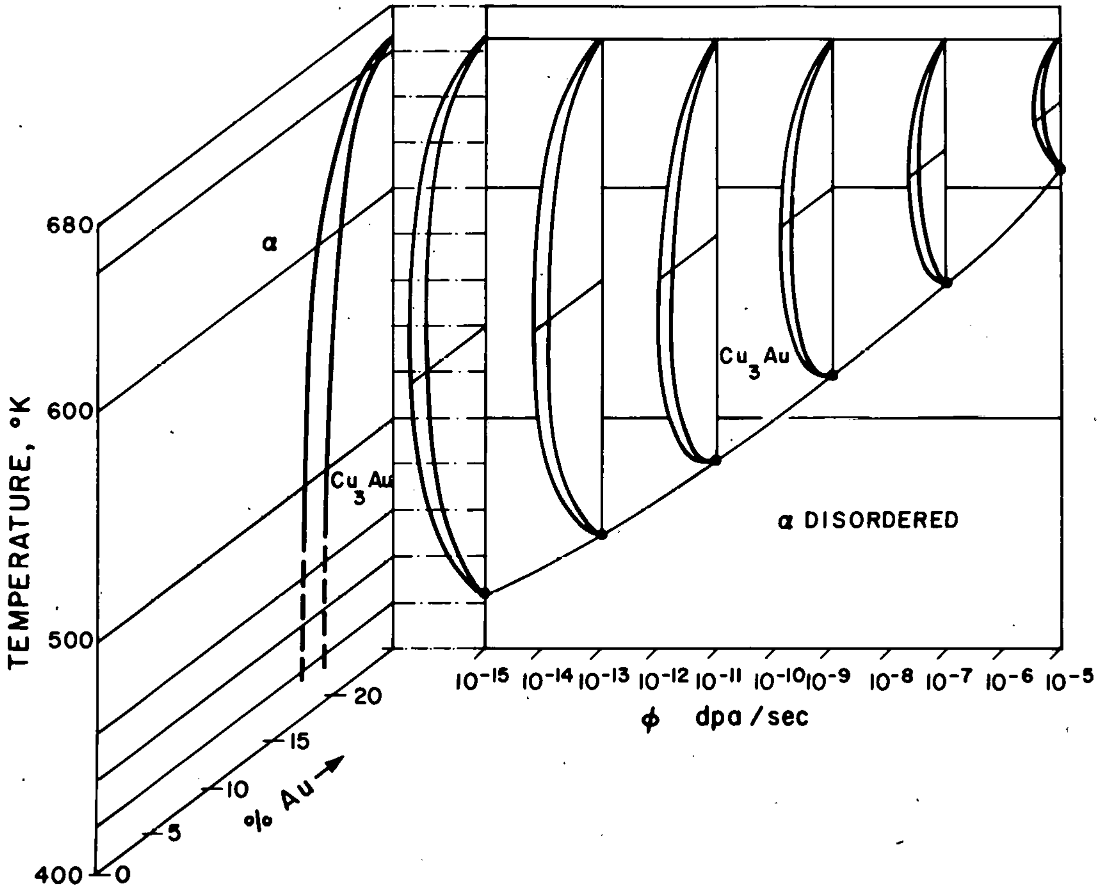

FIGURE 5. The radiation modified partial phase diagram from the Cu_3Au region of the Cu-Au system. The equilibrium phase diagram is on the left and radiation modified versions of the Cu_3Au loop are plotted as a function of dose rate on the third axis. The calculated points marking the minimum temperature for the ordered region are shown as dots at the base of each loop. The sides of the loops are schematic only.

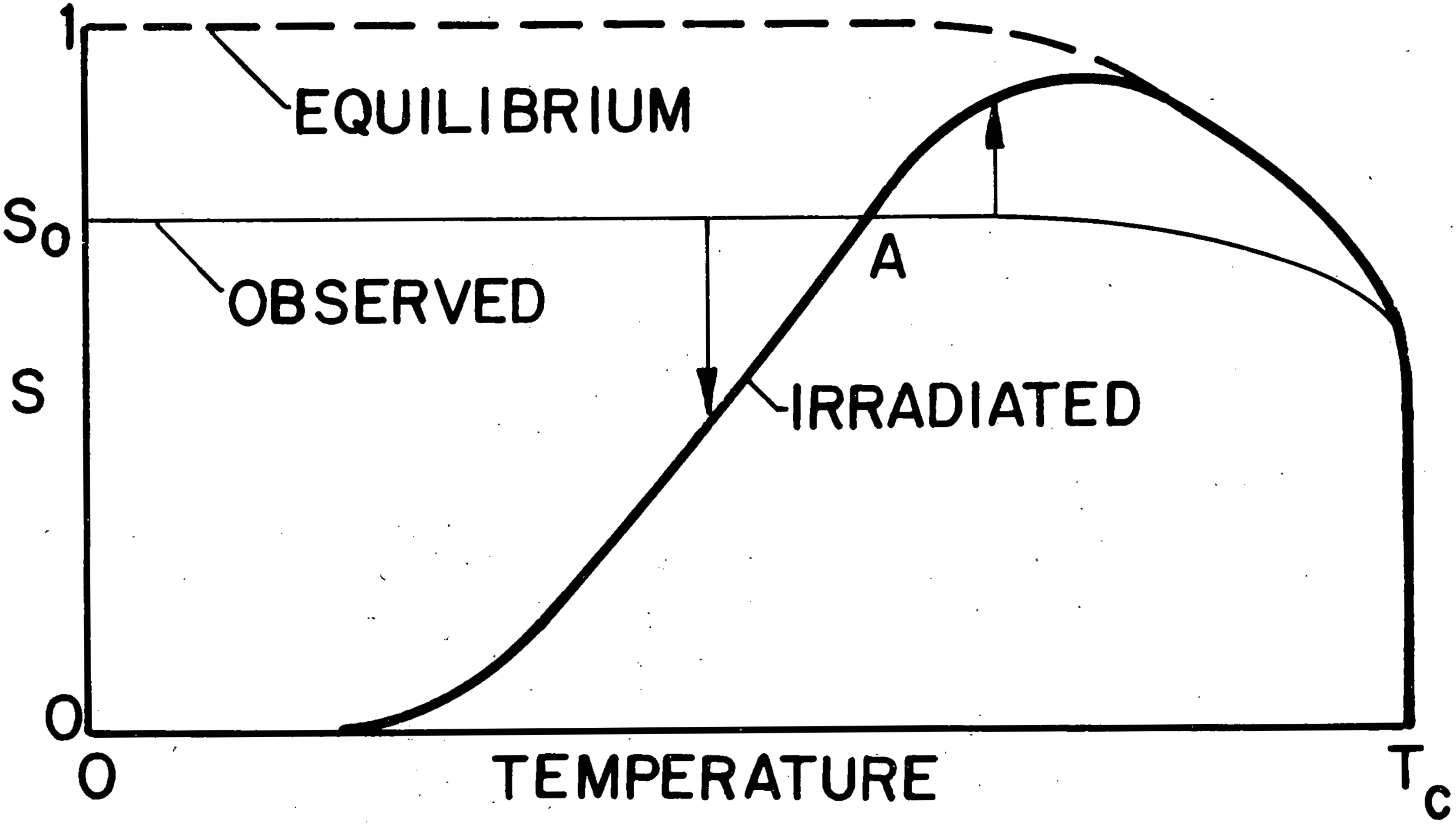

FIGURE 6. Showing how in the temperature range just above point A, radiation induces an increase in order over the incompletely aged state indicated by the line marked "observed". The arrows indicate how the order varies to the right and left of point A.

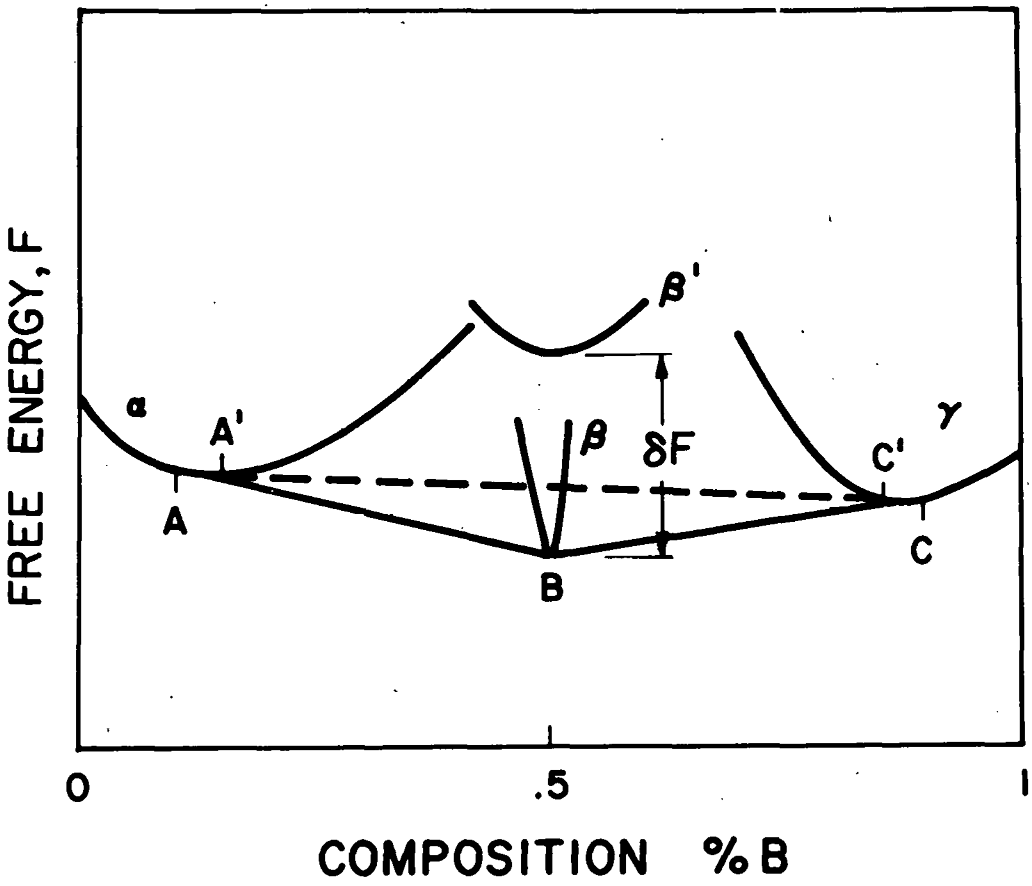

FIGURE 7. Showing how an ordered intermetallic compound β increases its free energy by an amount δF as it disorders to β' under irradiation. The new equilibrium is then indicated by the dashed tangent line A'C' between α and γ phases. Note the change in solubilities from A to A' and C to C' when this occurs.

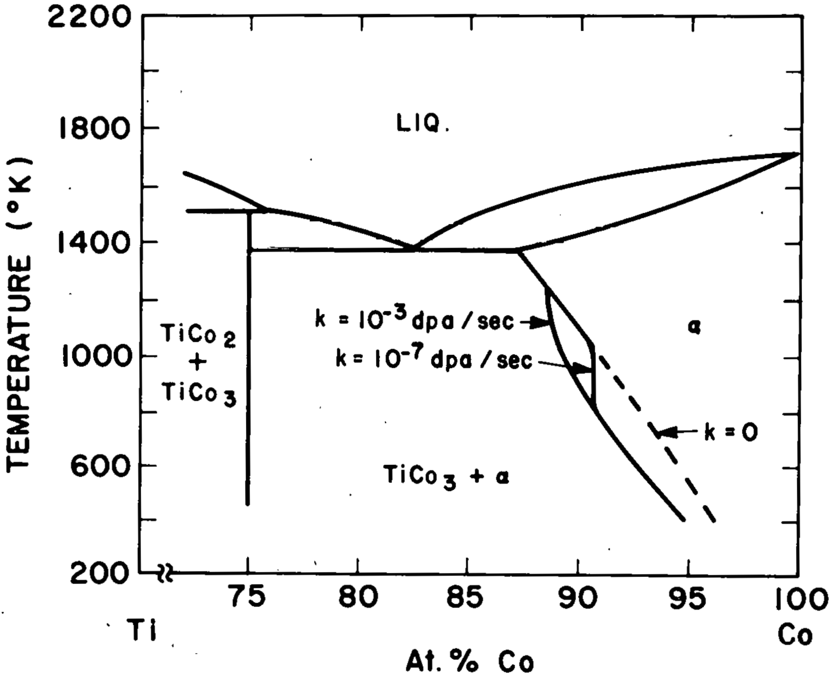

FIGURE 8. The calculated partial phase diagram for the Ti-Co system as modified by irradiation at the damage rates shown. The original equilibrium phase boundary is the k=0 line.

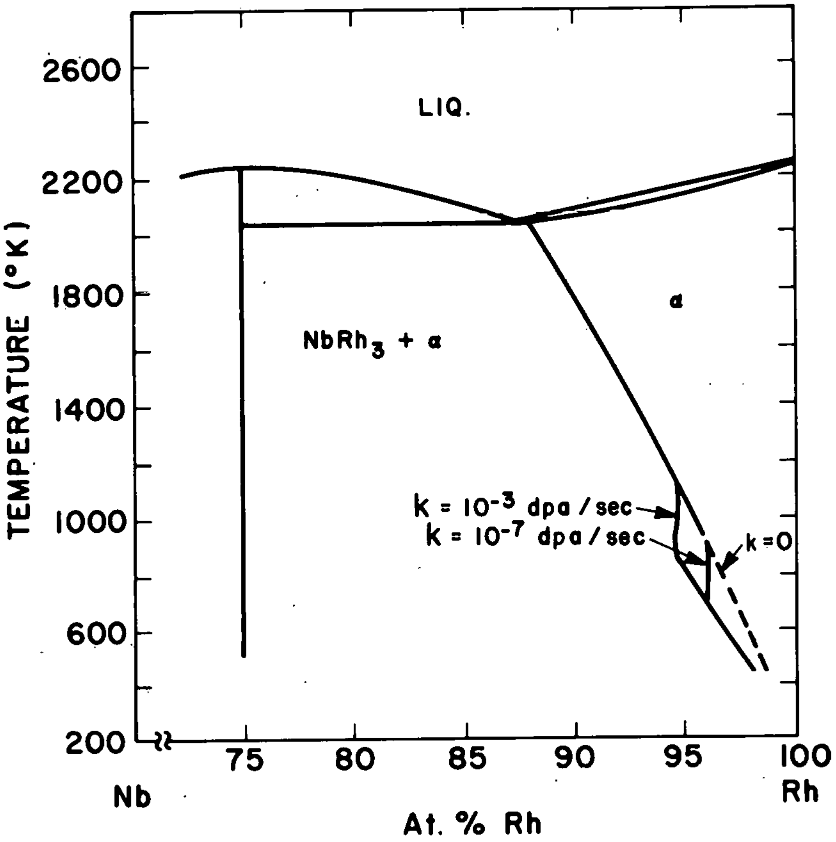

FIGURE 9. The calculated partial phase diagram for the Nb-Rh system as modified by irradiation at the rates shown.

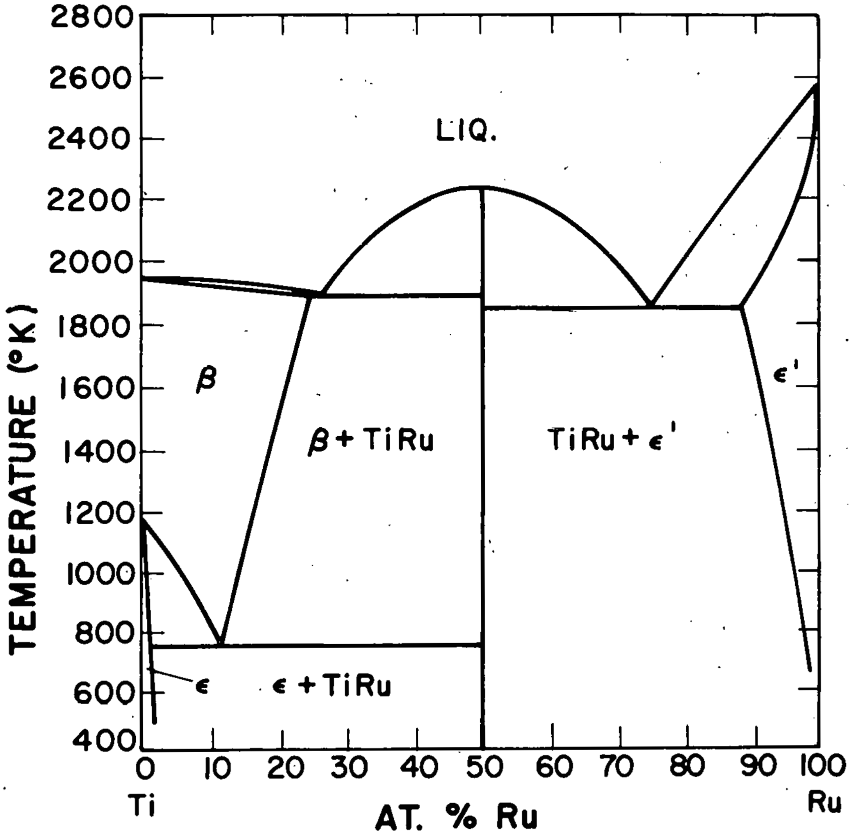

FIGURE 10. a) The equilibrium phase diagram for the Ti-Ru system as calculated by Kaufman.(39)

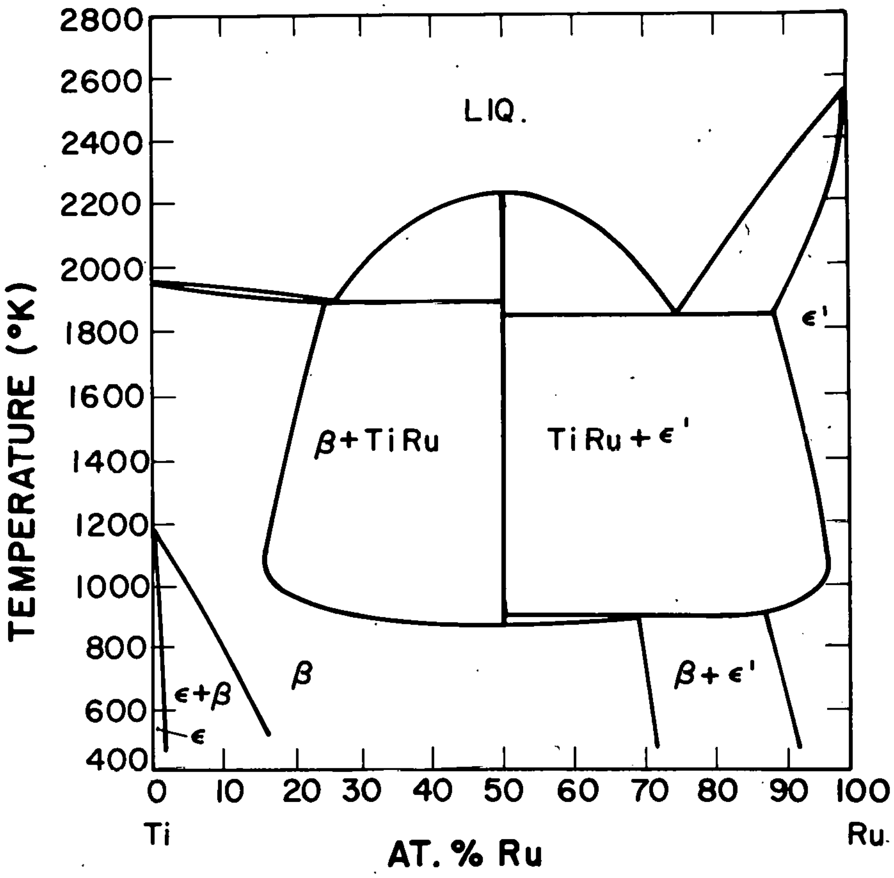

FIGURE 10. b) The radiation modified Ti-Ru system for a dose rate of 10^{-3} dpa/sec, calculated using the data in Table 2 and reference (39).

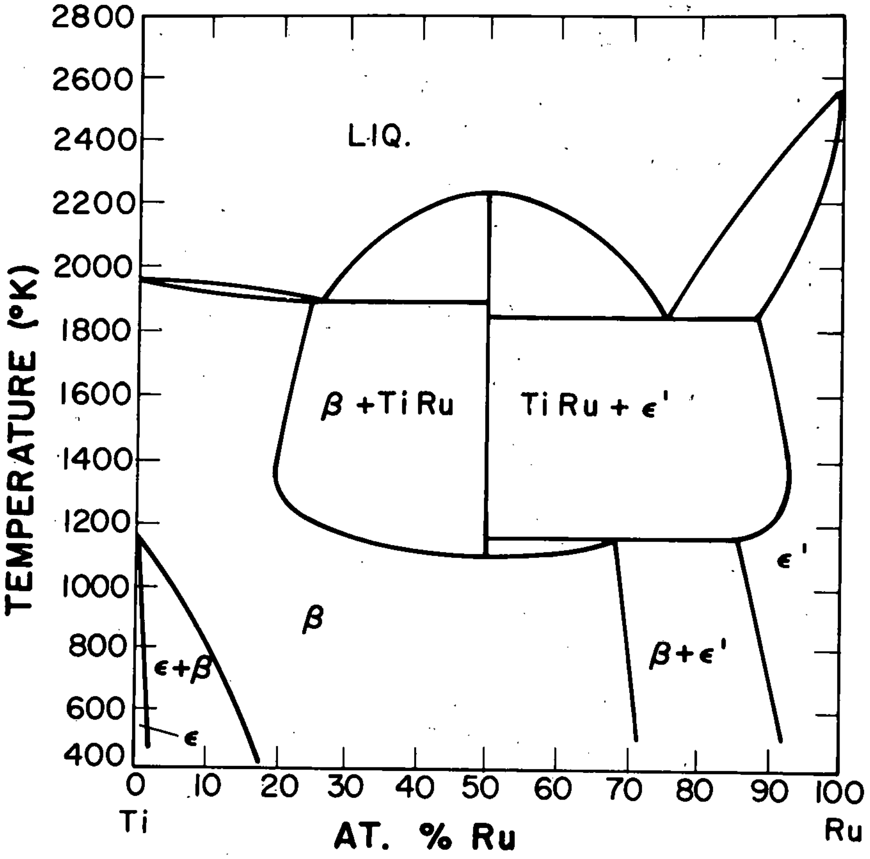

FIGURE 10. c) As 10b) for a dose rate of 10^{-7} dpa/sec.

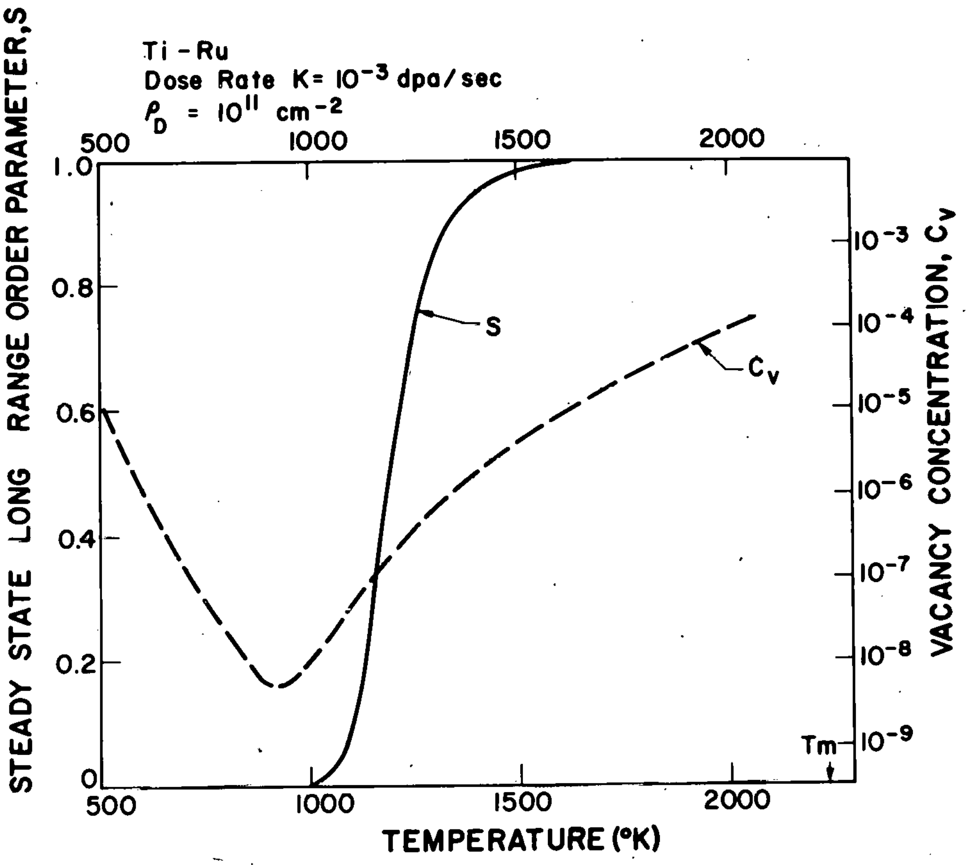

FIGURE 11. The variation of vacancy concentration C_v and order parameter S, in TiRu under a dose rate of k = 10^{-3} dpa/sec. Calculated using the data in Table 2 following the method of reference (24).

I. PROGRAM

Title: Mechanical Properties

Principle Investigator: R. H. Jones

Affiliation: Pacific Northwest Laboratory
Operated by Battelle Memorial Institute

II. OBJECTIVE

The purpose of this experiment was to determine a damage correlation parameter in metals irradiated with fusion energy neutrons and 16 MeV protons. The cluster density and yield strength increase of high purity nickel and niobium irradiated at 25°C with T(d, n) and Be(d, n) neutrons and 16 MeV protons were used to determine the correlation parameter.

III. RELEVANT DAFS PROGRAM PLAN TASK/SUBTASK

SUBTASK II.C.6.1	Effects of Damage Rate and Cascade Structure on Microstructure-Charged Particle/Neutron Correlations.
SUBTASK II.C.11.1 II.C.11.4	Effects of Cascades and Flux on Flow-Light Particle Irradiations and High Energy Neutron Irradiations.

IV. SUMMARY

The flow stress of T(d, n) and Be(d, n) neutron and 16 MeV proton irradiated nickel and niobium have been measured and found to have many similarities. Distinct hardening stages were observed in Be(d, n) neutron and 16 MeV proton irradiated niobium. The protons induced 1.6 times more hardening than the Be(d, n) neutrons in Stage I while the hardening rates were equal in the higher fluence stage. The hardening rate of T(d, n), Be(d, n) and 16 MeV proton irradiated nickel could be described by a single

relationship as a function of fluence. When the radiation induced hardening is compared on a damage energy basis using the damage energy cross-section for $T > 10$ keV the curves coincide exactly, but a shift occurs if the total cross-sections ($T > 0.01$ keV) are used.

V. ACCOMPLISHMENTS AND STATUS

Correlation of 16 MeV Protons with Fusion Neutrons - R. H. Jones (PNL)

Since last reporting on the correlation studies of 14 MeV neutron and 16 MeV proton damage in nickel and niobium, several irradiations have been completed which have helped elucidate the damage state. The most striking result is the observation of a hardening plateau in both the Be(d, n) neutron and 16 MeV proton irradiated niobium, as shown in Figure 1. The T(d, n) neutron irradiated niobium hardening shows a trend towards a plateau but more irradiations are needed to verify this. T(d, n) neutron irradiations to 3.5×10^{17} cm^{-2} and $\sim 2 \times 10^{18}$ cm^{-2} are complete and are being prepared for testing. A hardening plateau has been reported in fission neutron irradiated niobium by Loomis and Gerber,[1] so the present observation is not unique but is a confirmation that fusion energy neutrons do not induce a unique damage state.

The similarity in the hardening response of the 16 MeV proton and Be(d, n) neutron irradiated niobium suggests that they induce similar damage. The major difference in the response is in the initial hardening rate which corresponds to Stage I of Loomis and Gerber. The height of the plateau is a function of the hardening rate in Stage I. The hardening rate induced by protons and neutrons appears to be similar at the higher fluences which corresponds to Stage IV of Loomis and Gerber. They concluded that Stage I hardening is due to impurity atom-point defect complexes while Stage IV is due to defect clusters and dislocation loops. If the same hardening processes are operative in the 16 MeV proton and Be(d, n) neutron irradiated niobium, then the higher Stage I hardening rate of the protons could be explained by a softer PKA spectrum where a

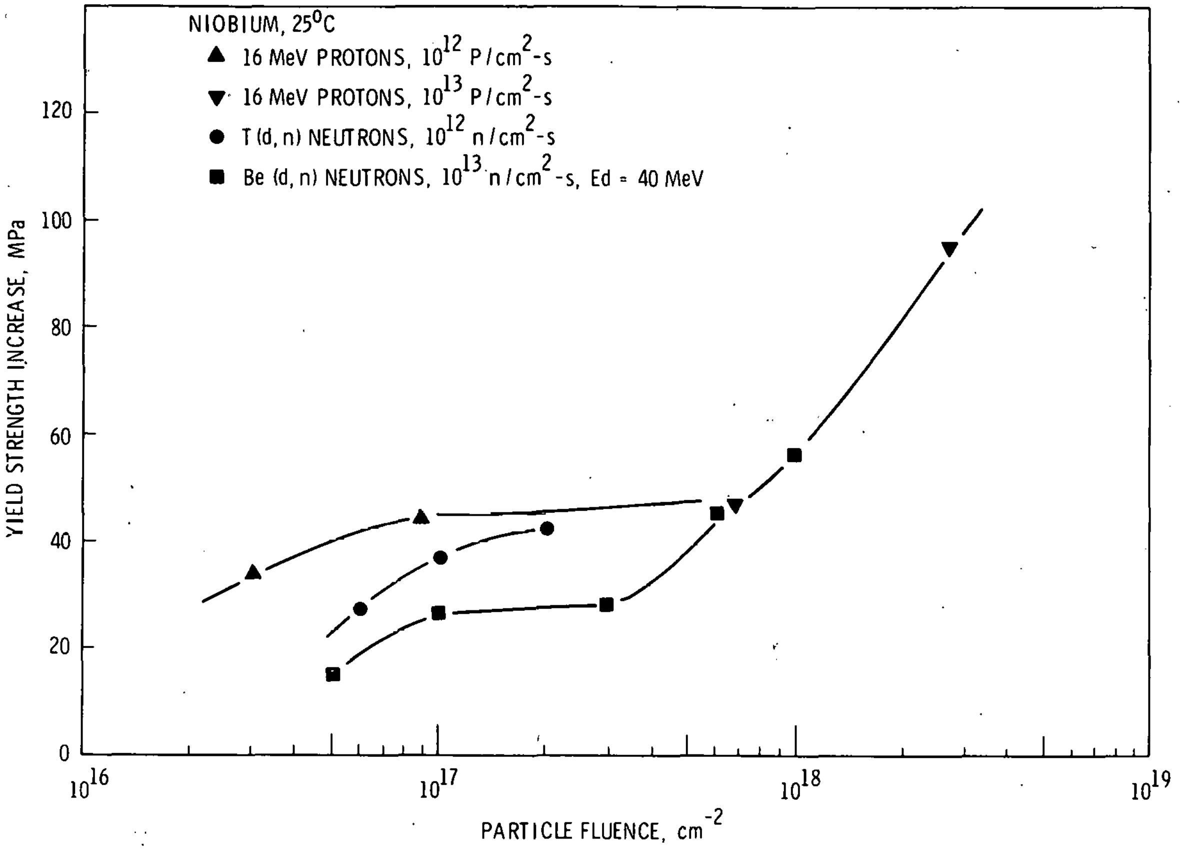

FIGURE 1. The Yield Strength Increase Versus Particle Fluence for Niobium.

larger fraction of the damage is in the form of simple point defect production. Using the yield strength increase of the plateau as a measure of the hardening rate, the 16 MeV protons induce 1.6 times more hardening than the Be(d, n) neutrons in Stage I. The 16 MeV protons and T(d, n) neutrons have similar hardening rates on this basis.

The similarity of the hardening rates in Stage IV suggests that the PKA spectrum are similar at higher energies. From the calculations of Omar et al.[2] and the results of Jones et al.[3] the damage energy cross-sections for 17 MeV protons and Be(d, n) neutrons (E_d = 40 MeV) on niobium are 723 b-keV (T > 0.01 kev) and 256 b-keV, respectively. The yield stress versus damage energy results shown in Figure 2 were calculated using these cross-sections. This figure compares the hardening response as a

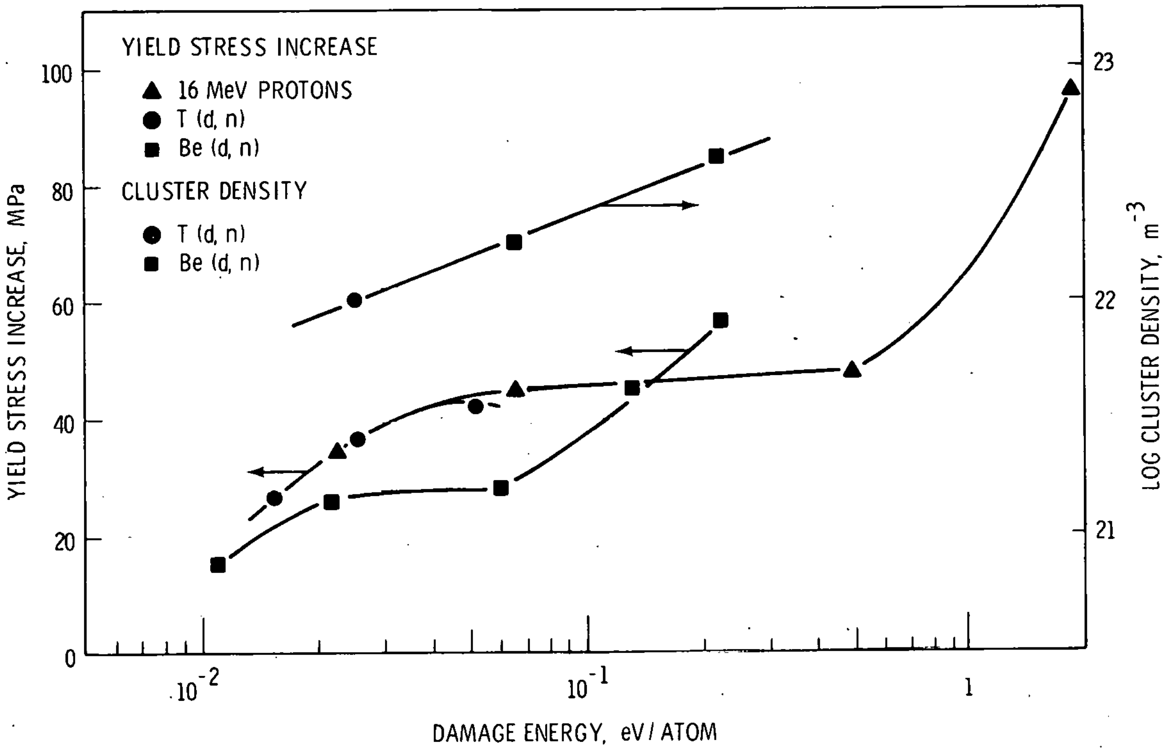

FIGURE 2. The Yield Strength Increase Versus Damage Energy for Niobium, 25°C.

function of the entire PKA spectrum but if the damage energy cross-sections for integration limits of T > 10keV were used, there would be little difference between the fluence and damage energy dependences. The damage energy cross-section for 17 MeV protons on niobium for integration limits of T > 10keV is 269 b-keV. The similarity in the damage energy cross-sections for energies > 10keV and the Stage IV hardening rates suggests that the Stage IV hardening mechanism is similar for niobium irradiated with Be(d, n) neutrons and 16 MeV protons.

The hardening rate of T(d, n), Be(d, n) and 16 MeV proton irradiated nickel can be described as a function of fluence by a single relationship as shown in Figure 3. Using damage energy cross-sections from Omar et al.[2] and Jones et al.[3] for nickel, the hardening response is shown as a function of damage energy in Figure 4. As was the case for niobium, the proton

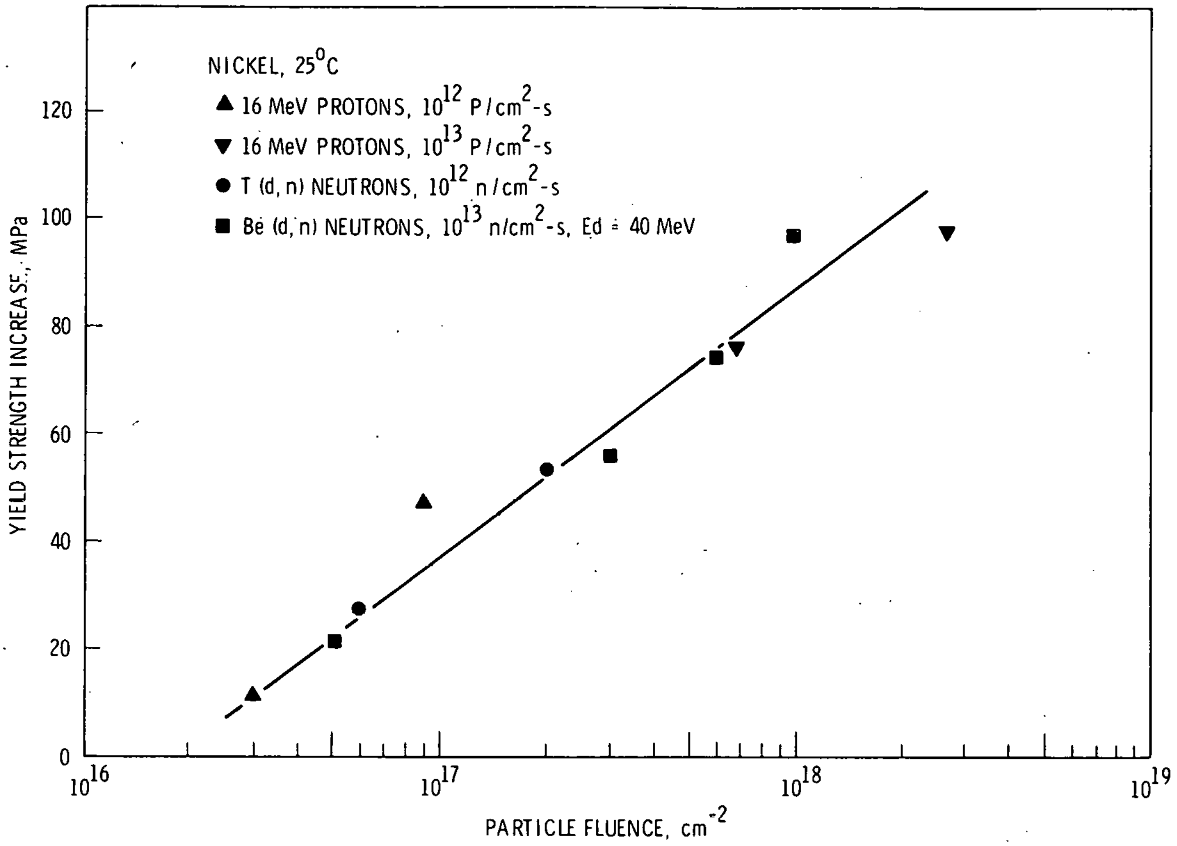

FIGURE 3. The Yield Strength Increase Versus Particle Fluence for Nickel

results for nickel are shifted to higher damage energies than the Be(d, n) neutron results. There would be little difference between the proton and Be(d, n) results if the cross-section for T > 10keV were used. The damage energy cross-section for 17 MeV protons on nickel with T > 10keV is 275 b-keV while the total cross-section for Be(d, n) neutrons on nickel is 295 b-keV. It is expected that the Be(d, n) cross-section changes very little for integration limits of T > 10keV and T > 0.01keV.

The similarity of the hardening rates and the damage energy cross-sections for T > 10keV suggest that the hardening mechanisms in Be(d, n) neutron and 16 MeV proton irradiated nickel is similar. These results are not too surprising since it is well known that the more complex defects produced by high energy cascades have a stronger interaction with dislocations than do point defects.

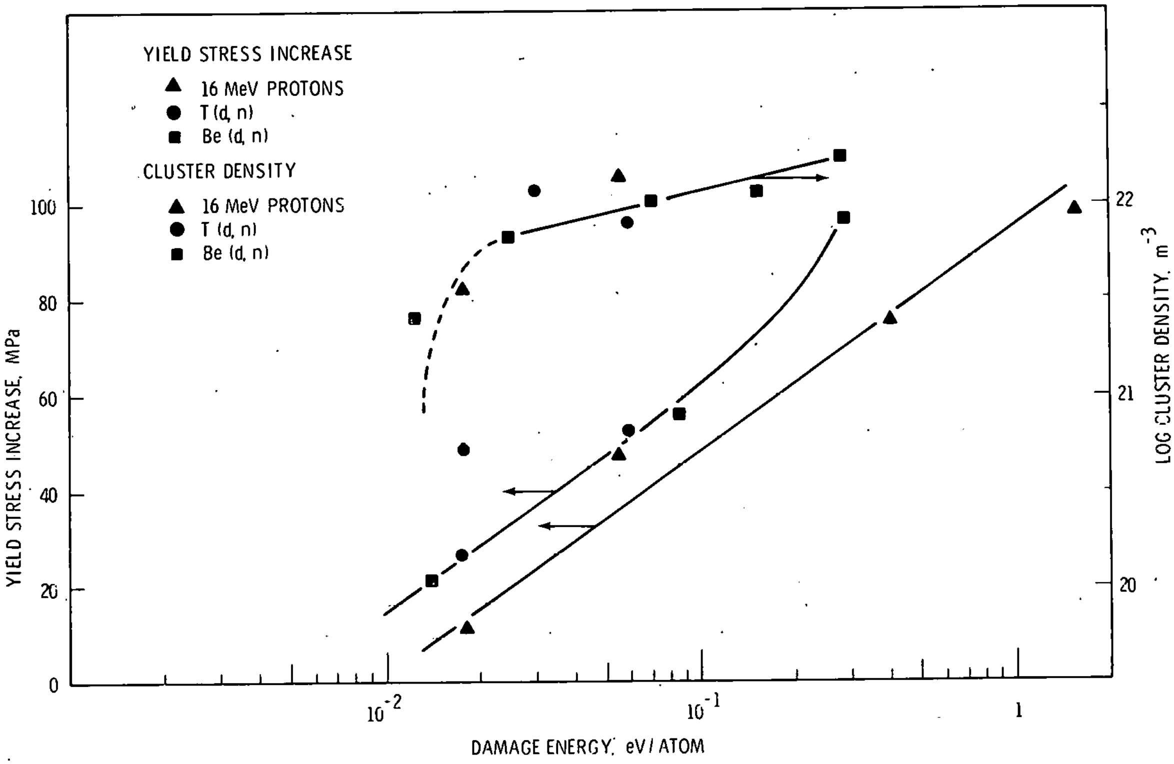

FIGURE 4. The Yield Strength Increase and Cluster Density Versus Damage Energy for Nickel, 25°C.

Serrated yielding was observed in nickel specimens irradiated to fluences greater than 3 x 10^{17} cm^{-2} with Be(d, n) neutrons and 16 MeV protons. The average load drop and plastic strain range for serrated yielding increases with increasing fluence. At a fluence of 10^{18} cm^{-2} the average load drop corresponds to a stress change of 14 MPa and persists to a strain of 0.008 while at a fluence of 3 x 10^{17} cm^{-2} these parameters were 8 MPa and 0.005, respectively.

VI. REFERENCES

1. B. A. Loomis and S. B. Gerber, Acta Met., 21, (1973), 165.
2. A. M. Omar, J. E. Robinson and D. A. Thompson, J. of Nucl. Matl., 64, (1977), 121.

3. R. H. Jones, D. L. Styris, E. R. Bradley, L. R. Greenwood and R. R. Heinrich, J. of Nucl. Mat., Proceedings of the First Topical Meeting on Fusion Reactor Materials.

VII. FUTURE WORK

No further proton irradiations are planned. T(d, n) neutron irradiations to 3.5 x 10^{17} cm^{-2} and ∿2 x 10^{18} cm^{-2} have been completed at the RTNS II source at LLL. Future RTNS II experiments are planned to determine the temperature dependence of the various hardening stages in niobium and to determine if similar stages are observed in vanadium and titanium. Also, an investigation of the role of oxygen in the radiation behavior of niobium, vanadium and titanium is being planned.

VIII. PUBLICATIONS

There were no publications for this task for April through July 1979.

I. PROGRAM

Title: Simulating the CTR Environment in the HVEM

Principal Investigators: W. A. Jesser, R. A. Johnson

Affiliation: University of Virginia

II. OBJECTIVE

The objective of this work is to investigate the influence of helium on fracture mechanisms and crack propagation in stainless steel.

III. RELEVANT DAFS PROGRAM TASK/SUBTASK

Subtask II.C.8.2 Post Irradiation Testing

Task II.C.13 Crack Initiation and Propagation

IV. SUMMARY

In-situ HVEM tensile tests of neutron irradiated type 304 stainless steel, unirradiated and helium irradiated type 316 stainless steel over a range of temperature from 25°C to 600°C showed that the nature of the crack propagation could be correlated with the nature of the failure mode. The angle defined by the crack edges at the tip of the crack tended to decrease as the brittle nature of the fracture increased. The width of the plastic zone at the crack flanks also tended to decrease as the brittle nature of the failure increased. In neutron irradiated samples increasing temperature increased the brittle nature of the failure. The same effect is true to a less extent in helium irradiated samples. In unirradiated samples decreasing the temperature increased the brittle nature of the failure. At 400°C neutron irradiated samples exhibited persistent slip on localized bands along which crack propagation subsequently occurred. Pronounced slip at the fracture surface was observed and revealed a channel fracture mechanism. All these results are consistent with failure behavior found in bulk samples.

V. ACCOMPLISHMENTS & STATUS

Effect of Temperature and Microstructure on Crack Propagation in Unirradiated and Irradiated Austenitic Stainless Steel.

J. A. Horton & W. A. Jesser, Department of Materials Science, University of Virginia, Charlottesville, Virginia

I. Introduction

A review of the fracture processes in austenitic stainless steel has been given by Bloom(1). The experimentally observed relationship among the variables stress (and thus strain rate), temperature and fracture mode is given schematically for unirradiated austenitic stainless steel as well as for neutron irradiated type 304 stainless steel. It is of interest, in the present case, to correlate the above fracture behavior, determined from neutron irradiated bulk samples, with crack propagation studies on microsamples of neutron irradiated type 304 stainless steel tensile tested in the HVEM. Further comparisons between unirradiated and helium irradiated type 316 stainless steel will be made with the case of neutron irradiated samples.

In the cases above of neutron irradiated bulk samples and microsamples the fracture behavior can be divided into the following three distinct types; ductile fracture, which is usually transgranular; brittle fracture, which is often intergranular; and a relative new fracture mode known as channel fracture(2), which follows preferred planes not along grain boundaries and is not observed in unirradiated samples. All of the above failure behavior has been reproduced in the HVEM tensile stage for neutron irradiated samples by selecting different test temperatures while maintaining roughly the same strain rate (and hence stress). The aim of the present study is to correlate the in-situ HVEM observations of crack propagation in unirradiated, neutron irradiated, and helium ion irradiated austenitic stainless steel microsamples with the failure behavior reported in the austenitic stainless steel literature for unirradiated and bulk neutron irradiated samples.

Crack propagation behavior will also be correlated with the appearance of the fracture surfaces obtained from the thick (~50μm) regions of the micro-tensile samples.

2. Experimental Details

Type 304 stainless steel microsamples were prepared from microsamples neutron irradiated in EBR-II at either 373°C to a fluence of 1×10^{23} n/cm^2 (> 0.1 MeV) or 442°C to a fluence of 6.5×10^{22} n/cm^2. The preparation and geometry of these samples, provided by J. O. Stiegler of ORNL, has been discussed previously(3).

Samples of type 316 stainless steel in the form of micro-tensile specimens were prepared to the same geometry as the above neutron irradiated samples. The type 316 stainless steel samples were either tensile tested in the unirradiated conditions or tensile tested after bombardment by 80keV helium ions. In all cases in-situ HVEM tensile tests were performed in a heating-tilt-tensile stage. The relevant sample and tensile test conditions are given in table I below. Further details of the helium irradiation conditions and resulting microstructure may be found elsewhere(4,5).

TABLE I HVEM TENSILE EXPERIMENTS

Exp #	Fig #		Irrad Temp °C	Flux (10^{14} cm^{-2} sec^{-1})	Fluence cm^{-2}	Test Temp °C	Microstructure	diameter	density (10^{13} cm^{-3})
3	5	neut	373		1×10^{23}	25	loops voids	<20nm <20nm	40 100
20	1	neut	373		1×10^{23}	25	loops voids	<20nm <20nm	40 100
11	8	He	600	3	3×10^{17}	25	loops	25nm	100
13		He	600	3	7×10^{17}	25	few bubbles	200nm	
17	7	He	600	20	2×10^{18}	25	bubbles	300nm	20
25	3,4	neut	373		1×10^{23}	400	loops voids	<20nm <20nm	40 100
5		neut	442		7×10^{22}	600	voids	300nm	10
10	2	neut	373		1×10^{23}	600	loops voids	<20nm <20nm	40 100
12		neut	373		1×10^{23}	600	loops voids	<20nm <20nm	40 100
16		He	600	9	5×10^{17}	600	few bubbles		
19		He	600	7	3×10^{18}	600	bubbles	300nm	3
24	6	He	600	1.5	3.6×10^{17}	600	bubbles	100nm	300

*All neutron irradiations are for type 304 stainless steel; other cases are for type 316 stainless steel.

3. Results

a. Fracture Characterization

In order to characterize the failure behavior of the microsamples, crack propagation behavior in the electron transparent (<0.5μm) regions of the sample was recorded and correlated with the appearance of the fracture surfaces obtained from the thick (~50μm) regions of the specimen. The crack was characterized in terms of two parameters: i) the projected angle of the crack edges measured at the crack tip and ii) the width of the plastic zone adjacent to the flanks of the crack. If the crack followed a grain boundary it is labelled (I), crossed a grain (T), and followed a narrow zone of plastic deformation (C). The fracture surfaces are designated as transgranular (T) when the typical appearance of dimples and rough surfaces are present; intergranular (I) when the smooth surfaces apparently following grain boundaries are present; and channel fracture (C) when the surfaces show pronounced slip steps and facetlike regions. The results of the measurements and observations are given in Table 2.

b. Effect of Temperature

It can be seen from the data of table 2 that in the unirradiated samples an increase in temperature is accompanied by an increase in the crack-tip angle as well as an increase in the width of the plastic zone associated with the crack flank. In the neutron irradiated samples an increase of temperature causes a decrease in the crack-tip angle and a decrease in the width of the plastic zone. These results for the neutron irradiated samples appear to be followed by

TABLE 2 CRACK TIP ANGLES & CRACK FLANK PLASTIC ZONE WIDTH

Exp #	Type Irradiation	Test Temp	Type Fracture	Type Crack	Crack Tip Angle degrees	Plastic Zone Width
	Unirradiated(316SS)	25	T	T	≈10	1µm
	Unirradiated(316SS)	600	T	T	20-30	>2µm
3,20	Neutron(304SS)	25	T	T	10-15	.1 to .3µm
25	Neutron(304SS)	400	C	C	5-10	.1 to .3µm
10,12	Neutron(304SS)	600	I	I	≈2	none evident
5	Neutron(with large voids)	600	T	T	≈20	.1µm
13	Helium(with bubbles)	25	T	T	≈17	1µm
19,24	Helium(with bubbles)	600	T	T	11-17	1µm
11	Helium(few bubbles)	25	T	T	≈10	.7µm

the helium irradiated samples. The plastic zone in the neutron irradiated samples appears more sharply defined than that of the helium irradiated samples.

The crack flanks of the neutron irradiated sample containing small voids (exp. 20) failed at room temperature in a ductile manner typical of that of unirradiated samples. This feature is manifested by the appearance of "teeth" caused by the shear processes localized to the thin ligaments at the crack flanks as is shown in fig. 1. Very similar micrographs have been obtained previously from tensile tests at room temperature of type 304 stainless steel$^{(6)}$. This crack appearance is to be compared to that obtained from tensile tests at 600°C which are narrow and follow grain boundaries (see Fig. 2). These cracks obviously are associated with intergranular fracture. The brittle appearance of the fracture surfaces from the thicker parts of the specimen supports this view.

At $400^{\circ}C$ the fracture occurs by a process known as channel fracture. The propagation of cracks proceeds in the following manner determined from dynamic observations during deformation. A slip band is created and persistent slip in this band continues until a crack is initiated and propagates along the narrow slip band. An example of this crack propagation in a channel is shown in fig. 3 for the case of neutron irradiated type 304 stainless steel (exp. 25). The fracture surface from the thick regions of the same sample exhibits pronounced slip along the (111) planes. This result is seen in figure 4. The exposed ledges are {111} planes as are the surfaces joining to form the pointed "roof-top" sections of the fracture surface. A similar behavior of crack propagation along a channel of plastic deformation has been observed in neutron irradiated samples which contain pre-existing slip bands and are deformed at room temperature. An example of this crack propagation is shown in fig. 5 which corresponds to experiment 3.

Another example of crack propagation along slip zones which are swept clean of defects is shown in fig. 6. Here the sample (experiment 24) was helium irradiated under stress to produce a population of bubbles with deformation induced bands free of bubbles. Crack propagation at $600^{\circ}C$ was along these bubble-free bands. Such bubble-free bands have been found adjacent to grain boundaries in some cases. (Fig. 7, exp. 17, shows a bubble-decorated grain boundary as well as several bubble-decorated incoherent twin boundaries. The zone free of bubbles does not extend along the entire boundary and is larger in the (110) grain than in the (103) grain.

A fracture surface from a helium irradiated specimen tensile tested at room temperature is shown in fig. 8, (exp. 11) to exhibit exaggerated slip similar to that observed in the case of neutron irradiated samples tested at 400°C. In the case of experiment 11 significant twinning was observed at the crack edge and may contribute to the morphological appearance of this fracture surface.

The serrated appearance of the fracture surface in the case of helium irradiated samples does not follow the same temperature dependence as that of the neutron irradiated samples which exhibit exaggerated slip only at intermediate temperatures of ~400°C.

c. Effect of Microstructure

From the data of table 2 a comparison of experiments 10, 12, and 5 shows that large voids (>30nm in diameter) in neutron irradiated samples cause the crack-tip angle and the width of the plastic zone to increase. This tendency is much less pronounced in the case of helium irradiated samples. A comparison of experiments 11 and 13 suggests that this trend is perhaps followed. The presence of large voids (or bubbles) apparently blunts the crack tip and promotes ductile fracture.

4. Discussion

The above results of crack-tip angle and width of the plastic zone adjacent to the crack flanks correlating with the ductile-brittle character of the failure are qualitative. Nevertheless they provide a useful means of studying the interactions between cracks and microstructure. The above correlation seems intuitively plausible and can be employed to better characterize such phenomena as channel fracture.

One of the first observations of localized slip bands serving as preferred regions for further slip has been provided about two decades ago(7,8). The mechanisms of the defect depletion in the slip band have been discussed in several review articles(9-11). Typically the defects eliminated from the channel are small dislocation loops and small point defect aggregates. In the classic picture of Fish et al.(2) channel failure is shown to affect a narrow region of sample without removing the voids from the channel. This result is consistent with the present HVEM observations; however there are cases in which channels have been created free of voids or bubbles. It is believed in the case of helium irradiations of microsamples that the action of localized slip during irradiation may give rise to bubble-free zones. This result is found even though examples of deformation assisted bubble growth have also been observed(5). It should be pointed out that while emphasis in this report is on crack propagation along narrow bands, many examples of crack propagation not restricted to a relatively straight path are also observed, but under other experimental conditions than the specialized ones which favor channel fracture.

The fracture surfaces show deep slip lines localized to a narrow region so that essentially single ledges of width 6μm are created corresponding to slip by over 20,000 dislocations in the same "channel". These fracture surfaces which show a series of the exaggerated slip lines are only observed in the neutron irradiated samples at intermediate temperatures (around 400°C) and suggest that the temperature of the tensile test is a critical variable. The detailed role of temperature is being explored. Perhaps during the tensile test subtle microstructural changes occur which favor channel formation.

5. Conclusions

In high fluence neutron irradiated type 304 stainless steel, unirradiated type 316 stainless steel and to a lesser extent in high fluence helium irradiated type 316 stainless steel, brittle cracks are associated with small crack-tip angles and small plastic zones at the crack flanks. Ductile cracks are associated with larger crack-tip angles and larger plastic zones than for brittle cracks.

In unirradiated type 316 stainless steel, increasing temperature causes wider plastic zones at the crack flanks and wider crack-tip angles. In irradiated samples decreasing temperature causes wider plastic zones and crack-tip angles.

The observation of slip band formation followed by crack propagation along the path of the slip band has been correlated with the appearance of exaggerated slip lines on fracture surfaces of neutron irradiated micro-tensile samples of type 304 stainless steel deformed at 400°C. This temperature is between the test temperatures of 25°C and 600°C for which ductile failure occurs in similar samples and conforms to the deformation behavior of similar bulk samples.

VI. Future Work

Similar HVEM tensile tests on heavy ion irradiated samples and RTNS-II irradiated samples are planned.

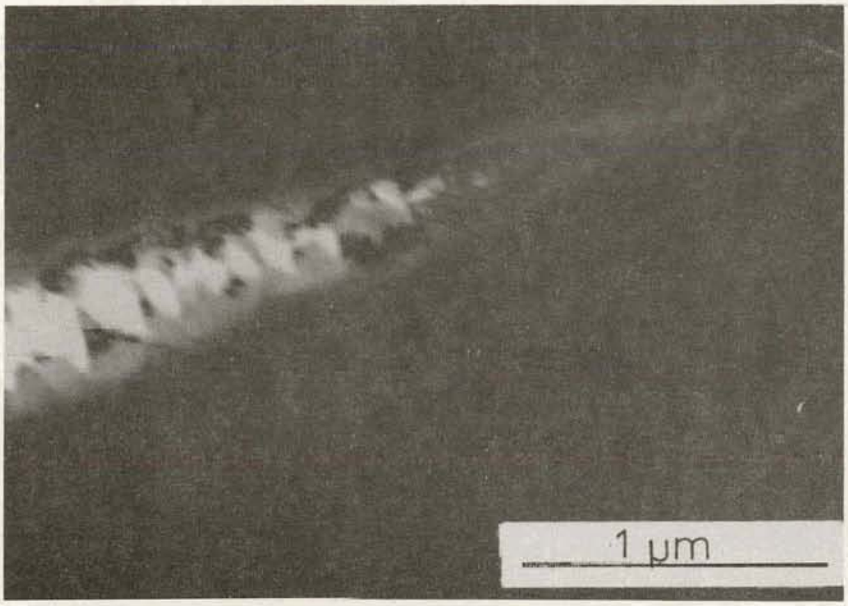

Fig. 1 HVEM micrograph (exp 20) of a neutron irradiated sample tensile tested at 25°C. Note the "teeth" in the plastic zone.

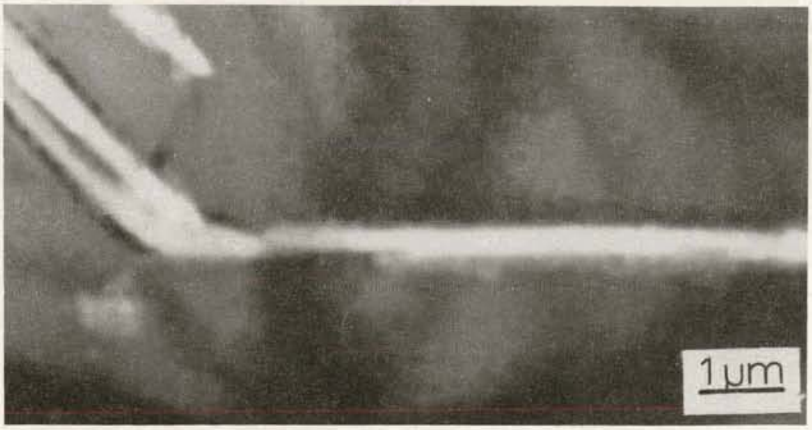

Fig. 2 HVEM micrograph (exp 10) of a neutron irradiated sample fracured at 600°C showing a much reduced plastic zone as compared to figure 1.

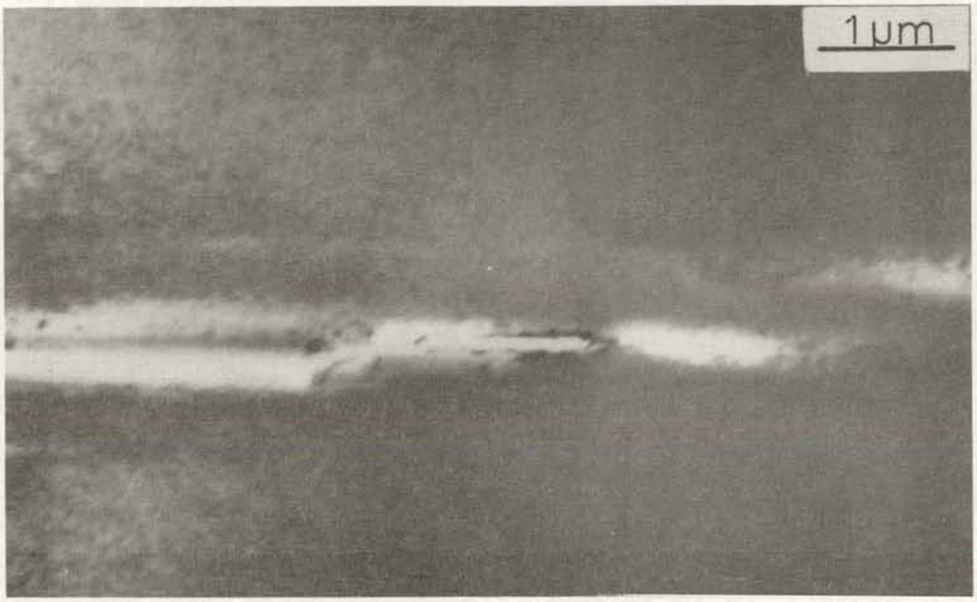

Fig. 3 HVEM micrograph (exp 25) of a neutron irradiated sample fractured at 400°C. Note that the crack is following a narrow slip band.

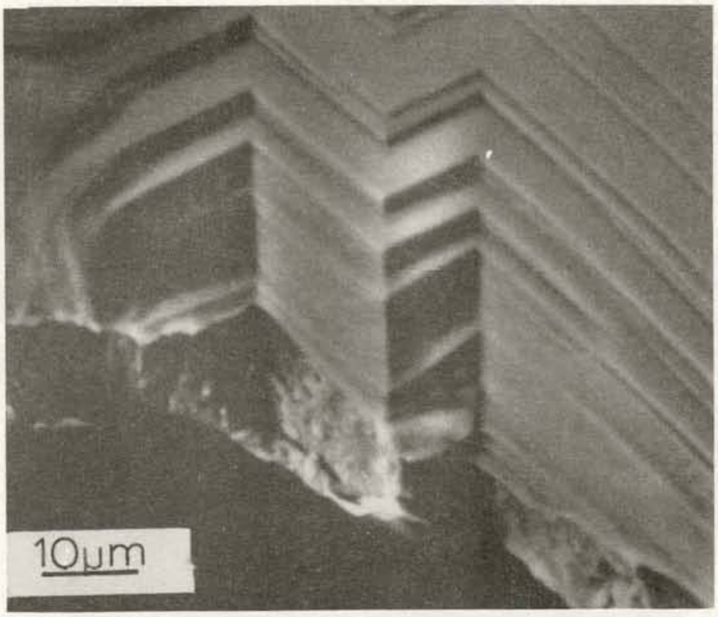

Fig. 4 SEM micrograph (exp 25) of the same sample as in figure 3 showing pronounced slip along the (111) planes. The exposed ledges are (111) planes as are the planes facing the front.

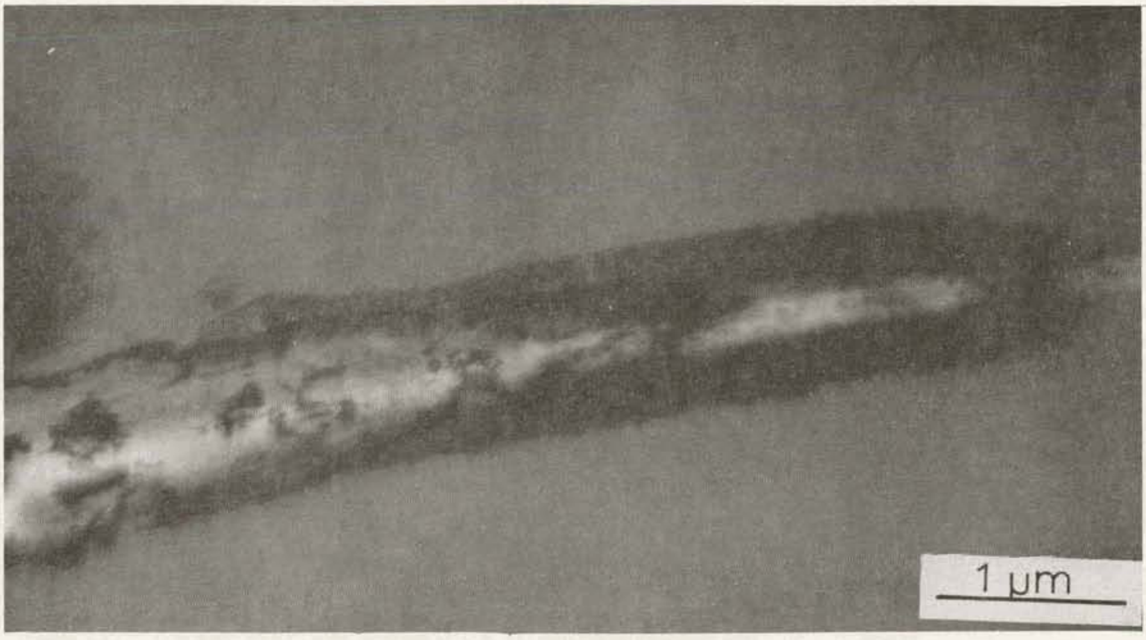

Fig. 5 HVEM micrograph (exp 3) of a neutron irradiated sample fractured at room temperature. The crack propagated along a pre-existing slip band.

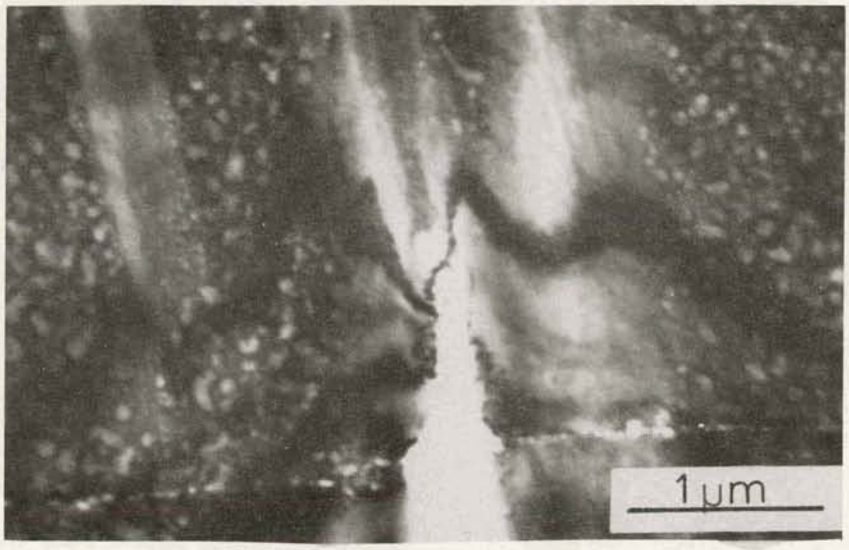

Fig. 6 HVEM micrograph (exp 24) of a helium ion irradiated sample fractured during irradiation at 600°C. Note the deformation induced bands that are kept free of bubbles. The crack propagated along one of these bands.

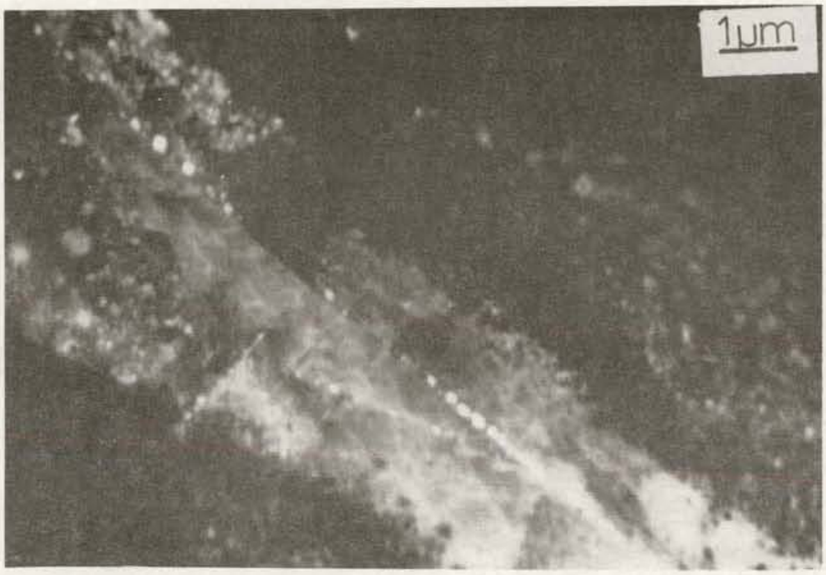

Fig. 7 HVEM micrograph (exp 17) of a helium ion irradiated sample fractured at 25°C. Note the bubble free band adjacent to the grain boundary and the bubble-decorated incoherent twin boundaries as well as a bubble-decorated grain boundary. The lower left grain has a (110) orientation (free surfaces). The upper right grain is (103).

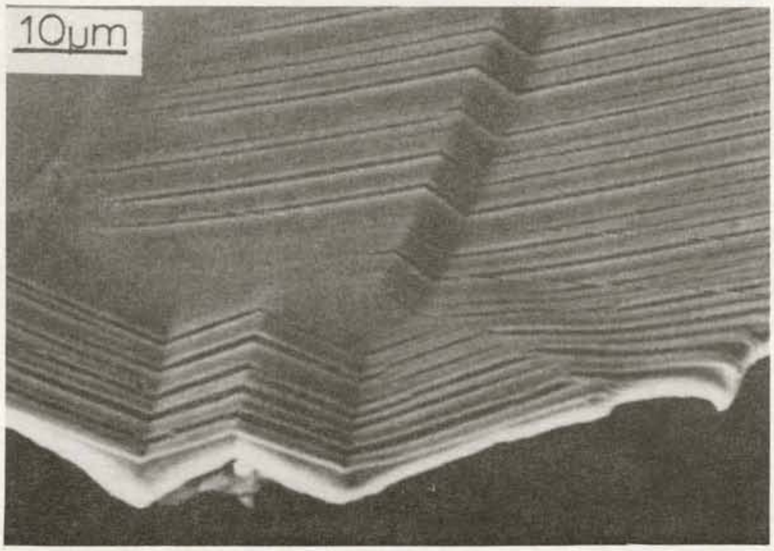

Fig. 8 SEM micrograph (exp 11) of a helium ion irradiated sample fractured at 25°C showing exaggerated slip similar to that of the neutron sample fractured at 400°C. Twinning was observed in the crack edge.

VII. REFERENCES

1. E. E. Bloom, "Irradiation Strengthening and Embrittlement," Radiation Damage in Metals, N. L. Peterson and S. D. Harkness, eds. American Society of Metals (1975) p. 295.

2. R. L. Fish, J. L. Straalsund, C. W. Hunter, and J. J. Holmes, "Swelling and Tensile Property Evaluations of High-Fluence EBR-II Thimbles," Effects of Radiation on Substructure and Mechanical Properties of Metals and Alloys, American Society for Testing and Materials STP 529 (1973) p. 149.

3. W. A. Jesser, J. A. Horton and J. I. Bennetch, "In-situ HVEM Tensile Tests of Irradiated and Unirradiated Stainless Steel," Damage Analysis and Fundamental Studies Report DOE/ET-0065/1 (1978) p. 205.

4. J. A. Horton, J. I. Bennetch and W. A. Jesser, "In-situ HVEM Fracture Studies of Helium Ion Irradiated Stainless Steel." First Topical Meeting on Fusion Reactor Materials to be published J. of Nuclear Materials.

5. J. I. Bennetch, M. L. Sattler, L. L. Schiestle Horton, J. A. Horton and W. A. Jesser, "HVEM Observation of In-situ He-Ion Bombardments." First Topical Meeting on Fusion Reactor Materials to be published J. of Nuclear Materials.

6. R. W. Bauer and H. G. F. Wilsdorf, "Void Initiation in Ductile Fracture," Scripta Met 7 (1973) p. 1213.

7. I. G. Greenfield and H. G. F. Wilsdorf, "Observations Concerning the Radiation Hardening in Copper and Nickel." Naturwiss. 47 (1960) p. 395; "Effect of Neutron Irradiation on the Plastic Deformation of Copper Single Crystals," J. Appl. Phys. 32(1961) p. 827.

8. H. G. F. Wilsdorf and D. Kuhlmann-Wilsdorf, "Considerations of the Interactions Between Thermal Vacancies and Dislocations," Phys. Rev. Letters 3(1959) p. 170.

9. D. Kuhlmann-Wilsdorf, R. Maddin, and H. G. F. Wilsdorf, "Point Defect Hardening in Face-Centered-Cubic Metals," Strengthening Mechanisms in Solids, J. J. Harwood, Coard., American Society of Metals, (1962) p. 137.

10. M. S. Wechsler, "Dislocations Channeling in Irradiated and Quenched Metals, *The Inhomogeniety of Plastic Deformation*, R. E. Reed-Hill, coord., American Society of Metals, (1971) p. 19.

11. M. S. Wechsler, "Radiation Embrittlement of Metals and Alloys," *Fundamental Aspects of Radiation Damage in Metals*, M. T. Robinson and F. W. Young, Jr. eds., U.S. NTIS, Springfield Va., CONF-751006-P2 (1975) p. 991.

I. PROGRAM

Title: Effects of Near Surface Damage and Helium on the Performance of the First Wall

Principal Investigator: O. K. Harling

Affiliation: Nuclear Reactor Laboratory, Massachusetts Institute of Technology

II. OBJECTIVE

The objective of this study is to understand and quantify the effects of near surface damage and implanted gas on the performance of the fusion reactor first wall.

III. RELEVANT DAFS PROGRAM TASK/SUBTASK

TASK	II.C.5	Effects of Cycling on Microstructure
	II.C.8	Effects of Helium and Displacement on Fracture
	II.C.12	Effects of Cycling on Flow and Fracture
	II.C.13	Effects of Helium and Displacement on Crack Initiation and Propagation
	II.C.15	Effects of Near Surface Damage on Fatigue

IV. SUMMARY

The in core cycling system has been shown to function as expected, with a full cycle time of 4 min. Premature failure of an irradiated specimen led to application of electron beam welding techniques for all future specimens. Accurate measurements and high magnification observations of the surface of highly radioactive specimens are possible with a just completed setup. The elastic behavior of the specimen has been characterized by finite element analysis. Safety related experiments showed that the use of much higher specimen pressures and thus thicker walls would be possible. Preparations for more irradiations are well advanced.

V. ACCOMPLISHMENTS AND STATUS -- H. Andresen (M.I.T./Hahn Meitner Inst.) G. Kohse, K. Kwok, A. Argon, O. Harling (M.I.T.)

1. In-Core Experiment

A description of the in core experiment has been given previously.(1) Irradiation of a pressurized capsule for about 20 reactor days showed that the system functions as expected. The sample was cycled between 350 and 550°C with a full cycle length of 4 minutes. Unfortunately the sample failed prematurely at a welded joint. Therefore, electron beam welding will be used for all future specimens.

A major difficulty of the experiment, namely intermittent specimen characterization with continuing irradiation has been resolved. A system has been completed, which allows accurate dimensional measurements of highly radioactive specimens together with optical observation of the surface at magnifications up to ∿1000 x. It consists of

a) a Nikon profile projector on which two precision translational stages and one rotational stage driven by step motors are mounted.

b) a Unitron microscope coupled to a TV camera, both of which are mounted on the stage of the profile projector.

The system is set up behind heavy shields near the hot cells in the MITR-II containment and all essential functions can be remotely operated. The hot specimens coming from the reactor can be inserted into a special precision holder mounted on the rotational stage which allows optical access to ∿80% of the sample surface.

This arrangement allows characterization of any asymmetries in the deformation of the samples in between irradiations as well as the detection of surface cracks, flaking and eventual blistering. Intermittent specimen characterization will probably be done on a biweekly basis. With this approach the failure of a sample after cycling it through its life in the reactor can be analyzed in much more detail than would be possible by a strictly post irradiation analysis.

2. Out-of-Core Experiments

A small vacuum furnace has been built, which allows annealing of samples up to 1300°C in an oil-free vacuum below 10^{-5} Torr. It is used for annealing of the samples before pressurization with a helium/argon mixture and for pure thermal creep measurements on some of the samples. These will help to sort out the influence of different experimental parameters in the in-core experiment. The same goal is pursued with the preparation of an experiment, which will simulate as accurately as possible the in-core experiment without the surface bombardment by α-particles and the fast neutron effects. A series of experiments has been performed which show that much higher pressures can be applied to the pressurized capsules in the in-core facility than the presently used allowed safety limit of $\sim$100 atm at 550°C. This allows thicker walls in the specimens at higher pressures without any risks to the reactor in the event of a rapid capsule failure.

3. Calculations and Theoretical Work

The geometry of the pressurized capsules used in the experiments is very simple. The tapered section (see Fig. 1) is designed mainly to provide a broad variation of the stress levels in different sections of one sample. In a relatively difficult scoping experiment like the present one it is important to limit the number of specimens. Since the stress level is very important for the mechanical behavior it was felt that simple analytic approximations are not sufficient for comparison of the experimental data with theory. Therefore finite element calculations were performed.

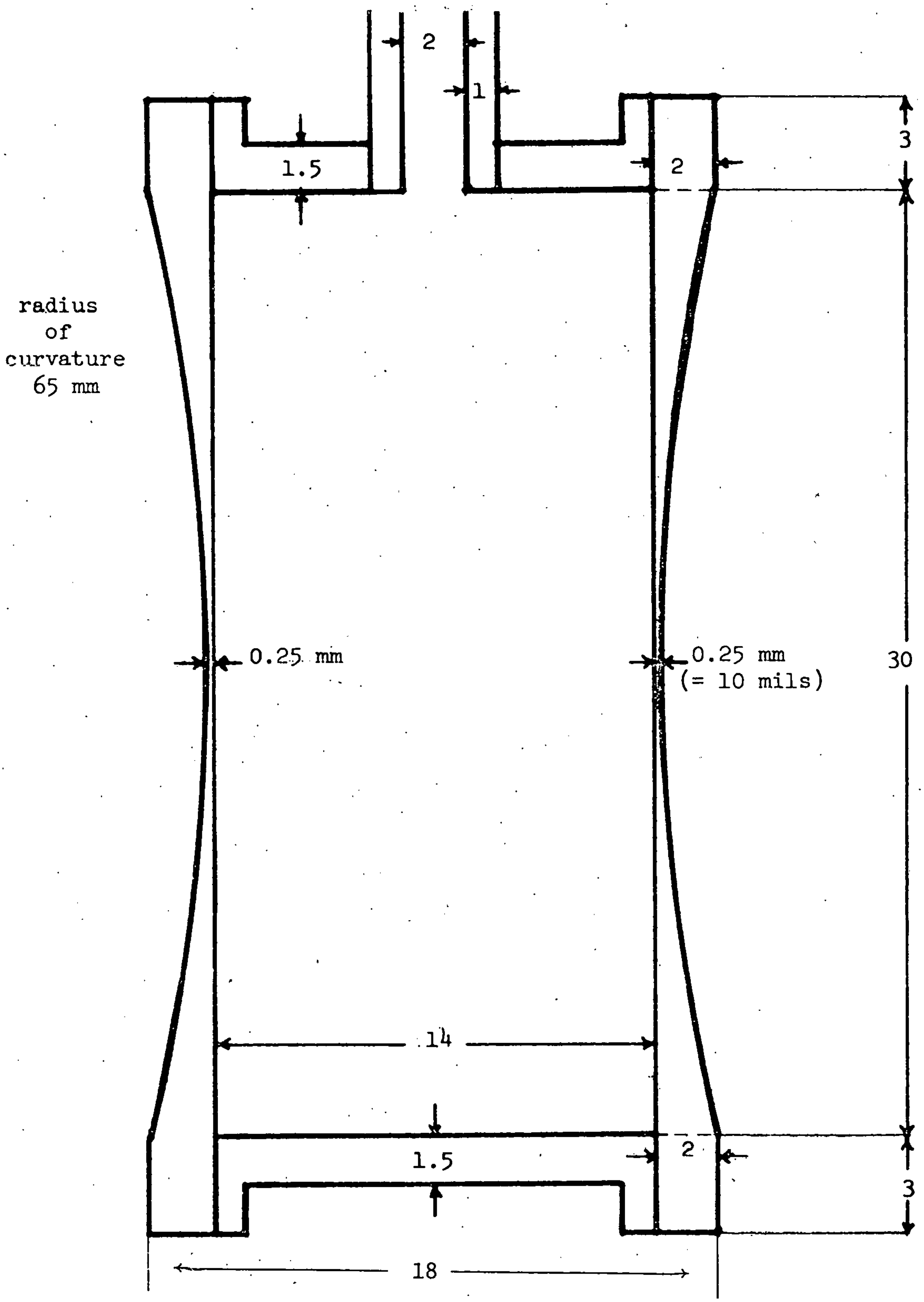

Figure 1. SAMPLE CAPSULE.

Stress distributions in the sample specimen of the fatigue cracking experiment were analyzed both by the finite element computer code, ADINA(3) (Automatic Dynamic Incremental Nonlinear Analysis), and by the thin wall approximation. The results are plotted in Fig. 2. Excellent agreement is found in the thin region of the sample, whereas only the finite element solutions provide adequate information about the coupling effects of the cap and shell. In this fatigue cracking experiment analysis, 96 eight-node elements were used as shown in Fig. 3. These solid elements are two-dimensional and axisymmetrical. Material properties were assumed to be linear-elastic at 450°C. A non-linear analysis with the same finite element mesh will be performed in the near future with the thermo-elastic plastic-creep material behavior and with the Von Mises yield criterion.

4. In-Reactor Tritium Trick

It has been shown that the tritium trick can be used for the simulation of helium buildup in fusion reactor walls made from materials with high hydrogen solubility. The related work has been presented at a conference and will be published in the Journal of Nuclear Materials.(2)

VI. REFERENCES

1. H. Andresen, O. K. Harling, "Effects of Near Surface Damage and Helium on the Performance of the First Wall," DAFS Quarterly Technical Progress Report, Oct. - Dec. 1978, DOE/ET-0065/4.

2. H. Andresen, O. K. Harling, "A New Approach to Synergistic Helium and Damage Simulation for Fusion Reactors -- In-Reactor Tritium Trick," presented at the First Topical Meeting on Fusion Reactor Materials, Miami, Fla., Jan. 29 - 31, 1979, to be published in the *Journal of Nuclear Materials*.

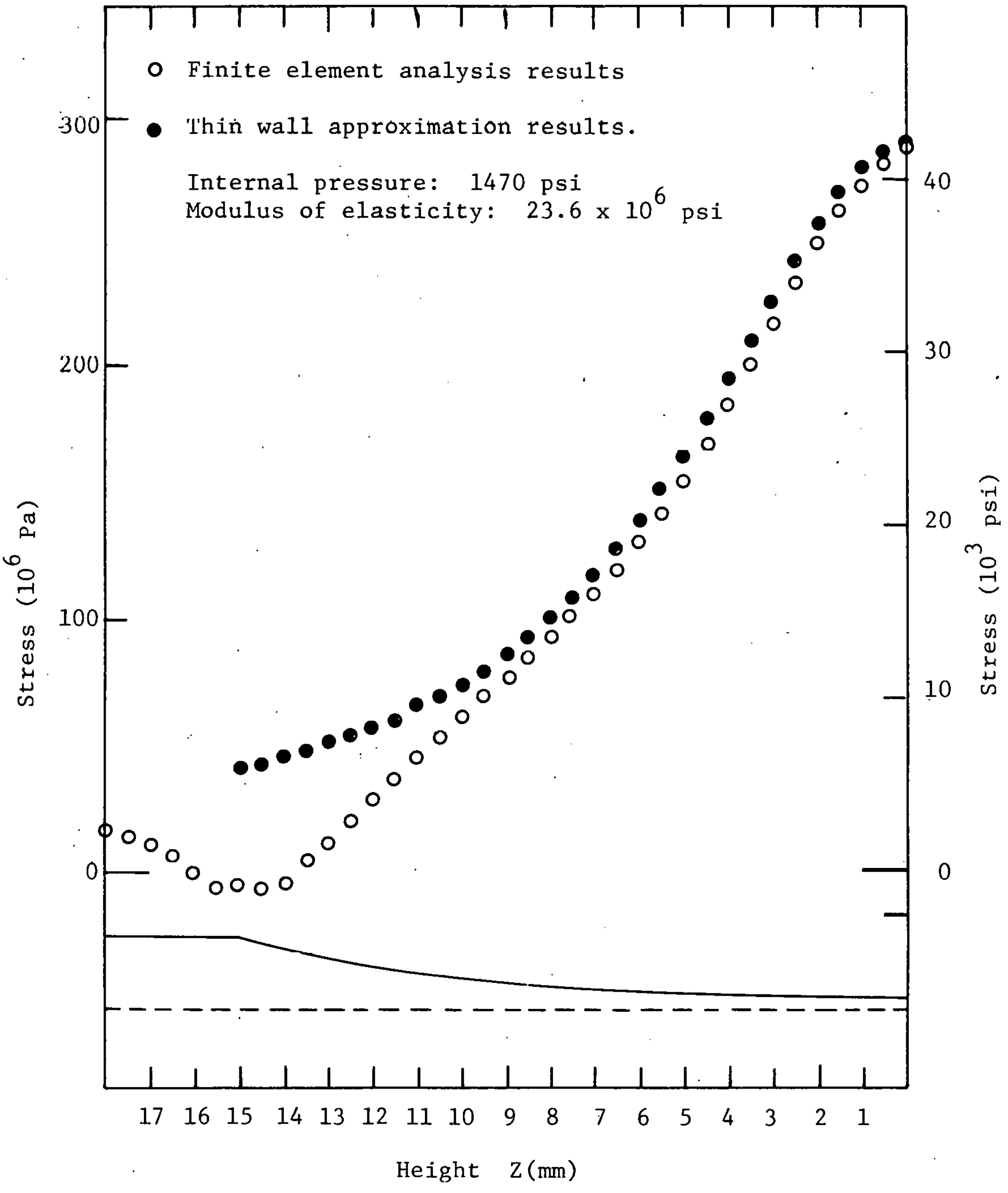

Figure 2. HOOP STRESS ON OUTER WALL OF FATIGUE CAPSULE.

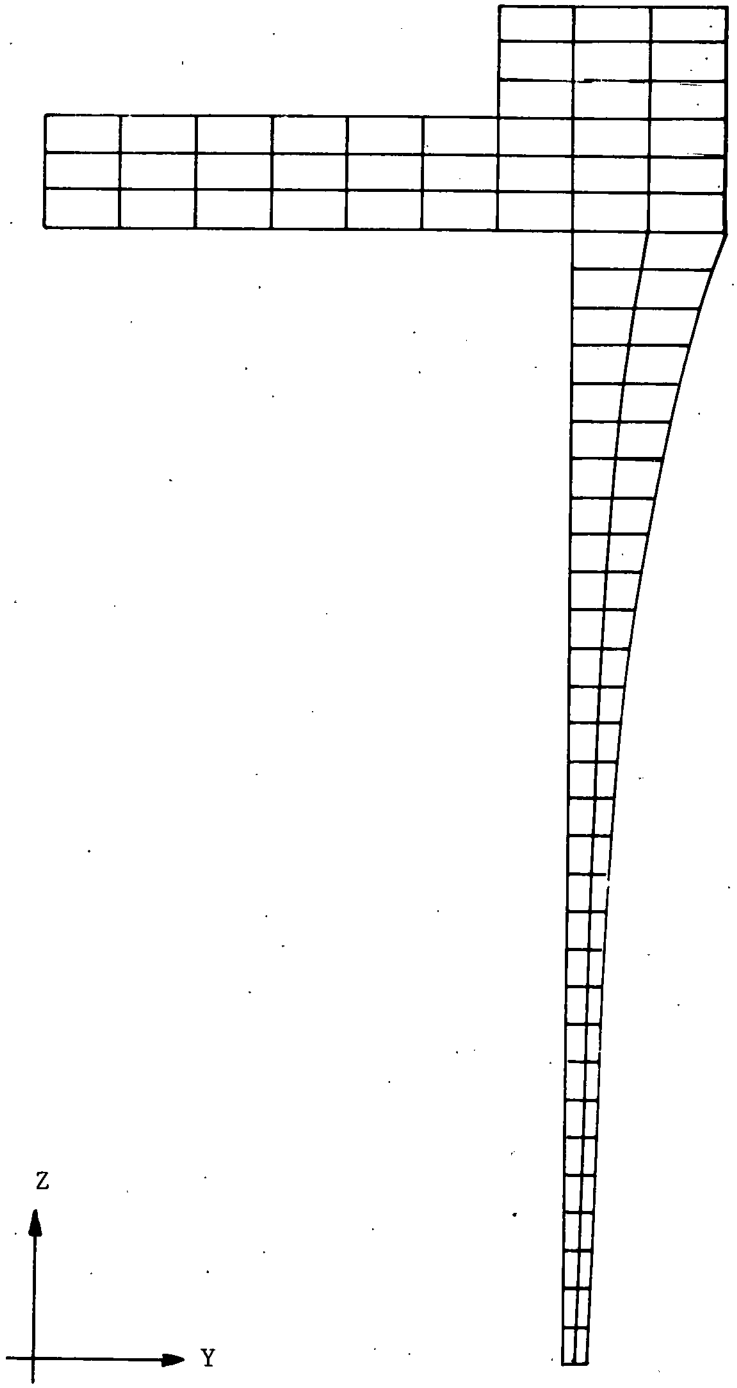

Figure 3. FINITE ELEMENT MESH.

3. Computer Code ADINA, developed at M. I. T. by Prof. K. J. Bathe. It is used for static and dynamic displacement and stress analysis of solid structures and fluid structure systems.

V. FUTURE WORK

Irradiations of specimens with accompanying characterizing measurements will continue through at least the next half year. Failed specimens will be dissected and carefully analyzed. Work on the out-of-core simulation experiment will be stepped up. The finite element calculations will be continued to include inelastic effects like thermal and irradiation creep.

I. PROGRAM

Title: Mechanical Properties
Principal Investigator: R. H. Jones
Affiliation: Pacific Northwest Laboratory

II. OBJECTIVE

1. Demonstrate a technique based on leak rate for generating low cycle fatigue data.

2. Compare the fatigue and stress rupture life data from a leak rate fatigue experiment to existing low cycle fatigue and stress rupture data from conventional tests.

3. Calculate the predicted leak rate from observed crack geometry and compare to the measured leak rate.

III. RELEVANT DAFS AND ADIP TASK/SUBTASK

II.C.8	Effects of Helium and Displacements on Fracture
II.C.9	Effects of Hydrogen on Fracture
II.C.12	Effects of Cycling on Flow and Fracture

IV. SUMMARY

Thin walled unirradiated 304 SS tubes have been cycled at 500°C at maximum tangential stresses ranging from 224 MPa to 348 MPa. The stress ratio, $\sigma_{min}/\sigma_{max}$ was +0.1 and the cycle frequency was 0.25 sec^{-1}. No indication of a leak was observed in 10^4 cycles at stresses below 286 MPa while a crack was developed in 4×10^3 cycles at this stress. This corresponds to 40 days for a tokamak with a 1000 second duty cycle. Life fraction analysis suggests that failure results primarily from the cyclic stress state.

V. ACCOMPLISHMENTS AND STATUS

A. Leak Rate Fatigue Experiment - S. M. Bruemmer and R. H. Jones (PNL)

1. Introduction

A tokamak vacuum first wall will be the primary boundary separating the magnetically confined plasma from the liquid or gaseius coolant. This primary boundary must maintain vacuum integrity under the radiation and chemical environment which will be agravated by cyclic stresses and temperatures accompanying the reactor burn-refueling cycle. A critical crack in this vacuum boundary can therefore be defined as one which allows the leakage of a critical quantity of coolant sufficient to contaminate the plasma to enter during the period of one burn cycle.

It is not possible at the present time to predict the lifetime of a vacuum first wall because the relationship between fatigue failure based on vacuum integrity and structural failure is unknown. A pressurized tube fatigue test which measures the leak rate of the pressurizing gas through the tube wall has been developed for the purpose of establishing such a relationship.

2. Experimental Apparatus

A schematic of the leak rate fatigue apparatus is shown in Figure 1. The specimen is a thin walled tube with one end plugged and a gas inlet tube welded into a plug at the other end for cyclic pressurization. The tube is positioned within an evacuated cyclinder and both internal and external pressures are continuously monitored. Temperature is measured from two thermocouples spot welded on the sample. The capabilities of the leak rate fatigue apparatus and several of the experimental specifics are listed in Table 1.

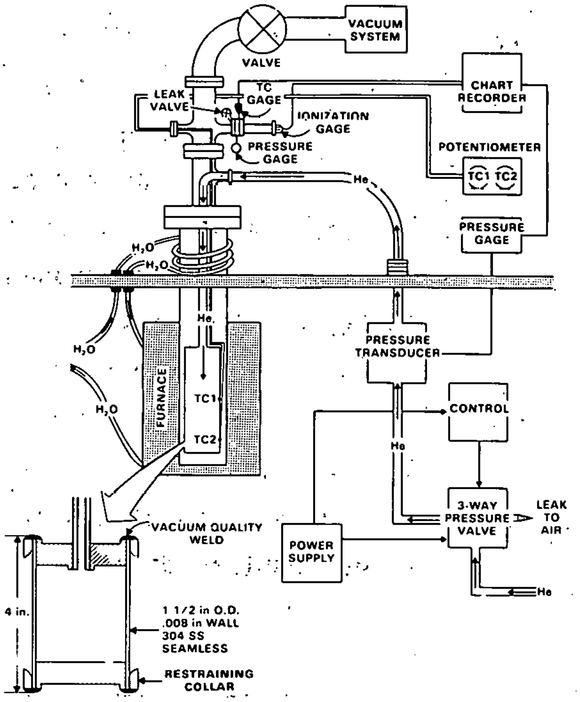

FIGURE 1. Leak Rate Fatigue Apparatus.

TABLE 1. Experimental Specifics

TEST MATERIAL	304 SS
MATERIAL CONDITION	ANNEALED 1000°C/1hr
INTERNAL PRESSURIZATION CAPABILITY	0-600 psi
EXTERNAL VACUUM	1×10^{-7}
CYCLE GAS	HELIUM
TEMPERATURE CAPABILITY	1000°C
TEST TEMPERATURE	500°C
TUBE WALL THICKNESS	0.008 in
CYCLE FREQUENCY	0.25 sec^{-1}
STRESS RATIO, $\sigma_{min}/\sigma_{max}$	0.1

The approximately saw tooth type stress-time profile is shown in Figure 2. In order to compare this cyclic loading to static stress rupture data, a conservative time at stress during each cycle has been estimated. For this simple analysis, it is assumed that the relevant portion of the cycle is the time at stresses between 70-100% of the maximum. It can be seen from stress rupture data$^{(1)}$ that reducing the stress level at any point on the stress versus time curve by 30%, increases the time to failure by greater than an order of magnitude. Thus any time during our cycle when the stress is below this level is believed to be insignificant. Instead of obtaining an average stress from this upper 30%, the maximum stress has been used in the life fraction calculations; hence it is assumed that the results will be biased high and can be considered maximum values for comparison with uniaxial stress rupture data.

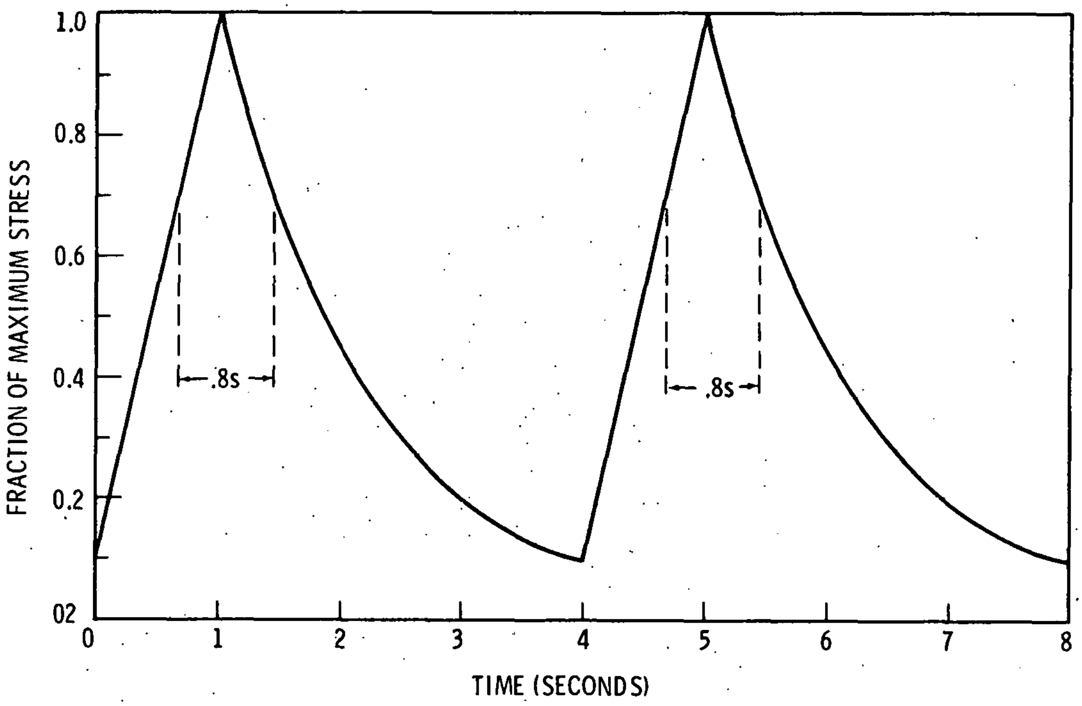

FIGURE 2. Pressurization Cycle and Time at Stress Approximation.

3. Leak Rate Fatigue Tests

3.1 Data Comparison: Experiment versus Literature

The internal pressurization of the test cylinder causes a biaxial state of stress with longitudinal and transverse stress components. In the low cycle fatigue regime in which these tests were conducted, it is believed that failure will be governed by the maximum shear stress, τ_{max}. Therefore, the comparison shown in Figure 3 considers only the relationship between τ_{max} and the number of cycles to failure for the low cycle fatigue case. The same is true in Figure 4 where τ_{max} is related to the time to failure.

In order to achieve failures in reasonable times, the stress level was stepped to higher levels during each test. The normal number of cycles at a particular stress level ranged from 1×10^3 to 2×10^4 cycles. Miner's summation rule(2) was employed to give an estimate of the life fraction, which is plotted in Figures 3 and 4. Thus, the steps shown for each test represent the damage fraction at each stress, not the actual number of cycles or time at stress. Only one of the four tests was found to fail as a result of a leak, the others exhibited rupture. However, using the life fraction calculations considerably more damage is observed when comparing the results to low cycle fatigue data (Figure 3). Even using the maximized time at stress, the cumulative damage reaches less than 3% of the uniaxial stress rupture data. In the fatigue comparison, the analysis indicates the life fraction at failure in one test to be over 60%. It is important to note that the uniaxial fatigue and stress rupture curves overpredict the data from these biaxial tests. This suggests that failure in such a biaxially loaded system may occur well before predictions using data from conventional tests. However, the maximum tensile stress levels employed in these tests are a factor of 1.3 to 1.6 times the yield stress for 304SS at 500°C and significantly higher than would be anticipated in service.

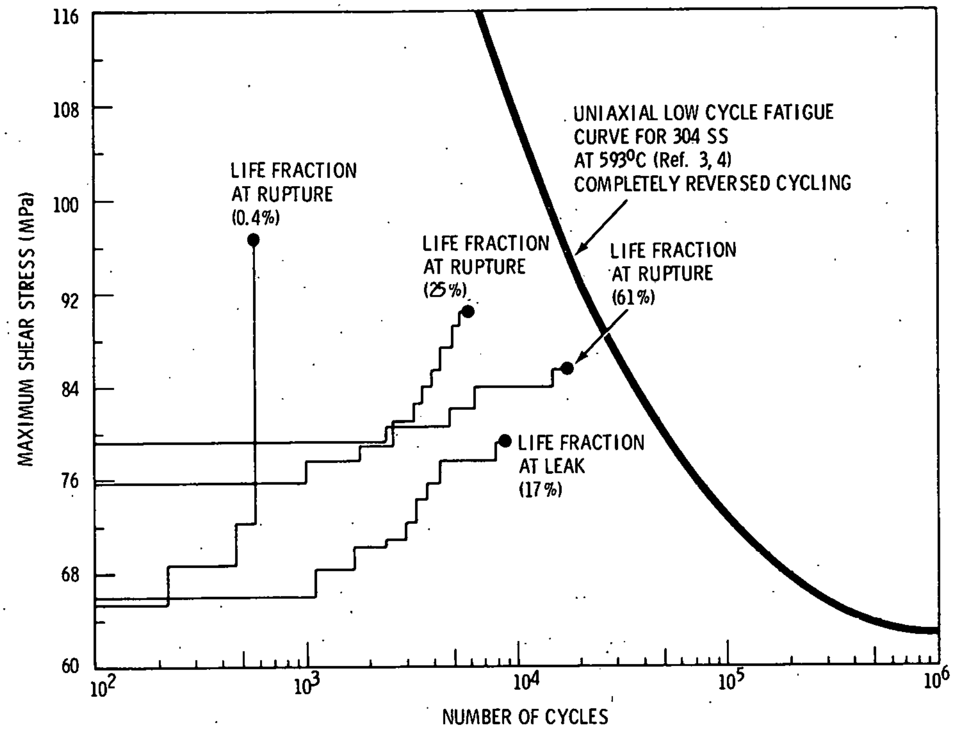

FIGURE 3. Comparison of Published Uniaxial Low Cycle Fatigue Data and Data from Leak-Rate Fatigue Experiment for 304 SS.

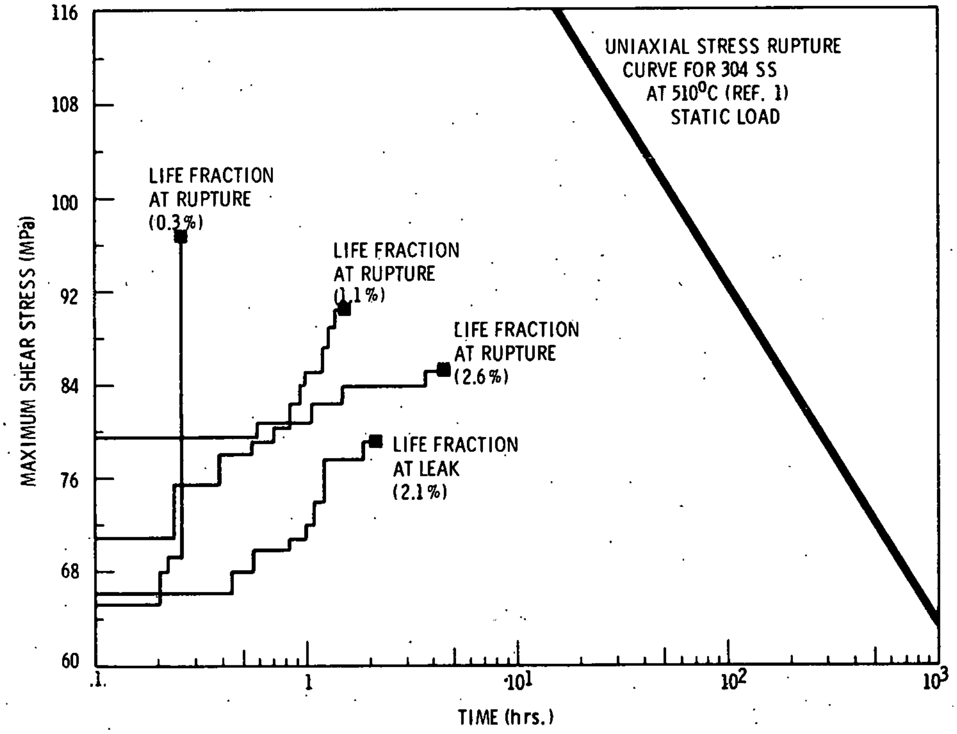

FIGURE 4. Comparison of Published Uniaxial Stress Rupture Data and Data from Leak-Rate Fatigue Experiment for 304 SS.

A definite conclusion regarding a difference between the leak rate fatigue life and structural fatigue life of a material is not possible with the present data because the samples failed by rupture and not by the formation of a slowly propagating crack. Tests at lower stresses and hence at higher cycles are needed to achieve slower crack growth rates. This will be accomplished by automating the fatigue apparatus to make higher cycle tests more practical.

3.2 Leak Rate Calculations

The leak rate of helium as a function of crack geometry has been estimated from equations for the flow of gases through orifices. The analysis was carried out for both viscous flow where the mean free path of the gas is controlled by intermolecular collisions and for molecular flow where the mean free path is controlled by the crack walls. Viscous flow will predominate on the coolant side of the wall while molecular flow may occur at the vacuum side of the crack; however, it is expected that viscous flow will dominate the leak rate of helium through a crack in the vacuum wall.

A critical leak for a tokamak reactor has been arbitrarily taken as that which allows the helium concentration in the plasma to equal the deuterium and tritium concentration in a 5000 second burn period. For viscous conditions, the resulting critical crack is 0.0254 cm x 0.00254 cm. This is a very small crack which may form readily under cyclic stress or temperature conditions and will also be difficult to detect for repair work.

This analysis can be seen to give a reasonable prediction of leak rate if the crack size is known in Figure 5. A sample with a small leak was removed and the crack dimensions measured at room temperature and pressure. Using this crack size the predicted leak rate was within an order of magnitude of the measured leak rate.

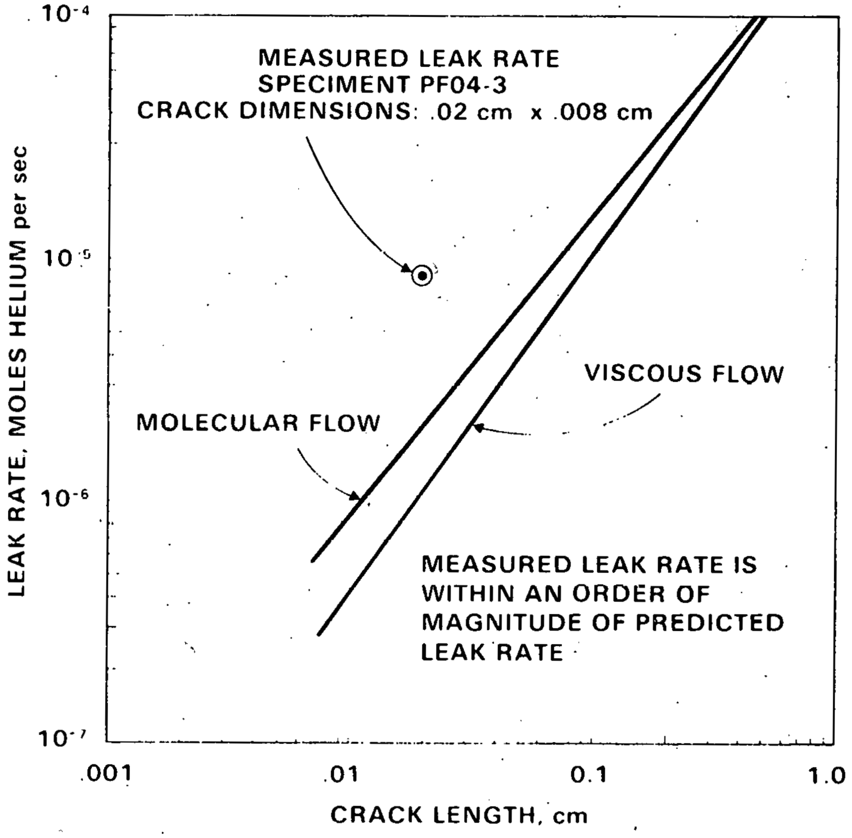

FIGURE 5. Helium Leak Rate Calculation for a Crack of Constant Width of 0.008 cm.

VI. REFERENCES

1. R. W. Swindeman, Structural Materials for Service at Elevated Temperatures, ASME MPC-1, 1975, Houston, Texas, p. 1.
2. N. H. Polakowski and E. J. Ripling, Strength and Structure of Engineering Materials, 1966, Prentice-Hall, Inc., New Jersey, p. 511.
3. R. W. Weeks, D. R. Diereka and C. F. Cheng, ANL-8009, November 1973.
4. C. R. Brinkman, et al., ANCR-1097, May 1973.

VIII. FUTURE WORK

The leak rate fatigue apparatus will be modified to make higher cycle tests more practical. Tests up to 5×10^5 cycles are needed to obtain a valid leak rate fatigue criteria.

I. PROGRAM

Title: Effects of Irradiation on Fusion Reactor Materials
Principal Investigator: F. V. Nolfi, Jr.
Affiliation: Argonne National Laboratory

II. OBJECTIVE

The objective of the work is to establish the effects of flux, stress alloying elements on the creep-deformation behavior of various classes of candidate MFR materials during light-ion irradiation.

III. RELEVANT DAFS PROGRAM PLAN TASK/SUBTASK

SUBTASK II.C.11.1 Light Particle Irradiations

IV. SUMMARY

Torsional creep-rate measurements were made on wire specimens of pure nickel and nickel - 4 at. % silicon alloy. At 350°C, irradiation is found to produce a greater enhancement of the creep-rate in pure nickel than in the alloy when stress levels are chosen to make the thermal creep-rates equal before irradiation. Comparison of preirradiation and postirradiation data shows considerable irradiation hardening in the alloy. Since no hardening is observed in the pure metal for the doses investigated, the hardening may be associated with radiation-induced segregation (RIS) and concomitant precipitation/decoration of Frank loops.

V. ACCOMPLISHMENTS AND STATUS

A. Radiation Induced Segregation and Irradiation Creep -- V. K. Sethi and R. Scholz

During measurements of irradiation creep on solution annealed and aged

Type 316 stainless steel (MHE Ht. # 15893), it was found that displacement-producing radiation consistently caused the sample to creep against the applied stress(1). This anamolous behavior is attributed to either modulus changes caused by irradiation enhanced precipitation in the metastable solution annealed Type 316 stainless steel, or dimensional changes caused by precipitation and/or swelling. In addition, this alloy is known to exhibit considerable radiation induced segregation (RIS) of both major and minor alloying elements during heavy-ion irradiation(2).

This report deals with experiments designed to determine the effect of RIS on creep deformation in a model system (Ni - 4 at. % Si), with a composition such that no second phase exists in the absence of irradiation. The alloy was chosen because it simulates the solution hardening present in stainless steel and because RIS and precipitation does occur in the alloy.

High purity nickel and nickel - 4 at. % silicon alloy were processed into 10 cm long, 0.075 cm diameter wires. The nickel wires were annealed at 700°C for 10 minutes, and the nickel - 4 at. % silicon wires were annealed at 815°C for 2 h in an inert environment. The heat treatments were selected to give comparable grain sizes in the two materials. The creep specimens were fabricated from these wires by electropolishing a reduced section (∿0.013 cm diameter and 0.65 cm long). A typical specimen fabricated in this fashion contains at least 10 grains across the diameter.

Creep measurements were made in the Torsional Creep Apparatus(3) at 350°C. A 21 MeV deuteron beam was used for irradiation experiments at a dose rate of $\sim 2 \times 10^{-6}$ dpa $\cdot$ s^{-1}. Preirradiation and postirradiation measurements were made to assess whether irradiation produced significant changes in the structure of the material.

The preirradiation and postirradiation data for the two materials are shown in Figs. 1-5. The main features of the data are:

1. Comparison of the data illustrated in fig. 1 reveals that in pure nickel, for the small doses involved in these tests (∿0.075 dpa), there are no large scale, irradiation-induced microstructural changes.

2. Figures 2 and 3 show the preirradiation and postirradiation deformation behavior of nickel - 4 at. % silicon alloy. The alloy exhibits considerable irradiation hardening. Since no such hardening is observed in pure nickel, it is likely that the effect is associated with RIS of silicon to internal immobile sinks, the hardening mechanism being precipitate/decorated loop intersection.

3. The stress and temperature dependence of the creep-rate of nickel - 4 at. % silicon for preirradiation and postirradiation conditions are shown in figs. 4 and 5 respectively. The stress exponent for creep of the alloy is essentially unchanged, and, similarly, the activation energy is unaffected by irradiation at least at lower temperatures. This observation suggests that the thermally activated process is the same for preirradiation and postirradiation conditions below about 400^{0}C. Thus, the irradiation induced hardening is athermal in nature.

Figure 6 shows the strain-time curves for nickel and nickel - 4 at. % silicon during 21 MeV deuteron irradiation. As illustrated by the accompanying thermal creep curves the stress levels for the two materials were chosen so as to approximately match the preirradiation thermal creep behavior. Some of the important features of the data are:

1. Irradiation enhancement of the creep-rate of pure nickel was by a factor ∿13, while the enhancement for nickel - 4 at. % silicon was ∿5 for the irradiated alloy, and ∿20 after alloy was irradiated to ∿0.075 dpa at a dose rate of 2×10^{-6} dpa · s^{-1}. Thus, irradiation hardening reduces the thermal creep rate of the alloy by a factor of ∿4.

2. Nickel appears to show a linear flux dependence, although this has to be explored further.

VI. REFERENCES

1. V. K. Sethi and F. V. Nolfi, Jr., DAFS Quarterly Progress Report for Period Ending December 31, 1978, p. 202.

2. V. K. Sethi and F. V. Nolfi, Jr., DAFS Quarterly Progress Report for Period Ending December 31, 1978, p. 103.

3. V. K. Sethi, A. P. L. Turner and F. V. Nolfi, Jr., DAFS Quarterly Progress Report for Period Ending September 30, 1978, p. 192.

VII. FUTURE WORK

Microstructural examination of irradiated nickel - 4 at. % silicon will be performed to determine the precipitate and dislocation structures. The temperature, stress and flux dependencies of irradiation creep in both nickel and nickel - 4 at. % silicon alloy will be determined.

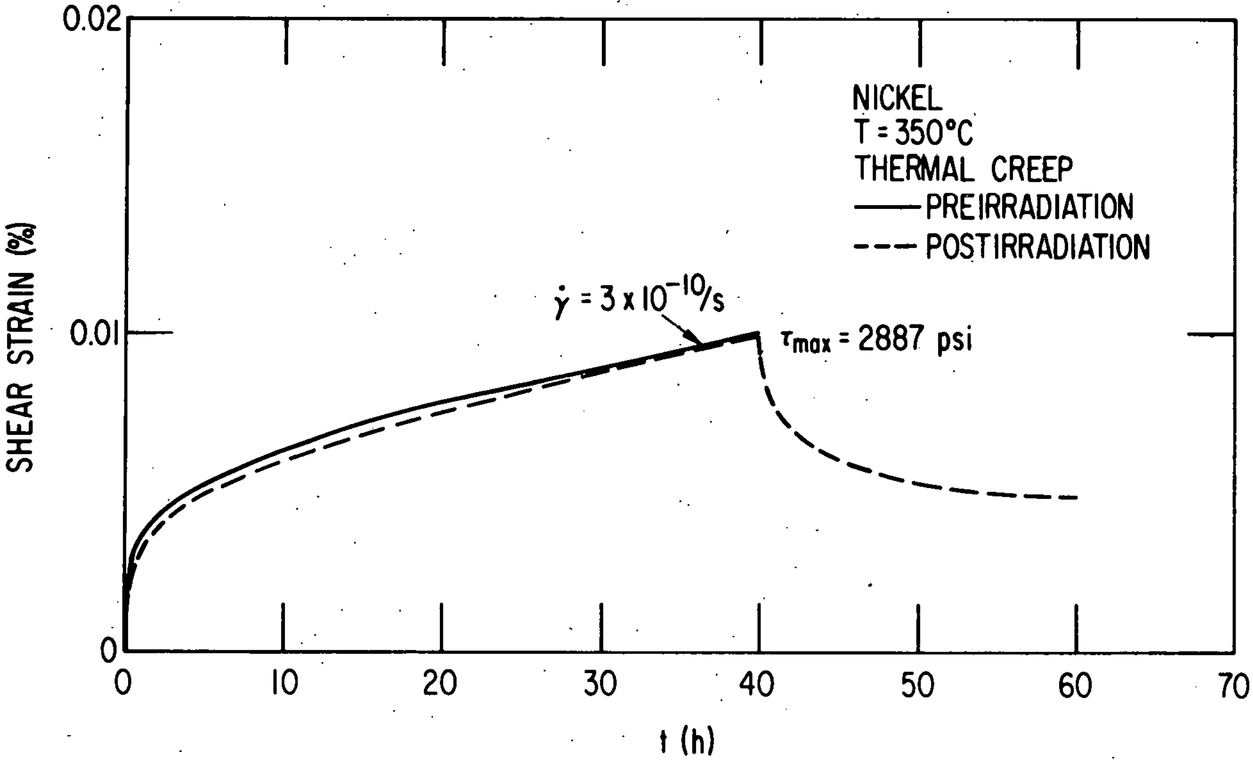

Figure 1. Comparison of the strain-time behavior of pure nickel in pre- & postirradiation conditions.

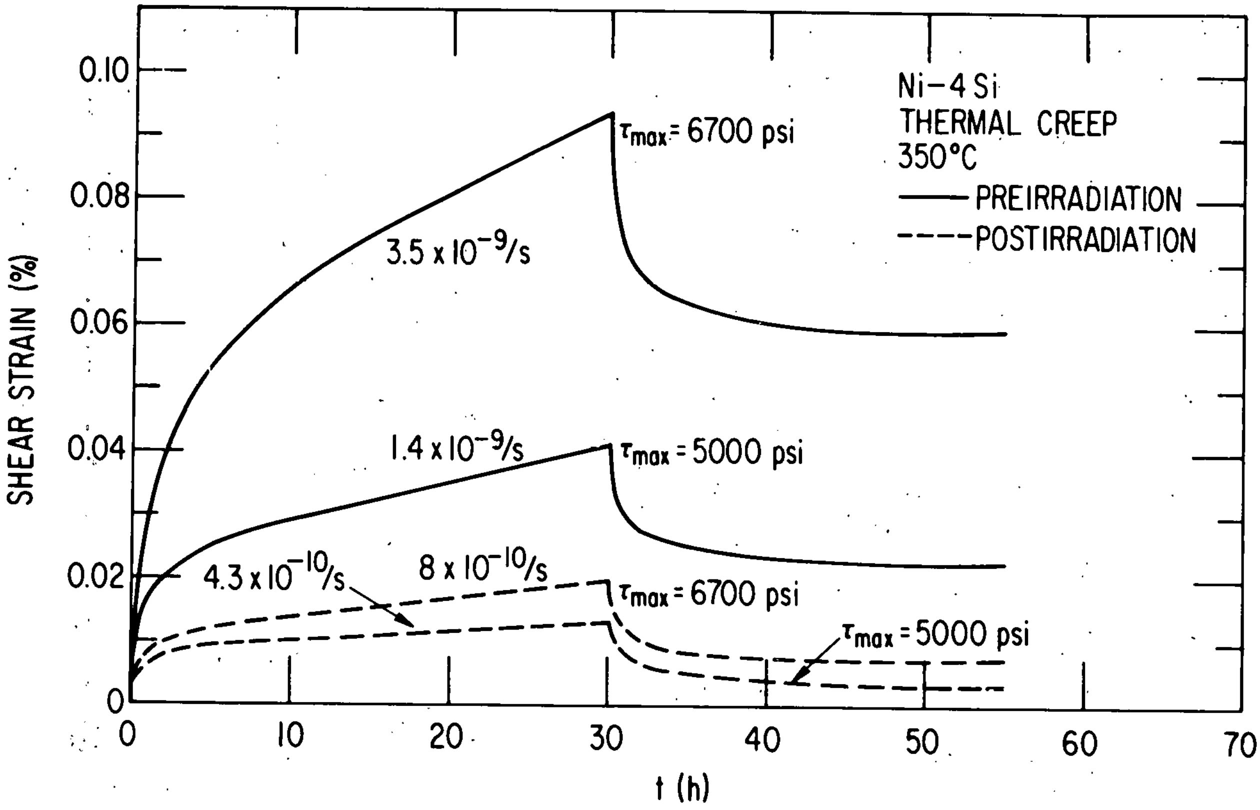

Figure 2. Strain-time behavior of nickel - 4 at. % silicon alloy in preirradiation and postirradiation conditions at 6700 & 5000 psi.

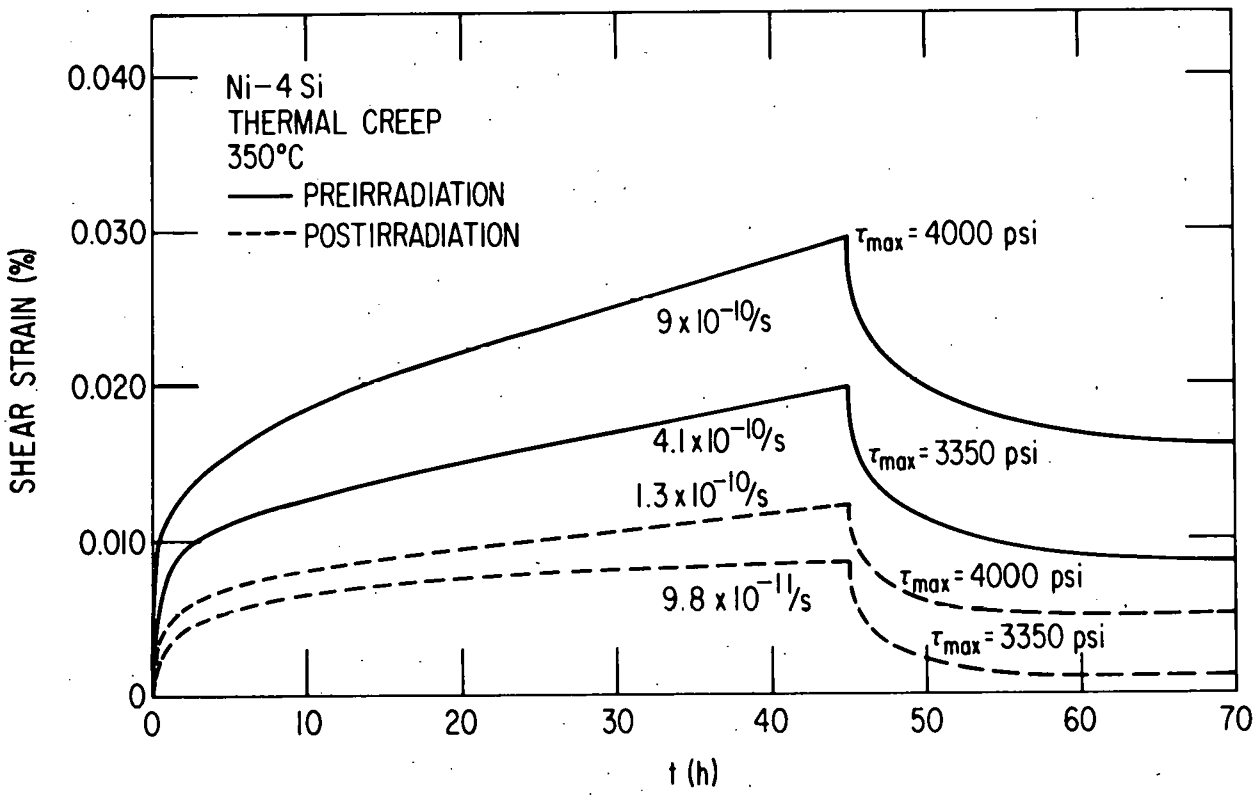

Figure 3. Strain-time of nickel - 4 at. % silicon alloy in preirradiation and postirradiation conditions at 4000 & 3350 psi.

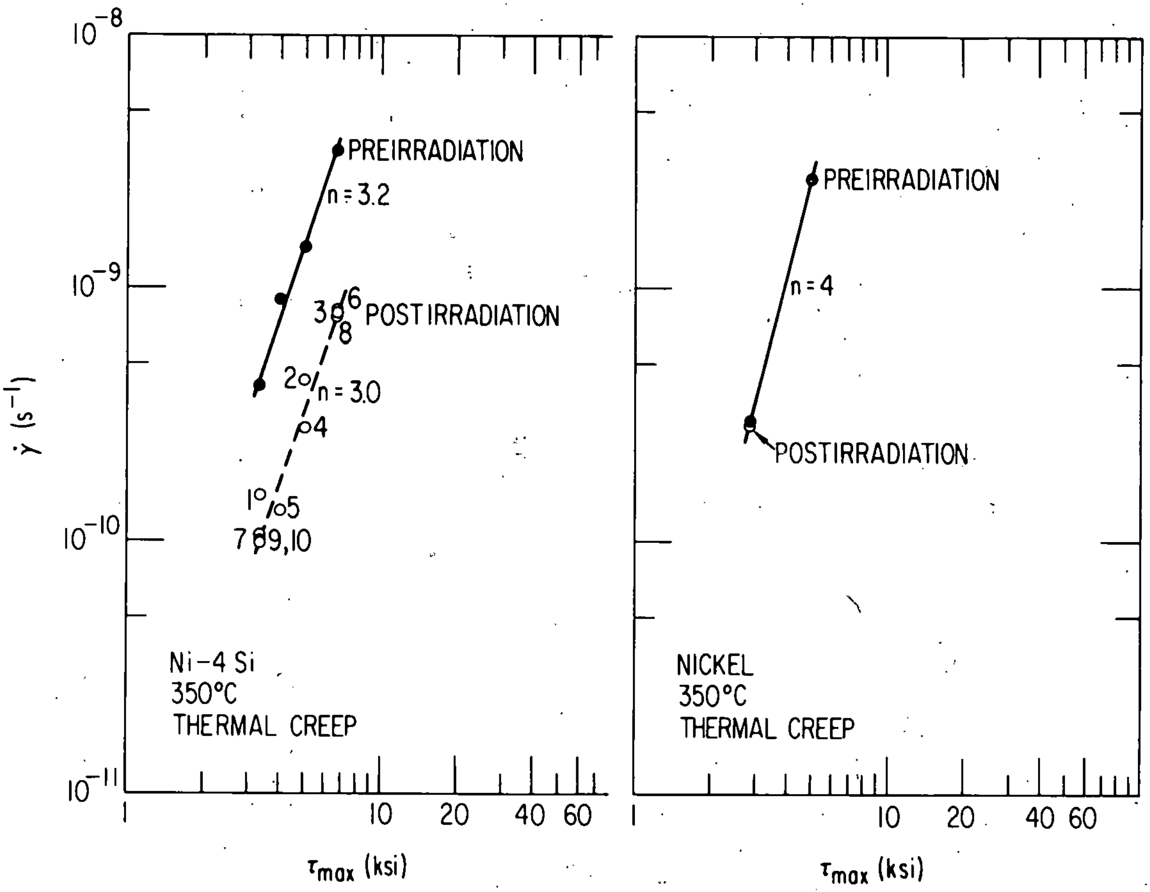

Figure 4. Stress dependence of the steady state creep rates for nickel and nickel - 4 at. % silicon alloy at 350°C in preirradiation and postirradiation conditions. Irradiation conditions - 21 MeV deuterons, 2×10^{-6} dpa · s^{-1}, 0.075 dpa at 350°C.

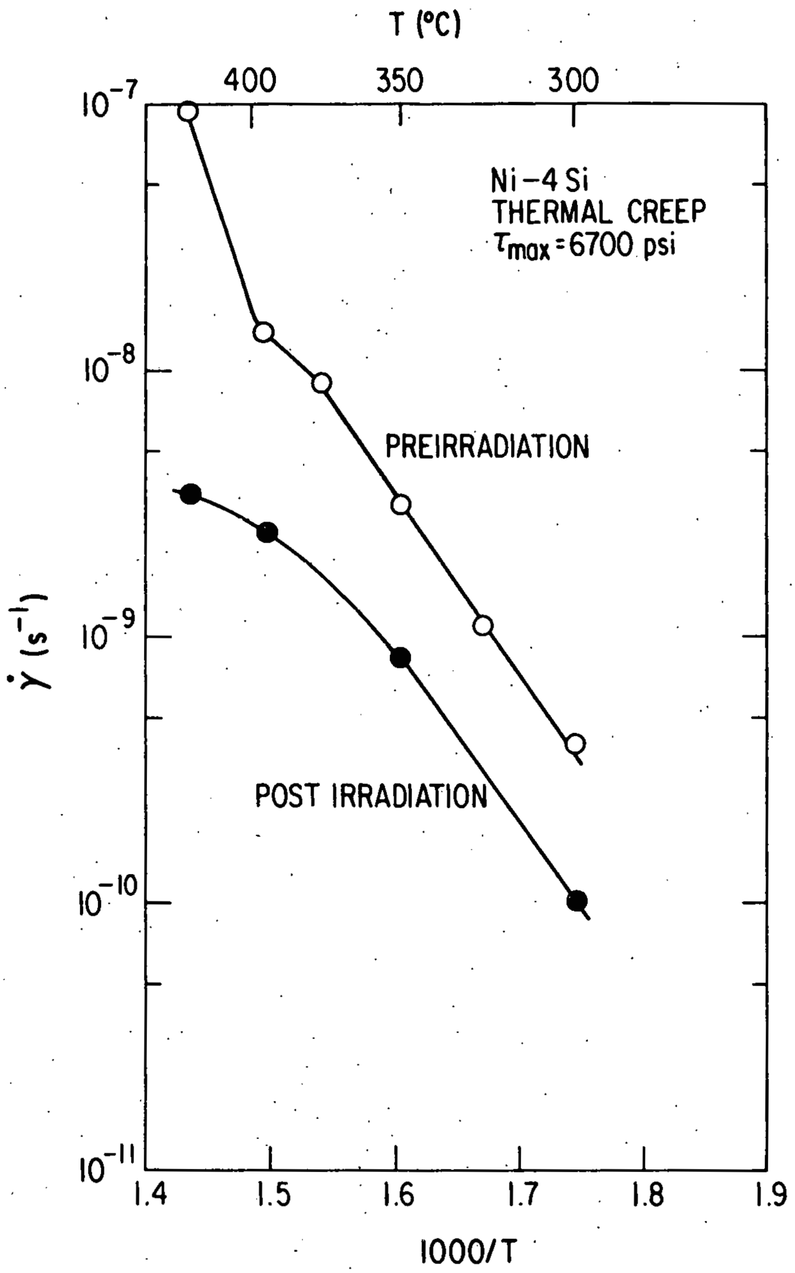

Figure 5. The temperature dependence of the steady state creep-rate of nickel - 4 at. % silicon alloy at 6700 psi maximum shear stress in preirradiation and postirradiation conditions. Irradiation conditions - 21 MeV deuterons, 2 x 10^{-6} dpa · s^{-1}, 0.075 dpa at 350°C.

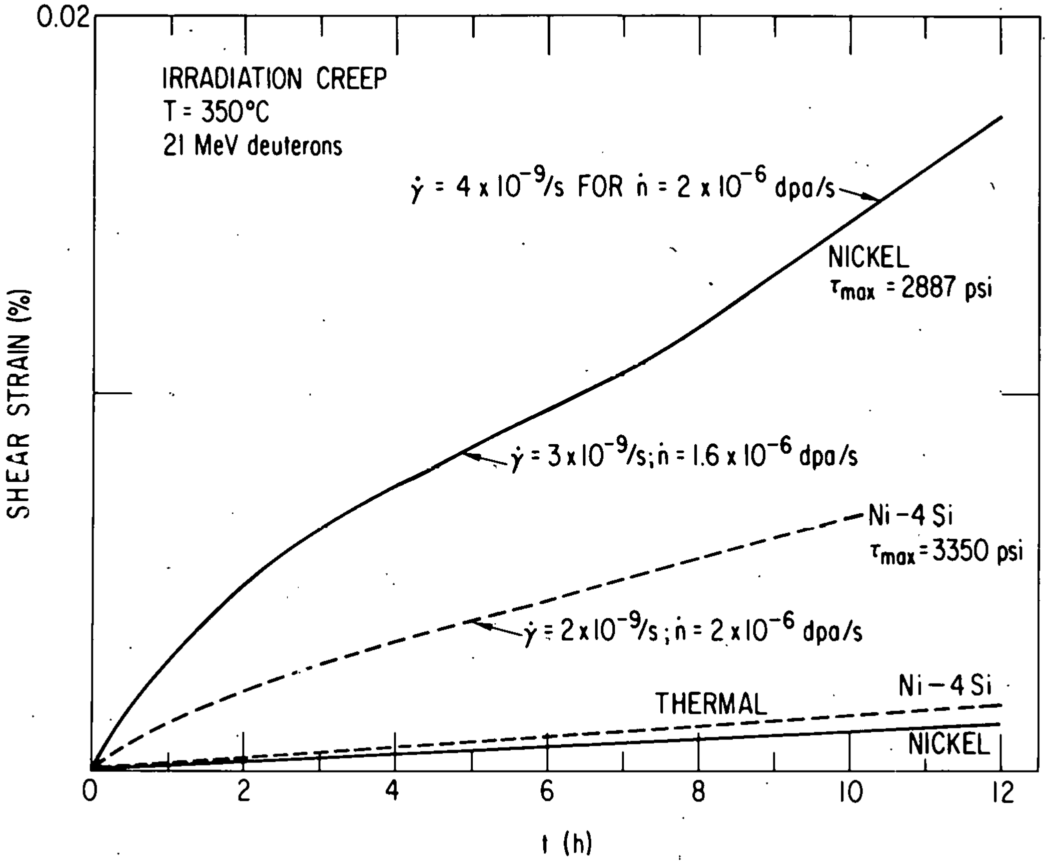

Figure 6. Irradiation enhanced creep deformation in pure nickel and nickel - 4 at. % silicon alloy during 21 MeV deuteron irradiation at 350°C at a dose rate of ∿2 x 10^{-6} dpa · s^{-1}.

DISTRIBUTION FOR DAFS QUARTERLY REPORTS

UC-20 (122)
UC-20c (80)
APPROVED SPECIAL DISTRIBUTION (82)

Argonne National Laboratory (3)
9700 South Cass Ave.
Argonne, Illinois 60439

L. R. Greenwood
A. Taylor
H. Wiedersich

Brookhaven National Laboratory (1)
Associated Universities
Upton, New York 11973

Chairman, Department of Nuclear Energy

Columbia University (1)
Plasma Physics Laboratory
New York, New York 10027

R. A. Gross

Department of Energy (7)
Mail Stop B-107
Washington, D.C. 20545

Assistant Director for Materials Technology, RRT
N. A. Davies
J. F. Decker
P. B. Hemmig
K. G. Moses
R. E. Price
F. T. Scott

Department of Energy (3)
Richland Operations
Richland, WA 99352

W. A. Burns
G. M. Chenevert
L. A. Pasquini

DISTRIBUTION (cont'd)

General Atomic Company (3)
P. O. Box 81608
San Diego, California 92138

C. Baker
G. R. Hopkins
L. Rovner

Hanford Engineering Development Laboratory (28)

W. L. Bunch/L. L. Carter	W/B-47
T. T. Claudson	W/C-16
D. G. Doran (10)	W/A-57
F. A. Garner	W/A-57
D. S. Gelles	W/A-57
R. E. Gold	W/C-39
H. L. Heinisch	W/A-57
F. M. Mann	W/FED-429
W. N. McElroy	W/C-39
G. H. Moulthrop	W/C-115
R. E. Nygren	W/A-58
E. K. Opperman	W/A-58
N. F. Panayotou	W/A-53
R. E. Peterson	W/E-18
E. W. Pottmeyer	W/E-14
R. W. Powell	W/A-57
R. E. Schenter	W/FED-420
J. O. Schiffgens	W/A-57
R. L. Simons	W/A-57

Lawrence Livermore Laboratory (2)
University of California
P. O. Box 808
Livermore, California 94550

M. W. Guinan
C. M. Logan

Los Alamos Scientific Laboratory (3)
University of California
P. O. Box 1663
Los Alamos, New Mexico 87544

D. J. Dudziak
C. R. Emigh
W. Green

DISTRIBUTION (cont'd)

Massachusetts Institute of Technology (1)
Cambridge, Massachusetts 02139

L. Lidsky, Department of Nuclear Engineering

McDonnell-Douglas Astronautics (1)
P. O. Box 516
St. Louis, Missouri 63166

D. Kummer

Mound Laboratory (1)
P. O. Box 32
Miamisburg, Ohio 45342

Manager, Technology Applications and Development

National Bureau of Standards (1)
Gaithersburg, MD 20760

C. D. Bowman

Naval Research Laboratory (2)
Metallurgy Division, Code 6390
Washington, D.C. 20375

I. Manning
J. A. Sprague

North Carolina State University (1)
Department of Nuclear Engineering
Raleigh, North Carolina 26707

J. R. Beeler, Jr.

Oak Ridge National Laboratory (8)
P. O. Box Y
Oak Ridge, Tennessee 37830

Director, Thermonuclear Division, Bldg. 9201-2
R. J. Colchin, Bldg. 9201-2
W. R. Martin, Bldg. 4500 S
F. G. Perey
M. Roberts, Bldg. 9204-1
J. O. Steigler
C. Weisbin
F. W. Wiffen

DISTRIBUTION (cont'd)

Pacific Northwest Laboratory (4)
P. O. Box 999
Richland, Washington 99352

- J. L. Brimhall
- T. Chikalla
- A. B. Johnson
- L. C. Schmid

Plasma Physics Laboratory (3)
Princeton University
Forrestal Campus
Box 451
Princeton, New Jersey 08540

- C. Osgood
- W. Price
- K. Wakefield

Rockwell International (1)
Energy Systems Group
8900 DeSoto Ave.
Canoga Park, California 91304

- D. Kramer

Sandia Laboratories (2)
Albuquerque, New Mexico 87115

- F. L. Vook (2)

Sandia Laboratories (1)
Livermore, California 94550

- W. D. Wilson

University of Michigan (1)
Nuclear Engineering Department
College of Engineering
Ann Arbor, Michigan 48105

- T. Kammash

DISTRIBUTION (cont'd)

University of Virginia (1)
Charlottesville, VA 22901

W. A. Jesser

University of Wisconsin (1)
1500 W. Johnson Drive
Madison, WI 53706

P. Wilkes

Westinghouse Electric Corporation (2)
Research and Development Center
Beulah Road
Pittsburgh, Pennsylvania 15234

H. R. Holland
J. A. Spitznagel